December 2020

Combustion Phasing Modeling for Control of Spark-Assisted Compression Ignition Engines

Dennis Robertson
Clemson University, dennis.m.robertson@gmail.com

Recommended Citation

Robertson, Dennis, "Combustion Phasing Modeling for Control of Spark-Assisted Compression Ignition Engines" (2020). *All Dissertations*. 2732.
https://tigerprints.clemson.edu/all_dissertations/2732

COMBUSTION PHASING MODELING FOR CONTROL OF SPARK-ASSISTED COMPRESSION IGNITION ENGINES

A Dissertation
Presented to
the Graduate School of
Clemson University

In Partial Fulfillment
of the Requirements for the Degree
Doctor of Philosophy
Automotive Engineering

---

by
Dennis Robertson
December 2020

Accepted by:
Dr. Robert Prucka, Committee Chair
Dr. Zoran Filipi
Dr. Benjamin Lawler
Dr. Jiangfeng Zhang

ABSTRACT

Substantial fuel economy improvements for light-duty automotive engines demand novel combustion strategies. Low temperature combustion (LTC) demonstrates potential for significant fuel efficiency improvement; however, control complexity is an impediment for real-world transient operation. Spark-assisted compression ignition (SACI) is an LTC strategy that applies a deflagration flame to generate sufficient energy to trigger autoignition in the remaining charge. For other LTC strategies, control of autoignition timing is difficult as there is no direct actuator for combustion phasing. SACI addresses this challenge by using a spark plug to initiate a flame that then triggers autoignition in a significant portion of the charge. The flame propagation phase limits the rate of cylinder pressure increase, while autoignition rapidly completes combustion. High dilution is generally required to maintain production-feasible reaction rates. This high dilution, however, increases the likelihood of flame quench, and therefore potential misfires. Mitigating these competing constraints requires careful mixture preparation strategies for SACI to be feasible in production. Operating a practical engine within this restrictive regime is a key modeling and control challenge. Current models are not sufficient for control-oriented work such as calibration optimization, transient control strategy development, and real-time control. To resolve the modeling challenge, a fast-running cylinder model is developed and presented in this work. It comprises of five bulk gas states and a fuel stratification model comprising of ten equal-mass zones within the cylinder. The zones are quasi-dimensional, and their state varies with crank angle to capture the effect of fuel spray and mixing. For each zone, combustion submodels predict flame propagation burn duration, autoignition phasing, and the concentration of oxides of nitrogen. During the development of the combustion submodels, both physics-based and data-driven techniques are considered. However, the best balance between accuracy and computational expense leads to the nearly exclusive selection of data-driven techniques. The data-driven models are artificial neural networks (ANNs), trained to an experimentally-validated one-dimensional (1D) engine reference model. The simplified model matches the reference 1D engine model with an R^2 value of 70–96% for key combustion parameters. The model requires 0.8 seconds to perform a single case, a 99.6% reduction from the reference 1D engine model. The reduced model simulation time enables rapid exploration of the control space. Over 250,000 cases are evaluated across the entire range of actuator positions. From these results, a transient-capable calibration is formulated. To evaluate the strength of the steady-state calibration, it is operated over a tip-in and tip-out. The response to the transients required little adjustment, suggesting the steady-state calibration is robust. The model also demonstrates the capability to adapt in-cylinder state and spark timing to offset combustion phasing disturbances. This positive performance suggests the candidate model developed in this work retains sufficient accuracy to be beneficial for control-oriented objectives. There are four contributions of this research: 1) a demonstration of the impact of combustion fundamentals on SACI combustion, 2) an identification of suitable techniques for data-driven modeling, 3) a quasi-dimensional fuel stratification model for radially-stratified engines, and 4) a comprehensive cylinder model that maintains high accuracy despite substantially reduced computational expense.

To my mother, Nancy. You have always encouraged me to pursue my passions.

ACKNOWLEDGMENTS

I would first like to acknowledge Dr. Prucka for his support and guidance throughout my doctoral studies. Despite several technical challenges, he made sure that my research continued, and that I would gain invaluable experience and knowledge from my work.

I would next like to acknowledge the faculty and staff of Clemson University's Automotive Engineering Department. Dr. Lawler always has his door open for technical discussions and has provided vital insight for my research. Dr. Filipi always pushes students to achieve more, and I am thankful for his guidance and suggestions.

I am particularly grateful for the friends and classmates during my time at Clemson. I have learned as much from others as I have in class, and I hope I returned the favor. I really enjoyed my time with everyone outside of class and research, which made the past few years a great time in addition to a great learning experience.

Finally, I would like to acknowledge the contributions of Oakridge National Laboratories, who provided the SACI combustion dataset. Their work was funded by the United States Department of Energy (US DOE).

TABLE OF CONTENTS

Table of Contents (Continued)

Page

LIST OF TABLES

LIST OF FIGURES

Page

List of Figures (Continued)

List of Figures (Continued)

Page

List of Figures (Continued)

List of Figures (Continued)

List of Figures (Continued)

List of Figures (Continued)

List of Figures (Continued)

Page

DEFINITIONS / ABBREVIATIONS

1D	One-dimensional
3D	Three-dimensional
AFR	Air-fuel ratio
AI	Autoignition
aTDC	After top-dead center
BDC	Bottom-dead center
BGF	Burned gas fraction (combustion products only)
CA50	Crank angle of 50% burn location
CAD	Crank angle degree
CCV	Cycle-to-cycle variation
CFD	Computational fluid dynamics
CI	Compression ignition
COV	Coefficient of variation
Da	Damköhler number
DISI	Direct injected spark ignited
DOE	Design of experiments
ECL	Exhaust cam location
eEGR	External EGR
EGR	Exhaust gas recirculation
EVO	Exhaust valve opening angle
FKGM	Flame kernel growth multiplier
G/F	Gas to fuel ratio
HCCI	Homogeneous charge compression ignition
HRR	Heat release rate
ICL	Intake cam location
ID	Ignition delay
IMEP	Indicated mean effective pressure
ISHR	Initial slow heat release
IVC	Intake valve closing angle
Ka	Karlovitz number
KFG	Kinetics-fit (gasoline)
LES	Large-eddy simulation
LTC	Low temperature combustion
LTHR	Low temperature heat release
MAP	Manifold absolute pressure
MBT	Maximum brake torque
MFB	Mass fraction burned
nIMEP	Net indicated mean effective pressure
NTC	Negative temperature coefficient
NVO	Negative valve overlap

PVO	Positive valve overlap
Re	Reynold’s number
RI	Ringing intensity
RON	Research octane number
SA-HCCI	Spark-assisted homogeneous charge compression ignition
SI	Spark ignited
SICI	Spark induced compression ignition
SOI	Start of injection
SPCCI	Spark-controlled compression ignition
SSCI	Spark assisted stratified charge compression ignition
TDC	Top-dead center
TFSM	Turbulent flame speed multiplier

I. INTRODUCTION

Substantial fuel economy improvements for light-duty automotive engines demand novel combustion strategies. Examining ideal thermodynamic cycles has been a catalyst for the development of new combustion strategies. Maximizing the net work of the cycle therefore focuses on raising compression ratio, increasing the ratio of specific heats, and reducing pumping work [1]. Achieving constant volume combustion is one key to improving engine efficiency, but realization of this concept is hindered by several practical obstacles. The high temperature from the rapid combustion drives significant heat transfer losses, decreases the ratio of specific heats, and causes CO_2 dissociation to CO and O_2 [1-3]. Furthermore, the high peak pressure and rate of pressure rise poses significant structural challenges and generate excessive combustion noise [4].

Resolving the challenges resulting from high temperature combustion is one pathway to improving engine efficiency. Low-temperature combustion (LTC) strategies have shown promise in achieving rapid combustion without excessive temperatures and have been thoroughly studied for over four decades. LTC strategies use high dilution to keep combustion temperatures below ~2000 K. This dilution can be from excess air (i.e., lean operation), exhaust gas recirculation (EGR), or a combination of the two. The reduced cylinder temperatures and high dilution have several additional benefits. The ratio of specific heats increases, yielding a higher thermal efficiency. Heat transfer and pumping work are also reduced, maximizing net work. Knock is also mitigated, enabling a higher compression ratio to further increase efficiency. Additionally, the dilution can be utilized to partially control rate of heat release and moderate combustion noise issues.

The LTC concept has enabled improvements to stratified charge compression ignition and homogeneous charge spark ignition strategies [5-9], as well as offering entirely new combustion strategies. Early research into novel LTC strategies considered lean-homogeneous mixtures driven by chemical kinetics. Onishi et al. (1979) first examined LTC on a two-stroke engine [10]. Following this work, several research groups including Noguchi et al., Najt et al., and Thring et al., demonstrated significant emissions and efficiency improvements compared to spark-ignited (SI) or compression ignited (CI) combustion for both two-stroke and four-stroke LTC variants [11-14]. Though different terms have been used, homogeneous charge compression ignition (HCCI) is the widely accepted term for this type of combustion.

Although the potential efficiency benefit of HCCI is high, there are several challenges. HCCI combustion phasing is sensitive to intake temperature, intake humidity, dilution level, type of dilution, equivalence ratio, fuel composition, combustion chamber deposits, charge mixing, among others [15-22]. The combination of these sensitivities often only allows for a narrow range of engine actuator positions that can achieve an autoignition event that satisfies all combustion constraints. Additional engine actuators, e.g., intake heaters, have been introduced to expand the control authority over HCCI combustion. The limited range of operation has also been a consistent obstacle. Typically, naturally-aspirated HCCI operation is limited to about 1–4 bar IMEP from about 1000–4000 RPM. The high load limit occurs because faster burn rate generates exceedingly high cylinder pressure rise rates. Low ignition energy is a challenge at low speeds and low loads, but the means of increasing ignition energy (e.g., increased compression ratio, thermal barrier coatings [17]) can have a detrimental effect on peak pressure rise rates at higher loads. Christensen et al. and Dec et al. expanded the high-load limit of HCCI through boosting, high dilution, and late combustion phasing [20,23,24]. Loads of up to 20 bar IMEP are achieved under steady-state conditions, however, transient operation remains a challenge.

Several strategies have emerged that at least partially mitigate many of the obstacles facing HCCI. Aiming to improve the low load limit of HCCI, researchers have investigated the use of a spark discharge to increase ignition energy. Urushihara et al. successfully extended the low-load limit of HCCI with a spark shortly before autoignition [25]. At these conditions, the mixture composition and temperature are too lean to support a flame, but the spark generates combustion radicals that help trigger the autoignition event. Zigler performed optical studies on this type of spark-assisted HCCI and demonstrated a radial reaction front that accelerated autoignition in regions of the combustion chamber [26]. No clear flame developed at these conditions, though the autoignition event timing is clearly linked to the use of the spark.

Alternatively, the in-cylinder conditions can be tuned such that the spark produces a flame kernel and a propagating flame. The additional energy from the deflagration flame then triggers autoignition in a significant portion of the charge, rapidly consuming the remaining charge. This two-stage combustion—spark-initiated flame propagation, then compression ignition—is spark-assisted compression ignition (SACI). This strategy leverages the slow burning of the flame to reduce peak pressure rise rates, enabling a wide range of operation. Control of combustion phasing is done using a spark plug, allowing the engine controller to achieve transient operation and quickly respond to transient in-cylinder conditions. SACI mitigates or resolves the production obstacles of HCCI, and thus has strong potential as a production-viable LTC strategy. Other terms for the same or similar modes of combustion include spark ignited-compression ignition (SI-CI), spark-assisted stratified compression ignition (SSCI), spark-induced compression ignition (SICI), spark-controlled compression ignition (SPCCI), and hybrid combustion.

SACI Combustion Description and Terms

SACI combustion is characterized by a flame propagation phase that triggers autoignition of the remaining charge. The spark event generates a flame kernel typical of SI combustion. The kernel develops into a propagating flame, increasing in-cylinder temperature and pressure. The elevated temperature and pressure from the flame are therefore a controllable source of ignition energy. Numerous optical studies have confirmed flame propagation and autoignition each consume a significant portion of the charge [26-28]. Zigler [26] performed optical studies focusing on a wide range of SACI operation, capturing conditions with and without a flame. The propagating flame triggers autoignition which rapidly consumes the remaining charge.

The typical SACI heat release rate depicts this dual-stage character (Figure I-1). The initial combustion phase exhibits a much slower rate of heat release than the later stage. A useful metric in understanding SACI combustion is the SI portion, defined as the proportion of deflagration flame heat released compared to the total heat released, (1). An SI percent of 0% is HCCI, and an SI percent of 100% is SI combustion (Figure I-2). Another synonymous term is initial slow heat release (ISHR), and the inverse of SI portion is the autoignition fraction (*AIfrac*).

$$\text{SI Portion [\%]} = 100 \times \frac{SI\ Heat\ Released}{Total\ Heat\ Released} \tag{1}$$

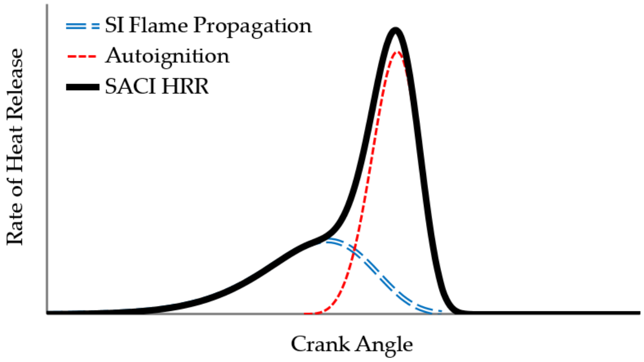

Figure I-1: SACI heat release rate (HRR) shown as a composition of SI and AI components. Both the flame propagation and autoignition consume significant portions of the charge.

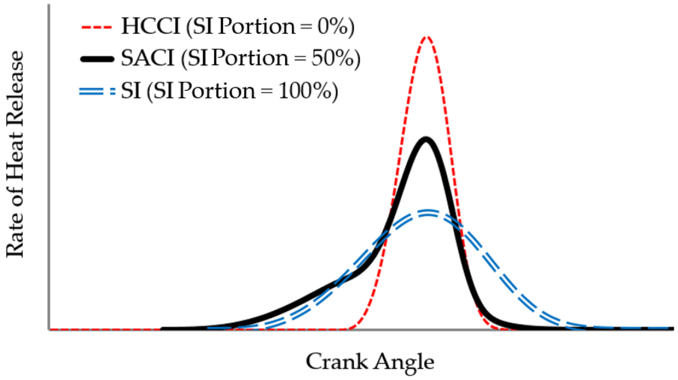

Figure I-2: Comparison of SI portion from 0% (i.e., HCCI) to 100% (i.e., SI). The SI portion = 50% has a clear dual-stage character that demonstrates the two different combustion regimes.

The optimal SI portion is anticipated to be the SI portion that achieves the maximum efficiency within noise, controllability, emissions, and drivability constraints. The relative dominance of each constraint varies considerably with load. A production-intent control strategy considers two SI portion strategies in their implementation of SACI [29]. At low loads, the SI portion will increase from ~30% to ~75%. This is achieved by maintaining the total EGR rate constant but shifting the balance of EGR towards high levels of external EGR as load increases. As the cooled EGR lowers cylinder temperatures, the SI portion must increase to maintain the same autoignition phasing. Under high-load boosted conditions, however, the SI portion target remains constant at ~75% (Figure I-3).

As a function of load, there are multiple factors that combine to produce alternative SI portion responses. Olesky et al. found that for fixed in-cylinder composition, autoignition occurred at ~1040 K regardless of spark timing [30], which is consistent with [29]. The SI portion decreases as spark timing is retarded, as more ignition energy is being provided by compression from the piston. However, dilution level, temperature at the start of compression, and injection strategy can vary significantly as load increases. Therefore, there is no general trend for SI percent as a function of load.

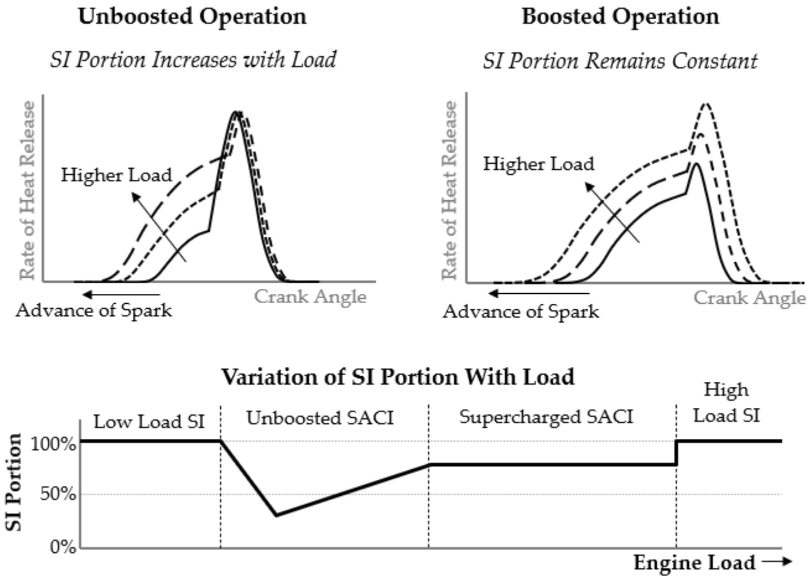

Figure I-3: Depiction of SI portion as a function of load for two different regimes. In the unboosted regime (top left), SI portion increases with load. In the supercharged regime (top right), SI portion remains constant with load. The variation of the SI portion over the entire engine load is shown in the bottom plot. Adapted from [29].

Autoignition events can produce high levels of combustion noise. The ringing intensity (RI) metric quantifies this fast heat release typical in LTC combustion. It is defined in (2), where typical limits are approximately 5 MW/m^2 [4].

$$RI = \frac{1}{2\gamma}\frac{\left(0.05 \cdot \frac{dP}{dt}_{\max}\right)^2}{P_{\max}}\sqrt{\gamma R T_{\max}} \tag{2}$$

The majority of SACI engine research has focused on stoichiometric conditions to enable a three-way catalyst. To aid in comparing lean burn to stoichiometric conditions and understand the impact of dilution, additional metrics have been introduced to reflect both air and EGR dilution. One of these terms is the gas/fuel ratio (G/F) [1] and is defined in (3). The other term is ϕ' [31], and is defined in (4). *BGF* in this equation is the burned gas fraction.

$$G/F = \frac{Air + EGR\ Mass}{Fuel\ Mass} \tag{3}$$

$$\phi' = \frac{\left(\frac{Fuel\ Mass}{Air + EGR\ Mass}\right)_{actual}}{\left(\frac{Fuel\ Mass}{Air\ Mass}\right)_{stoich}} \approx \phi(1 - BGF) \tag{4}$$

Motivation for SACI

SACI does not significantly sacrifice the efficiency potential of HCCI in achieving a practical solution to the challenges facing LTC. Fuel conversion efficiency has widely been reported to be improved by 10% (~3 percentage points) over spark ignition engines with values near 38% fuel conversion efficiency [32-37]. Several studies directly compared SACI with SI on the same engine with no change in compression ratio [32-34]. The compression ratios for these three studies are 10.7:1–11.9:1. Each confirms a 10% improvement with broad agreement on the sources of improvement. Pumping work is measurably lower with SACI. Reduced heat transfer and combustion duration is also indicated as potential source of improvement. Combustion efficiency is studied in [34], with the authors noting similar or improved combustion efficiency compared to SI. High-speed high-load SACI operation is only examined for a lean-burn performance engine by Chiodi et al. and Koch et al., where engine speeds of up to 8500 RPM are considered [38,39].

A production-intent SACI engine suggests 20% improvement compared to the a conventional gasoline engine, which implies a SACI brake efficiency of about 44% [40-43]. Chiodi et al. demonstrated an efficiency improvement of 25% at high load [38], although these results are under lean conditions compared to SI operation for rich mixtures. Additionally, Chiodi et al. do not consider emissions or noise constraints. Specific data is limited, but the efficiency improvements are generally attributed to pumping work reduction, reduced combustion duration, high compression ratio, and similar or increased combustion efficiency. The efficiency benefits derive from high compression ratio, high ratio of specific heats, reduced pumping work, lower heat transfer, and shortened burn duration. Stoichiometric operation is feasible, enabling a three-way catalyst. Alternatively, if the efficiency benefits of lean operation are sufficient, development of lean aftertreatment systems may be a preferential pathway to stoichiometric operation. Table I-1 lists key SACI configuration and performance parameters.

Table I-1: Key SACI performance and configuration parameters.

Parameter	**Value**
Compression Ratio	11:1–16.5:1
Overall Dilution	Air (1 ≤ λ < 2) EGR: 20–35%
Efficiency Improvement[1]	10–25%
Peak Load (nIMEP)	Naturally-aspirated: 10 bar
	Boosted: 27 bar[2]

[1] Compared to SI under various conditions.

[2] Achieved with ~3 bar boost pressure in [39].

A final advantage of SACI combustion compared to HCCI is the relative ease in transitioning from SACI to SI. The use of SACI during a transition from HCCI to SI has been successfully demonstrated by Zhang et al. and Yang et al. [44,45]. The need for SACI combustion in their transition highlights the potential transient benefits of SACI. The Zhang et al study is performed on a single cylinder pent-roof port-fueled engine with a compression ratio of 10.7:1 and a fully-flexible valvetrain. The fuel is 93 RON gasoline in a stoichiometric mixture for HCCI, SACI, and SI. The transition is performed at 1500 RPM, 3 bar IMEP and 3000 RPM, 2 bar IMEP. The HCCI-SACI-SI transition took about 10 cycles where SI portion gradually shifted from 0% to 100% as the residual gas fraction transitioned from 40% to less than 10%. The Yang et al. study is performed on a similar engine, although the valvetrain is a two-stage lift design, as opposed to a fully-flexible valvetrain.

SACI Challenges

Though there are potential efficiency benefits, SACI combustion magnifies the controls complexity of conventional engines. Additional actuators are required, the degrees of freedom are expanded, and the engine may need to transition between different combustion modes. Mode switching is likely required, which increases the controls complexity as the charge preparation requirements (e.g., EGR, air-fuel ratio, effective compression ratio) can vary significantly between modes. Furthermore, the charge composition requirements for the SI and AI combustion phases are different and often competing. These competing constraints lead to a potentially narrow operating range and charge preparation challenges.

The precise phasing of autoignition is critical to controlled SACI combustion, and consideration of fuel properties is necessary. The chemical reactions that lead to autoignition occur over a finite time called the ignition delay. For typical engine conditions, autoignition is triggered by self-heating or chain-branching reactions [1,2]. Ignition delay and the mechanism of autoignition are both nonlinear and highly sensitive to several parameters. Combinations of pressures, temperatures, and dilution highlight different reaction pathways with a given chemical mechanism. Furthermore, as the unburned gas temperature approaches autoignition during compression and flame propagation, the chemical kinetics pass through a region with a negative temperature coefficient (NTC) region. Within this region, additional temperature produces an increase in ignition delay. While the detailed study of chemical mechanisms is outside of the scope of this study, it is important to note that fuel composition has a strong influence on autoignition timing for a given set of conditions [1-3]. This behavior creates a major obstacle to production since fuel blends are somewhat unregulated and variable from pump to pump [46,47]. This variation in fuels must be considered as part of a production control algorithm for SACI engines.

Few studies have performed a thorough evaluation of the fuel sensitivity on SACI combustion specifically. One study, performed by Weall and Szybist, compared the combustion performance of SACI on a wide range of fuels on a highly modified pent-roof direct injection spark ignited (DISI) engine [33]. The test fuels include 91 RON E0 gasoline, E85, and a 50% mix of gasoline and isobutanol (IB50). E85 has the lowest propensity for autoignition, and thus requires a greater SI portion and early spark timing to generate sufficient pressure and temperature to trigger autoignition. The sensitivity to autoignition phasing is similar for gasoline and IB50 at the points tested. E85, however requires an advance of 10–20 CAD spark timing to achieve a similar CA50. This difference decreased with load. Using a coarse assumption of a linear relationship between ethanol content and required spark advance, the data suggests a ~0.2 CAD advance of spark timing required per 1.0 percentage point change in ethanol content. If the linear assumption is valid, spark timing differences from E0 to E10 could be in the range of 2 CAD. This change in spark timing is significant enough that it needs consideration in control algorithms.

The impact of low-temperature heat release (LTHR) may be critical to consider for SACI. The effect on end-gas autoignition has been thoroughly assessed for SI combustion. Szybist and Splitter evaluated the impact that fuel types and the unburned gas state had on SI knock [48]. Unlike the study performed by Weall and Szybist, the SI knock study used no external EGR and is performed at a lower compression ratio, limiting the application of their study to SACI. However, they note that under these conditions, LTHR is a significant factor that affected end-gas autoignition. Consistent with the sensitive nature of autoignition, the precise trend varies with fuel type and load. These results further suggest a method of fuel property identification is needed when a significant number of fuels are available to the consumer. For production purposes, it is likely that accurate feedback of heat release is required to characterize LTHR behavior of a given fuel. In this case algorithms and/or models are also required to translate the feedback information and correct feed-forward spark timing values.

Most studies considered stoichiometric combustion with high amounts of EGR, with some studies reporting over 30% total EGR. This dilution level is high for a deflagration flame and requires high charge motion, charge stratification, and/or low SI portion to achieve. Typically, as load increase, EGR shifts from internal to external EGR [29,35,49]. At low loads, the higher temperature from internal residuals increases flame speeds and accelerates autoignition. At higher loads, the increased charge density reduces the need for hot internal residuals, so the EGR balance shifts to cooled external EGR. Additionally, ringing and knocking limits become relevant at high loads. The cooler external EGR lowers the autoignition reaction rates and the propensity to knock. Yun et al., Manofsky et al., and Matsumoto et al. all transitioned to a higher proportion of external EGR as load increased [29,35,49]. All three studies are performed on a pent-roof combustion chamber research engine with a similar gasoline composition. The total EGR rate for Yun et al. and Manofsky et al. decreases with increasing load to increase volumetric efficiency. The decrease in total EGR is greater in the study by Yun et al., and Matsumoto et al. suggests a constant 30% total EGR level for all SACI operation. At low loads, where the engine transitions from low-load SI to low-load SACI, all EGR is internal. This fraction decreases to near-zero throughout the naturally aspirated load range. Under boosted operation, internal EGR is minimized.

Internal EGR control is often achieved with negative valve overlap (NVO), [29,34,35,37,50]. NVO is common for HCCI as it enables a high quantity of residual fraction with a relatively straightforward implementation [14]. NVO is also less sensitive to the pressure ratio between the intake and exhaust manifolds, providing less complex residual gas fraction estimation. Two studies examine the differences between NVO and PVO in a SACI engine. Both sources report an increase in thermal and volumetric efficiency with PVO as compared to NVO. Yun et al. examine internal EGR on a pent-roof combustion chamber research engine with a fully flexible valvetrain and 87 AKI gasoline fuel [49]. They find that for a given fuel mass under stoichiometric conditions, the internal residual fraction is lower with PVO. The cooler temperatures enabled earlier combustion phasing, which coupled with pumping work reduction, yielded higher efficiencies. Li et al. also evaluate NVO and PVO on a single cylinder research engine with a pent-roof combustion chamber and a fully-flexible valvetrain [32]. 93 RON gasoline is used for this study. They consider two PVO strategies: early intake valve opening and late exhaust valve closing. The authors propose a combination of the two PVO strategies to suit the advantages of each strategy as a function of load. Compared to NVO, the improved pumping work of either PVO strategy leads to a greater efficiency gain compared to stoichiometric SI flame propagation. Matsumoto et al. depict NVO as the strategy to achieve internal EGR at low loads, but mention that PVO may be used instead [29]. Consistent with the findings from the other studies, the EGR balance shifts towards external EGR as load increases.

Particular attention must be paid to how the EGR concentration varies with transients, and this is a significant research gap for SACI. In-cylinder residual fraction under transient conditions can vary greatly as external EGR transport delay is generally several engine cycles. Rapid tip-outs can result in high EGR fractions which is detrimental to flame propagation. Conversely, tip-ins may decrease EGR levels and produce excessive ringing intensity. For these reasons, transient operation has been a significant obstacle to high-EGR strategies. Mixture stratification is likely to evolve quickly within a cycle so there may only be small range where combustion can occur. At later combustion phasing, the combustion chamber has been shown to be more homogenous, and therefore ignition or robust control may not be possible [51].

Several studies are successful in achieving a wide range of SACI operation with a single early injection or made no mention of injection strategy [34,35,50]. Despite a single early injection, Olesky et al. demonstrate in simulation that significant fuel stratification is present. The start of injection for their study is fixed at 330° bTDC, and the earliest spark timing of their spark sweep is 210 CAD later. The local equivalence ratio at the spark plug is richer than the global equivalence ratio by up to 0.6 [51]. The local mixture composition approaches the global composition as spark timing is delayed, reaching mixture homogeneity at around 40° bTDC. The control authority of the flame to control autoignition strongly correlates with mixture heterogeneity. As the flame propagates through richer local mixtures, laminar flame speed increases which improves the flame stability.

The fuel mixture can be stratified to add another degree of combustion control. As the volume surrounding the spark plug is relatively small, large changes in fuel composition near the plug have a small impact on overall air-fuel ratio (AFR). Early research on spark-assisted HCCI by Urushihara et al. [25] uses a small bowl near the spark plug to geometrically define this region, and work by Chiodi et al. utilizes a pre-chamber spark plug design [38]. An alternative fuel-stratification strategy is a central injector with a late injection. This strategy has been used in stratified-charge lean-burn gasoline engines to achieve the same effect [52]. A small amount of fuel is injected immediately before spark to produce a relatively rich zone near the spark plug. Flame speeds increase as equivalence ratio increases from lean, peaking at an equivalence ratio of about 1.2 [1]. Higher flame speeds push the flame operation away from the flame quench limit, which helps to improve the sensitivity of the spark timing on autoignition. Fuel stratification as a SACI combustion control method has been suggested by Olesky et al. [51] and implemented by Urushihara et al. [25], Matsumoto [29], and Chiodi et al. [38]. Charge mixing, fuel injection strategies, and specialized combustion chamber designs have all shown promise in achieving sufficient fuel stratification for control.

SACI Modeling

Spark-ignited (SI) and stratified charge compression ignition engines already have a significant calibration burden [53]. The industry has already responded with expanded use of model-based control and optimization methods, with promising success [54-56]. For SACI, the complexity of the two-regime combustion adds further control and calibration complexity. Recognizing these modeling challenges, Yang and Zhu developed a control-oriented model specifically for SACI [57]. Their model is crank-angle resolved, two-zone, and leverages physics-based submodels. Their results show excellent agreement, but the model is limited to two zones, which precludes fuel stratification. Expanding on previous work, Ortis-Soto also developed a simplified model for SACI [58]. This work, as well, is two-zone and crank-angle resolved. Additionally, control-oriented models that consider only a subset of in-cylinder state and combustion are not found in the literature. For example, as previously mentioned, fuel stratification is likely a key enabling strategy for practical SACI applications. One technique for evaluating fuel stratification is three-dimensional computational fluid dynamics (CFD) modeling. However, this approach is computationally intensive, thus eliminating it from consideration for real-time control and calibration optimization. Grenda developed a radially-focused charge stratification model for HCCI [59] using about 100 zones and several partial differential equations to solve temperature and fuel distribution. While certainly less computationally expensive than CFD, it is unlikely that this level of complexity is tractable for some control-oriented models.

Research Objectives

- Objective: develop a model with sufficient accuracy for control-oriented tasks with a low computational expense. This will consist of the following tasks:
    - Model bulk gas states and a spatial and temporal fuel stratification based on actuator position. The in-cylinder states consist of pressure, temperature, equivalence ratio, mass, and burned gas fraction. (CHAPTER THREE)
    - Model combustion by using the in-cylinder state submodel results to predict combustion phasing, duration, and other quantities. (CHAPTER FOUR)
    - Compile the individual submodels together to form the complete cylinder model, compare to the reference model, and explore the model response (CHAPTER FIVE)

- Map the input space of the model to evaluate potential control strategies and produce a steady-state calibration. (CHAPTER SIX)
- Evaluate the model against a 1D engine model under transient schedules and input disturbances to demonstrate the capability of this model. (CHAPTER SIX)
- Consider the balance between computational expense and accuracy for several candidate combustion model structures. (APPENDIX A)
- Investigate potential synergies with mild-hybridization to ease the challenge of mode-switching. (APPENDIX B)

II. CONTROL-ORIENTED MODEL FRAMEWORK

The primary experimental test platform is a BMW B38A15 from a 2015 Mini Cooper F55. This engine is representative of a modern, high-feature SI engine. The SACI reference engine model is developed from this experimental platform in GT-Power, a one-dimensional (1D) engine simulation software. The base engine specifications are in Table II-1, and a picture of the combustion chamber and installed engine are in Figure II-1.

Table II-1: Experimental platform engine specifications.

Parameter	**Value**
Engine Displacement and Type	1.5 L, inline 3-cylinder
Peak Torque and Power	220 Nm @ 1250–4300 RPM 100 kW @ 4400 RPM
Bore x Stroke	82 mm x 94.6 mm
Compression Ratio	11.0:1 (stock)
Other features	Dual cam phasers Intake continuously variable valve lift 245 bar central GDI injection

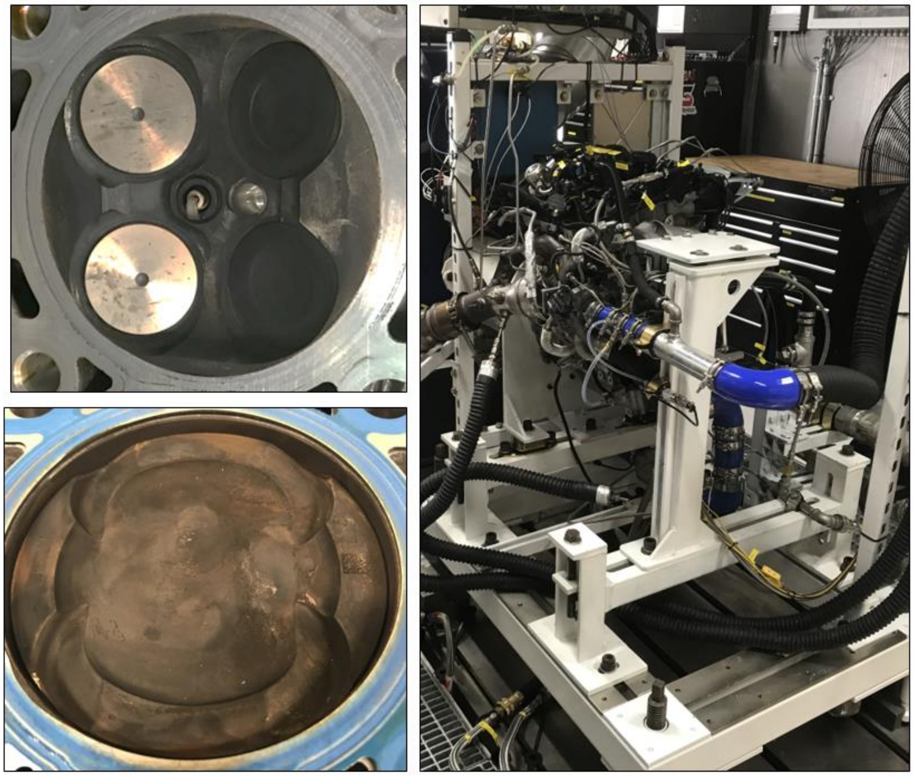

Figure II-1: Experimental platform combustion chamber (top left), piston top (bottom left), and installation (right).

The engine control module (ECM) for this engine is Pi Innovo OpenECU M670B. The programming of the ECM is conducted in MATLAB Simulink, a control-focused programming environment platform that is representative of a production ECM. The ECM has a single-core 267 MHz processor and 128 kB RAM. Figure II-2 depicts an image of the installed controller. A selection of control actuators available on this engine is listed in Table II-2.

Table II-2: Control actuators for experimental engine (baseline configuration).

Air/Exhaust Path	Camshafts and Valves	Combustion
Electronic Wastegate	Dual cam phasing	Direct Injector
Electronic Throttle	Continuously variable intake valve lift	Spark Plug

Figure II-2: Pi Innovo OpenECU M670B installed in the test cell.

Experimentally Validated Simulation Model

Experimental results are processed and used to develop a model in a 1D engine simulation software. This 1D engine model provides noise-free computation of all relevant system states including those that are challenging to measure, critical for accurate in-cylinder submodels. It is configured to match the experimental setup, Figure II-3. Validation against experimental data is performed with the agreement between the 1D engine model and experimental data depicted later in this chapter.

Where possible, direct engine measurements are used. Valve lifts are measured on the engine at several intake valve lift positions. Figure II-4 depicts the valves lifts for both valves including the progression of intake valve lift as the variable valve lift actuator moves from one extreme to the other. Where direct engine measurements are not possible, engineering judgment or sample data from GT-Power examples are used.

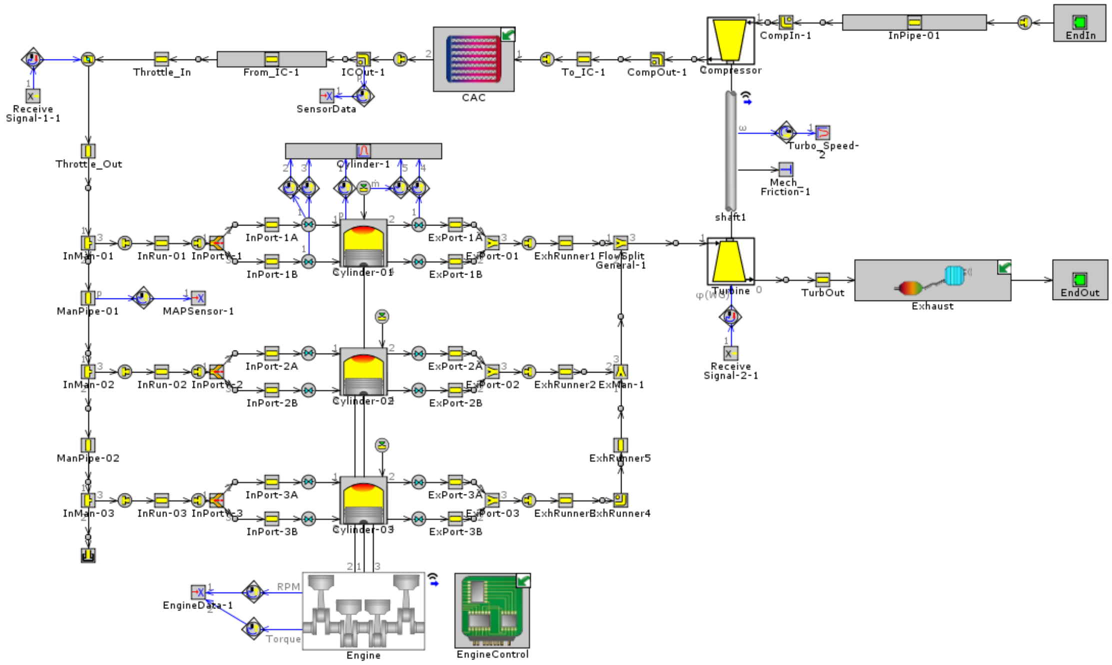

Figure II-3: 1D engine model of the 1.5 L turbocharged engine.

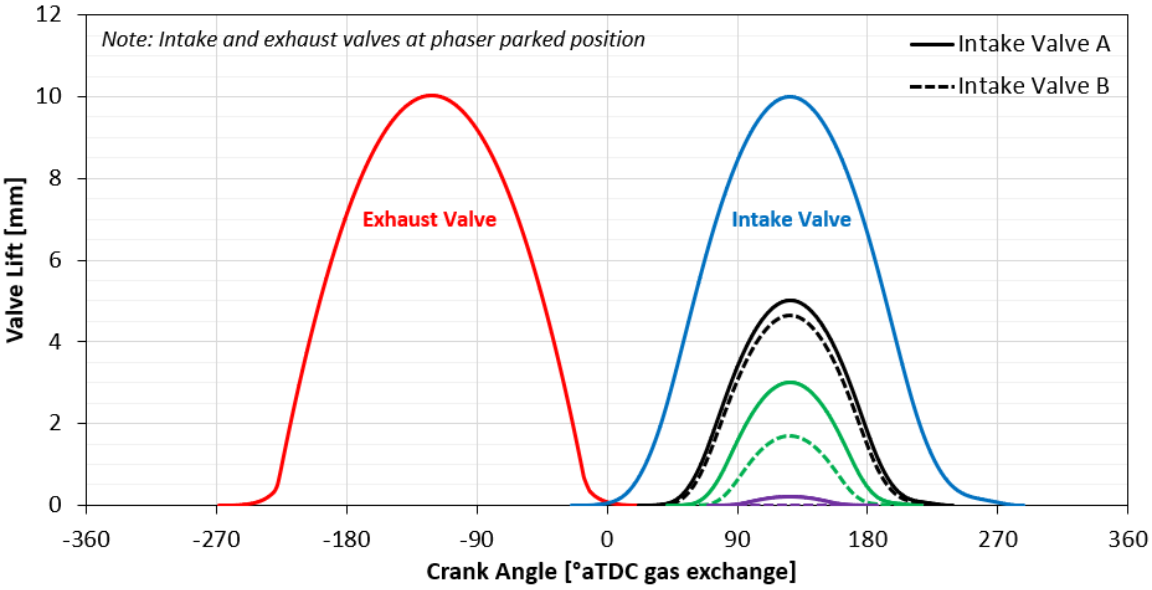

Figure II-4: Valve lift profiles for the intake and exhaust valves.

The combustion chamber is modeled and reproduced in computer-aided design software. This is a useful input for predictive SI combustion modeling and is depicted in Figure II-5.

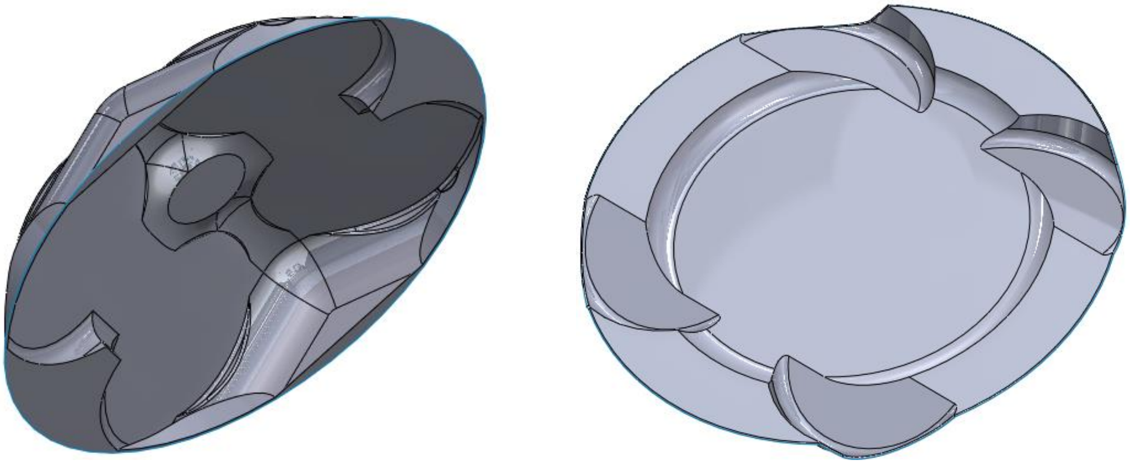

Figure II-5: CAD model of the B38 engine combustion chamber.

Further tuning of flow and combustion parameters to match experimental results yields a validated base 1D engine model. A sample comparison of pressure-volume diagrams at several points is illustrated in Figure II-6. Though there are some discrepancies at specific operating conditions, overall, the trends in the pumping loop and valve events match well.

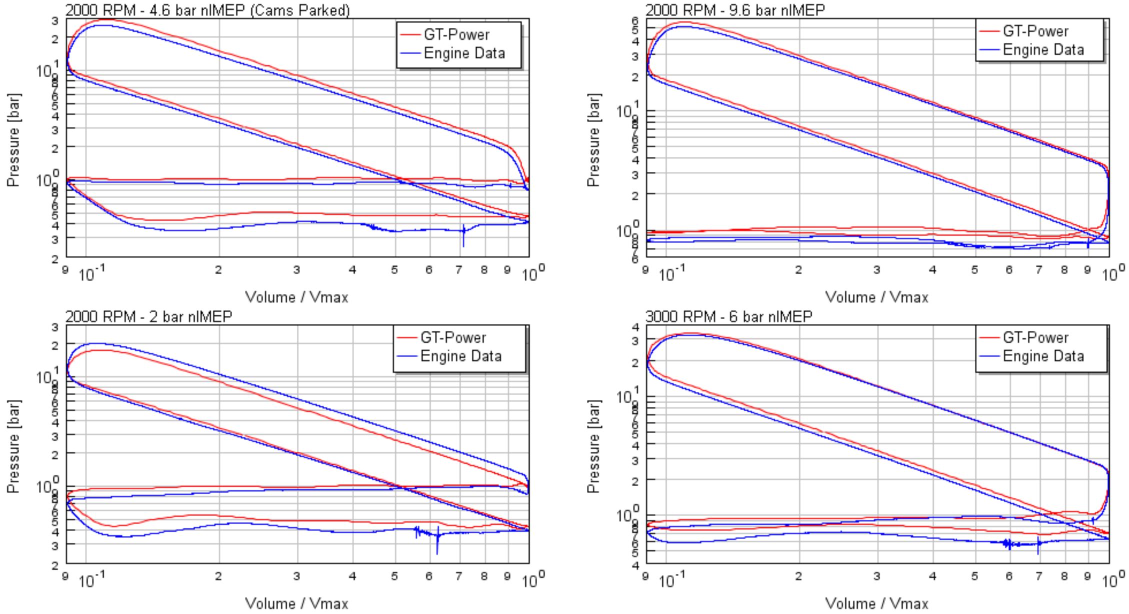

Figure II-6: Comparison of pressure-volume diagrams between GT-Power and experimental results.

This model is adapted to a design more suitable to a production SACI engine. The engine specifications used for both engine models are described in Table II-3, and the BSFC map of each engine is pictured in Figure II-7. The BSFC maps are generated using anticipated HRR curves for both SI and SACI. The SACI engine displacement is increased to produce the same peak torque and peak power as the stock engine, as the power density of the SACI engine is expected to be reduced because of high dilution. The 1D engine model of the stock B38 engine is modified to account for these engine platform changes. The geometric compression ratio is also increased, consistent with [60], where the production-intent engine compression ratio is 16:1. This model is presented in Figure II-8, and serves as the reference engine model for the control-oriented cylinder model discussed in the next section.

Table II-3: Engine configuration for the test engine and the SACI engine. The SACI engine is derived from the test engine with minimal configuration changes.

	Test Engine	**SACI Engine Variant**
Type	I-3 four-stroke spark-ignited	I-4 four-stroke Multi-Mode: Spark-ignited / Lean SACI / Stoichiometric SACI
Displacement	1.5 L	2.2 L
Compression Ratio	11.0:1	18:1
Nominal Operating Equivalence ratio	1.0 >1.0 at high power for exhaust component protection	SACI: 0.5 / 1.0 SI: 1.0
Boost Device	Turbocharger	Supercharger
Peak Torque	220 Nm @ 1250-4000 RPM	220 Nm @ 2000-3500 RPM
Peak BMEP	18 bar @ 1250-4000 RPM	13 bar @ 2500-3500 RPM
Peak Power	100 kW @ 4000 RPM	100 kW @ 5000 RPM

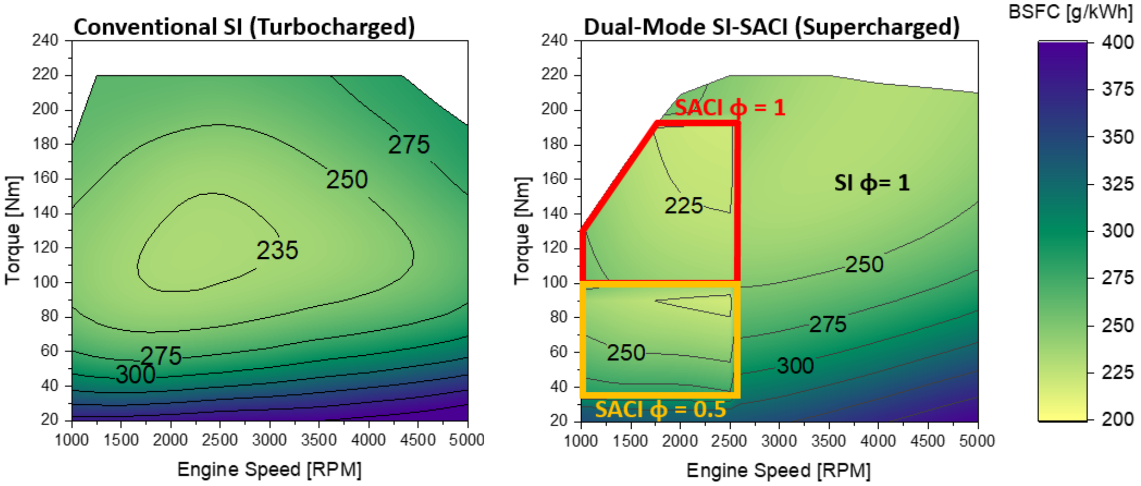

Figure II-7: BSFC maps for the conventional engine and the multi-mode SACI engine. SACI is limited to low engine speeds except for very low or very high loads.

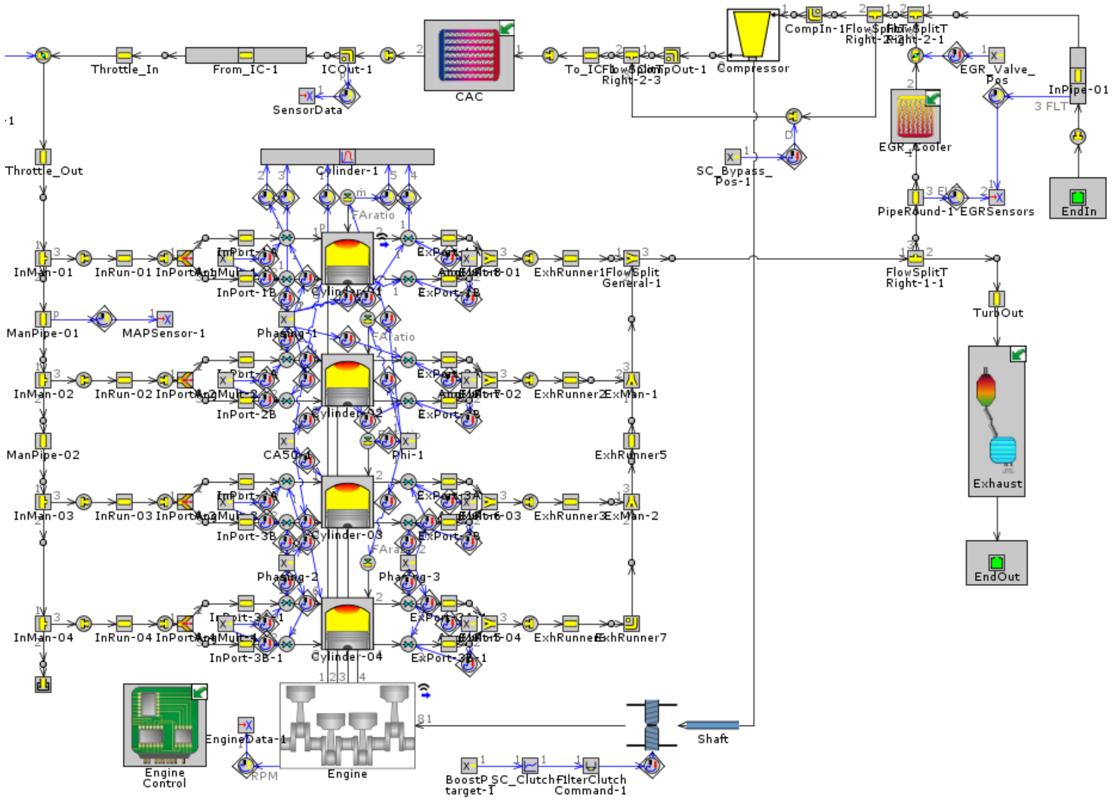

Figure II-8: 1D simulation model of the dual mode SACI engine.

Control-Oriented Model

While the previously mentioned 1D engine model possesses high accuracy, the computational expense is not suitable for SACI calibration optimization or real-time control. Resolving the calibration and control hurdles for SACI is achieved through the development of a fast-running model. This model will target similar accuracy as a 1D engine model at a fraction of the computational expense. In-cylinder state and combustion submodels are the focus of this work. Each state requires an appropriate submodel, which will be described in following chapter. Figure II-9 depicts the flow of data from measured engine states and current actuator positions through state and combustion models to the updated actuator positions.

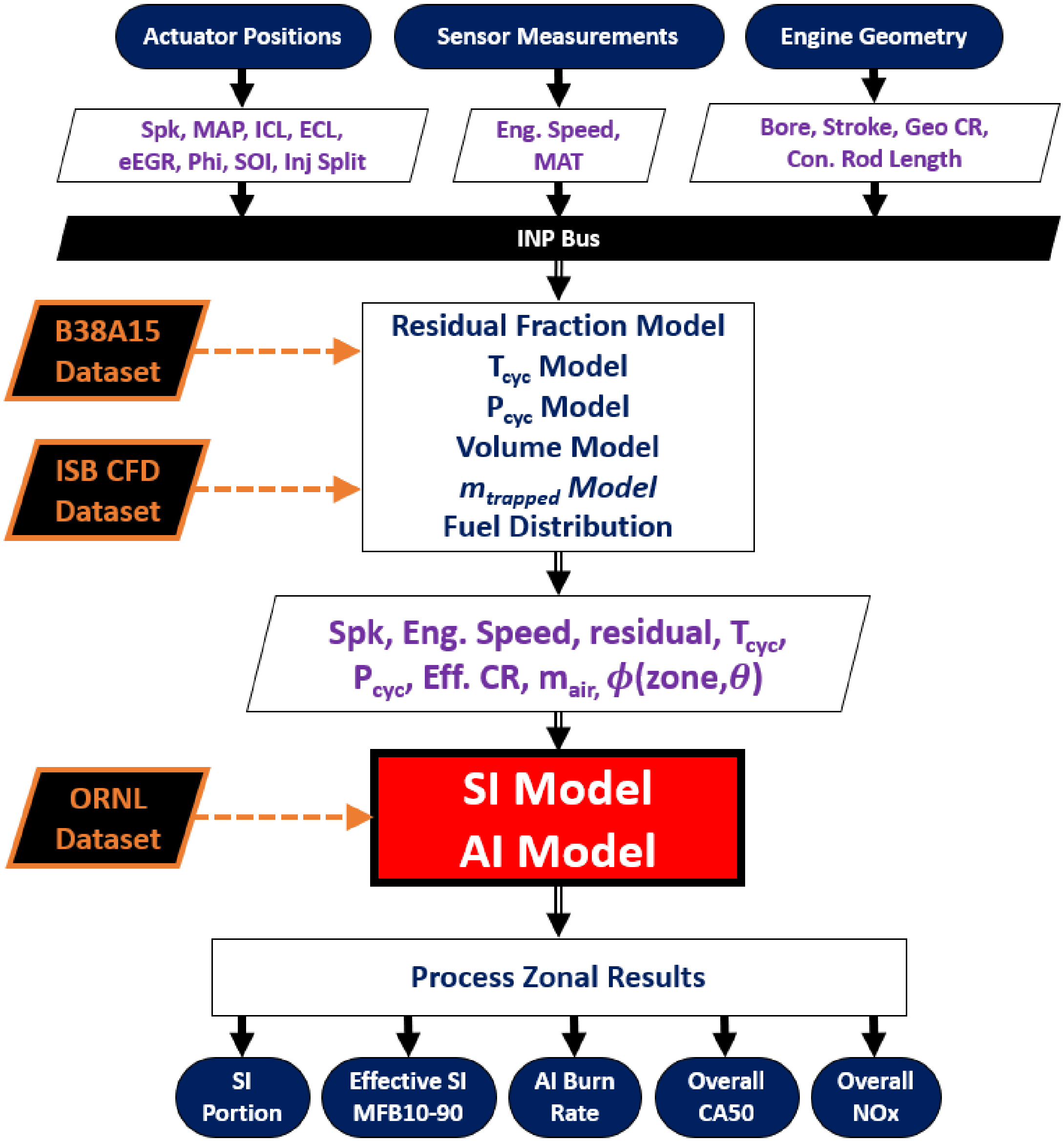

Figure II-9: Schematic of modeling framework demonstrating the data flow from actuator positions, sensor measurements, and engine geometry to combustion metrics.

The in-cylinder state and combustion models include models for in-cylinder mass, temperature at cycle start, pressure at cycle start, and burned gas fraction (BGF). Cycle start is defined at a particular crank angle (e.g., -70° aTDC), and is used instead of IVC or BDC as it is a fixed crank angle, corresponds well with simulation outputs, and can be easily converted to other crank angle locations assuming a polytropic process. The burned gas fraction (BGF) is the total amount of combustion products during the cycle. It does not include any air if the engine is operated lean. Figure II-10 depicts the schematic for the overall cylinder model.

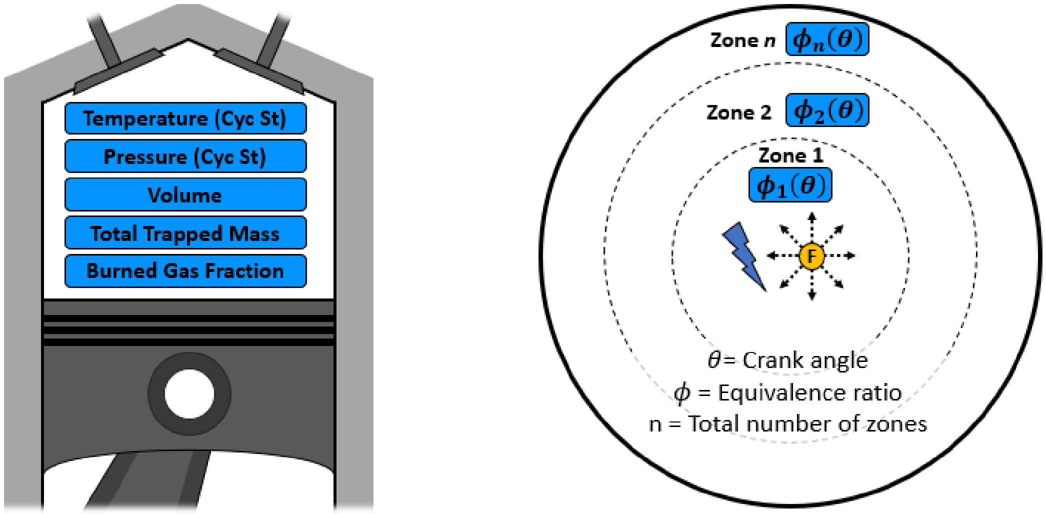

Five (5) Bulk Cylinder States

Fuel Distribution
Varies Spatially and w.r.t. Crank Angle

Figure II-10: Schematic for in-cylinder model used for control and optimization.

Figure II-10 also depicts the model used for the equivalence ratio distribution. Though the zones are modeled as concentric cylindrical regions, their geometry is largely arbitrary. There are only two constraints on the zone geometry. First, all zones have the same mass. Second, the model assumes the injector and spark plug in zone 1. The fuel concentration and mass of fuel burned by the flame monotonically increase from zone 1 to the last zone. A production SACI combustion chamber is anticipated to have a central injector and spark plug with a spray design to radially stratify the combustion chamber [60]. Additionally, combustion occurs near top-dead center (TDC), where the distance between the piston top and combustion chamber is small. Therefore, the axial distribution of fuel is assumed to be negligible. Consequently, the model form is depicted as annular rings concentric with a central circle (zone 1).

Though a uniform BGF and pressure is assumed throughout the cylinder, temperature at cycle start will vary zonally as a function of equivalence ratio. This captures the impact of charge cooling from fuel evaporation.

Model Structure

Two major classes of model structure are physics-based and data-driven. As the name suggests, physics-based models aim to replicate the physical relationships between inputs and outputs with the most appropriate mathematic functions. While a physics-based model is desirable, the model complexity must expand to account for higher complexity. At some point, however, the computational expense will exceed hardware and time constraints, limiting the minimum achievable error.

Physics-based models have been augmented or replaced with data-driven models such as machine learning to achieve accurate performance where an appropriate physical model exceeds complexity constraints. Artificial neural networks (ANNs), a machine learning technique, are a set of mathematical equations that self-learn through an optimization process. Figure II-11 depicts an ANN in graph form, where each circle is a node or neuron and represents a particular value. ANNs aim to map inputs to outputs, for example, temperature and pressure to autoignition phasing. Rather than do this directly, several hidden neurons are added to improve the predictive capability. Each node is connected to all nodes to its right via weights or coefficients multiplied to the output of the previous layer (represented by arrows). The weights in Figure II-11 are labeled according to the layer they feed (in parentheses), and the node of the previous and next layer in the subscript. The previous node outputs are multiplied by the corresponding weight values, then added together along with a constant term called the bias (b). An example computation for the first (and only) hidden layer node ($HL1_i$) is illustrated in (5). The result of this computation is passed to a sigmoidal function (also called a squashing function) to bound the node outputs. An example sigmoidal function is the logistic function shown in Figure II-12. The learning element comes from the selection of the weights and biases, which is performed though an optimization process called backpropagation. Backpropagation aims to minimize the error of the ANN compared to the target values.

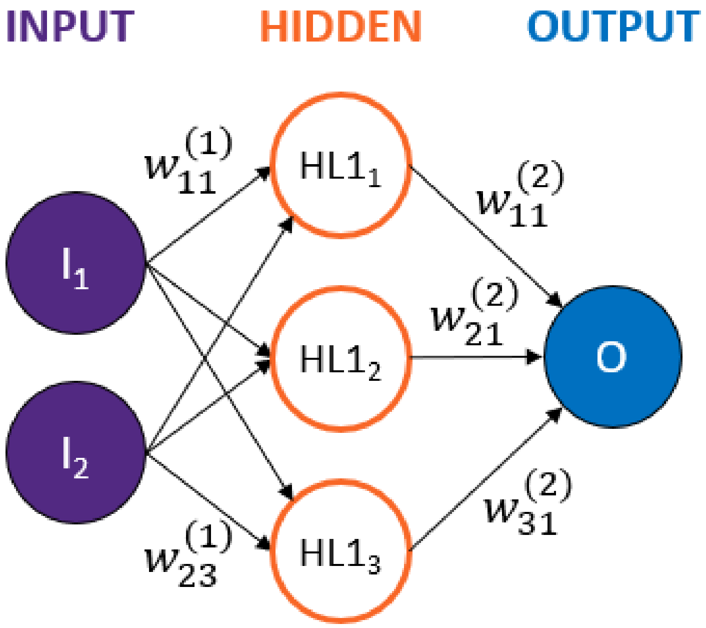

Figure II-11: Artificial neural network structure and sample computation.

$$HL1_i = sig(I_1 \cdot w_{1i}^{(1)} + I_2 \cdot w_{2i}^{(1)} + b_i^{(1)}) \qquad (5)$$

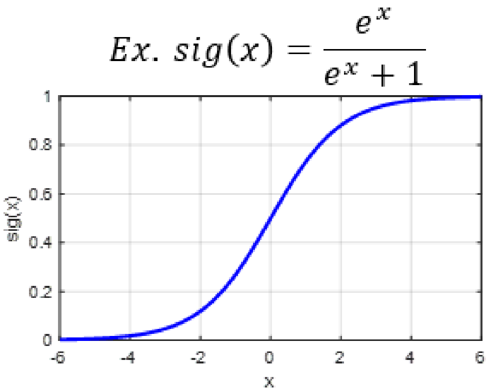

Figure II-12. The logistic curve, an example sigmoidal function.

The training algorithm in this work is the Levenberg-Marquardt backpropagation algorithm which interpolates between the Gauss-Newton method and gradient descent [61,62]. Both Gauss-Newton and gradient descent aim to progress to lower objective function (i.e., error) values by following the shape of the function. Gradient descent uses only the local gradient (i.e., the first derivative), while the Gauss-Newton method uses both the gradient and the curvature (the second derivative). The Gauss-Newton method is faster but can be more complicated to compute than gradient descent. The Levenberg-Marquardt algorithm enables an interpolated combination of the two methods that can be updated during optimization to ensure robustness and speed.

The challenge for machine learning is an appropriate fit to the underlying phenomenon while maintaining good prediction capability to unforeseen cases. Maximizing both the fit to in-sample data and minimizing out of sample error (generalizability) is the key machine learning objective. Maximizing generalizability consists of two components: a properly selected model structure that can capture enough of the complexity of the underlying phenomenon, and not fitting to the noise in the training data ("overfitting"). The noise may be stochastic or deterministic. Stochastic noise is random, and the source of noise is not part of the model. Deterministic noise, on the other hand, occurs when the complexity of the target function is greater than the model. Both present similar challenges, and techniques to mitigate overfitting are similar for both. As the name suggests, overfitting occurs when the training process has progressed too far (by fitting noise), leading to an overall worse out-of-sample performance.

For ANNs, there are several techniques to avoid overfitting. These techniques are called “regularization,” and there are several strategies to implement regularization [63]. Early-stopping is the primary technique used. Once the test dataset error stabilizes, the network training ceases. As a test of model generalizability, “hold-out” is used to test the regression against data for which the model has not seen. Another means of regularization used in this work is weight decay Bayesian regularization [64]. Non-regularized training targets the minimum of the sum of squared errors (6), weight decay regularization also includes the sum of the squares of the weights in the network (7). In these equations, *F* is the objective function, *n* is the number of training points, a_i is the ANN result, t_i is the target result, *N* is the number of parameters in the network, w_j^2 is each weight value, and λ is the scaling coefficient to select the importance of the weight decay term. Therefore, the optimal solution for weight decay regularization is the solution that minimizes both error and weights. In Bayesian regularization, Bayes’ rule is used to compute λ. This is in opposed to non-Bayesian weight decay regularization where the user selects λ. An additional advantage of Bayesian weight decay is the potential to have relatively accurate extrapolation performance.

$$F = \sum_{i=1}^{n} (a_i - t_i)^2 \tag{6}$$

$$F = \sum_{i=1}^{n} (a_i - t_i)^2 + \lambda \sum_{j=1}^{N} w_j^2 \tag{7}$$

III. IN-CYLINDER STATE SUBMODELS

Combustion control and calibration demands a strong understanding of the in-cylinder state. This is not unique to SACI, and most of the models discussed in this chapter have been developed for SI engines in alternate forms. The reference 1D engine model is exercised to obtain the residual fraction for a wide range of conditions. Each submodel is validated to this reference model. In total, 6000 test points are simulated. Table III-1 lists the input variables and the ranges for the dataset and depicts the distribution of a selection of inputs. The first 2000 points are selected by the Latin hypercube method to provide one point for every region in the seven-dimensional space [65]. The next 3000 points are a full-factorial design of experiments (DOE) to achieve a set of spark timings for the same condition. The final 1000 points are to ensure that rich operation is sufficiently covered. The selected ranges are determined based on three justifications: 1) typical operating range for most drive-cycles, 2) actuator limits, and 3) conditions anticipated to be favorable to SACI combustion. Several (e.g., cam phasers) are extended beyond typical constraints, to evaluate potential benefits for wider-range actuators.

Table III-1: Input ranges for submodel development.

Input	**Range**
Engine Speed[1]	1000 RPM–3000 RPM
Intake Manifold Pressure[1,2]	30 kPa–140 kPa
Spark Timing[2]	-70–0° aTDC[3]
Equivalence Ratio[2]	0.5–1.4
External EGR[2]	0%–30%
Intake Cam Location[3, 4]	0–100 CAD
Exhaust Cam Location[3, 4]	0–100 CAD

[1] Typical operating range for most drive cycles.

[2] Conditions anticipated to be feasible for SACI combustion.

[3] Actuator constraints.

[4] Crank degrees from parked position.

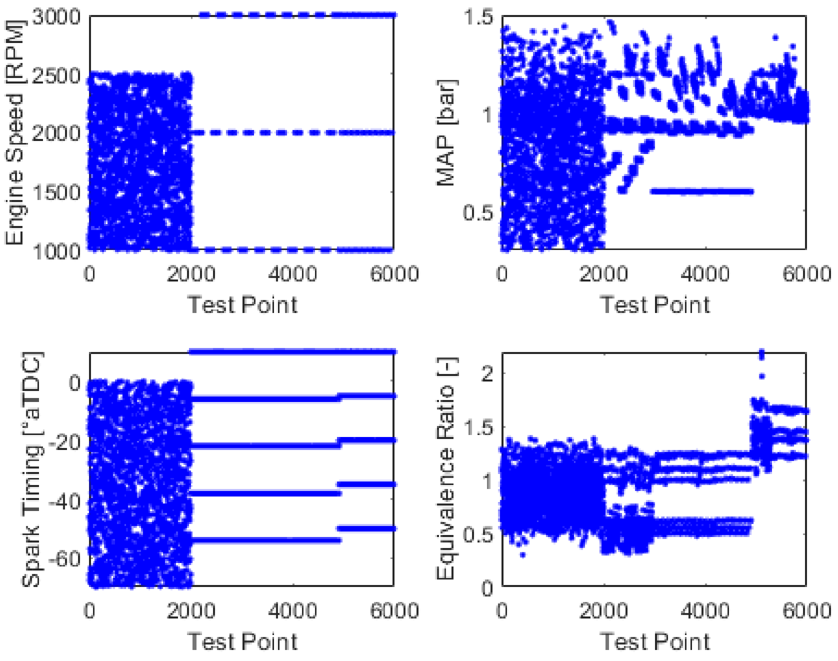

Figure III-1: Values for a selection of inputs used in the design of experiments.

Neural Network Modeling Techniques

Each cylinder state neural network model uses the same process to reach the final network structure and size. These models generally have fewer inputs and are much less sensitive to inputs than the combustion submodels. For example, from a thermodynamic assessment, pressure at cycle start is largely a function of starting pressure (i.e., MAP) and how much compression occurs (a function of only intake phasing for a fixed geometric compression ratio). Therefore, it is expected that a small network can accurately capture the relationship between these inputs and the desired output. Consequently, single-layer networks are used exclusively, varying in size only to accommodate the anticipated model complexity. A sweep of hidden neurons identifies the minimum size required to capture sufficient accuracy, without overfitting. An example hidden neuron sweep is shown in Figure III-2 for the pressure at cycle start network. Starting from a low number of hidden neurons, once the test error stabilized, the model size is fixed. The other regularization technique used is early stopping during the training process.

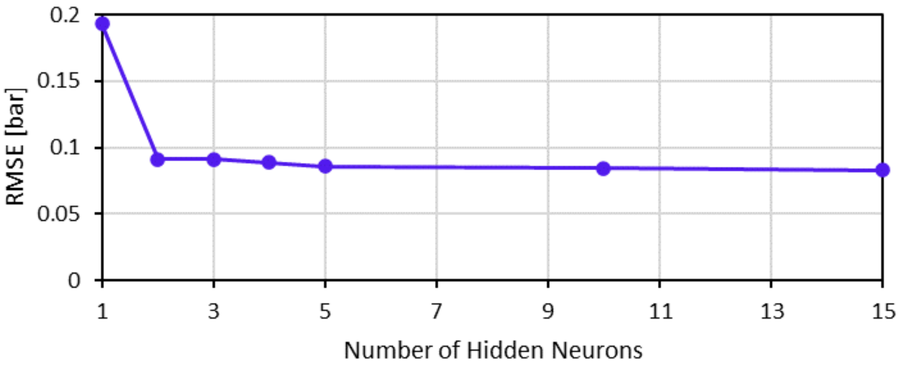

Figure III-2: RMSE from a sweep of hidden neurons for the pressure at cycle start network. Note that for 5 neurons and above, the error stabilizes. On this basis, five hidden neurons are selected for this network, and a similar process is followed for other in-cylinder state networks.

Cylinder Volume at IVC Model

The model for volume at intake valve closing is based on a crank-slider cylinder volume at the crank angle at IVC. The crank angle at IVC is determined by a measurement of the intake valve lift of the B38 engine (Figure II-4). Equation (8) is the relationship between engine geometry and volume at a particular crank angle θ. The total cylinder volume V is computed relative to the clearance volume V_c. Compression ratio r_c and the ratio of stroke to connecting rod length R are the relevant engine geometric parameters.

$$\frac{V}{V_c} = 1 + \frac{1}{2}(r_c - 1)\left[R + 1 - \cos\theta - \sqrt{R^2 - \sin^2\theta}\right] \tag{8}$$

Cylinder Pressure at Cycle Start Submodel

The submodel for pressure at cycle start is an artificial neural network. It is validated against the results from the reference 1D engine model and is of the form depicted in Figure III-3. The neural network inputs are selected based on the independent variables that have a strong influence on in-cylinder pressure. The network structure is chosen based on an investigation of the tradeoff between overfitting and accuracy. A single layer of 5 hidden neurons is trained to 70% of the data points using the Levenberg-Marquardt backpropagation algorithm. The remaining 30% of the data is split evenly between the validation and test datasets. The resulting ANN demonstrated a root mean square error (RMSE) of 0.1 bar. Figure III-4 illustrates the comparison between the reference and ANN models for each data subset: training data, validation data, and test data.

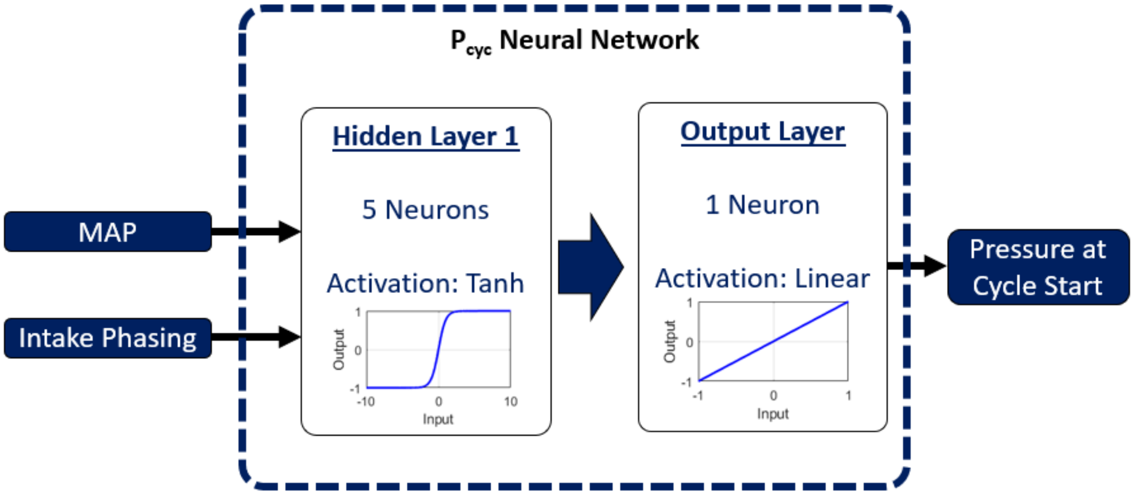

Figure III-3: Neural network structure used for cylinder pressure at cycle start.

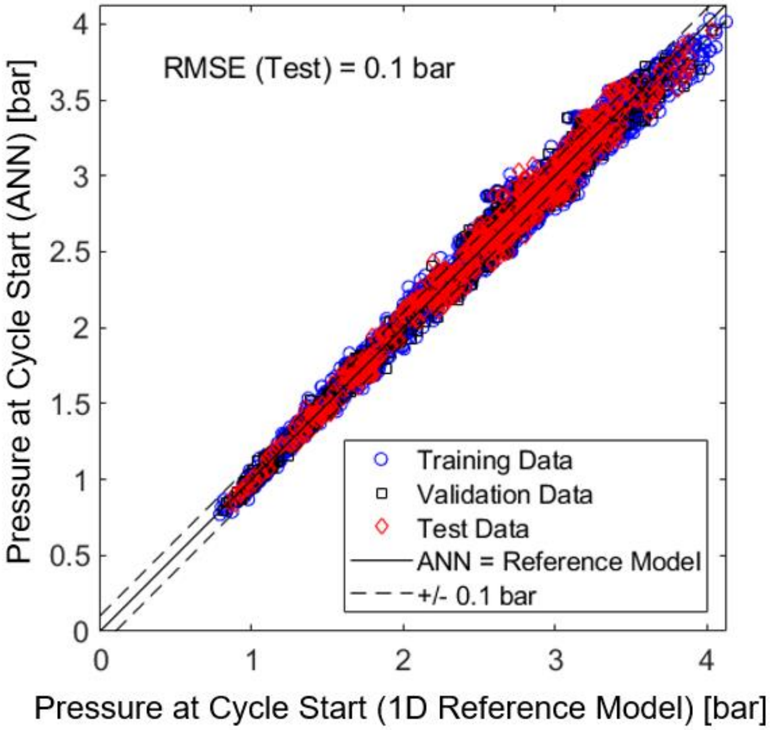

Figure III-4: Comparison between the 1D engine model (Reference Model) and the artificial neural network (ANN) for the pressure at cycle start submodel.

Residual Fraction Submodel

The submodel for residual fraction is an artificial neural network. It is validated against the results from the reference 1D engine model and is of the form depicted in Figure III-3. The neural network inputs are selected based on the independent variables that have a strong influence on in-cylinder pressure. The network structure is chosen based on an investigation of the tradeoff between overfitting and accuracy. A single layer of 15 hidden neurons is trained to 70% of the data points using the Levenberg-Marquardt backpropagation algorithm. The remaining 30% of the data is split evenly between the validation and test datasets. The resulting ANN demonstrated good accuracy, with a root mean square error (RMSE) of 4.0 percentage points. Figure III-4 illustrates the comparison between the reference and ANN models for each data subset: training data, validation data, and test data.

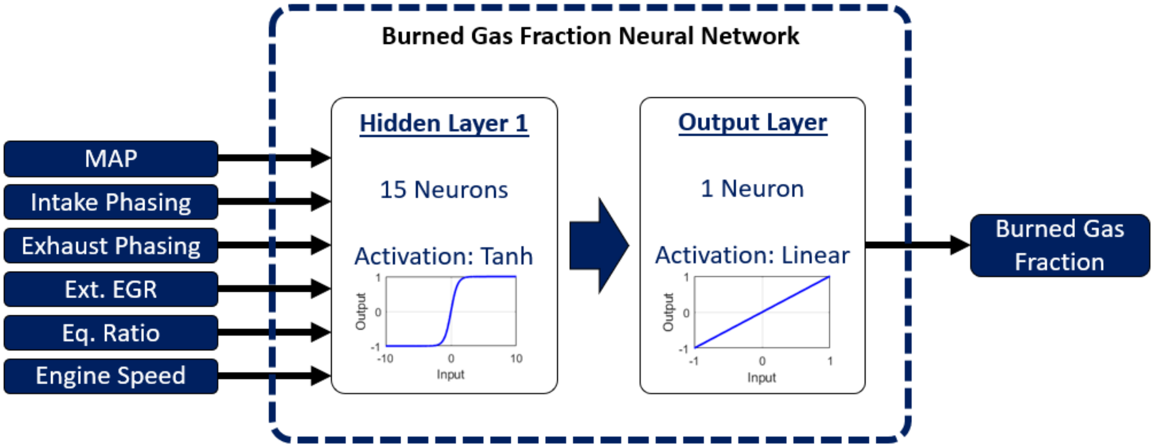

Figure III-5: Neural network structure used for residual fraction.

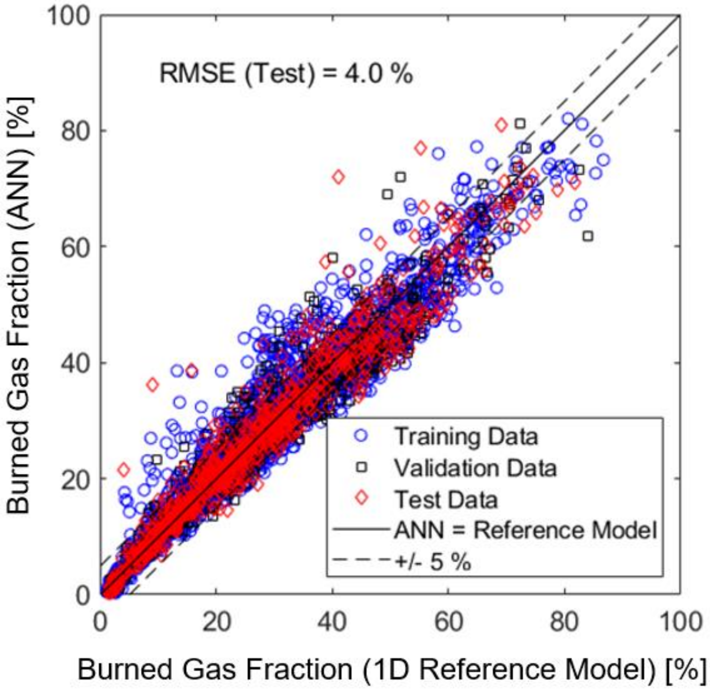

Figure III-6: Comparison between the 1D engine model (Reference Model) and the artificial neural network (ANN) for the burned gas fraction (BGF) submodel.

Temperature at Cycle Start Submodel

The submodel for temperature at cycle start is an artificial neural network (ANN). It is validated against the results from the reference 1D engine model and is of the form depicted in Figure III-3. The neural network inputs are selected based on the independent variables that have a strong influence on in-cylinder temperature. The network structure is chosen based on an investigation of the tradeoff between overfitting and accuracy. A single layer of 15 hidden neurons is trained to 70% of the data points using the Levenberg-Marquardt backpropagation algorithm. The remaining 30% of the data is split evenly between the validation and test datasets. The resulting ANN demonstrated good accuracy, with a root mean square error (RMSE) of 8.8 K. Figure III-4 illustrates the comparison between the reference and ANN models for each data subset: training data, validation data, and test data. This submodel is evaluated for each zone, based on the zonal equivalence ratio.

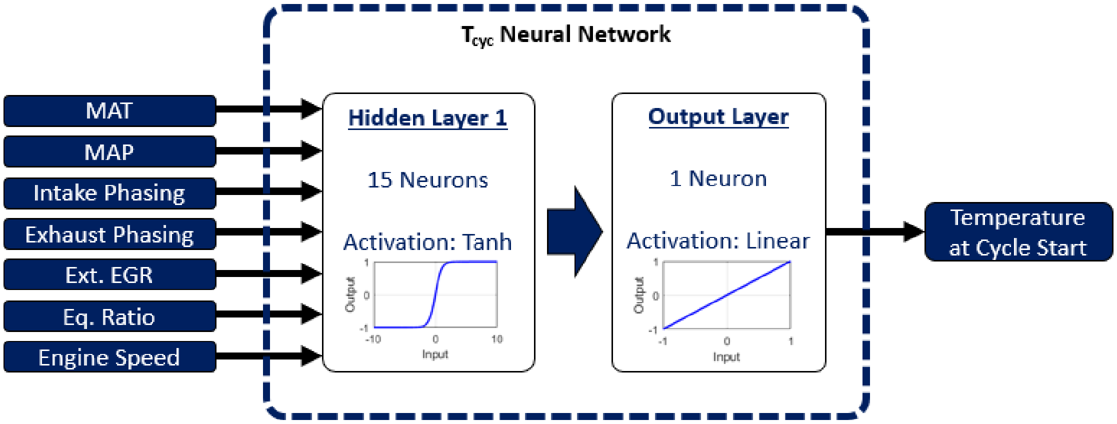

Figure III-7: Neural network structure used for cylinder temperature at cycle start.

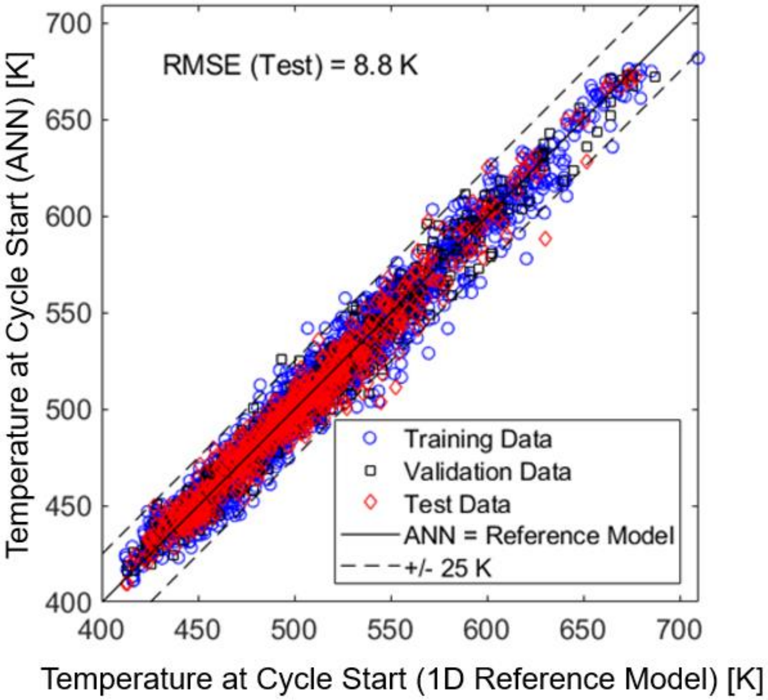

Figure III-8: Comparison between the 1D engine model (Reference Model) and the artificial neural network (ANN) for the temperature at cycle start submodel.

In-Cylinder Mass Submodel

The in-cylinder mass *m* submodel leverages the ideal gas law to compute the trapped mass (9). In this equation, pressure *P*, volume *V*, and temperature *T*, are all evaluated at the cycle start crank angle (-70° aTDC). The gas constant R_{air} is assumed to be constant and equal to 287 J/kg·K.

$$m = \frac{P_{cyc}V_{cyc}}{R_{air}T_{cyc}} \tag{9}$$

Fuel Distribution Submodel

A control-oriented model of radial fuel stratification throughout the engine cycle is critical for engine calibration and control. Both phases of combustion are often operated near their limits (flammability limit for flame propagation, and pressure rise rate limit for autoignition). Careful tuning of injection strategy can enable a wider range of operation by allowing each phase to operate further from the limits, as these limits are a strong function of fuel-air equivalence ratio. One technique for evaluating fuel stratification is three-dimensional computational fluid dynamics (CFD) modeling. However, this approach is computationally intensive, thus eliminating it from consideration for real-time control and rapid iteration during the calibration process. Grenda developed a radially focused charge stratification model for HCCI [59], however, this model is likely too computationally expensive for a control-oriented model.

There are limited models available to represent in-cylinder fuel distribution for radially stratified engines without high computational load. However, simplified models have been successfully developed for other purposes. Nishida and Hiroyaso developed a spray model for diesel engines which focuses on the spray penetration and mixing with air [66]. A set of concentric packets represent a discretized zone for fuel concentration for both liquid and vapor independently.

Sjöberg et al. demonstrated a five-zone temperature distribution model is capable of matching experimental HCCI data for in-cylinder pressure during combustion [67]. Several other groups have applied this approach for HCCI. Babajimopoulos et al. leverage a ~100 zone model to accurately predict HCCI burn rates on a crank-angle basis [68]. Aceves et al. and Fiveland et al. demonstrate a 10-zone model again to predict HCCI burn rates [69,70]. These zonal breakdown in these articles is not spatial, rather the charge is divided into similar temperature zones. These concepts are synthesized and extended to establish a spatial radial stratification model suitable for SACI.

The distribution of fuel within the cylinder will influence flame propagation, autoignition, zone temperature from evaporative cooling, and NO_x formation. The model must address both spatial and temporal distribution, and therefore must have an appropriate model of the injection event and fuel and air mixing.

Reference Model

A three-dimensional computational fluid dynamics (CFD) model is used as a high-fidelity reference model. This model aids in physical understanding of important model features and to determine the magnitudes of features for calibration. The model is tuned to match a Cummins ISB engine, and the spray simulations use a six-component E10 gasoline surrogate. The details of the engine geometry, injector geometry, and several test conditions used in the CFD simulation are in Table III-2 and Table III-3. Three test points are considered that examine the response at different fueling amounts. Late injection (near firing top-dead center) strategies are selected as it would most likely be used to introduce charge stratification for SACI.

Table III-2: Engine geometry and injector parameters used for the reference model.

Parameter	**Value**
Type	5.9 L inline six-cylinder
Bore x Stroke	102 mm x 120 mm
Compression Ratio	15:1
Injector	Eight-hole, 30° spray cone
Fuel	E10 Gasoline surrogate: - n-pentane (16.5% mol) - iso-octane (23.8 % mol) - 1-hexene (5.9 % mol) - Cyclo-pentane (12.4 % mol) - Toluene (21.3 % mol) - Ethanol (20.1 % mol)

Table III-3: Test point parameters used for the reference model.

	Test Pt. 1	**Test Pt. 2**	**Test Pt. 3**
Engine Speed	1200 RPM	1200 RPM	1200 RPM
Overall Equivalence Ratio	0.12	0.20	0.35
Start of Injection [°aTDC]	-15	-32	-45
Injection Duration [CAD]	4.8	7.9	13

The CFD model is adapted from a model referenced in [71] to study late compression stroke injections of gasoline for stratified LTC. A one-equation Large Eddy Simulation (LES) turbulence model is used which includes a transport equation to model the sub-grid scale kinetic energy [72]. Converge CFD is used to perform this simulation, using about 9,000,000 cells at bottom-dead center with adaptive mesh refinement [73]. Additionally, fixed embedding refines the mesh further near the combustion chamber walls to resolve the near-wall boundary layer. The boundary conditions are set according to experiments performed on the medium-duty engine.

The liquid fuel injection model is a Lagrangian-based approach using liquid parcels that are introduced at the location of the injector. The behavior of the liquid spray is governed by various sub-models that are identical to those referenced in [71]. The injector used for the experiment is Bosch HDEV 1.2 GDI injector. Validation of this injector is performed by Priyadarshini et al. against Spray G experiments from the engine combustion network (ECN) [71]. The average of five cycles using this CFD model shows that the mean penetration length over time sufficiently agrees with these experiments [71].

Figure III-9 illustrates the equivalence ratio distribution at four crank angles for a vertical plane that crosses through the center of the chamber for the high load Test Point 3. The first plot occurs during the spray, which has a start of injection (SOI) of -45 degrees after firing top-dead center (aTDC), and an end of injection (EOI) of -32° aTDC and the remaining three occur in succession for a total of 47 crank angle degrees (CAD) after the end of injection.

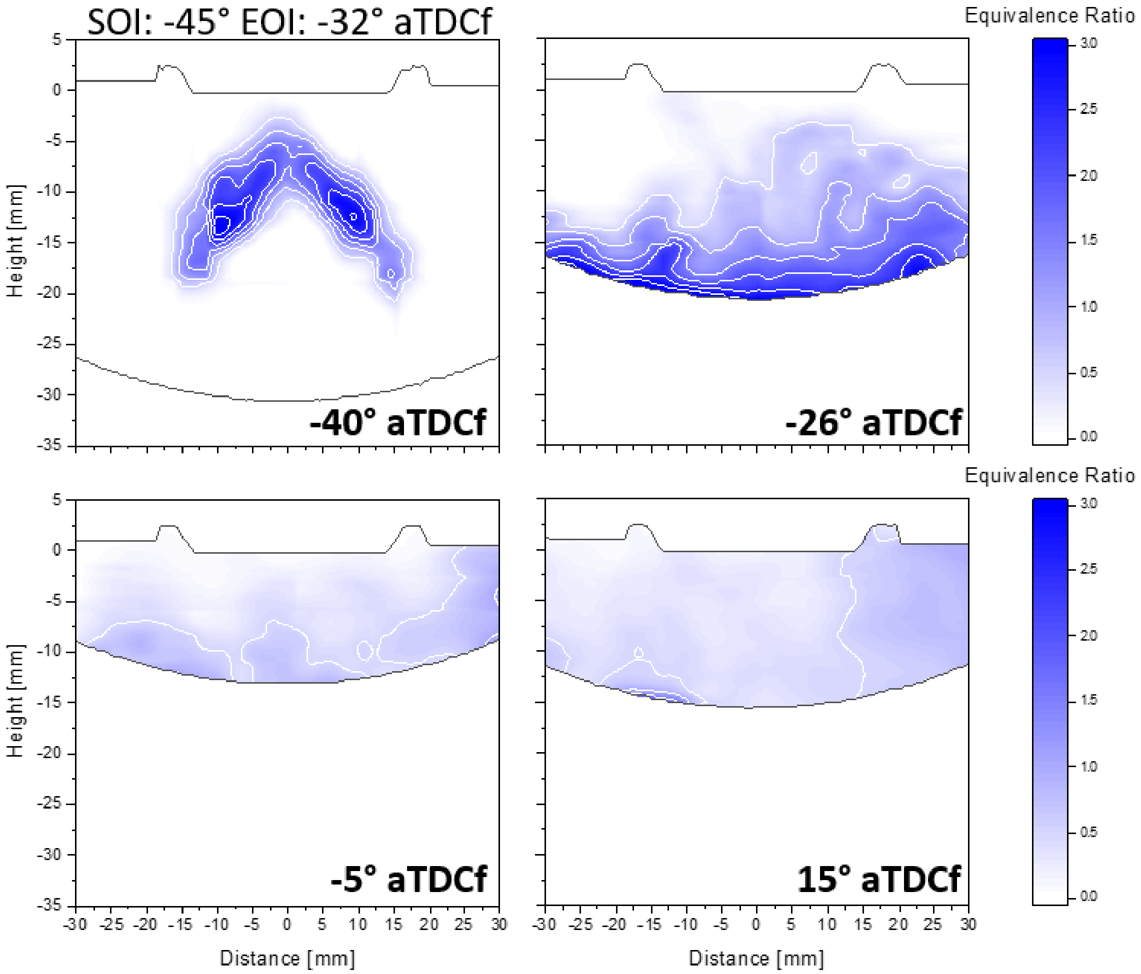

Figure III-9: Equivalence ratio distribution along a vertical plane for select crank angles.

Spray Penetration

The first step in the fuel distribution model is the introduction of the fuel into the chamber. An estimate of spray penetration is based on Desantes et al. and Tetrault et al. which includes the effects of injector geometry, in-cylinder conditions, and empirical coefficients [74,75]. As the precise penetration length is not required, reasonable assumptions are made for each factor. The spray penetration (S) equation is developed based first on the momentum flux ($\dot{M}$) computation along the spray axis. Assuming a gaussian distribution of flow velocity perpendicular to the main spray axis (with shape factor α), the flow velocity in the spray can be computed. The spray tip penetration is assumed to proportional to the spray flow velocity with a proportionality constant of *K*. Further assumptions of quiescent conditions and constant air density yield (10) and (11). Table III-4 lists the parameters used in computing the penetration length.

$$\mathrm{S(t)} = \left(\frac{2\alpha}{\pi}\right)^{0.25}\frac{2}{K}(1-\exp(-2\alpha))^{-0.25}\dot{M}^{0.25}\rho_{air}^{-0.25}t^{0.5}\tan\left(\frac{\psi}{2}\right)^{-0.5} \tag{10}$$

$$\dot{M} = \frac{\dot{m}_{fuel}}{\rho_f\left(\frac{\pi d_0^2}{4}\right)} \tag{11}$$

Table III-4: Parameters used to determine penetration length.

Parameter		Value	Justification
α	Gaussian shape factor for fuel velocity distribution	4.605	Reference [75]
K	Ratio of fluid velocity to spray penetration	7.2	Reference [75]
$\dot{m}_{fuel}$	Fuel mass flow	6.9 mg/ms	Engine data
d_0	Injector hole diameter	100 µm	Reference [75]
ρ_{fuel}	Fuel density	0.740 g/m^3	Assumed value
ρ_{air}	Air density	– kg/m^3	Computed at injection timing
ψ	Spray cone angle	30°	Injector documentation
$\dot{M}$	Momentum flux	Computed	

A key factor in the determination of spray length is the effect of short injection durations, as would be common for a second injection to induce stratification for SACI operation. During short injections, the injector is in the so-called “ballistic” region, where the injector valve is moving and has a nonlinear impact on fuel quantity injected [76,77]. To account for this, the injector fuel mass is adapted below injection durations of 0.4 ms to be consistent with the literature on the behavior of solenoid injectors in the ballistic region [77] (Figure III-10). The overall spray penetration is computed and illustrated in Figure III-11, is consistent with the results in [74,75].

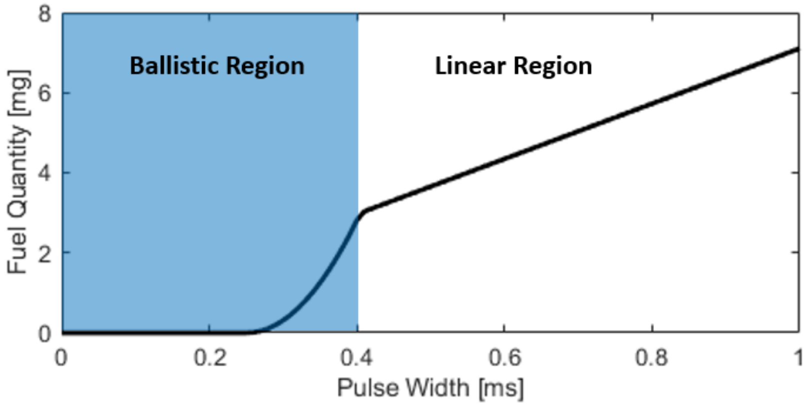

Figure III-10: Injector mass flow rate as a function of injector pulse width duration.

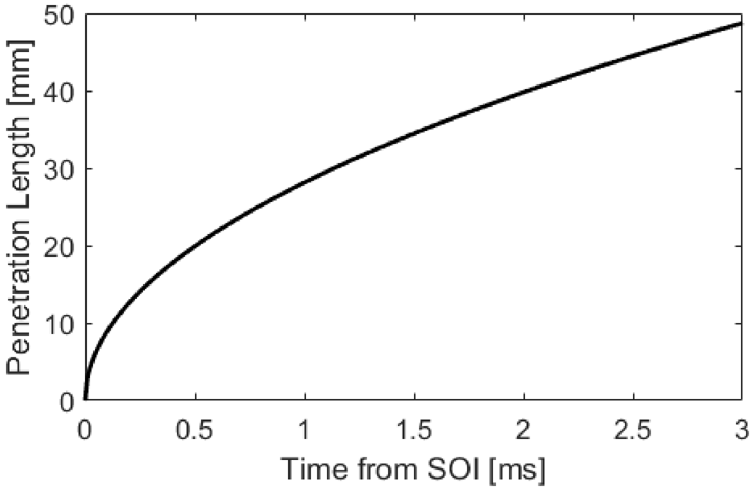

Figure III-11: Spray penetration versus time and injector pulse widths based on (10).

Fuel Distribution Along Spray

While a uniform distribution of fuel vapor may be a suitable assumption, a careful analysis of the literature indicates that equivalence ratio may not be uniformly distributed along the spray. Perini et al., for example, perform a simulation study on mixture preparation for a light-duty diesel engine [78]. Though the combustion chamber geometry is different from a SACI engine, the nature of fuel distribution along the spray length is still applicable. Their work indicates a peak fuel distribution just beyond halfway along the spray, with the lowest fuel concentration at the end of the spray. Zhang et al. also perform a simulation study on a similar combustion chamber, however, their focus is gasoline compression ignition [79]. Much like SACI, gasoline compression ignition requires more homogenously distributed fuel than a diesel engine. Examining the reported fuel distribution along the spray axis indicates a similar distribution as Perini et al.

Though a literature review can provide a qualitative view of the fuel distribution, a quantitative representation is necessary for model calibration. The results from the CFD study are synthesized to produce an estimated distribution of fuel along the spray axis. The two lower load test points produced a nearly uniform distribution along the spray axis. However, as Figure III-12 illustrates, the distribution for the longest duration produced a peak fuel concentration just beyond halfway along the spray. It is anticipated that as the plume slows from interacting with the quiescent air, the continued spray into the plume will increase the equivalence ratio towards the tip of the plume. This is consistent with the literature, and results from the spray penetration velocity slowing as time increases. The complex mixing of the fuel and air due to air entrainment is evident from the non-continuous nature of the CFD results. For the purposes of the fuel distribution submodel, precise spray mixing is of low importance as there will be some time between the conclusion of the spray and spark timing. Thus, a relatively simple equivalence ratio distribution along the spray axis is sufficient to ensure that the appropriate mean in-cylinder fuel distribution is achieved. A cubic fit to the data is performed, as indicated in Figure III-12. This fit is only used for longer injections. A uniform distribution is more suitable for shorter durations, where the impact of continued spray from the injector into a slowing plume is negligible.

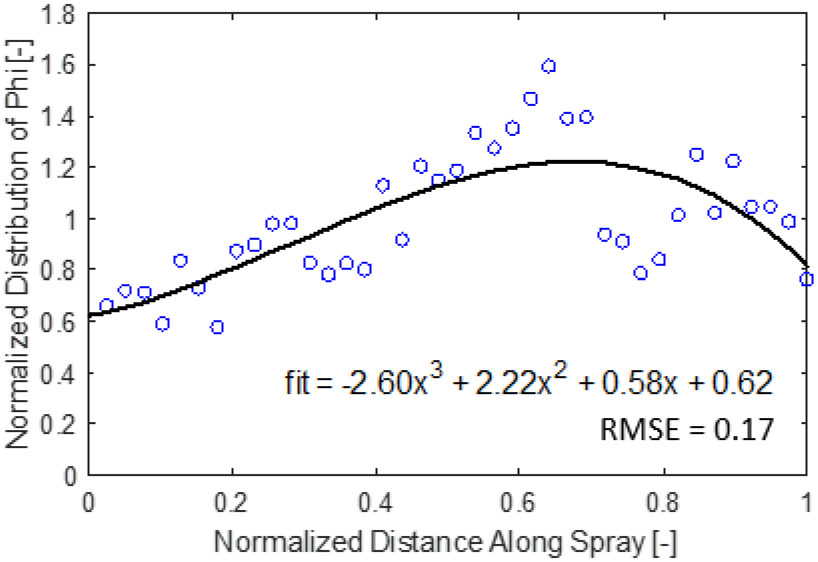

Figure III-12: Fuel distribution along spray length for long injections.

The spray penetration (and therefore fuel distribution along the spray) must be transformed to the radial dimension. In the CFD simulation, the spray angle within the cylinder is about 45° downward from the head surface. Therefore, the radial component of the spray axis must be reduced by cosine (45°) ≈ 0.7. The fuel distribution along the spray axis must be compensated by dividing by the same factor.

Fuel and Air Mixing Post Injection

After the injection event is complete, some mixing will occur as the cycle progresses. Several research groups have identified significant stratification for the start of combustion. Sellnau et al. depict an equivalence ratio range of about +/- 0.25 near the start of combustion for their gasoline direct injection compression ignition engine [80]. Giovannoni et al., Buri et al., Chen et al., and Dong et al. all demonstrate a similar equivalence ratio distributions for direct-injected spark-ignited engines [81-84]. As the simplified cylinder model does not allow for high-fidelity stratification, mixing across zones is determined based on the difference in equivalence ratio among neighboring zones. Figure III-13 depicts the zonal relationship used to evolve the equivalence ratio after injection for each zone.

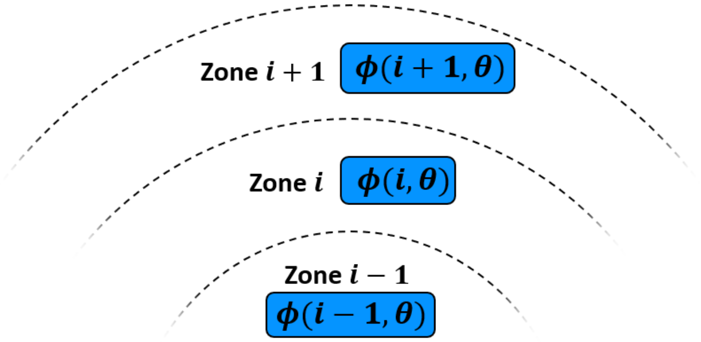

Figure III-13: Schematic describing the post-injection mixing of fuel across zones.

The equivalence ratio for a particular zone i at crank angle θ is given by $\phi(\mathrm{i}, \theta)$. The zones interact with neighboring zones with a mixing strength coefficient μ. Equation (12) depicts the relationship between neighboring zones. When $\mu = 0$, the mixing submodel is disabled, and the spatial distribution of fuel is based on the spray model alone.

$$\phi(i,\theta+1) = \phi(i,\theta) + \mu[\phi(i,\theta) - \phi(i-1,\theta)] + \mu[\phi(i+1,\theta) - \phi(i,\theta)] \tag{12}$$

To tune the coefficient μ, the previously described CFD results are leveraged. Using the same computation method for the fuel distribution submodel, the CFD results are divided into 50 hollow cylindrical zones each of equal volume accounting for actual cylinder geometry. For the crank angles following the end of the spray, the phi distribution versus the radial distance from the center of the combustion chamber is computed. The μ coefficient is swept from 0.0 to 1.2 in 0.01 increments. Values above 1.2 produced numerical instability. The high resolution CFD results are transformed to a 10-zone model equivalent and compared to the candidate 10 zone model. The root mean square error (RMSE) is computed for all available crank angles for each of the three test points. In total 18 cases are evaluated for each value of μ. For each of the three test points, the mean RMSE of all crank angles is used to evaluate the performance for each value of μ. The minimum of the mean of the three test points is the optimum μ. This occurs at μ = 0.76 and is depicted in Figure III-14. Above a μ of about 0.6, there is little sensitivity to the coefficient.

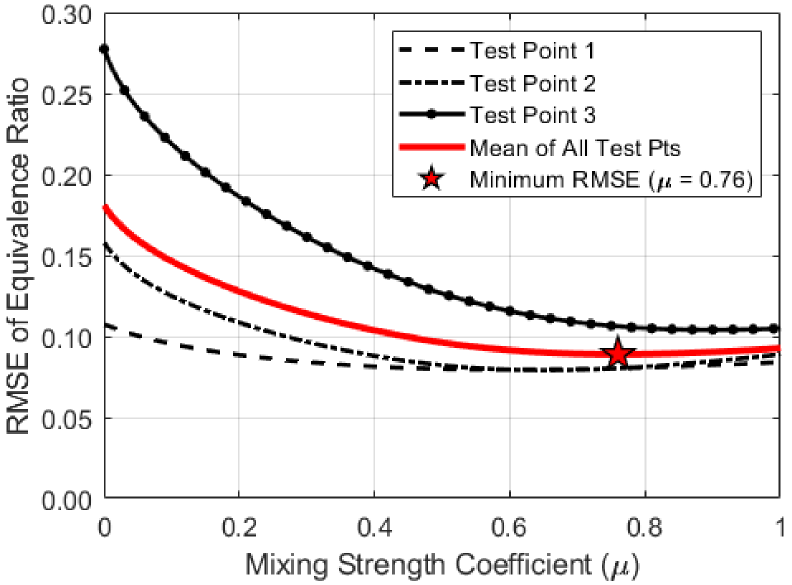

Figure III-14: Evaluation of the mixing strength coefficient (μ). The optimum coefficient value of 0.76 is indicated in the figure.

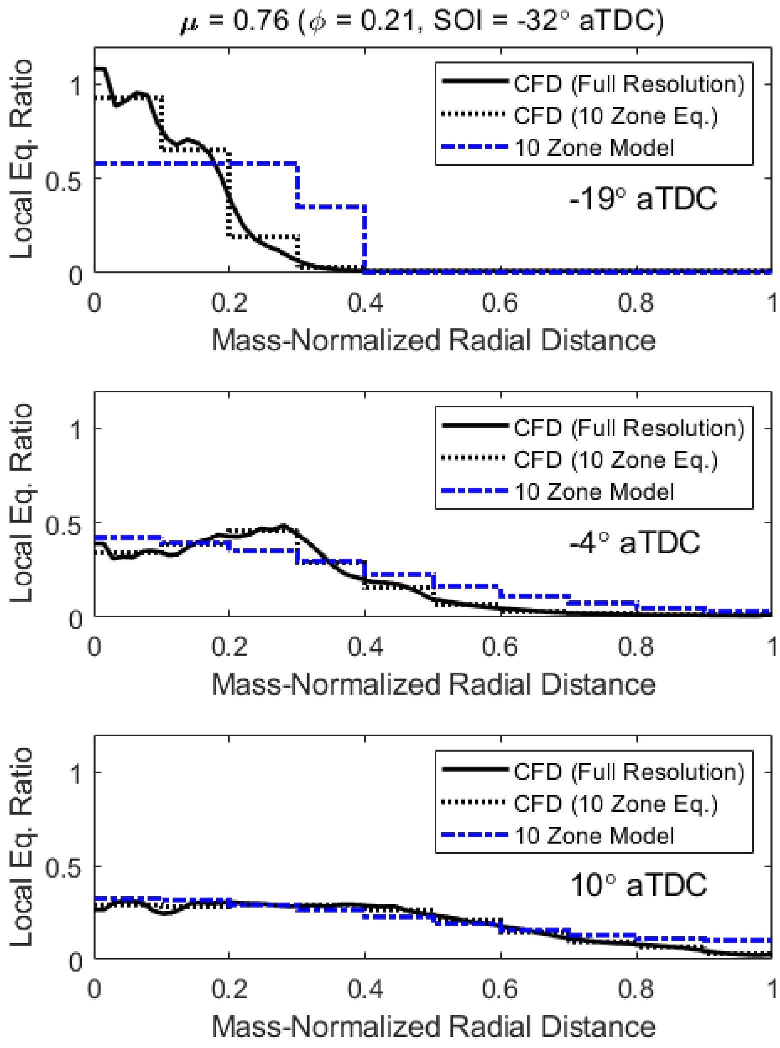

Figure III-15: Comparison of CFD results and the simplified 10-zone fuel distribution model.

A sample comparison between the CFD results and the quasi-dimensional model is presented in Figure III-15. A more complete comparison can be found in the Appendix. Three results are included in Figure III-15: the full resolution CFD (50 cylindrical sections of equal mass), the full-resolution CFD results transformed to an equivalent 10-zone model, and the 10-zone quasi-dimensional model results. Overall, there is good agreement. The earliest crank angle shows the greatest error, though this is expected as the simplified model cannot capture the complex mixing during and immediately after injection. The quasi-dimensional model matched the CFD results with a root mean square error (RMSE) for equivalence ratio of 0.08–0.11. This is a ~50% improvement over the 0.16–0.20 RMSE for a model that assumes a uniform fuel distribution immediately after injection.

Selection of Number of Zones

A sweep of the number of zones is performed to identify the sensitivity of model results to the selected number of zones. Figure III-16 depicts the results from the sweep, comparing two conditions: a highly stratified condition and a minimally stratified condition. The highly stratified condition is about 6 CAD after the end of injection, and the minimally stratified condition is 47 CAD beyond the end of injection, both for Test Point 3. If the spray is nearly homogenous, then there is little sensitivity to the number of zones, as expected. It is important to note that while the slope of the trendline is slightly positive, this is not statistically significant. A zero slope is within a 95% confidence interval. When stratified, there is a significant error associated with a small number of zones. Therefore, if there is stratification, a multi-zonal model is required. In this work, 10 zones are selected as at least 5 or 6 are required to minimize error, and 10 zones divides the mass of the charge evenly for computational convenience.

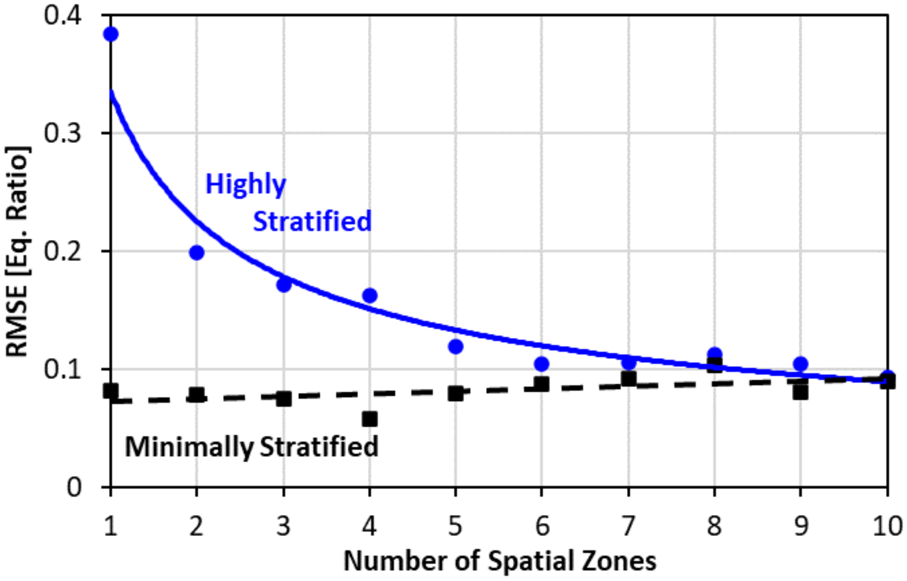

Figure III-16: Results from a sweep of zones for highly-stratified and minimally stratified conditions. When stratification is present, at least five zones are needed to minimize error.

Summary

In-cylinder state submodels for temperature, pressure, burned gas fraction, mass, and volume are developed. The temperature, pressure, and burned gas fraction models are artificial neural networks with one hidden layer with a varying number of hidden neurons. The ANN is trained to results from the 1D reference model. The in-cylinder volume model is geometric and based on the slider-crank mechanism. Finally, the in-cylinder mass model is derived from the ideal gas law.

Additionally, a simplified model for radial fuel stratification is developed to achieve a control-oriented injection strategy model. The modeling objective is to reproduce radial stratification with a computational expense suitable for real-time control or calibration optimization. The model consists of three submodels: spray penetration, fuel distribution along the spray, and post-injection mixing. Each submodel is tuned to injection spray results from a CFD model. The submodels matched well across three different test points. The quasi-dimensional model matched the CFD results with a root mean square error (RMSE) for equivalence ratio of 0.08–0.11. This is a ~50% improvement over the 0.16–0.20 RMSE for a model that assumes a uniform fuel distribution immediately after injection.

IV. COMBUSTION SUBMODELS

The high dilution typical of SACI improves efficiency by lowering heat transfer and pumping work, as well as increasing the ratio of specific heats. Though these are significant improvements, the high dilution has a negative impact on deflagration flame propagation and raises the ignition energy required for autoignition. The unique controls challenge for SACI is resolving the competing demands of the two combustion regimes. Identifying key parameters and their influence for each mode can aid in developing real-time control strategies.

This chapter thoroughly investigates model type and structure for the combustion submodels. An independent evaluation of neural networks versus physics-based model structures is performed for autoignition and can be found in Appendix A. However, these specific submodels are not considered in the final cylinder model and are therefore excluded from this chapter. Instead, new models are developed in this chapter based on the findings in Appendix A.

Combustion Fundamentals: Spark Ignited Flame Propagation

For SI combustion, dilution is limited to maintain appropriate flame speeds and cycle-to-cycle variation (CCV). SACI, however, must balance ringing intensity during autoignition and flame propagation constraints, which drives dilution levels near the flame stability limit. A detailed understanding of turbulent flame propagation can be used to optimize the combustion chamber, flow field, and control actuator strategies.

The nature of turbulent flame propagation is strongly dependent on the flame structure, which is itself a function of chemical and fluid flow behavior. Two non-dimensional numbers aid in translating these behaviors to quantifiable metrics: the Damköhler number, *Da*, and the Karlovitz number, Ka. *Da* is the ratio of characteristic flow time to characteristic chemical reaction time and is defined in (13). Ka is the ratio of flame stretch rate to characteristic chemical reaction rate and is defined in (14). In these equations, l_I is the integral length scale, δ_L is the flame thickness, S_L is the laminar flame speed, u' is the turbulence intensity, and Re_T is the turbulent Reynolds number (15) [1,3].

$$Da = \left(\frac{l_I}{\delta_L}\right)\left(\frac{S_L}{u'}\right) \tag{13}$$

$$Ka = 0.157\left(\frac{u'}{S_L}\right)^2 \mathrm{Re}_{\mathrm{T}}^{-1/2} \tag{14}$$

$$Re_T = \frac{u' l_I}{\nu} \tag{15}$$

There are limited ranges for *Da* and *Ka* that are suitable to flame propagation in an engine. Abdel-Gayed and Bradley conducted thorough constant-volume combustion vessel experiments that identified various flame regimes, including flame quench [85]. Their analysis is summarized on the Leeds diagram (Figure IV-1). The regions where the *Da* is less than about 1.0 or *Ka* is greater than about 1.5 represent the region of flame quench. In this region, the chemical reaction rates within the flame are not sufficient to overcome the strain induced by in-cylinder charge motion. Dai et al. [86] and Lewis et al. [87] both demonstrated that this turbulent flame model satisfactorily predicted misfire in SI engines. Both engine models are representative of modern light-duty stoichiometric gasoline engines with high levels of cooled external EGR (~25%). The prediction of misfire is considered at either the $Ka > 1.5$ or $Da < 1$ flame quench boundary. Their simulation results correlated well with experimental data. However, several sources suggest EGR levels for SACI are beyond 25% [35,37,49], and Matsumoto et al. suggests up to 40% EGR [29]. Though production EGR levels may not be this high after considering transients, the nature of SACI likely requires higher dilution than has been used for deflagration flames. This higher dilution translates to SACI operation closer to the flame quench boundary than traditional SI engines.

An additional application of *Da* is identifying the transition from flame propagation to autoignition. As *Da* decreases, the flame structure transitions to distributed reactions as opposed to a localized flame. Yang et al. [88] and Martz [89] evaluate this criterion in 3D simulation, where a particular *Da* is considered the threshold for autoignition of a computational cell. Both demonstrate a high sensitivity of overall combustion performance to the selected *Da* threshold. Martz specifically considers this a weakness of this criteria for high-fidelity simulation. The application of this criteria for a reduced-order real-time engine control is not considered in their work.

Olesky et al. evaluate the in-cylinder conditions at spark onset for experimental SACI combustion results [51]. Their simulation is performed in KIVA without combustion. The in-cylinder conditions at spark onset are placed on the Leeds diagram, Figure IV-1. The SACI points are consistently closer to the flame quench boundary than SI, as expected. Those conditions predicted by simulation to occur in the flame quench region correlate to misfires in experimental results found in [35].

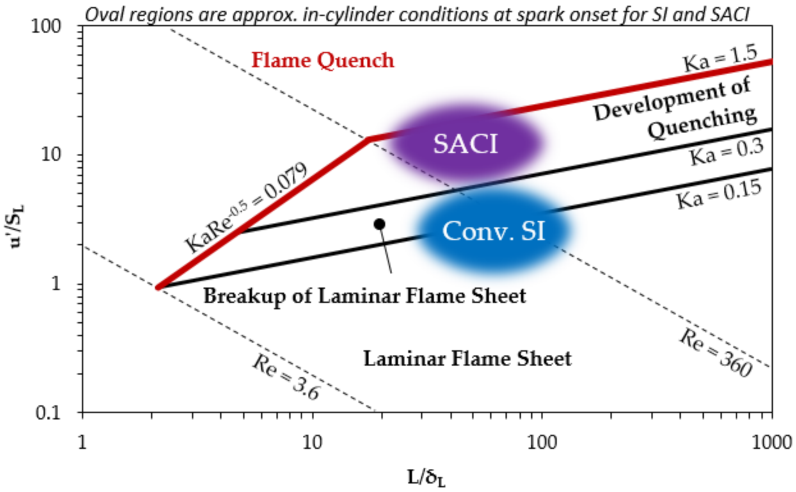

Figure IV-1: Leeds diagram depicting regions of different flame regimes and typical conditions at spark onset for SI and SACI. SACI operation is expected to trend closer to the flame quench limit from the high dilution. The diagram is adapted from [86], the SI operating region is adapted from [51,86,87], and the SACI spark onset region is adapted from [51].

This result highlights the fundamental challenge in achieving reliable SACI combustion: an appropriate dilution level for autoignition can result in flame quench for the flame propagation regime. EGR stratification and tuned charge motion is a potential solution that provides suitable conditions for both flame propagation and autoignition. Understanding the influence of dilution and charge motion on the flame propagation phase of SACI combustion is therefore critical for a robust production solution. Empirically-based tables and correlations have been developed, but they may require a substantial calibration effort and be limited in their predictive capability [57,90,91]. The flame model presented here may be a suitable basis for robust real-time predictive control.

Combustion Fundamentals: Autoignition

In the context of engines, autoignition (AI) is a rapid combustion event that occurs without a spark. The chemical reactions that lead to autoignition occur over a finite time called the ignition delay. For typical engine conditions, autoignition is triggered by self-heating or chain-branching reactions [1,2]. Ignition delay and the mechanism of autoignition are both nonlinear and highly sensitive to several parameters. Combinations of pressures, temperatures, and dilution highlight different reaction pathways with a given chemical mechanism. To clarify the impact on control, it is important to study the sensitivity of autoignition timing to temperature, pressure, and fuel type. Figure IV-2 depicts characteristic ignition regimes for isooctane across a range of temperatures and pressures. These regimes include cool flames, hot flames, and low-temperature reactions. A cool flame is a slightly exothermic, but incomplete reaction [1,2]. Isooctane strongly exhibits the cool flame phenomenon under certain conditions [1,92]. For other conditions, the cool flame may be followed by a hot flame. This two-step ignition process is characteristic of low-temperature heat release (LTHR). Each of these regimes can be encountered for several gasoline combustion strategies.

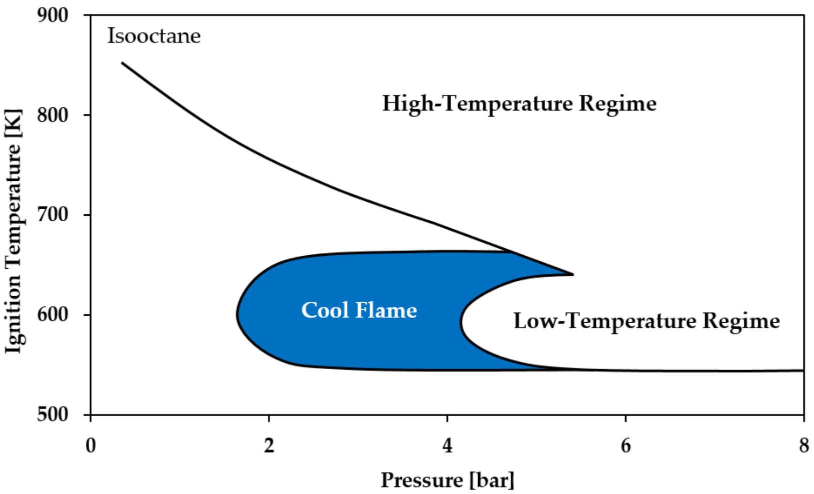

Figure IV-2: Different flame regimes for isooctane. The nature of isooctane combustion varies nonlinearly with both pressure and temperature. Adapted from [92].

In addition to distinct flame regimes, some fuels exhibit a negative temperature coefficient (NTC) region under certain conditions. NTC behavior occurs as the competition for radicals between reaction pathways shifts from chain-branching to non-chain branching. The chain-branching pathway does not require self-heating to autoignite, while the non-chain branching pathway does. The non-branching reactions become dominant at conditions where the reaction rate does not produce sufficient self-heating. This results in the NTC region, where ignition delay increases despite rising temperatures. Raising temperature further increases the reaction rate to the point that the reaction becomes self-heating and autoignition occurs more readily. Understanding the impact of the NTC is critical for SACI combustion phasing control.

The NTC behavior is sensitive to several parameters including fuel type, pressure, dilution, and air-fuel ratio [1,2,93]. Figure IV-3 and Figure IV-4 depict comparisons of ignition delay for multiple fuel chemistries and several pressures for isooctane, respectively. The analysis shown is performed by the author using Cantera, MATLAB-based chemical kinetics software. The chemical kinetics mechanism used is the gasoline surrogate mechanism developed by Lawrence Livermore National Laboratories (LLNL) [94]. The fuel-type comparison clearly illustrates the strong variation in ignition delay behavior among automotive fuels. Aromatic and alcohol fuels, such as toluene and ethanol, do not exhibit the NTC phenomenon. Furthermore, for isooctane, the influence of pressure affects both the location and strength of the NTC region. These factors create control and calibration problems that likely require a feed-forward sensing strategy or a feedback mechanism.

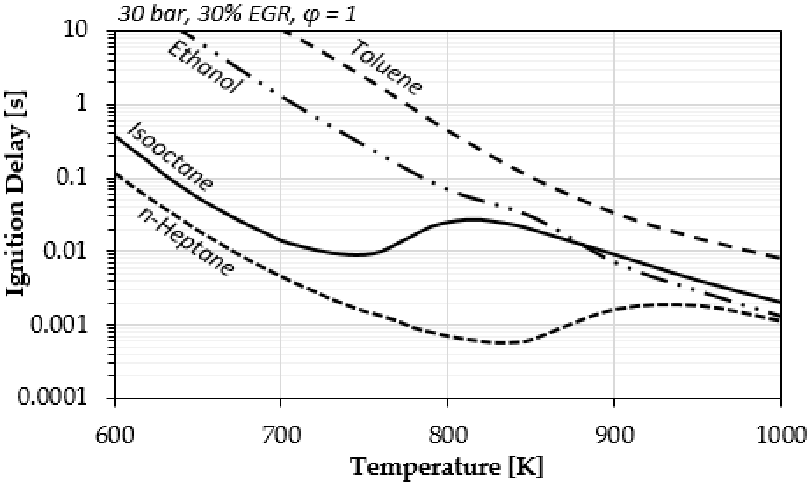

Figure IV-3: Ignition delay curves comparison between alkane fuels (n-heptane and isooctane), an alcohol fuel (ethanol), and an aromatic fuel (toluene). The variation in the presence and location of the NTC region possess an obstacle to production SACI control. Results generated by the author in Cantera using the LLNL detailed chemical mechanism [94].

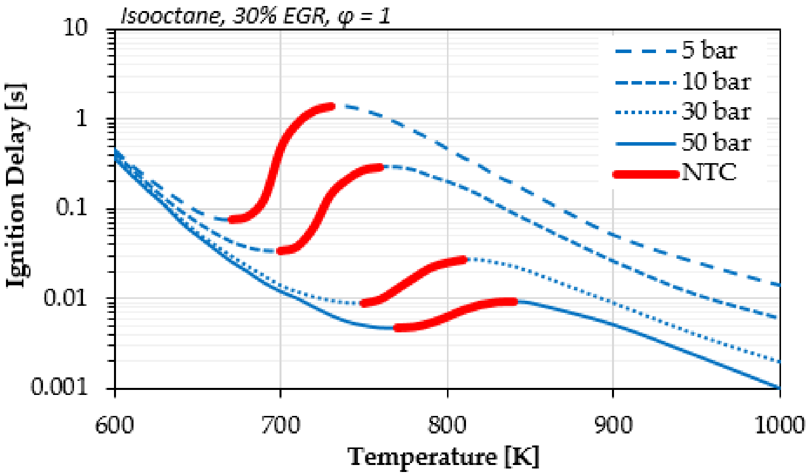

Figure IV-4: Ignition delay curves for isooctane at several pressures. The substantial changes in the NTC region strength and location for these conditions possess an obstacle to production SACI control. Results generated by the author in Cantera using the LLNL detailed chemical mechanism [94].

The mixture states and composition in an engine may encompass multiple flame regimes and can also include the NTC regime if present. Automotive fuels are blends which contain several components that have significantly different autoignition responses. In an SI engine, autoignition can occur in the unburned region ("end-gas") and is commonly referred to as "knock." It is analogous to the autoignition phase of SACI, though SI knock has much higher rates of heat release that can cause engine damage. Though not strongly considered in the pioneering SI knock research [95,96], fuel chemistry sensitivity has been more recently evaluated for SI engines. Kim et al. and Szybist et al. both investigated the effect of fuel type on knock in SI engines [48,93]. Between the two studies, four fuel types are evaluated: two alkylate fuels, one high-aromatic fuel, one gasoline surrogate, and two high-ethanol fuels. Both studies are controlled for Research Octane Number (RON), but there are clear variations in autoignition behavior attributed to specific fuel chemistry. The differences in autoignition timing and/or knock-limited spark advance among the fuels in several instances is about 10 CAD. The relative performance among the fuels varies with load and dilution, further complicating the controls challenge.

For SACI, the challenge is predicting the timing of the autoignition event under widely varying conditions and different fuel compositions. Computationally-efficient autoignition models or empirical calibrations may not be sufficiently accurate. Calibrating for variations in fuel composition prior to combustion is particularly challenging, as high-fidelity fuel sensors are required to sufficiently characterize fuel chemistry. Considering these challenges, the use of cylinder-pressure based feedback in production may be unavoidable.

Experimental Reference

A single-cylinder SACI engine dataset is used to validate both the SI burn durations and AI phasing. The dataset is provided by Oakridge National Labs (ORNL) and was funded by the United States Department of Energy (DOE). The engine is a research-focused single cylinder engine based on the GM 2.0 L Ecotec engine. Table IV-1 lists key engine geometry and Figure

IV-5 depicts a sample pressure trace along with the valve lift profiles. The engine has a hydraulically actuated fully flexible valvetrain. It is configured in either exhaust rebreathe (where the intake valve opens again during the exhaust stroke) or a high negative valve overlap (NVO). Both strategies aim to increase the amount of in-cylinder hot residual.

Table IV-1: Experimental SACI engine parameters for combustion model validation.

	SACI Engine
Bore x Stroke [mm]	86 x 86
Compression Ratio	11.85:1
Valvetrain	Fully flexible (hydraulically actuated), configured for both exhaust rebreathe or negative valve overlap
Valves Per Cylinder	4
Fueling	Direct Injection
Equivalence Ratio	1.0

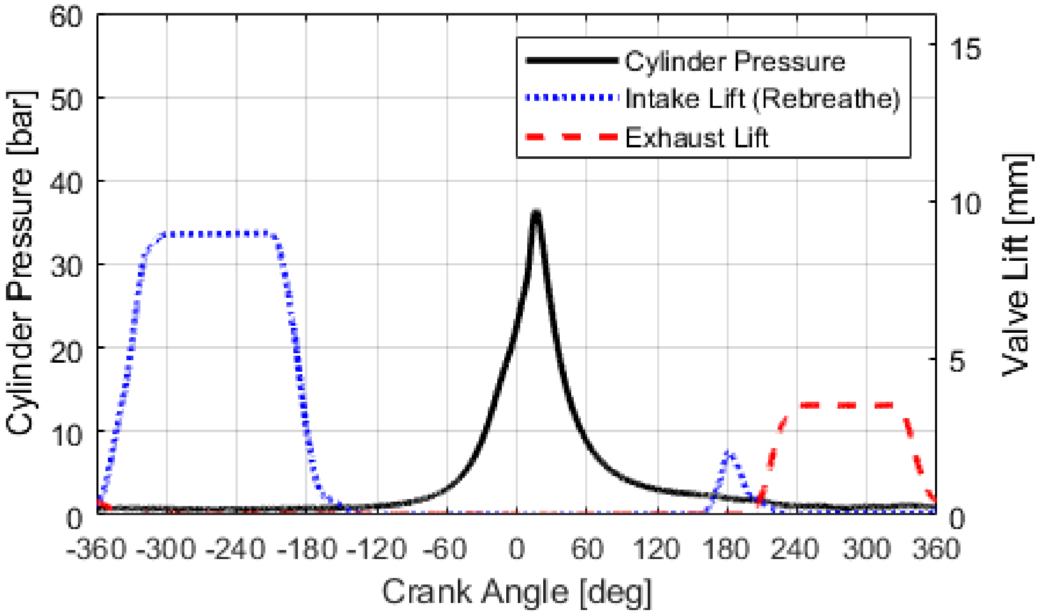

Figure IV-5: Sample pressure trace and valve lift from the experimental SACI engine data.

A separate 1D engine model is developed to match the breathing characteristics of the experimental SACI engine dataset (Figure IV-6). The tuned model is only a simulation platform to tune the combustion submodels that are then transferred to the reference 1D SACI engine model. A total of 210 experimental runs are included in the dataset, with 181 runs being stable, firing runs suitable for a model validation. The experimental SACI engine model is configured to match the experimental setup, including the measured valve lifts for each case. The intake and exhaust manifold conditions are specified via end environments.

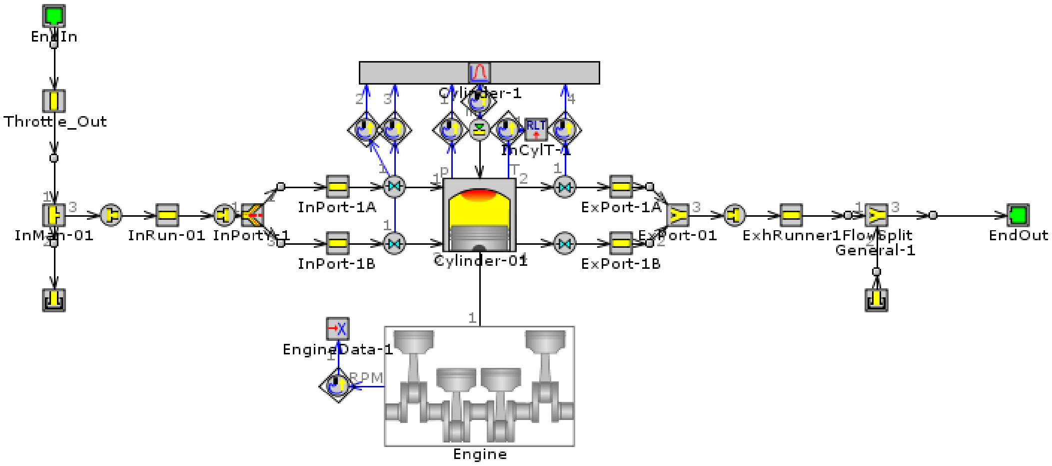

Figure IV-6: Experimental SACI 1D engine model for combustion submodel tuning.

After minor tuning of the engine model, a good match on engine state is produced. Figure IV-7 depicts the comparison between airflow and fuel flow, suggesting the in-cylinder state is matched well. Figure IV-8 illustrates a comparison of pressure-volume diagrams for two cases. One case is the exhaust rebreathe case, the other is a high NVO case. The valve events, pumping loop, and much of the compression and expansion strokes match well. The only major discrepancy is during combustion, where GT-Power underpredicts pressure. However, in these cases, autoignition does not produce any heat release, so this behavior is expected.

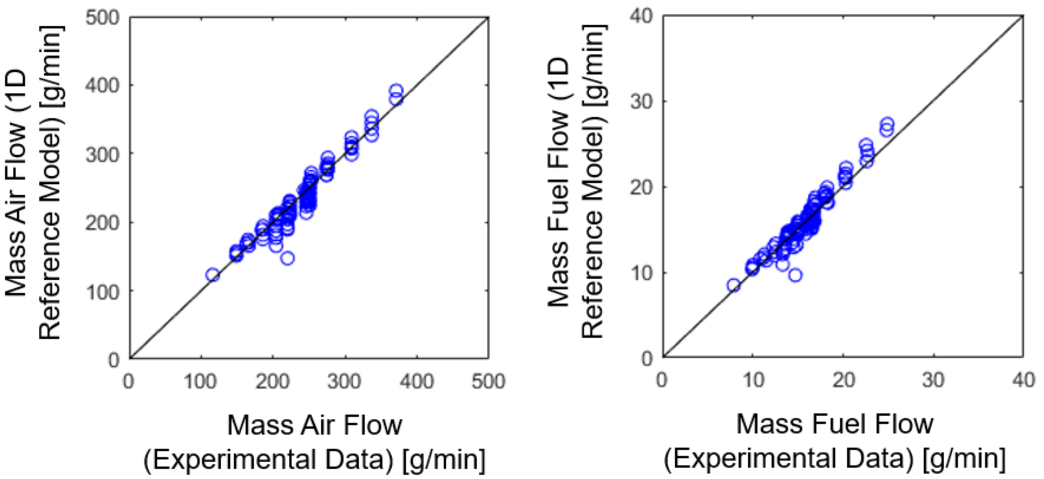

Figure IV-7: Airflow and fuel flow comparison between GT-Power results and experimental data. Overall, the 1D engine model matches the experimental results well.

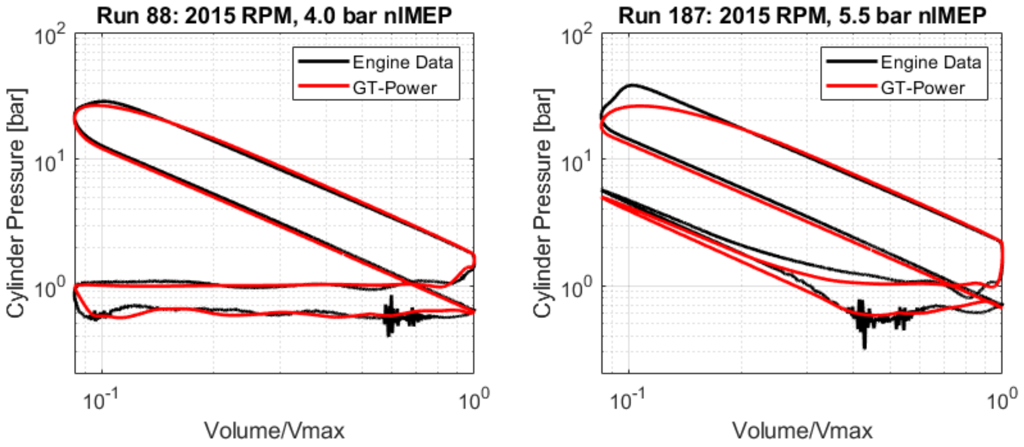

Figure IV-8: Pressure volume diagram comparison. Exhaust rebreathe (left) and long NVO (right) phasing are both represented. The overall good match indicates valve events and in-cylinder state match well. The deviation near the end of combustion is expected, as the GT-Power model does not model heat release from autoignition.

The next step is to identify the SI burn duration and autoignition phasing. To accomplish this, the AI phasing must first be identified to separate the two combustion phases. The heat release rate curve is twice differentiated to compute the curvature. With careful windowing, the peak positive curvature identifies the transition point between SI and AI. Figure IV-9 depicts the process for a sample run. The crank angle where the high-curvature region begins is defined as the autoignition phasing.

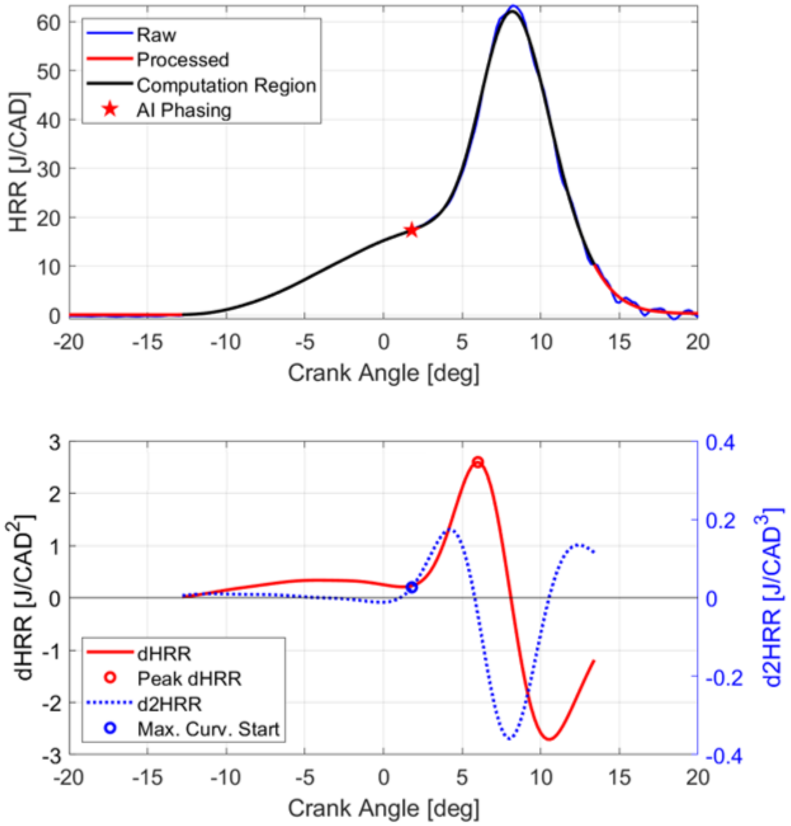

Figure IV-9: Process for determining AI phasing from experimental results. The peak positive curvature of the heat release rate curve indicates the transition from SI to AI.

From this point, the AI phasing model within GT-Power is validated. For the reference SACI 1D engine model, the built-in kinetics fit gasoline (KFG) ignition delay model is selected and tuned to the experimental SACI engine dataset. The relevant KFG model tuning coefficients are the octane number (set to 87 AKI), and the ignition delay multiplier (set to 1.05). This produced the best response, however, the KFG model has a greater spread than the experimental data (Figure

IV-10). To identify if a chemical kinetics model would perform better, a reduced mechanism is configured in GT-Power. The mechanism is a 165-species tuned for toluene primary reference fuel with ethanol [97]. This model had a similar performance to the KFG, suggesting the autoignition model structure is not the primary driver for this response. A thorough analysis comparing the error to 21 other independent and dependent variables did not identify any trend in the error. As autoignition phasing is highly sensitive to several parameters, and the rest of the 1D engine model matches well, the KFG model is accepted despite the relatively poor performance. One compounding factor may be that GT-Power does not model the autoignition event. This results in a different temperature profile throughout the cycle than if autoignition is modeled. This is especially important during compression, where the previous cycles temperature through the expansion stroke impacts the following cycles compression stroke due to residual composition. Though not a perfect match to the experimental data, it is representative of a SACI engine, which is the primary objective of the reference SACI 1D engine model.

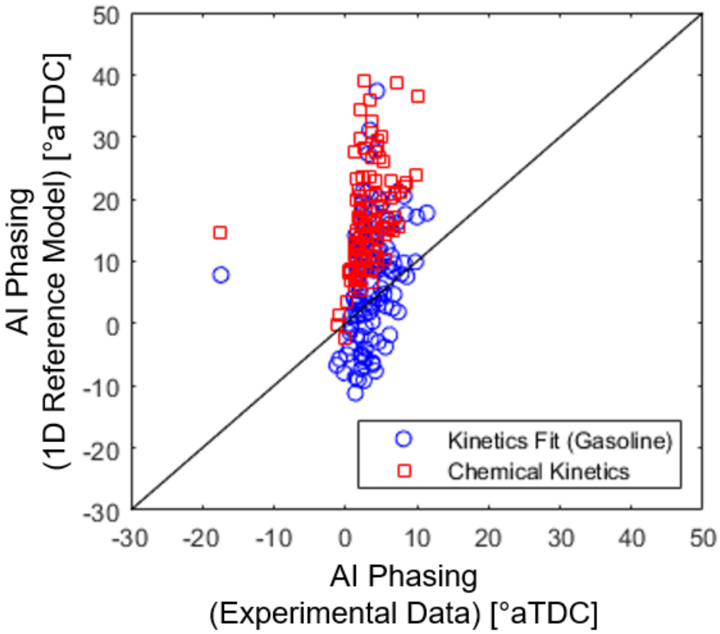

Figure IV-10: AI phasing comparison demonstrating a much greater sensitivity than experimental results.

Finally, the SI burn duration can be validated. Two burn durations will be considered: spark to CA10, and MFB10–90. The GT-Power combustion model used for this analysis is the *EngCylCombSITurb* predictive turbulent combustion model. This model has several tuning variables, but two key ones are the flame kernel growth multiplier (FKGM) and turbulent flame speed multiplier (TFSM). The FKGM impacts the spark to CA10, and the TFSM impacts both burn durations.

As it represents the earliest stage of flame propagation, tuning the FKGM is performed first. The tuned model requires only a constant value to match the nearly 200 points well. Computing the experimental spark to CA10 duration is straightforward. The spark timing is measured, and an assumption is made that the overall CA10 point is sufficiently close enough to the SI CA10 for the computation. The final tuning value for the FKGM is 5.0, and the comparison can be found in Figure IV-11.

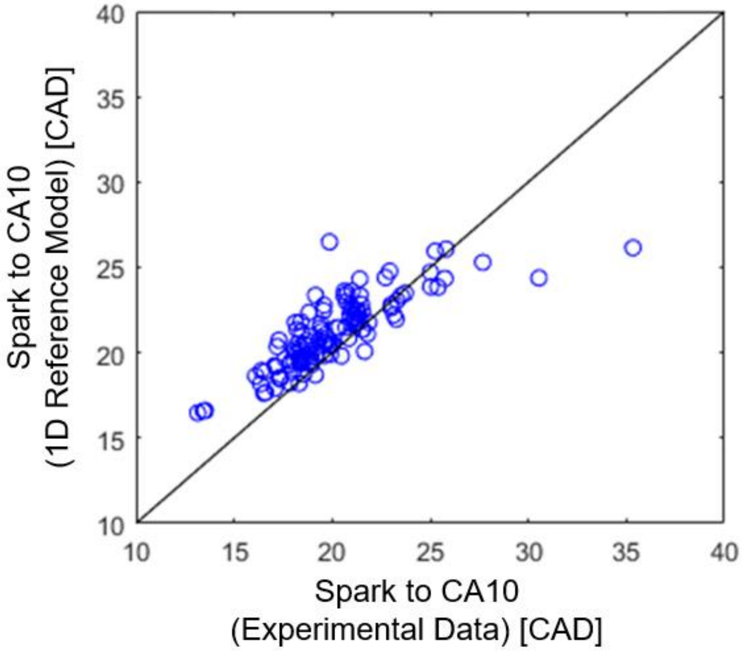

Figure IV-11: Comparison between GT-Power and experimental data of spark to CA10 duration.

The MFB10–90 duration, however, must be computed in a more indirect way. Because of the influence of autoignition, only cases with an SI portion above 10% are considered. For each of these points, the HRR from the 1D engine model and experimental results are truncated at the point of autoignition. The 1D engine model heat release rate is then shifted to eliminate error from the spark to 10% point from negatively impacting the calculation of the SI MFB10–90. Finally, the error between these two curves is computed and integrated. The TFSM is varied until the mean error is near zero without a wide variance. A constant TFSM of 0.65 is sufficient to achieve this.

The final reference combustion model is illustrated in Figure IV-12. Autoignition is modeled, but only the crank angle at autoignition onset is reported. No heat release from autoignition is modeled for clarity. Overall, all phases of combustion match well: spark to 10%, SI MFB10–90, and autoignition phasing. With the combustion model tuned, it is transferred to the reference SACI 1D engine model to be exercised over a wide range of conditions and used to tune the combustion submodels used in the simplified cylinder model.

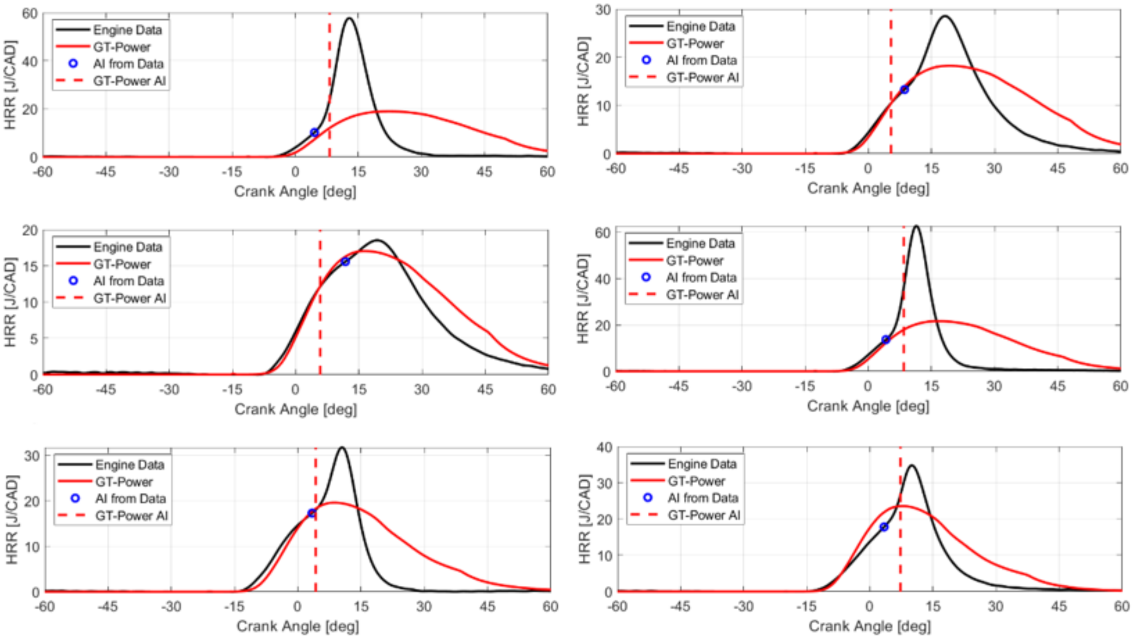

Figure IV-12: Comparison of experimental data and 1D engine simulation results. No autoignition heat release is modeled, the dotted vertical line indicates the crank angle of autoignition onset.

Flame Propagation Physics-Based Submodel

Rather than compute the physics-based model on a crank-angle basis, the model will be evaluated for the engine operating point. The model focuses on laminar flame speed (S_L) as well as the previously described dimensionless numbers: *Ka*, *Da*, and Re_T. Determining these values from non-crank-angle resolved inputs requires a series of submodels, as indicated in, as indicated in Figure IV-13.

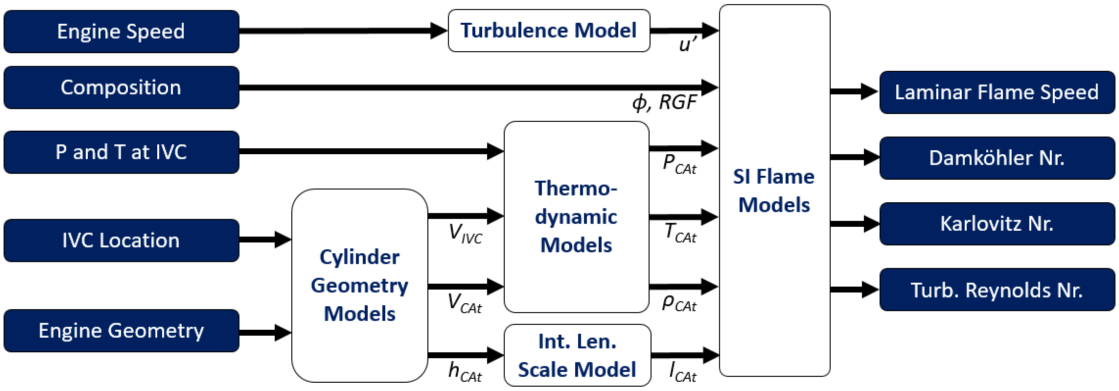

Figure IV-13: Model structure and data flow for burn duration model. Values at the target crank angle are indicated with a "CAt" subscript.

Submodel Description

The turbulence model is a proportionality constant related to mean piston speed (16). Wang et al. are successful in their application of this relationship between mean piston speed (MPS) and turbulence intensity (u') [98]. This relationship is based on prior work [99], where the typical value of coefficient c_1 range from 0.5 to 1.5. The results from the 1D engine model suggests 0.4 is appropriate, and this value of c_1 is selected for this model, though it is just outside the typical range.

$$u' = c_1 \cdot \mathrm{MPS} \tag{16}$$

The thermodynamic models are derived from the assumption of an ideal gas and a polytropic compression process. The pressure, temperature, and density at the target crank angle (e.g., TDC) are computed using the following equations. Equations (17) and (18) are derived from the polytropic relationship as the gasses are compressed from IVC to the target crank angle. The volume at a particular crank angle is computed using the volume submodel previously described. The ratio of specific heats (γ) is assumed to be 1.32. The ideal gas law is used to compute the density of the gas ρ, (19). The universal gas constant R is set equal to 287 J/kg·K.

$$T_{CAt} = \mathrm{T_{IVC}} \left(\frac{V_{IVC}}{V_{CAt}}\right)^{\gamma-1} \tag{17}$$

$$P_{CAt} = \mathrm{P_{IVC}} \left(\frac{V_{IVC}}{V_{CAt}}\right)^{\gamma} \tag{18}$$

$$\rho_{CAt} = \frac{P_{CAt}}{R \cdot T_{CAt}} \tag{19}$$

The integral length scale l_I is another key input for the dimensionless parameters (20). It is assumed to be proportional to the instantaneous cylinder height (h) [99]. Liu et al. recommend a value of $\mathrm{c_2}$ between 0.2–0.4. This is consistent with an analysis performed by Lewis et al., where a detailed study of SI flame structure for high-dilution engines indicates $\mathrm{c_2} = 0.2$ as a reasonable value [87]. For this study, a value of $\mathrm{c_2} = 0.2$ is selected.

$$l_I = \mathrm{c_2} \cdot h \tag{20}$$

Kinematic viscosity ν is necessary for the computation of the dimensionless parameters. It is calculated by dividing the dynamic viscosity (μ) by density (ρ). Assuming the dynamic viscosity is a function of temperature and equal to air [1], the kinematic viscosity can be computed as shown in (21).

$$\nu = \frac{\mu_{air}(T)}{\rho} = \frac{(3.3 \times 10^{-7}) \cdot T^{0.7}}{\rho} \tag{21}$$

The first critical flame model is the laminar burning velocity, S_L. Heywood describes a relationship between S_L and temperature, pressure, and equivalence ratio (ϕ) [1]. For gasoline, the laminar flame speed (in cm/s) at 1 atm and 298 K with zero residual $S_{L,0}$ is computed in (22). This can be extended for non-zero burned gas fractions (BGF) using (23). Finally, at elevated temperatures and pressures, the laminar burning velocity can be further extended using (24), where α and β are defined in (25) and (26).

$$S_{L,0} = 30.5 - 54.9(\phi - 1.21)^2 \tag{22}$$

$$S_{L,RGF} = S_{L,0}(1 - 2.06 \cdot BGF^{0.77}) \tag{23}$$

$$S_L = S_{L,RGF}\left(\frac{\mathrm{T}}{298\ \mathrm{K}}\right)^{\alpha}\left(\frac{p}{1\ \mathrm{atm}}\right)^{\beta} \tag{24}$$

$$\alpha = 2.18 - 0.8(\phi - 1) \tag{25}$$

$$\beta = -0.16 + 0.22(\phi - 1) \tag{26}$$

Though these are widely accepted relationships, infeasible results from these equations emerge near SACI conditions. For example, $S_{L,0}$ is less than zero below a ϕ of ~0.46. While flame speeds are low under lean conditions, the second-order polynomial nature of the fit does not capture a gradual decrease to zero at these conditions. A similar phenomenon occurs as BGF increases beyond 39%. While both conditions are challenging for flame propagation, either will produce a (slowly) propagating flame. For example, Gukelberger et al. demonstrated about 30% external EGR (stoichiometric) on a gasoline spark-ignited engine [100]. Some internal residual would also be present, indicating a total residual gas fraction of above 0.3 and likely close to 0.4. A high-energy continuous discharge ignition system is leveraged, however, the flame successfully propagated well after the influence of the ignition system is significant. These results are also performed within cycle-to-cycle variability limits. Consequently, though flame speeds will be relatively low at

BGF = 0.4, the second-order polynomial nature of the Heywood fit does not capture the gradual decrease to zero at these conditions. A slightly modified laminar flame speed model is introduced to address this behavior. The goal of these models is to closely match the Heywood models near stoichiometric, low-BGF conditions, but provide a continuous, positive output. The laminar flame speed function is an exponential function centered around the same point (ϕ = 1.21), with the same amplitude (30.5 cm/s). A single tuning parameter is tuned to -2.14 to minimize the error at ϕ = 0.8 (27). A similar process is followed for the $S_{L,RGF}$. An exponential decay function from 1.0 to 0.0 is selected, and a single tuned parameter is found to be -4.93 to minimize error at BGF = 0.25 (28).

$$\mathrm{S_{L,mod}} = 30.5 \cdot \exp\left(-2.14 \cdot [\phi - 1.21]^2\right) \tag{27}$$

$$\mathrm{S_{L,RGF}} = \exp\left(-4.93 \cdot \mathrm{BGF}\right) \tag{28}$$

A comparison between the original functions defined by Heywood and the modified versions is illustrated in Figure IV-14. For the range around stoichiometric, the two functions produce similar values. However, at equivalence ratios lower than 0.8, the modified laminar flame speed function gradually approaches zero, while the original function approaches negative infinity.

These modifications are critical because the SACI engine will operate either at low-BGF around ϕ = 0.5, or stoichiometric with high BGF (0.3–0.4). At ϕ = 0, for example, the actual laminar flame speed should be zero, as there is no fuel. The modified laminar flame speed function suggests 1.3 cm/s, while the original Heywood function reports -50 cm/s. Several laminar flame speed studies are investigated to justify this model; however, none could be found that considered equivalence ratios below 0.6.

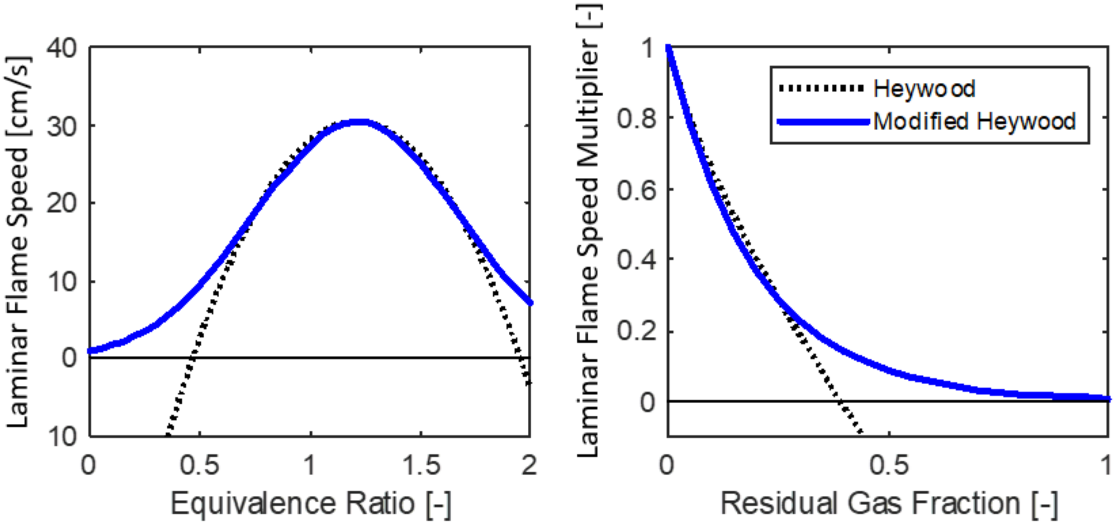

Figure IV-14: Comparison between the Heywood functions for laminar flame speed and the modified versions.

The final submodel is the flame thickness model. According to Abdel-Gayed et al. [85] and Dai et al. [86], the flame thickness δ_L (determined by thermal diffusion) can be expressed as the ratio of kinematic viscosity and laminar flame speed, (29).

$$\delta_L = \frac{\nu}{S_L} \tag{29}$$

Physics-Based Burn Duration Model Results

Prior to computing the burn duration, the models are evaluated to determine if the predicted SI flame parameters were reasonable. Laminar flame speed, *Da*, and *Ka* are plotted as a function of the reference model MFB10–90 burn durations (Figure IV-15). The in-cylinder parameters are computed at a single point during the cycle. After several trials, the best results are obtained by computing parameters for MFB10–90 at the target CA50 location.

Each parameter in Figure IV-15 demonstrates a trend with the reference burn duration, and substantial noise is present. This noise is deterministic and likely the result of the reduced fidelity of the model. Eliminating this noise will likely require a dramatic increase in computational expense as these calculations would be performed within each cycle as a function of crank angle.

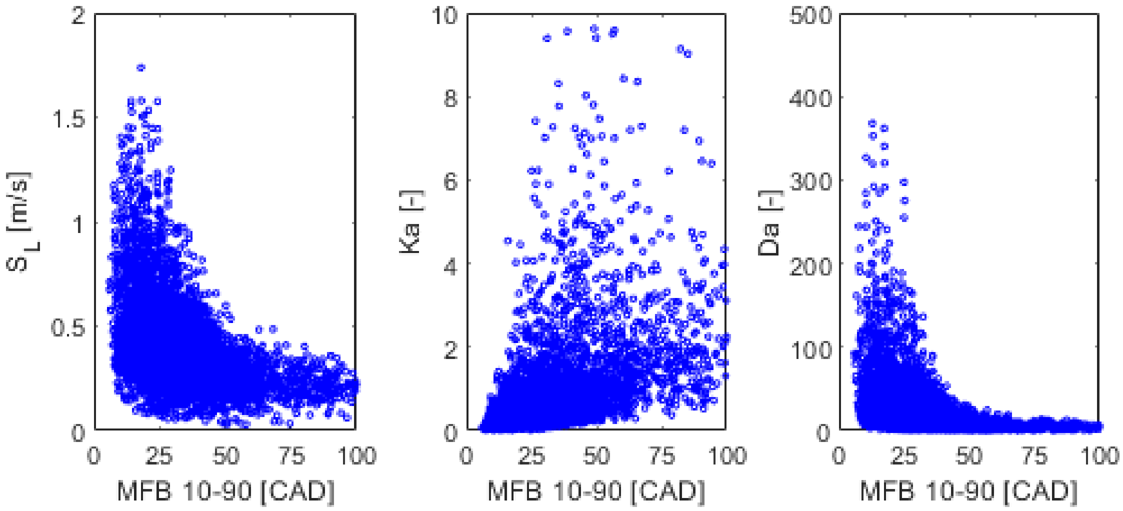

Figure IV-15: Laminar flame speed, Da, and Ka results as a function of reference model burn durations.

Each of the previously described submodels contributes to the final determination of the burn rate. To determine the numerical value for a particular burn duration, the method used by Chen et al. is selected [82]. In their work, they consider the ratio of turbulent flame speed proportional to the ratio of burn durations for two cases. However, as the turbulence intensity is a single value for each case dependent on only engine speed, turbulence is largely constant for all cases. Instead, laminar flame speed forms the basis of this model. In-cylinder conditions and composition greatly affect the laminar flame speed. This relationship can be leveraged to produce a fitted equation based on laminar flame speed alone to predict burn durations. The relationship is presented in (30), where S_L is the laminar flame speed in m/s evaluated at the target CA50. The relatively imprecise coefficients result from the poor model accuracy.

$$\theta_{BD}(S_L, \mathrm{N}) = 10\left(\frac{1}{S_L}\right) + 10 \tag{30}$$

The overall results are presented in Figure IV-16. The data is divided into three sets of MFB10–90 values for later investigations. The physics-based submodel showed poor sensitivity to spark timing relative to the reference 1D engine model. Additionally, the deterministic noise evident on each of the key parameters (Figure IV-15) has translated to significant noise for the burn duration model.

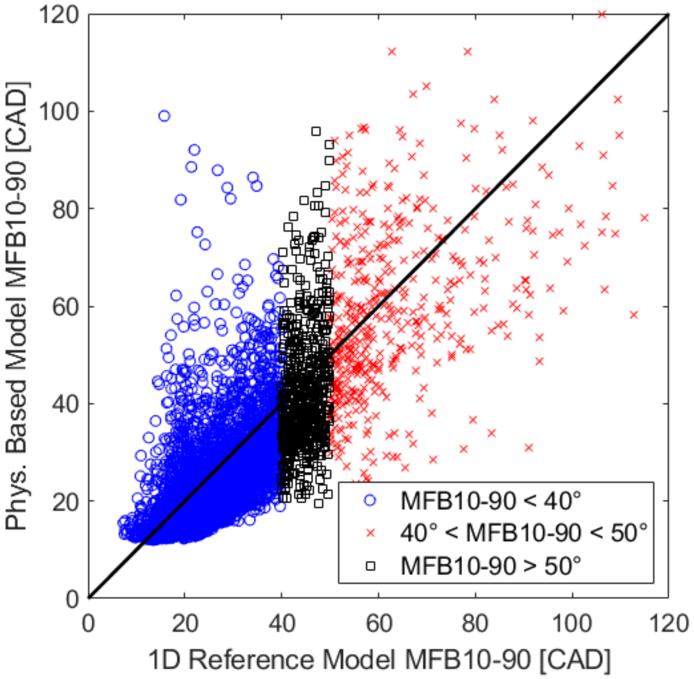

Figure IV-16: Results comparing the physics-based burn duration models to the results from the reference model.

The model error is evaluated as a function of the input parameters. Figure IV-17 depicts a selection of parameters for the MFB10–90 burn duration model. Several trends are apparent, including most notably the poor performance of the model as phi prime ϕ' decreases below 0.5. Low speeds and low loads (examine air mass in Figure IV-17) also illustrate greater noise and error, though some of this may be due to the low charge equivalence ratio ϕ'. No significant trend with *Ka* or *Da* (not shown) is observed.

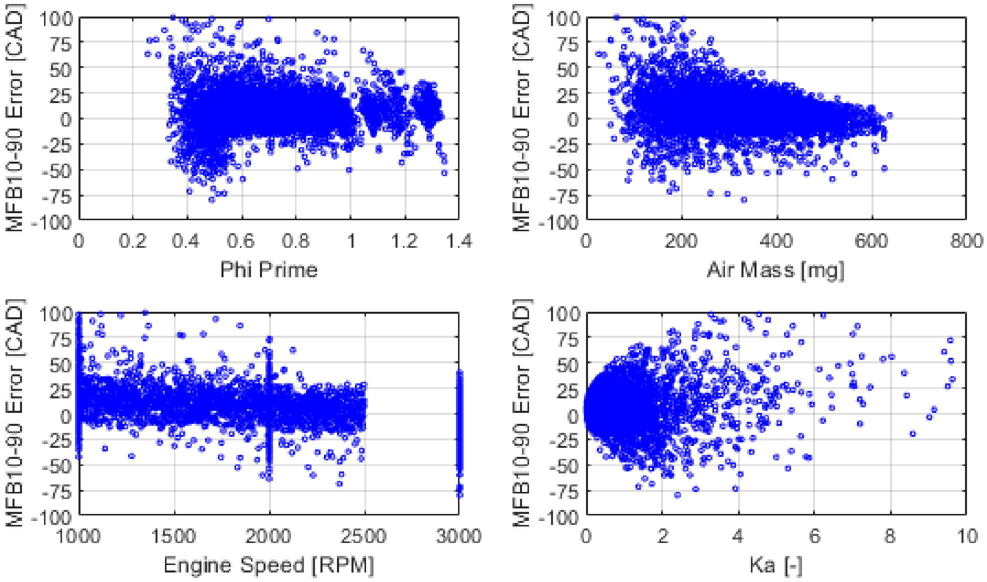

Figure IV-17: Model error for MFB10–90 physics-based model for select parameters. No trend is observed that could be corrected with inclusion of additional parameters in the model.

As indicated in the earlier section, the flame structure suggested by the Leeds diagram may provide insight into flammability limits. The results of the physics-based models for MFB10–90 are plotted on the Leeds diagram and divided into three groups (Figure IV-18). The groups are isolated by burn duration: MFB10–90 < 40 CAD, 40 CAD < MFB10–90 < 50 CAD, and MFB10–90 > 50 CAD. These represent acceptable, borderline, and unacceptable burn durations, respectively. The trend is clear, as burn durations lengthen, they approach or enter the flame quench area above the *Ka* = 1.5 line. Though there is significant noise in these results, the trend is encouraging considering the limited fidelity of the model. However, since a data-driven approach (discussed in the following section) produces a lower error, the physics-based burn duration model is not selected. However, the key result from this investigation is that burn duration is a suitable analogue for flame structure. This enables a data-driven model to imply that a condition will produce poor flame propagation.

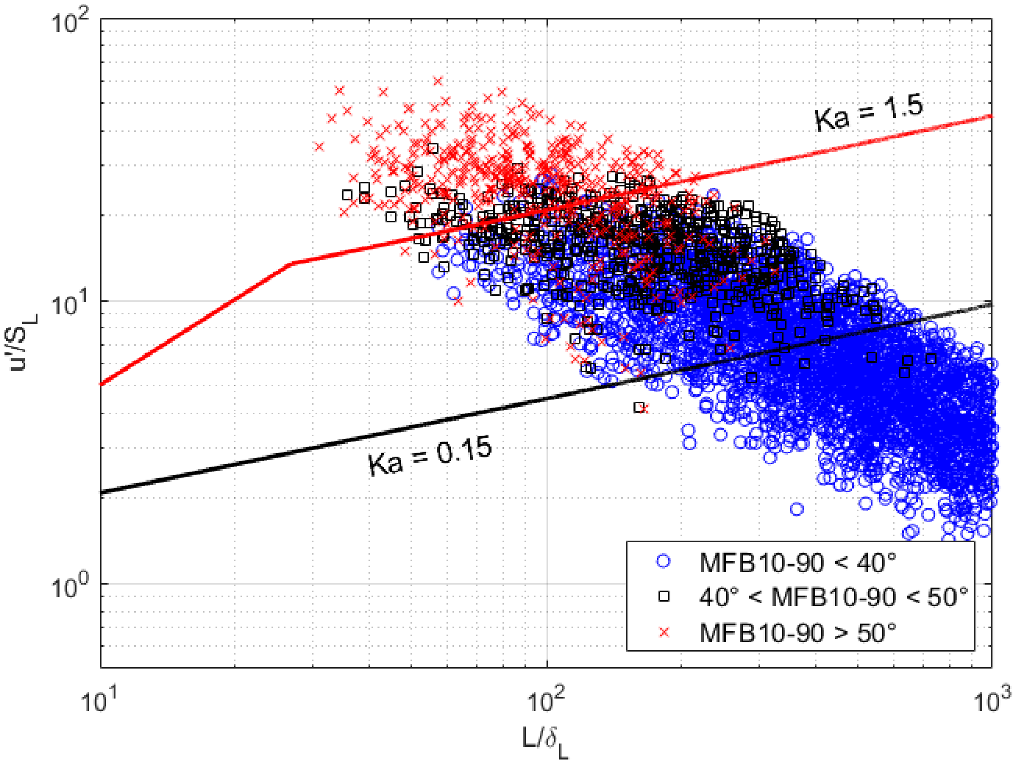

Figure IV-18: Leeds diagram with physics-based model results plotted and grouped by reference model burn duration.

Flame Propagation Neural Network Submodel

Based on the success of the artificial neural network for autoignition (Appendix A) and in-cylinder state models (Chapter III), it is considered for the models for flame propagation. An appropriate model must estimate both the spark timing and the overall burn duration. The spark to 50% burn point is critical as the overall combustion phasing target (CA50) to the control input (spark timing). The overall burn duration (MFB10–90) determines how fast heat is released and how quickly the charge mass is consumed. Both are critical for autoignition performance.

Burn Duration Submodel Structure

To begin the ANN tuning, the independent variables are identified. The 1D engine model results include a wealth of results, some of which are unlikely to be feasible for a control-oriented model. A subset of parameters is down selected from all available parameters. Each parameter in the subset is first evaluated independently to identify the strength of each parameter in explaining the observation. A network of 15 neurons in a single hidden layer is used for this preliminary study. The parameters are then ranked in order from highest strength to lowest strength. Redundant parameters are removed (e.g., total mass, if burned mass and air mass are ranked higher). For the next step, the network inputs are expanded to include the next ranked parameter cumulatively. In other words, the highest ranked parameter if first evaluated alone, then the highest two ranked parameters, then the highest three ranked parameters, etc. At each step, the model results improved as the network is provided with more input data. Figure IV-19 depicts the progression of reducing root mean square error (RMSE) as more input parameters are included. Based on the results, once the input parameters include external EGR, burned mass, target CA50, air mass, equivalence ratio ϕ, engine speed, and intake manifold pressure, no further error benefit is observed. These inputs, therefore, are the inputs used for the model formulation.

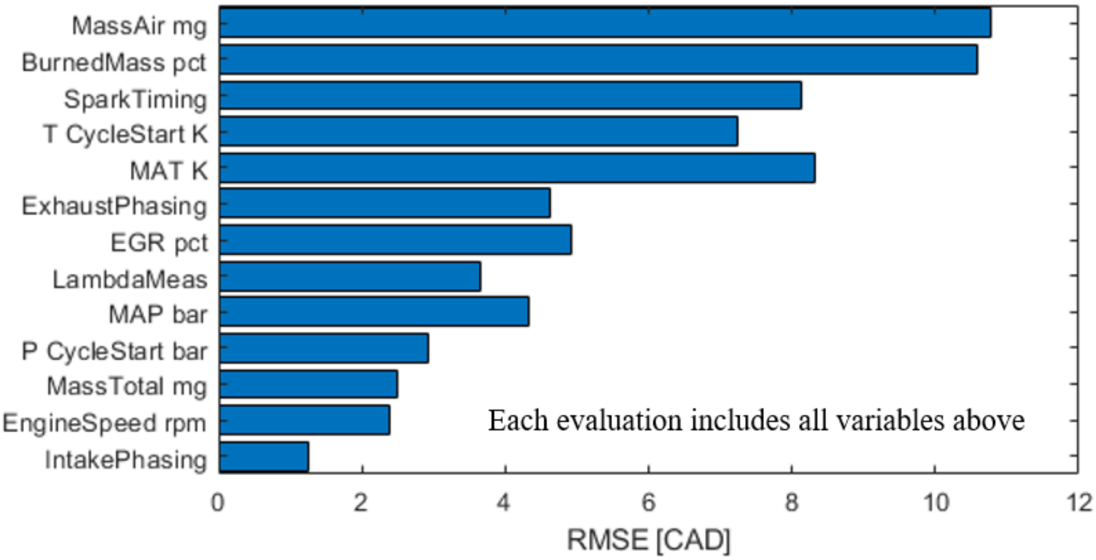

Figure IV-19: The progression of root mean square error (RMSE) as more parameters are included.

With the model inputs selected, the next step is to identify the network structure. A sweep of hidden neurons and hidden layers is performed. The results are plotted against both the total number of tuning parameters and total number of neurons. The number of tunable parameters in a network is computed using (31), where m_h the total number of hidden layers, and n_i are the number of neurons in layer i. Layer 1 is the input layer, and last layer is the output layer.

$$Tunable\ Parameters = \sum_{i=1}^{m_h+1} n_i n_{i+1} + n_{i+1} \tag{31}$$

Figure IV-20 illustrates the results. As model complexity increases, model error decreases. However, the performance of the multilayer networks is significantly better than a single hidden layer network for the same number of tunable parameters or neurons. There is no significant improvement for three hidden layers versus two. Based on these results, a two-layer network with about 300 tunable parameters and 25 total neurons is selected. There are several network architectures that can achieve this. To evaluate the effect of the network architecture, the results that satisfied the specified network size are plotted against the network reduction factor. This factor is computed by dividing the number of second hidden layer by the number of first hidden layer neurons. A value less than one indicates the second layer is smaller than the first. Figure IV-21 illustrates the findings, which suggest that the optimal performance occurs when the second layer is slightly smaller than the first, though the sensitivity is weak.

This is one of the several methods used to prevent overfitting and maximize generalizability. A more complex model (i.e., a model with a high number of parameters) can more easily fit noise, both stochastic and deterministic. Stochastic noise is random noise outside of the domain of the target function (e.g., electrical interference on a measurement). Deterministic noise is the result of reducing highly complex models to simpler ones. Both types of noise are characterized by high frequencies relative to the underlying behavior. By constraining the model complexity, the ability to fit to noise is also limited. The smallest model size that is indistinguishable from a higher-order model is selected (including the impact of noise). The noise present in the error response occurs because the starting point for the weights is selected at random. Early stopping is also implemented, which reduces the potential for the training from overfitting the noise. Generalizability is achieved by the same regularization techniques and is evaluated using a hold-out of 15% of data, called the test data. This test data is not part of the training process in any way and therefore illustrates model behavior outside of the training set.

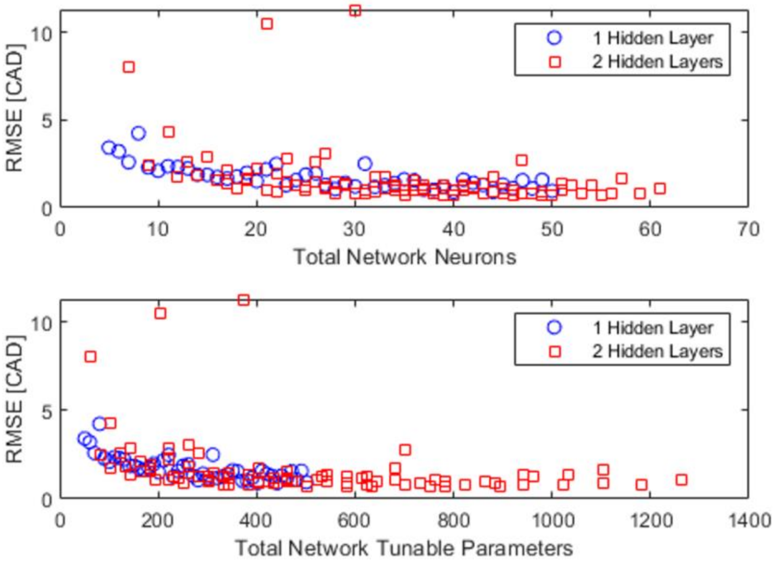

Figure IV-20: RMSE results of a sweep of network size.

The final structure of the network is pictured in Figure IV-22. It consists of the seven previously described inputs, and 27 total hidden neurons in two hidden layers. The first layer has 15 hidden neurons, the second has 12, and these produce a total of 340 tunable parameters. The training process took 50 epochs to identify optimal performance as indicated in Figure IV-22.

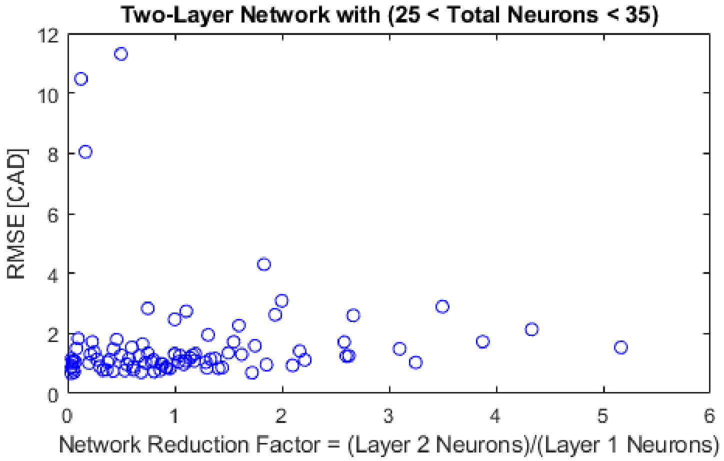

Figure IV-21: RMSE results of a sweep of network structure.

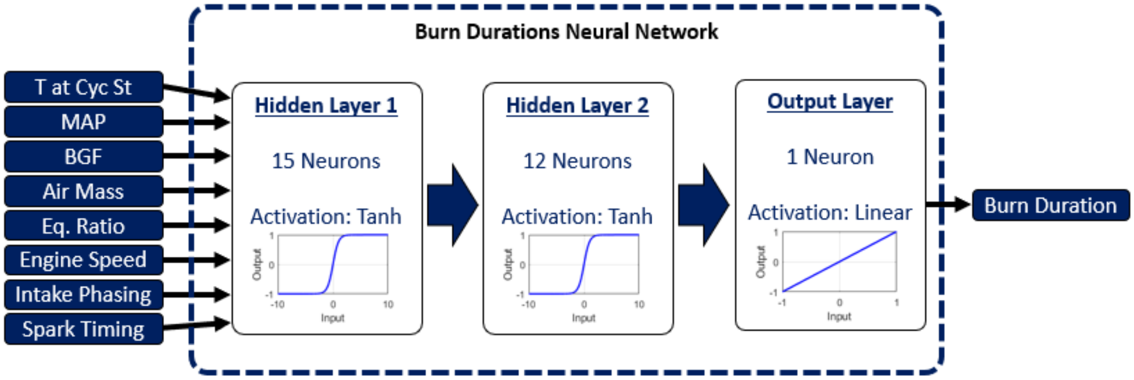

Figure IV-22: Neural network architecture for all SI burn duration networks.

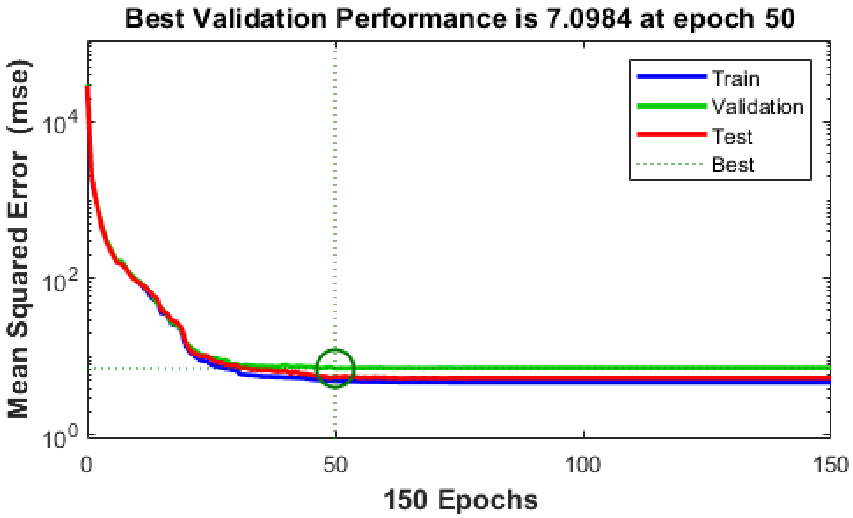

Figure IV-23: Training performance of the spark to CA50 duration neural network.

Burn Duration Submodel Performance

Three burn durations are evaluated: Spark to CA10, Spark to CA50, and MFB10–90. The Spark to CA10 duration encompasses the flame kernel development period and is therefore critical for determining spark timing. Figure IV-24 depicts the comparison between the ANN and the reference 1D engine model. Most results are less than about 50 CAD, which is consistent with feasible burn rates for SI combustion. Within this range, there is good agreement between the candidate model (ANN) and the reference model. The overwhelming majority of points are within 5 CAD of the reference model, and the overall RMSE (for all points) is 2.4 CAD. Above a duration of 50 CAD, the spread is larger. However, these points represent sufficiently long durations that will likely be excluded based on one or more combustion constraints. The data is broken down into three groups: training dataset, validation dataset, and test dataset. The training dataset is the dataset the optimization algorithm uses to compute the objective function, the validation dataset is used by the training algorithm to determine when to stop training, and the test dataset is not used at all during the training process. The test dataset represents the best evaluation of the ANN performance. The result indicates that there is no significant difference between the three datasets, especially below 50 CAD. This suggests the model has not been overfit and the results can be accepted with high confidence.

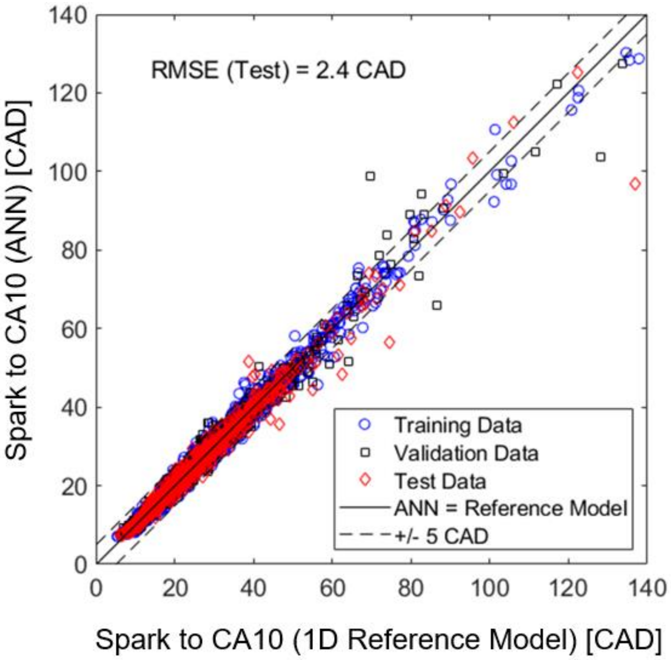

Figure IV-24: Spark to CA10 duration ANN submodel evaluation.

The Spark to CA50 duration is a key metric as it identifies the duration between the control input (spark timing) and the target output (CA50) directly. Figure IV-25 depicts the comparison between the ANN and the reference 1D engine model. Most results are less than about 60 CAD, which is consistent with feasible burn rates for SI combustion. Within this range, there is good agreement between the candidate model (ANN) and the reference model. The overwhelming majority of points are within 5 CAD of the reference model, and the overall RMSE (for all points) is 2.4 CAD. Above a duration of 60 CAD, the spread is larger. However, these points represent sufficiently long durations that will likely be excluded based on one or more constraints. The result also indicates that there is no significant difference between the three datasets, especially below 60 CAD. This suggests the model has not been overfit and the results can be accepted with high confidence.

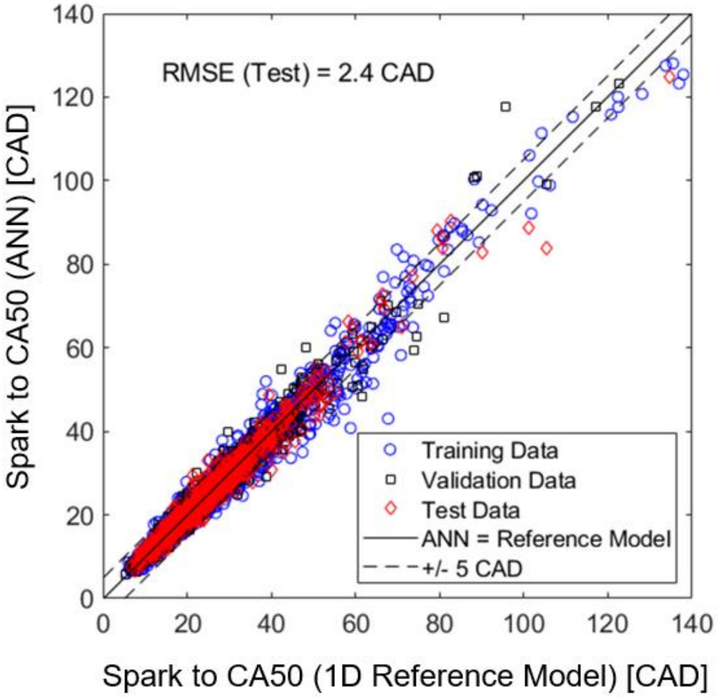

Figure IV-25: Spark to CA50 duration ANN submodel evaluation.

The MFB10–90 duration is the bulk burn duration for SI and is important to accurately predict as it can be used as an analogue for potential misfires. A MFB10–90 of 45 CAD is selected as the threshold for unacceptable cycle-to-cycle-variation (CCV). While this value is above the typical limit for SI combustion, SACI combustion can tolerate longer SI burn durations than only SI [35] and a higher limit is more challenging for the model. Figure IV-26 depicts the comparison between the ANN and the reference 1D engine model. Most results are less than about 50 CAD, which is again consistent with feasible burn rates for SI combustion. Within this range, most points are within 5 CAD of the reference model, and the overall RMSE (for all points) is 3.0 CAD. Below 45 CAD, the RMSE is 1.4 CAD. Above a duration of 45 CAD, the spread is larger. However, these points represent long durations that will be excluded based on the CCV constraint. The result also indicates that there is no significant difference between the three datasets, especially below 50 CAD. This suggests the model has not been overfit.

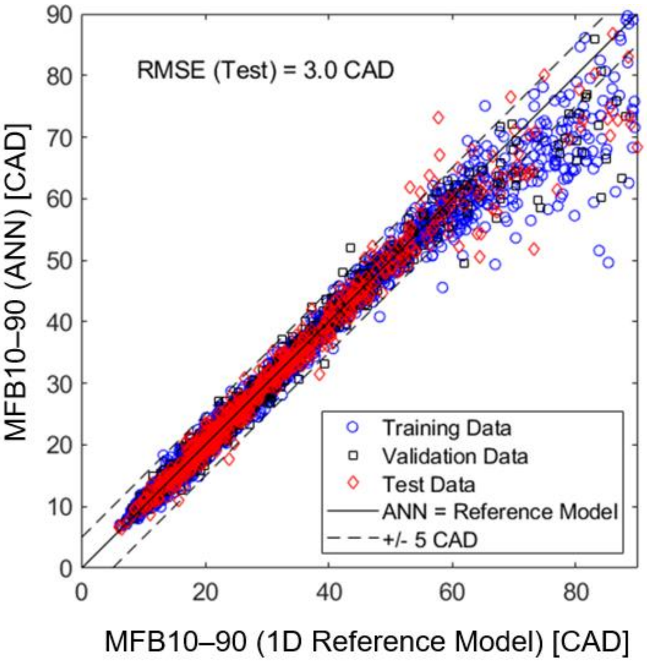

Figure IV-26: MFB10–90 duration ANN submodel evaluation.

The results above 45 CAD are potentially problem as significant burn duration errors can be compounded throughout the simplified cylinder model and yield poor overall results. However, at these long burn durations, the cylinder model will consider the burn duration to be infeasible and reject these conditions. At this point, the model must only accurately predict that the burn duration is above the threshold. Below the 45 CAD threshold, the network is a regression network and must accurately predict MFB10–90. Above this threshold, the ANN must only correctly indicate the burn duration is above the threshold, and is essentially a classification network. Figure IV-27 depicts this dual-mode operation. Note that there are only two points in the "false negative" region. While these points may have been misclassified, the effect is minor. A negative classification for MFB10–90 above the threshold means that the regression result is used. These two points are still relatively close to the reference model, with errors of 8 and 13 CAD (20% and 22%, respectively). Though not ideal, this is reasonable, as the RMSE of the regression region is 1.4 CAD and the classification error for the higher burn duration points is 99.5%.

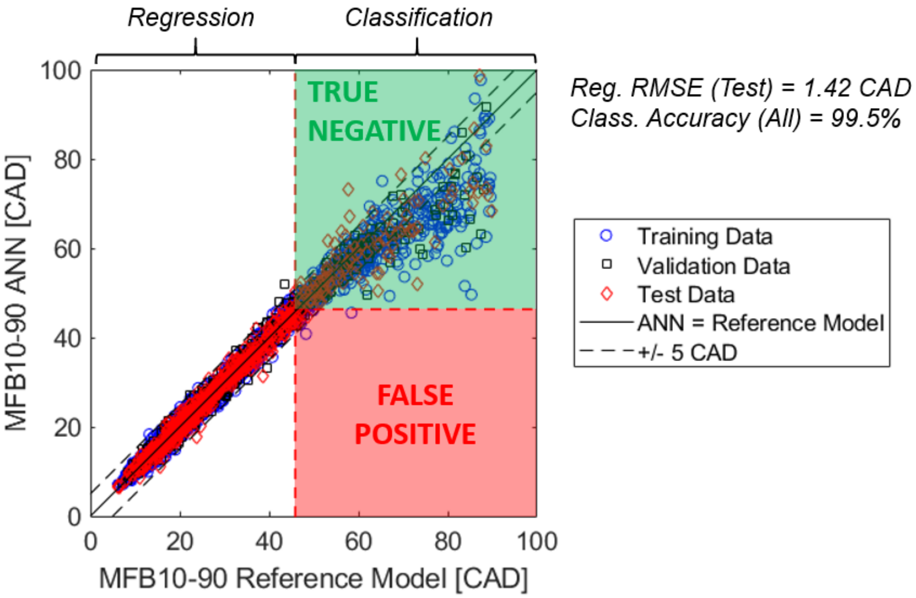

Figure IV-27: MFB10–90 ANN serving as both a regression and classification network.

Autoignition Submodel

A data-driven submodel is selected for autoignition based on the success of the ANN for SI burn duration and an independent investigation presented in Appendix A. The timing of autoignition plays a major role in both combustion phasing and combustion constraints. Prior to tuning the model, a clear understanding an acceptable accuracy is defined. Three approaches are combined to determine a reasonable model accuracy: the variability in CA50 for acceptable SACI combustion, the sensitivity of ringing in HCCI to autoignition phasing, and example results for a production SACI engine autoignition model.

First, the SACI combustion data is analyzed to identify the standard deviation for overall CA50 under stable SACI combustion. For the 210 runs, the median standard deviation of SACI CA50 is 2.52 CAD. To help illustrate this, a run with a similar standard deviation of CA50 is examined (Figure IV-28). This run is 4.1 bar nIMEP at 2500 RPM and stoichiometric. The standard deviation of CA50 is also 2.52 CAD and the COV of nIMEP is 2.1%. This illustrates that a point well within a typical COV of IMEP limit of 3% can still have over 2 CAD of CA50 variation.

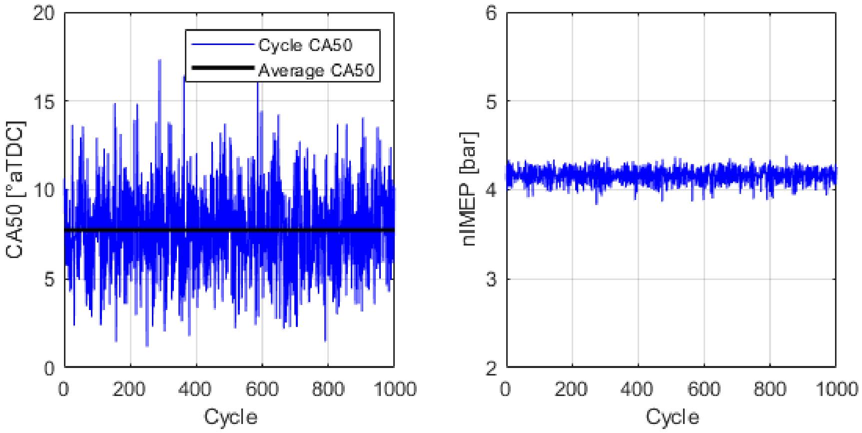

Figure IV-28: CA50 variation of 2.5 CAD for a SACI operating point with a COV of IMEP of 2.1%.

Additionally, the sensitivity of ringing intensity for HCCI is evaluated. In pivotal research by Eng, the response to CA50 for HCCI combustion is quantified [4]. Eng demonstrates that the increase of ringing intensity (RI) is gradual with combustion phasing and displays no inflection point as SI knock does with respect to combustion phasing. From the data, the inference is made that to reduce RI from the limit to 50% of the limit requires 4 CAD later combustion phasing. The response is depicted in Figure IV-29. As there is no production HCCI engine, no practical RI margin is established. However, from this result, it can be reasonably inferred that if autoignition accuracy is on the order of ~1 CAD, the RI limit can be avoided or quickly mitigated.

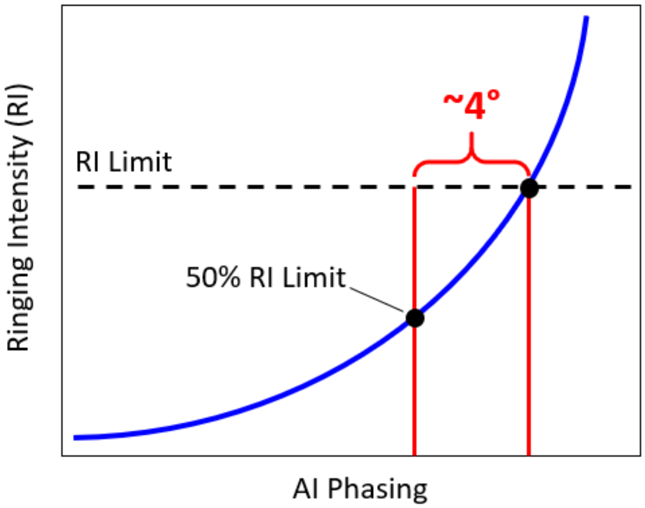

Figure IV-29: Ringing intensity response to combustion phasing for HCCI.

Finally, an example of a SACI autoignition model response is evaluated. Work by Nakai et al. briefly describe their model-based approach to production autoignition control [60]. Their work presents a redacted plot which suggests the typical model error is 1–3 CAD.

Synthesizing these results is particularly straightforward as each individually suggests about a 2 CAD error is tolerable. Therefore, for the autoignition submodel in this work considers a

2 CAD error as suitable evaluation criteria. As previously described, the high sensitivity of autoignition to external factors such as fuel composition will likely demand combustion feedback sensors. If these sensors are in place, the requirements on the autoignition model can be relaxed as the model results are not the sole identifier of AI phasing.

To tune the network structure, the same method describe for the flame propagation model is used. The same eight inputs are found to have the most sensitivity, and a sweep of network size and number of hidden layers suggests the error approaches the minimum around 35 hidden neurons for two or three hidden layers (Figure IV-30). Consequently, a two hidden layer network with 20 hidden neurons in the first layer and 16 in the second is selected. This network, depicted in Figure IV-31, has 36 neurons arranged in two layers.

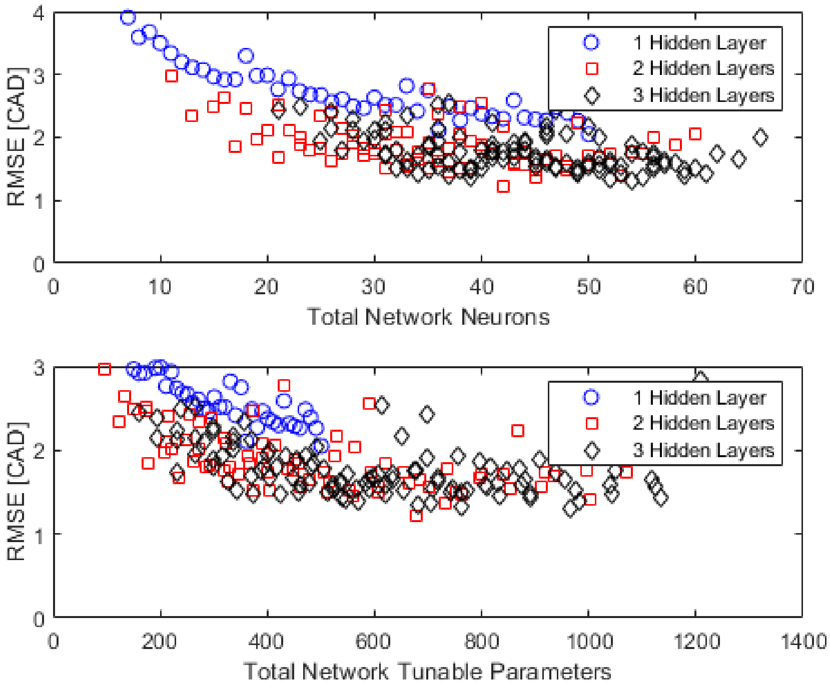

Figure IV-30: RMSE of neural network as a function of network size and structure for the autoignition submodel.

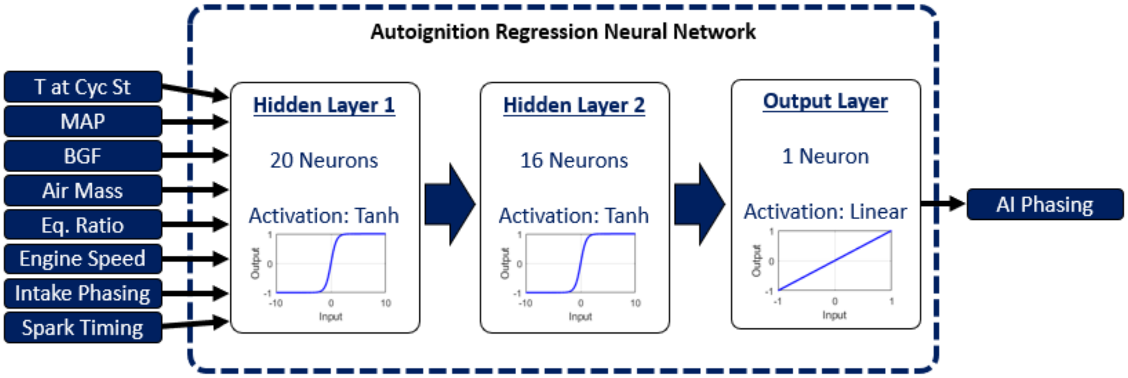

Figure IV-31: Autoignition regression model neural network structure.

Because of the high sensitivity of autoignition, an investigation is performed to identify if additional regularization techniques would benefit the accuracy. Bayesian regularization (BR) is compared to the non-regularized Levenberg-Marquardt (LM) method. Figure IV-32 depicts 11 randomly selected spark sweeps from the reference 1D engine model. Both performed similarly, with only slight deviation at very late spark timings, where CA50 is unlikely to be feasible for SACI. Both methods matched the reference data well, with no significant overfitting. Extrapolation to later spark timing is improved with Bayesian regularization.

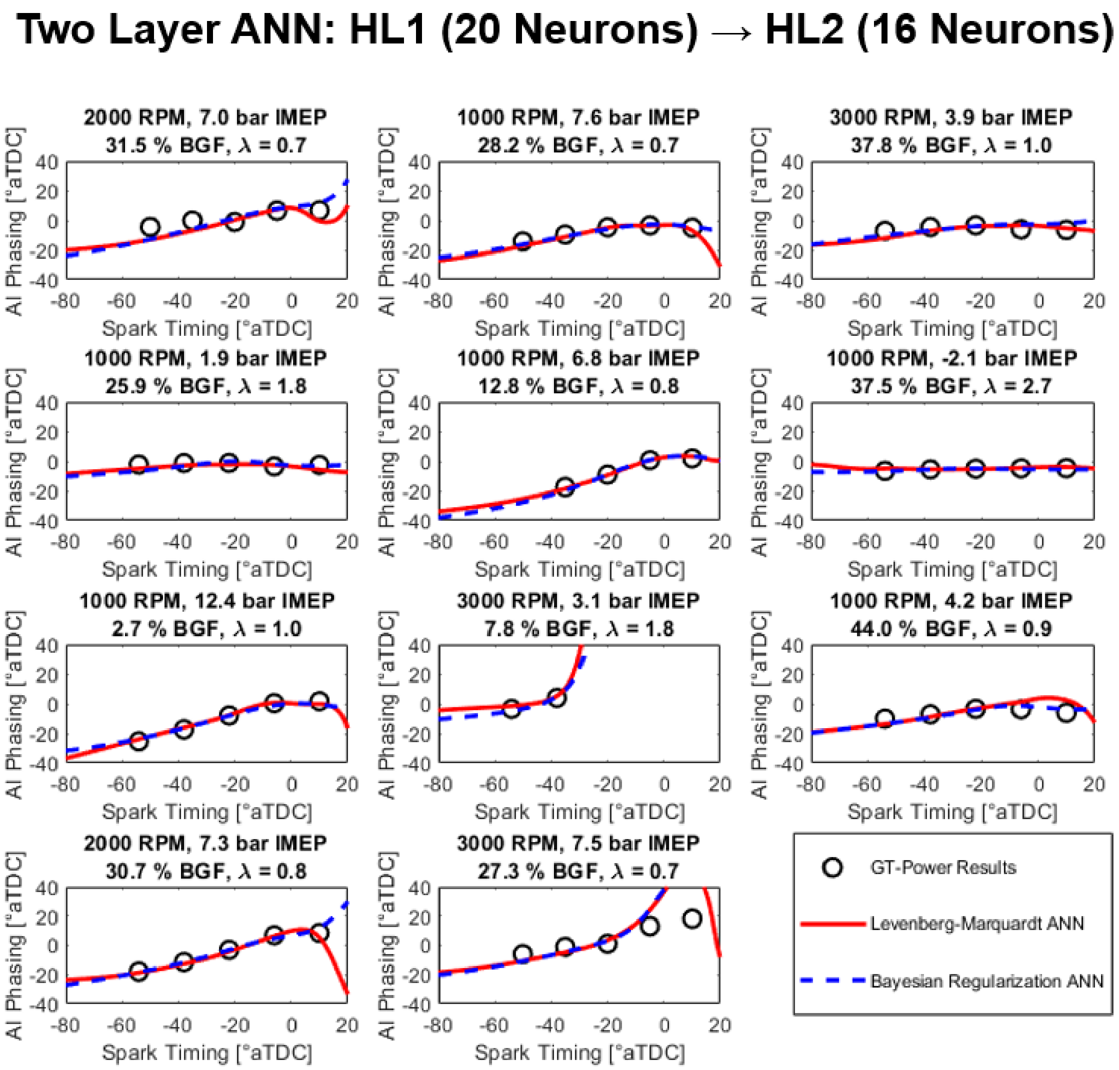

Figure IV-32: Comparison of Levenberg-Marquardt and Bayesian Regularization training methods for a two-layer network.

Some conditions indicate noise for the reference data. As these results are derived from simulation, no stochastic noise is present. However, there are other potential explanations for these results. First, the engine modeled is a full-engine simulation, including appropriate engine controllers. These may resolve to a different value for similar input conditions. The sensitive nature of autoignition may demonstrate an otherwise unexplained variation from these small differences in, say, intake manifold pressure. Additionally, deterministic noise is likely present. For example, consider a case where autoignition phasing is inexplicably earlier than its neighboring points. An investigation into these points indicates that late combustion from the previous cycle resulted in the highest temperature at cycle start for a middle point in the spark sweep. This occurs because earlier spark timings burn completely and release a considerable amount of heat. But this heat is turned into useful work when spark timing is early, lowering the in-cylinder temperature at the end of the cycle. As spark timing retards, combustion occurs later in the cycle, resulting in less expansion work and higher in-cylinder temperatures for the following cycle. Eventually, however, there is so little heat released at late spark timings (because of low combustion efficiency) that the temperature at cycle start for the following cycle decreases again. Figure IV-33 depicts this condition. Note that the earliest spark timing has the second-lowest compression temperature, and the highest temperature during compression is when spark is -5° aTDC.

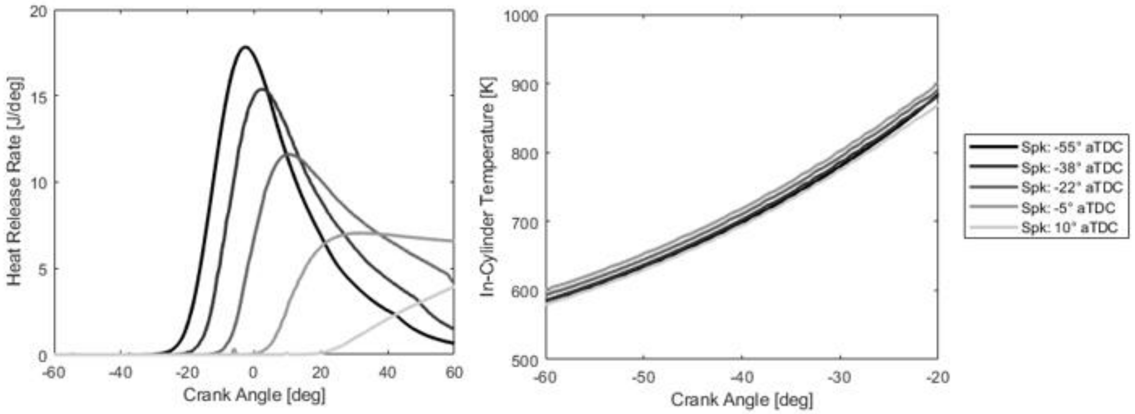

Figure IV-33: Example point with non-monotonic autoignition. The late burn from the previous cycle drives compression temperatures higher, resulting in a slightly elevated induction time integral value during compression.

This regression model is only tuned on points where autoignition occurred. To account for non-autoignition cases, a separate classification network is also developed. This network will only determine if autoignition occurs. If the model predicts autoignition, the regression network will provide the expected autoignition phasing. This network uses the scaled conjugate gradient training method and evaluates the optimization performance based on the cross-entropy. A network structure sweep is also performed (Figure IV-34). Based on these results, a single layer of 20 hidden neurons is sufficient to accurately predict autoignition with about 1% error (Figure IV-35).

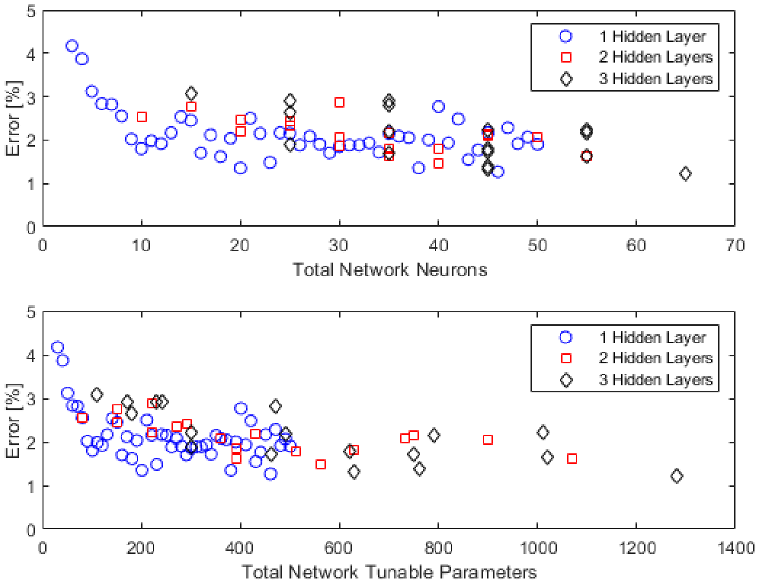

Figure IV-34: Parameter sweep for autoignition classification neural network.

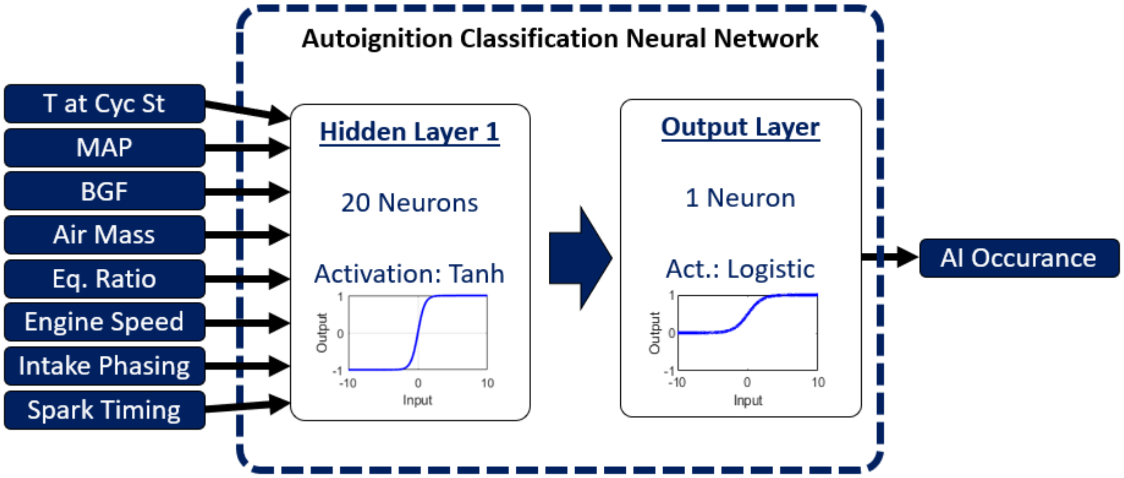

Figure IV-35: Autoignition classification submodel structure.

Autoignition Submodel Performance

The regression and classification networks are evaluated separately. The regression model is evaluated using the root mean square error (RMSE) metric. The data is broken down into three groups: training dataset, validation dataset, and test dataset. The training dataset is what the optimization algorithm uses to compute the objective function, the validation dataset is used by the training algorithm to determine when to stop, and the test dataset is not used at all during the training process. The test dataset represents the best evaluation of the performance of the ANN.

Most points occurred before 20° aTDC, which is consistent with a significant AI event. Late autoignition is more likely to occur after a significant portion of the fuel is burned by the flame. In these cases, variation in AI phasing will not produce a significant change in SI portion, as much of the fuel is already consumed by the flame. If autoignition occurred prior to TDC, the error is within 2 CAD. There is a single outlier in the test dataset that has a reference AI phasing of about 0° aTDC, but the ANN predicts about a 25° aTDC phasing. However, this point represents a significant misfire, and would therefore be outside of the reasonable range of operation for the engine.

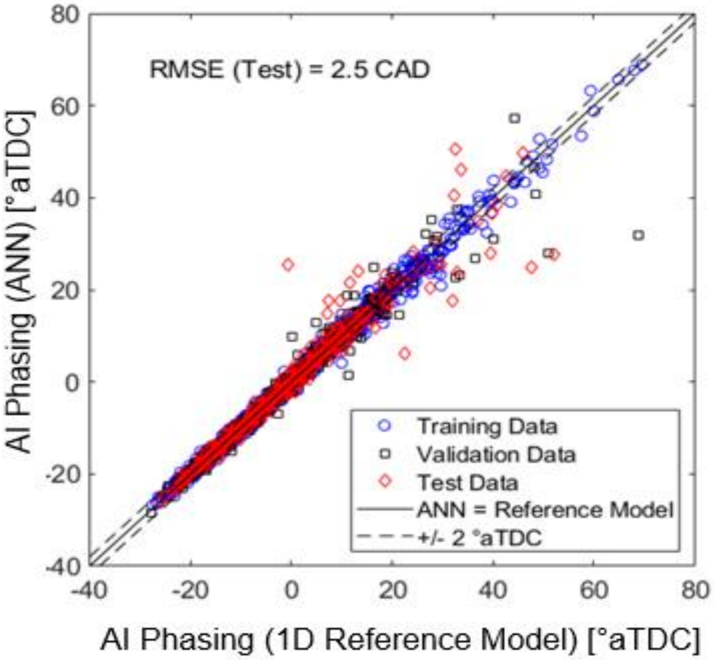

Figure IV-36: Autoignition phasing ANN submodel evaluation.

A selection of responses from the regression ANN is presented in Figure IV-37 to Figure IV-40. In each of these figures, the *x* and *y* axes represent the pressure and temperature at TDC without combustion, respectively. The models for pressure and temperature at cycle start are used, and their results are translated to TDC by assuming a polytropic process. All other ANN inputs are held constant. Four sample conditions are considered: the cams phased at 10 CAD and 50 CAD from parked position each for two equivalence ratios: 0.5 and 1.0. An appropriate burned gas fraction is selected for each equivalence ratio and held constant. These plots illustrate a few key points. First, the response is generally smooth, which indicates that the regularization techniques used in the training process are working. The training data for all points is contained in a region bounded by 15–50 bar P_{TDC} and 850-1200 K T_{TDC}. The pressure and temperature limits in the plots exceed these values sufficiently to demonstrate that extrapolation performance is encouraging. Additionally, the effect of NTC region is evident in each of the plots, though some are much more pronounced. Thus, despite the ANN being a data-driven model, it can capture physical behavior and extrapolate to beyond the training data region. It is important to note that these plots are not ignition delay response plots. The pressure and temperatures are dynamic (not constant like ignition delay response plots), and the autoignition phasing is different that ignition delay. Ignition delay is an instantaneous metric, with no impact from a flame. Autoignition phasing in these figures is a result of the cumulative impact of pressure, temperature, and to some degree the flame. Spark timing at TDC is selected to minimize this impact.

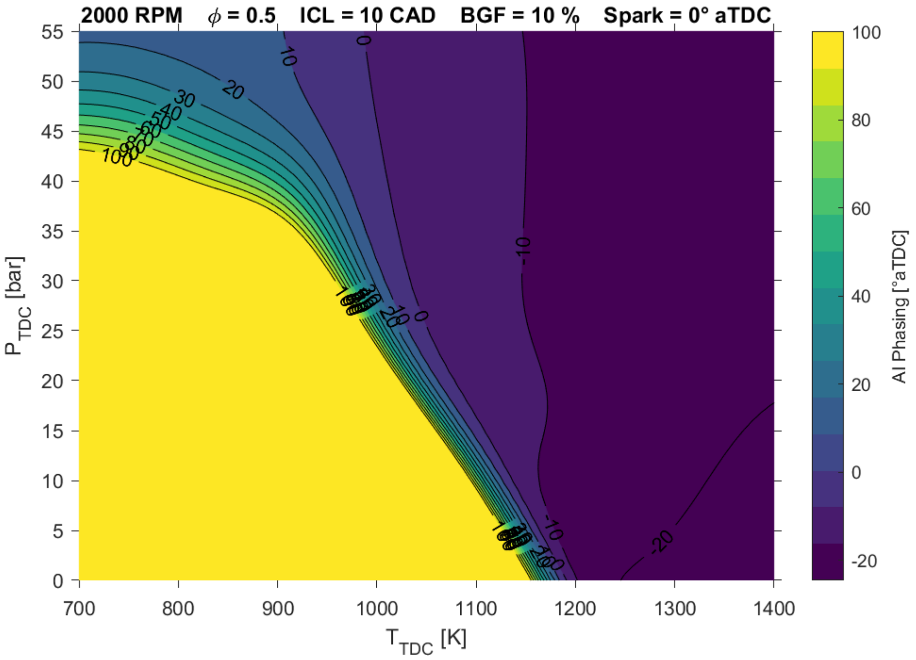

Figure IV-37: ANN response for a sweep of temperature and pressure at cycle start for fuel-lean SACI with ICL at 10 CAD from parked position. The conditions at cycle start are adapted to conditions at TDC by assuming polytropic compression.

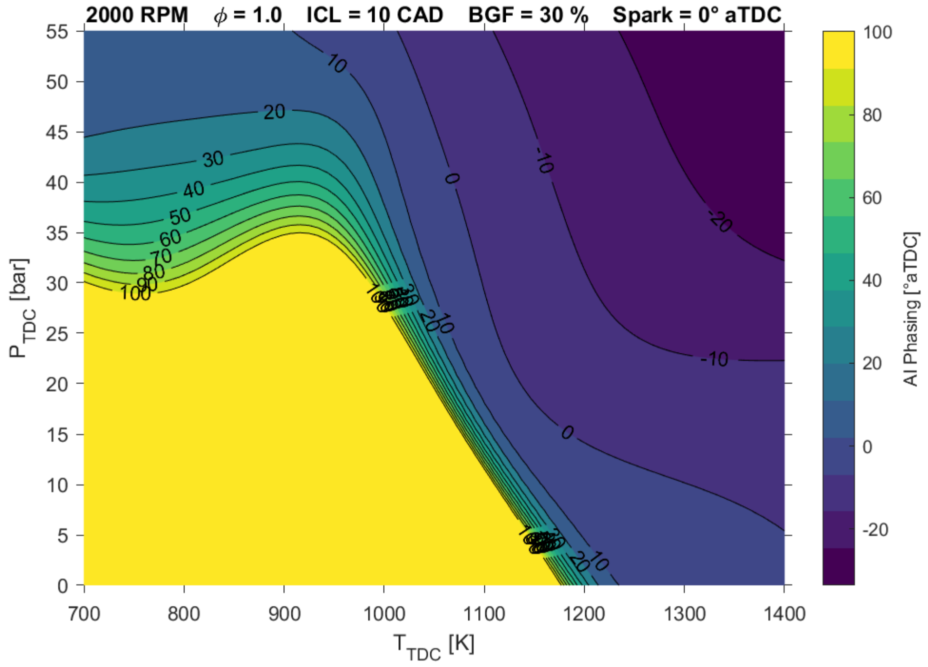

Figure IV-38: ANN response for a sweep of temperature and pressure at cycle start for stoichiometric SACI with ICL at 10 CAD from parked position. The conditions at cycle start are adapted to conditions at TDC by assuming polytropic compression.

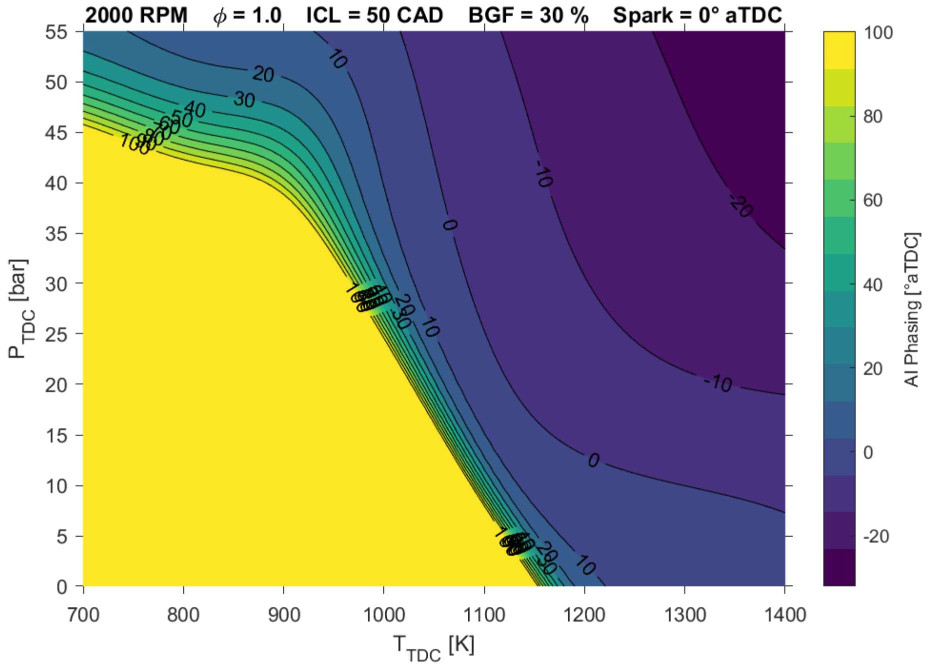

Figure IV-39: ANN response for a sweep of temperature and pressure at cycle start for fuel-lean SACI with ICL at 50 CAD from parked position. The conditions at cycle start are adapted to conditions at TDC by assuming polytropic compression.

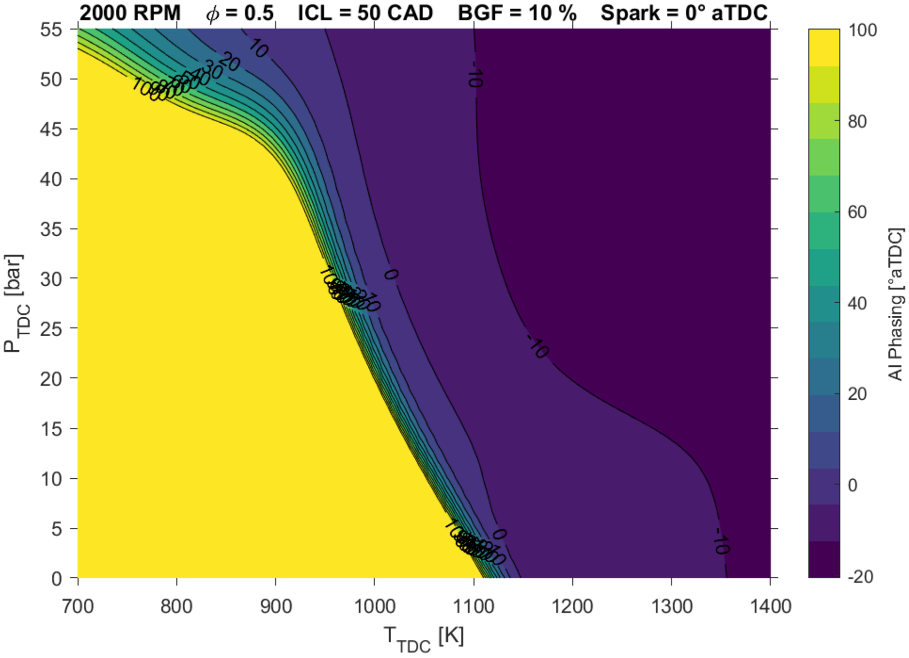

Figure IV-40: ANN response for a sweep of temperature and pressure at cycle start for stoichiometric SACI with ICL at 50 CAD from parked position. The conditions at cycle start are adapted to conditions at TDC by assuming polytropic compression.

The classification network is evaluated by comparing the target result to the network output. A "confusion matrix" identifies the errors by type and dataset (Figure IV-41). Ideally, the error is small and distributed relatively evenly across all datasets and the two types of error. In the case of this network, the error is about 1% and is consistent from one dataset to the next. The "false positive" type of error is slightly higher than "false negative," however, this is acceptable. If a false positive occurs, the simulation will query the regression model for the AI phasing. As the regression model is well-tuned, it should predict a late AI phasing. As late autoignition has little influence on overall combustion metrics, the impact of a false positive is minimal. Considering this, the classification network has about a 1% error, which is sufficiently high enough to proceed.

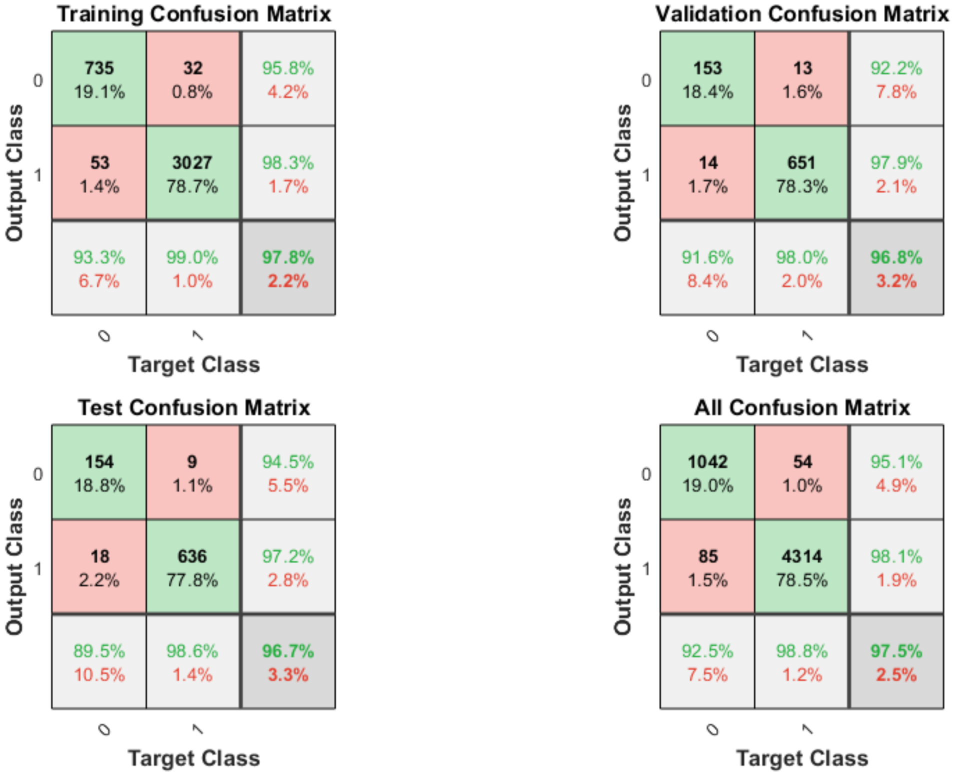

Training Confusion Matrix

Output Class \ Target Class	0	1	
0	735 19.1%	32 0.8%	95.8% 4.2%
1	53 1.4%	3027 78.7%	98.3% 1.7%
	93.3% 6.7%	99.0% 1.0%	97.8% 2.2%

Validation Confusion Matrix

Output Class \ Target Class	0	1	
0	153 18.4%	13 1.6%	92.2% 7.8%
1	14 1.7%	651 78.3%	97.9% 2.1%
	91.6% 8.4%	98.0% 2.0%	96.8% 3.2%

Test Confusion Matrix

Output Class \ Target Class	0	1	
0	154 18.8%	9 1.1%	94.5% 5.5%
1	18 2.2%	636 77.8%	97.2% 2.8%
	89.5% 10.5%	98.6% 1.4%	96.7% 3.3%

All Confusion Matrix

Output Class \ Target Class	0	1	
0	1042 19.0%	54 1.0%	95.1% 4.9%
1	85 1.5%	4314 78.5%	98.1% 1.9%
	92.5% 7.5%	98.8% 1.2%	97.5% 2.5%

Figure IV-41: Confusion matrices for autoignition classification ANN for each data subset as well as the overall confusion matrix.

Autoignition Burn Duration Submodel

The single-zone model is augmented with a burn duration correlation. Three correlations are compared. Two are tuned for HCCI combustion and one for both HCCI and SACI. Babajimopoulos et al. [101] developed their correlation based on HCCI simulation results, while Zhou et al. [102] considers HCCI engine data. Both are a function of ϕ' and autoignition timing, among other variables. Ortiz-Soto developed an HCCI and SACI autoignition burn duration model [58].

The two HCCI correlations produce similar burn durations for autoignition near top-dead center (TDC). However, as AI phasing is retarded, the burn duration increases significantly for the Babajimopoulos et al. model. This likely represents a cycle-cycle variation (CCV) limit for HCCI. Unlike HCCI, SACI can sustain later AI timings because the flame continues to release heat after TDC. Experimental results by Manofsky et al. [35], Nakai et al. [60], and Triantopoulos et al. [103] all demonstrated the CA50 up to ~15° aTDC within CCV limits. To achieve the wider range of operation for SACI combustion, Ortiz-Soto adds several additional parameters, including the temperature at pressure at autoignition and the fraction of charge remaining at autoignition. However, as intra-cycle pressure and temperature data is not available for this model, the Zhou et al. model is selected. This model is compared to the SACI burn duration extracted from the ORNL engine data (Figure IV-42). For test points with a COV of IMEP at or below 3% and a phasing between 0 and 15° aTDC, the trend matches with an RMSE of 2.7 CAD. Lean operation is not evaluated as the engine dataset consists of exclusively stoichiometric. However, the selected model is tuned for lean HCCI operation. Acceptable performance for lean SACI operation is assumed.

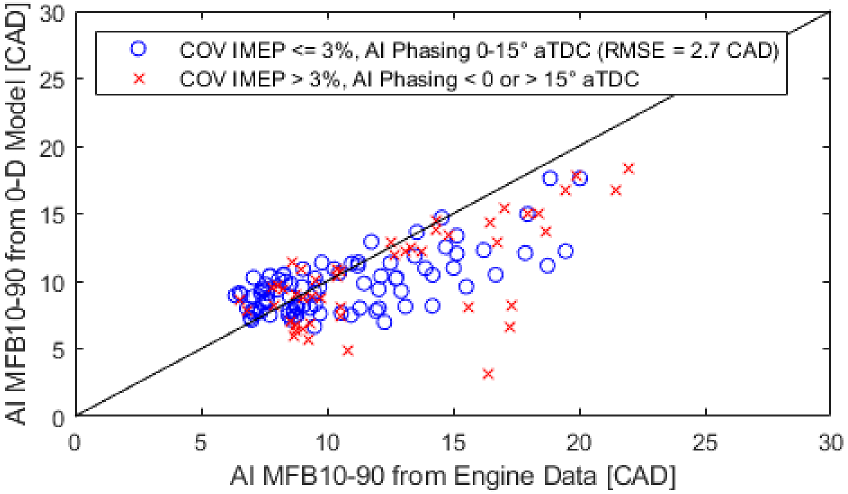

Figure IV-42: Autoignition burn duration comparison between ORNL engine data and the AI burn duration model.

Nitrogen Oxide Emissions Submodel

Oxides of nitrogen (NO_x) are one of several regulated combustion products. Stoichiometric or rich operation enables a three-way catalyst that passively perform a reduction reaction to convert NO_x to form N_2 and H_2O. Lean operation, however, cannot take advantage of a three-way catalyst an either requires engine-out NO_x emissions to be below the regulatory threshold, or use lean aftertreatment. Lean-aftertreatment requires a separate chemical to perform the reduction in a high-oxygen environment and adds cost to the aftertreatment system. The reduction chemical can be fuel or a separate chemical such as diesel exhaust fluid, a urea solution. Using fuel as the reductant harms fuel efficiency, and the separate chemical imposes a cost and convenience challenge upon the customer.

A data-driven NO_x model is selected that enables a prediction of NO_x emissions based solely on air-fuel ratio and total residual for SI combustion. The data is generated using the *EngCylCombSITurb* model along with a *EngCylNOx* submodel. The default options are selected for all NO_x model parameters. Both internal and external EGR is varied, though, the model performs well based on the total burned gas fraction. The input range is plotted in Figure IV-43 illustrating the spread of points well beyond the anticipated range of the model when in use.

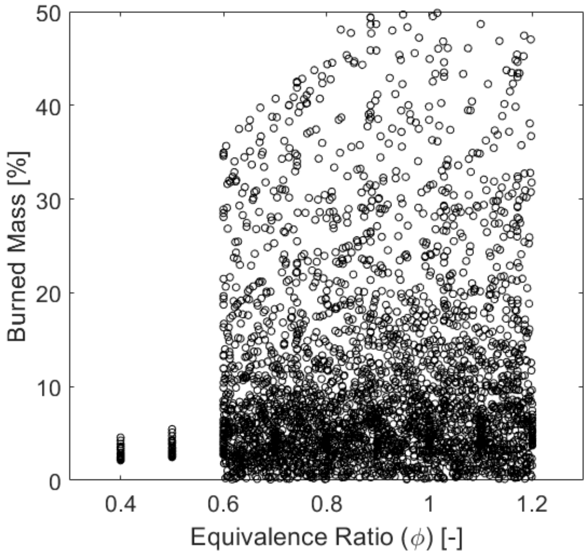

Figure IV-43: Input range for NOx model.

The model is constructed as a two-layer neural network (Figure IV-44). A two-layer network has sufficient complexity to match the nonlinear NO_x output over a wide range of points. Only 5 (five) and 2 (two) neurons are selected for the first and second hidden layer, respectively. A larger number of hidden neurons increases overfitting as indicated by the application of the model over an even wider range of inputs than the model training input range.

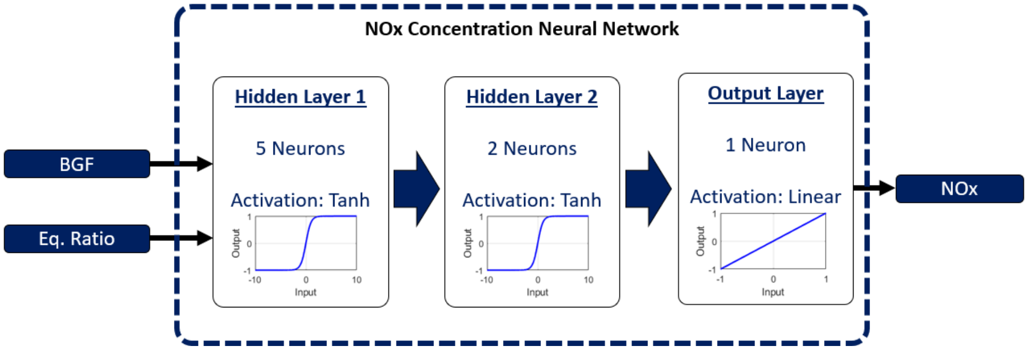

Figure IV-44: NO_x model neural network structure. Total residual and equivalence ratio are the only two inputs.

The result of the model is illustrated in Figure IV-45. Nearly all points are within 200 ppm. While there is some spread, this is likely a result of the combination of internal and external EGR into total burned gas fraction. Since this model is only used for an approximate guideline for emissions constraints, this deterministic noise is acceptable. The model is exercised over a wide range of input conditions to evaluate performance outside of the training range (Figure IV-46). Peak NO_x occurs near $\phi = 0.9$ and zero residual, and there is no sign of overfitting. Preliminary models that are overfit are observed to have additional peaks in regions that should have near-zero NO_x, e.g. $\phi = 2$. The model also indicates that around stoichiometric fueling, about 20% burned gas significantly reduces NO_x emissions.

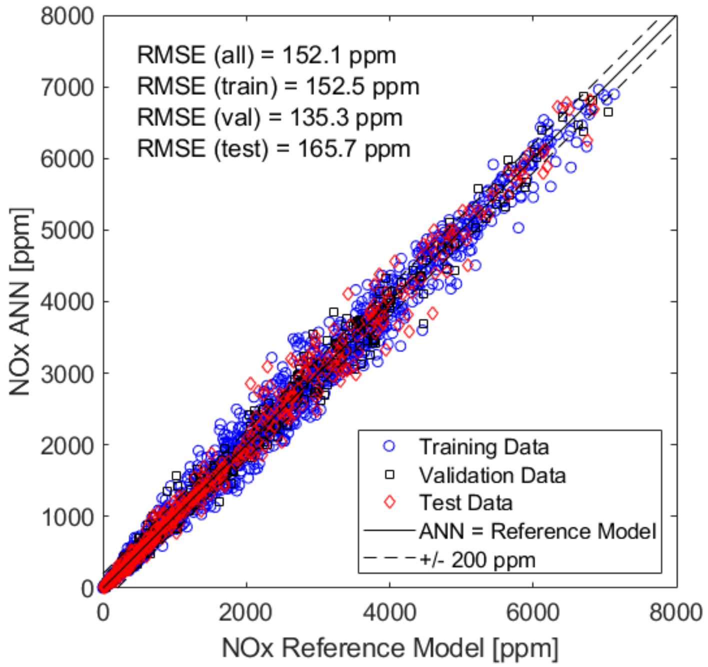

Figure IV-45: NO_x model comparison to the reference model.

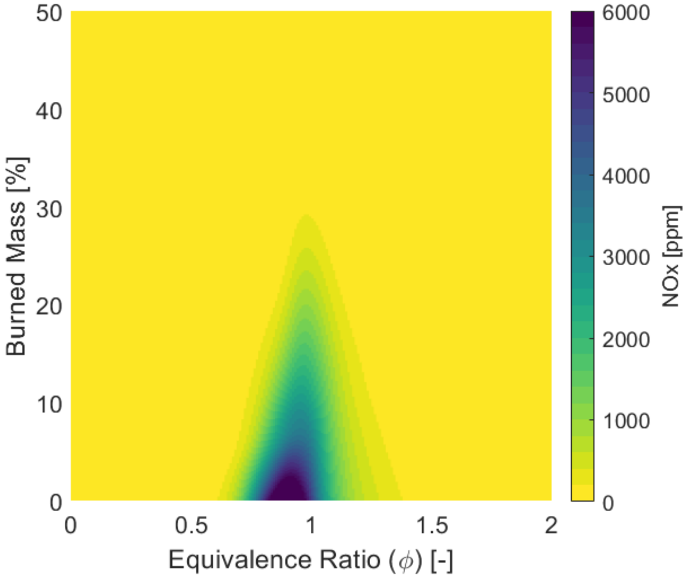

Figure IV-46: NO_x model as a function of equivalence ratio and burned mass portion for zero external EGR.

The NO_x submodel is coupled with the SI burn duration model and the fuel stratification model to identify the overall NO_x produced. As the flame progresses into a particular zone (determined by burn duration), the equivalence ratio will be fixed for that zone. This equivalence ratio value along with the global BGF value produce the NO_x concentration for that zone. Since all zones are equal volume, the average NO_x concentration for all zones burned by the flame represents the global concentration of NO_x. For simplicity, the NO_x produced by an autoignition zone is assumed to be zero. While the actual NO_x value will be non-zero, for autoignition to occur within practical constraints, the in-cylinder conditions are assumed to produce sufficiently low NO_x. In order words, the NO_x produced by the flame dominates NO_x production. Therefore, the overall NO_x concentration of the cylinder can be described with the following expression (32). For the *i*-th zone from zone 1 to the highest zone with SI combustion, zone *k*, compute the sum of the NO_x concentration and divide by the total number of zones *n*.

$$NO_x\ [ppm] = \frac{1}{\text{n}}\sum_{i=1}^{k} NO_x(i) \tag{32}$$

Net IMEP Submodel

The submodel for net IMEP is an artificial neural network. It is validated against the results from the reference 1D engine model and is of the form depicted in Figure III-3. The neural network inputs are selected based on the independent variables that have a strong influence on in-cylinder pressure. The network structure is chosen based on an investigation of the tradeoff between overfitting and accuracy. A single layer of 15 hidden neurons is trained to 70% of the data points using the Levenberg-Marquardt backpropagation algorithm. The remaining 30% of the data is split evenly between the validation and test datasets. The resulting ANN demonstrated good accuracy, with a root mean square error (RMSE) of 0.1 bar. Figure III-4 illustrates the comparison between the reference and ANN models for each data subset: training data, validation data, and test data.

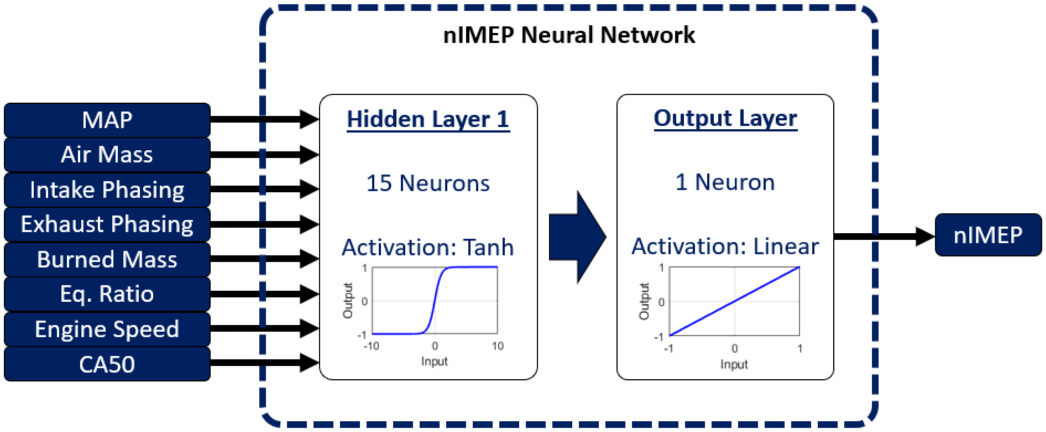

Figure IV-47: Neural network structure used for net IMEP.

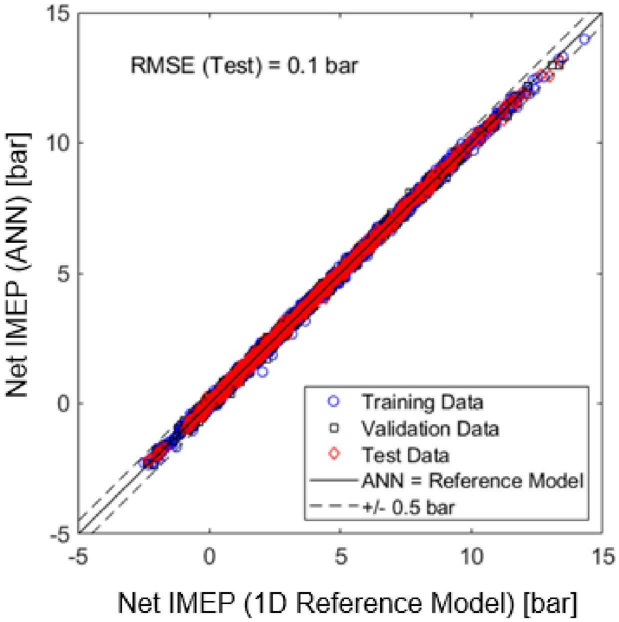

Figure IV-48: Comparison between the GT-Power engine model (Reference Model) and the artificial neural network (ANN) for the net IMEP submodel.

<u>ISFC Submodel</u>

The submodel for ISFC is an artificial neural network. It is validated against the results from the reference 1D engine model and is of the form depicted in Figure III-3. The neural network inputs are selected based on the independent variables that have a strong influence on in-cylinder pressure. The network structure is chosen based on an investigation of the tradeoff between overfitting and accuracy. A single layer of 15 hidden neurons is trained to 70% of the data points using the Levenberg-Marquardt backpropagation algorithm. The remaining 30% of the data is split evenly between the validation and test datasets. The resulting ANN demonstrated good accuracy, with a root mean square error (RMSE) of 3.4 g/kWh. Figure III-4 illustrates the comparison between the reference and ANN models for each data subset: training data, validation data, and test data.

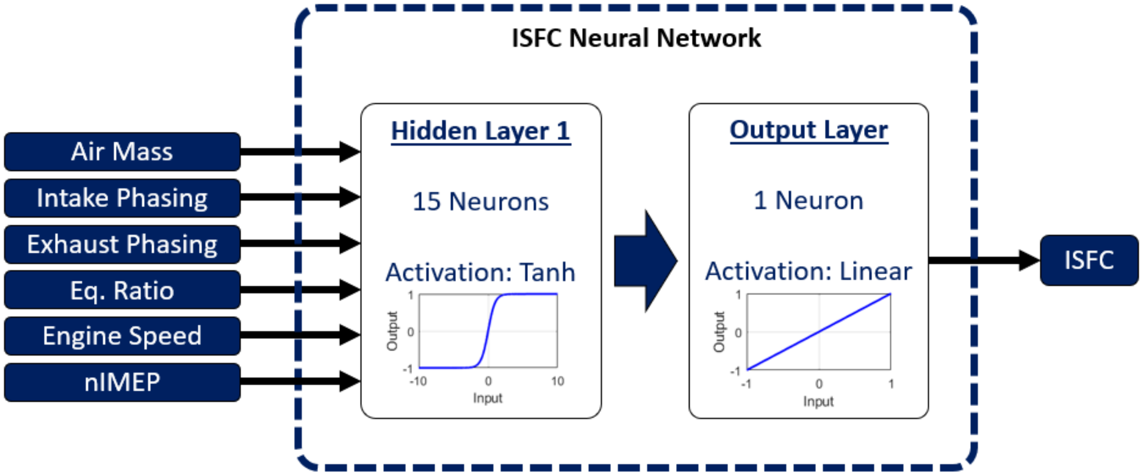

Figure IV-49: Neural network structure used for indicates specific fuel consumption (ISFC).

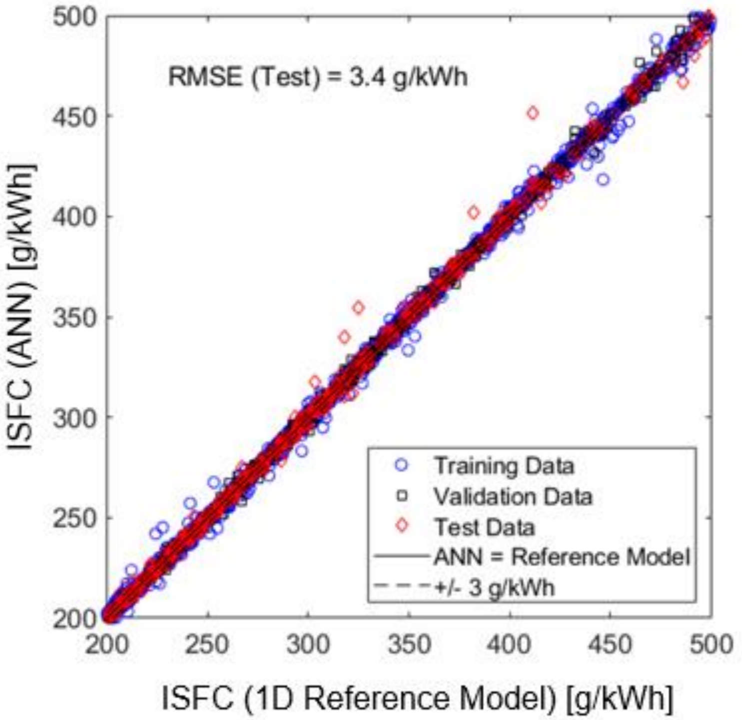

Figure IV-50: Comparison between the GT-Power engine model (Reference Model) and the artificial neural network (ANN) for the ISFC submodel.

Summary and Conclusions

A 1D engine model is validated to data from a stoichiometric SACI engine. This 1D reference model is exercised over a wide range of simulated actuator positions and ambient conditions. These results are used to develop combustion submodels. Both physics-based and data-driven modeling techniques are considered. Data-driven models in the form of an artificial neural network (ANN) are selected for all models. The accuracy of the ANNs are superior to physics-based models. Careful neural network modeling techniques are used to prevent overfitting, including early-stopping and Bayesian regularization.

V. CANDIDATE CYLINDER MODEL

The suite of submodels is combined to produce a single model of the cylinder, with a focus on combustion response. The candidate cylinder model is structured to take control inputs, sensor measurements, and engine geometry and produce predicted values for the in-cylinder state. The combustion submodels use this data to anticipate SI and AI performance and constraints. Figure V-1 depicts the flow of data from the inputs through the submodels and to the final outputs for the in-cylinder state. The experimental dataset and source for each submodel is indicated to the left of each submodel. The output of the in-cylinder state submodels is input to the combustion submodels (Figure V-2). As with the in-cylinder state submodels, the experimental dataset and source for each submodel is indicated to the left of each submodel.

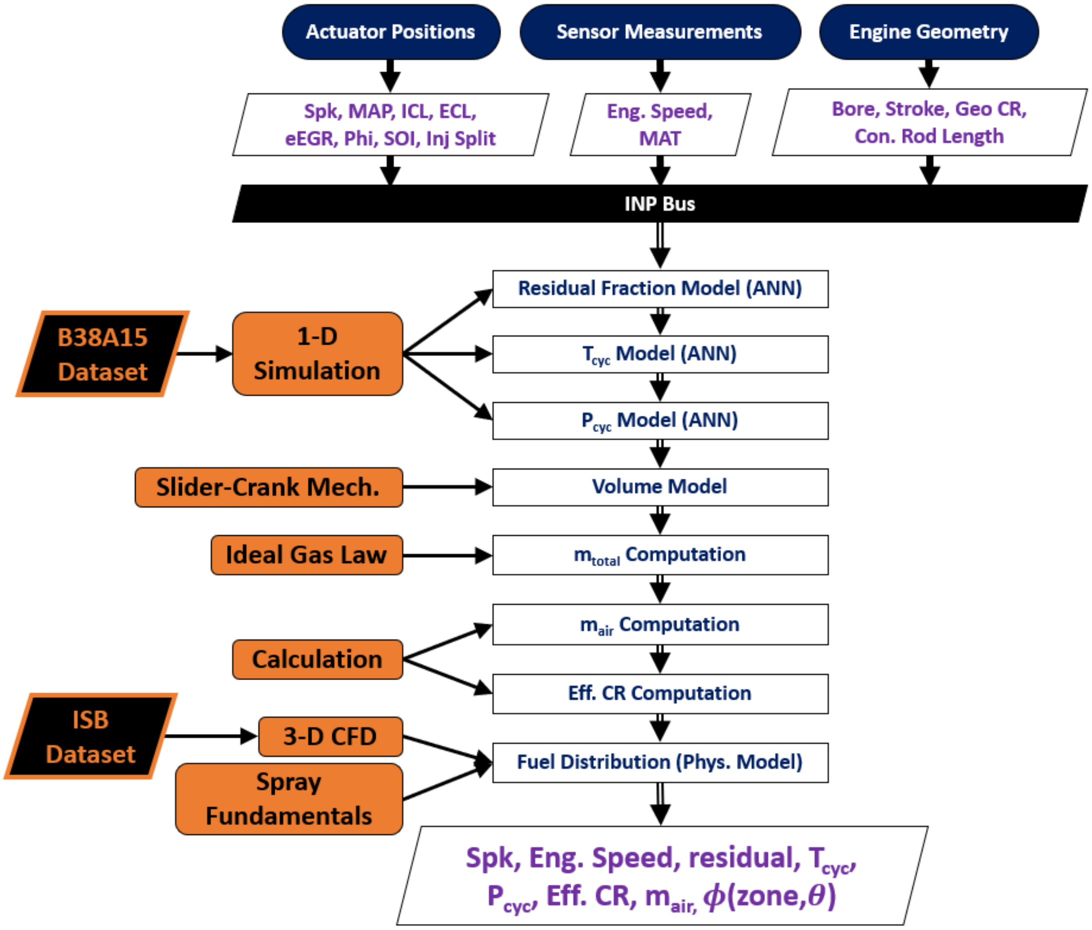

Figure V-1: In-cylinder state submodel data flow. The rectangular boxes represent submodels and computations, the rounded boxes represent the basis for the models, and the black-filled parallelograms indicate the experimental source for submodel validation.

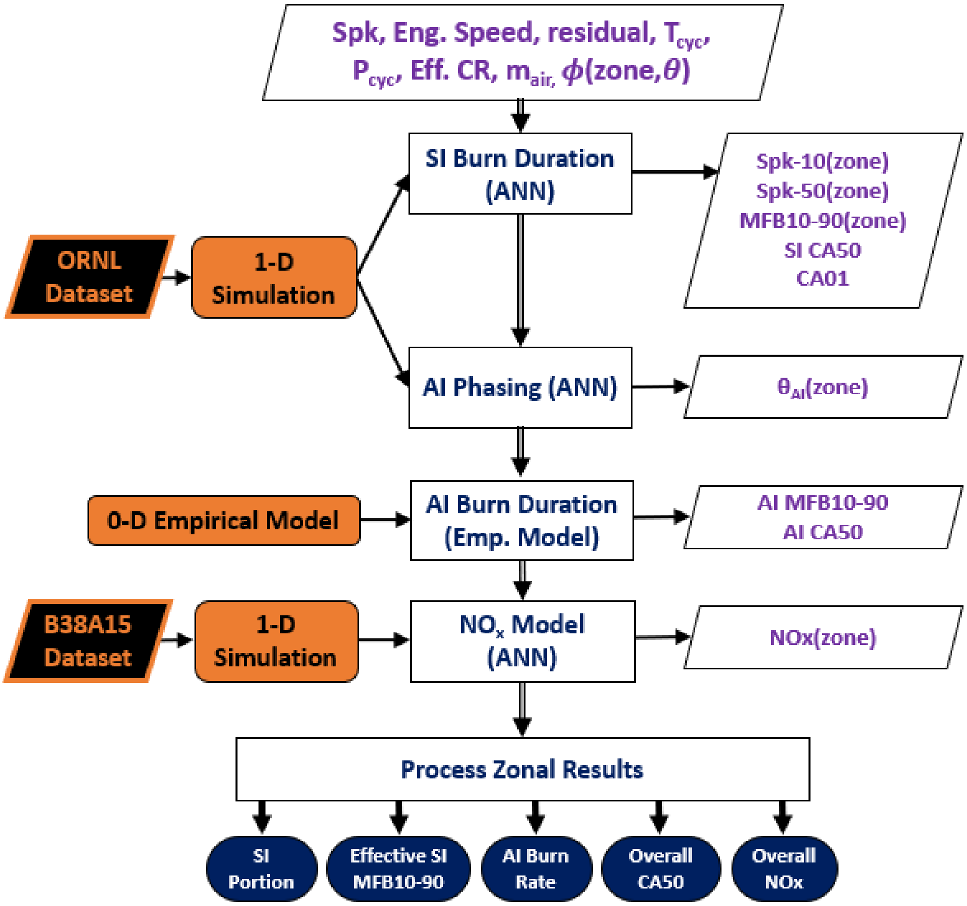

Figure V-2: Combustion submodel data flow. The rectangular boxes represent submodels and computations, the rounded boxes represent the basis for the models, and the black-filled parallelograms indicate the experimental source for submodel validation.

Candidate Cylinder Model Compared to Reference 1D Engine Model

Evaluating the candidate cylinder model begins by inputting the same actuator positions as the reference 1D engine model. The reference 1D engine model is simulated in GT-Power using an Intel Xeon E5-1630 v3 (3.50 GHz) processor and takes about 183 seconds (3 minutes, 3 seconds) per case. Solving all 6000 cases requires 12 days and 17 hours with no parallelization. The candidate cylinder model, however, simulates the same 6000 cases in 1.4 hours on the same machine without parallelization. This equates to 0.82 seconds per case, which is a 2230% improvement over the reference 1D engine model.

Rapid model execution is not helpful if the model accuracy degrades significantly. For the purposes of evaluating the relative accuracy of this model, the R-squared value of autoignition phasing of the simplified model versus that predicted by the reference 1D engine model is examined. The R-squared value, known as the Coefficient of Determination, quantifies the degree that a dependent variable is explained by a set of independent variables. Autoignition and SI burn durations are selected for evaluation as these are critical component of SACI combustion and can be difficult to model accurately. The model is evaluated over feasible conditions, to illustrate the practical usefulness of the model. A subset of 689 points that represents nIMEP above zero with combustion phasing between MBT and about 25 °aTDC is selected. The R-squared value for each combustion metric is noted in Figure V-3. Despite a 99.6% reduction in computational time, the accuracy only reduced by 4–25%. A thorough discussion on the model accuracy is presented the following sections.

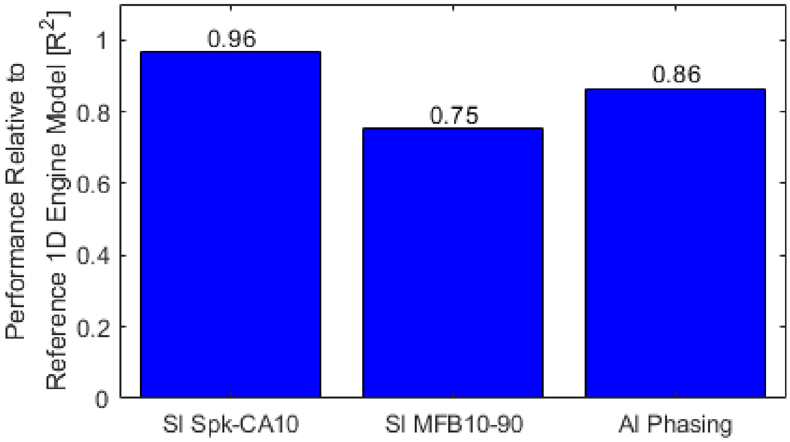

Figure V-3: Comparison between the reference 1D engine model and the fast-running cylinder model.

Submodel Evaluation

Accurate in-cylinder state submodels are the first step in an accurate cylinder model. There is potential error stack up as several submodels use the output of other submodels as inputs. Therefore, the results presented in Chapter III represent the upper limit of model accuracy. The submodels matched the reference model with the RMSE indicated for each submodel (Figure V-4).

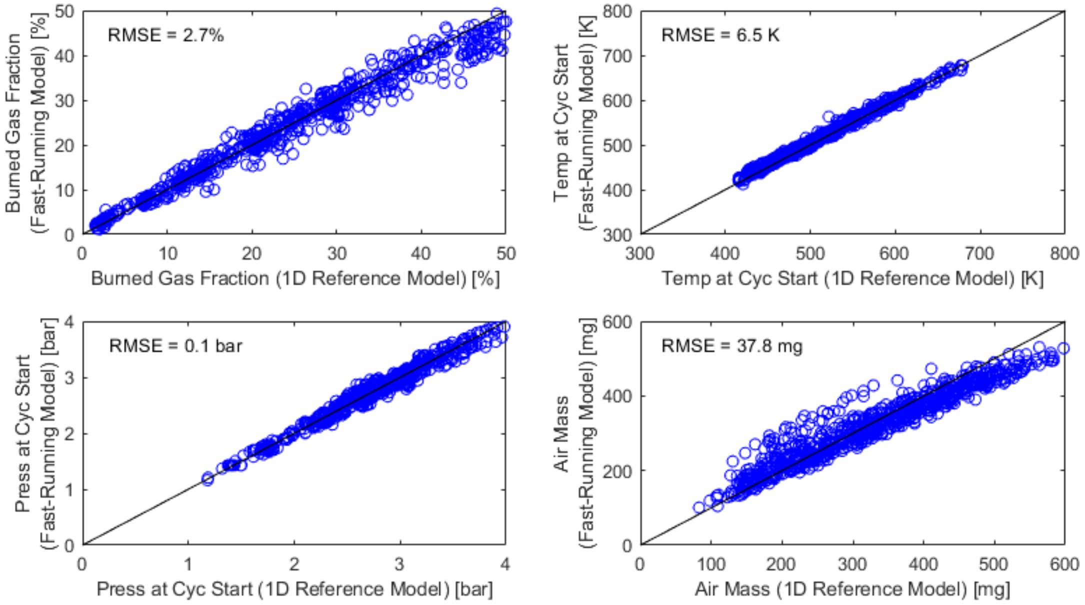

Figure V-4: Comparison of in-cylinder state between the fast-running cylinder model and the reference 1D engine model (GT-Power).

The combustion submodels are the key component of this model. The difficulty in modeling each mode of combustion is further compounded by the error in the in-cylinder state used as the input. Figure V-5 depicts the comparison between the simplified cylinder model and the reference 1D engine model. Despite the potential error stack up present, the RMSE for each is acceptable. Additionally, the error increases as combustion phasing becomes later or combustion duration lengthens. These conditions represent the limit or outside of the limit of feasible combustion. Error for these points is less significant.

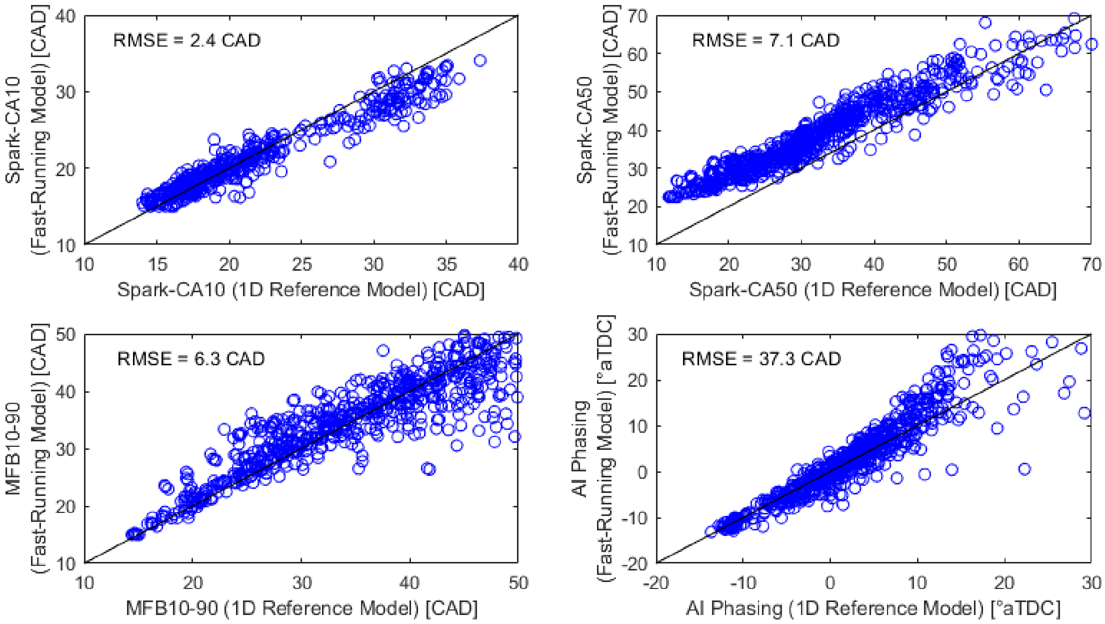

Figure V-5: Comparison of combustion metrics between the fast-running cylinder model and the reference 1D engine model (GT-Power).

Combining the SI and AI models yields the metric for SI portion. This computation adds one more layer of error stack up, resulting in degraded accuracy. However, the simplified model predicts SI portion with an RMSE of 9.4 percentage points. Below an SI portion of 40%, the RMSE improves to 6.6 percentage points. Figure V-6 depicts the comparison between the simplified model and GT-Power results.

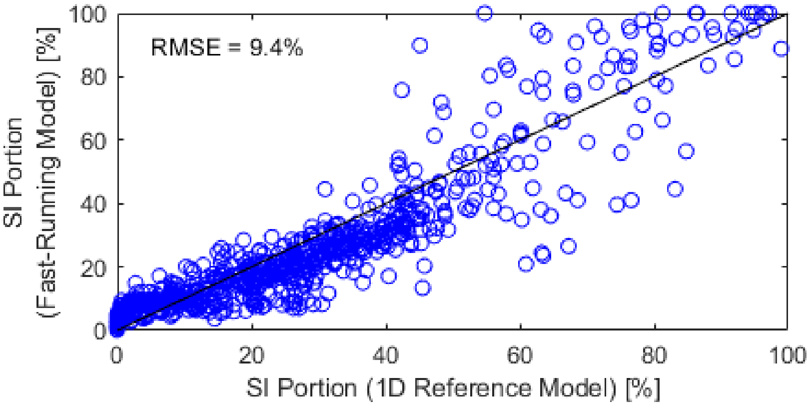

Figure V-6: Comparison of SI portion between the fast-running cylinder model and the reference 1D engine model (GT-Power).

Finally, IMEP and ISFC are critical to evaluating a point. Both models will struggle to produce accurate results at low SI portions, as the autoignition component of combustion is not modeled in GT-Power. Overall, though, the simplified model captures the trend of both IMEP and ISFC. The RMSE for IMEP is 0.8 bar, and the RMSE is 60.3 g/kWh for ISFC (Figure V-7).

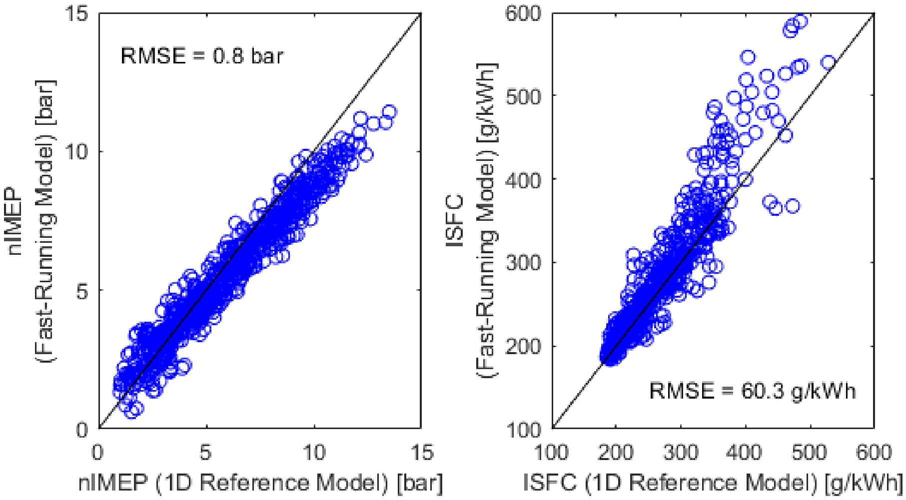

Figure V-7: Comparison of nIMEP and ISFC between the fast-running cylinder model and the reference 1D engine model (GT-Power).

Calibration Exploration

A sweep of a wide range of inputs identifies potential calibration solutions and control strategies. As seen in the previous section, the candidate model matches the trends of the 1D engine simulation and can produce absolute values with acceptable accuracy.

A set of actuator positions that demonstrate a range of SI portion is selected to illustrate the deeper understanding of the control and calibration techniques that can be achieved. Figure V-8 depicts the combustion response for a sweep of spark timing at a particular location. Noted on the subplots are three constraints: 1) *constraint A* is the minimum burn duration for autoignition (used as an analogue for ringing intensity or knock), 2) *constraint B* is the maximum burn duration for flame propagation (used as an analogue for cycle-to-cycle variation), and 3) *constraint C* is where the overall CA50 timing is near MBT. Clearly, an MBT point is not feasible at this condition without violating constraint B.

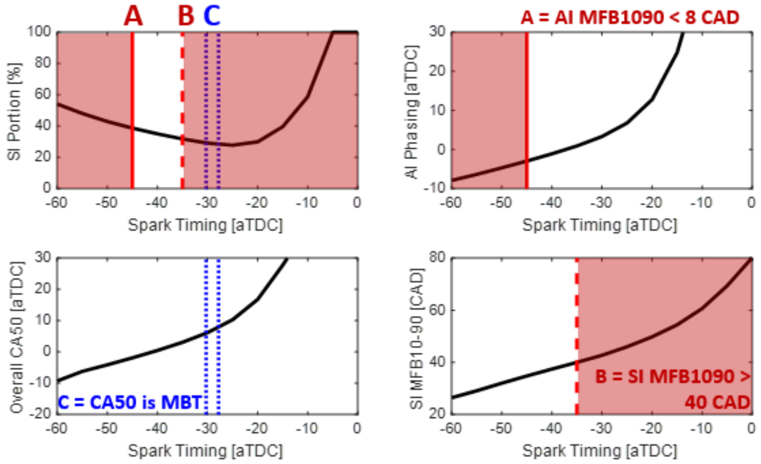

MAP = 1.0 bar
ICL = 30 deg from Parked
ECL = 30 deg from Parked
eEGR = 0%
Eq. Ratio = 0.5
Engine Speed = 2000 RPM
Inj 1 SOI = -300° aTDC
Inj 2 SOI = -30° aTDC
Split = 100% Inj 1
Burned Gas = 11%

Figure V-8: Key combustion parameters for a sweep of spark timing.

Because of the wealth of data, several control strategies can be evaluated. The first strategy to consider is reducing the burned gas fraction within the cylinder to strengthen flame propagation.

The cams are phased to reduce negative valve overlap, by setting both intake and exhaust to 50 crank degrees from parked position. Figure V-9 depicts this response, and indeed, flame propagation is strengthened, and the limit of SI combustion is retarded by 5 CAD, enough to operate at MBT timing. However, the margin for this operation is effectively zero.

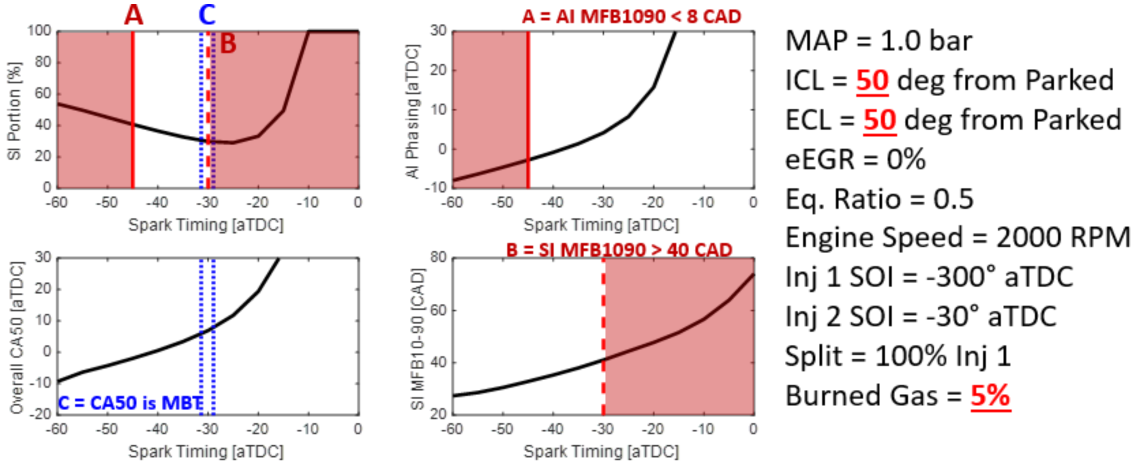

MAP = 1.0 bar
ICL = 50 deg from Parked
ECL = 50 deg from Parked
eEGR = 0%
Eq. Ratio = 0.5
Engine Speed = 2000 RPM
Inj 1 SOI = -300° aTDC
Inj 2 SOI = -30° aTDC
Split = 100% Inj 1
Burned Gas = 5%

Figure V-9: Combustion response for reducing negative valve overlap.

Instead of an adjustment to the cam positions, fuel stratification is introduced (Figure V-10). Of the total quantity of fuel, 75% is injected during the first injection, which mixes roughly homogeneously. The remaining 25% is injected 30° before TDC to produce a relatively rich zone near the spark plug. This significantly improves the SI burn duration and pushes the burn duration limit (constraint C) later by 20 CAD. The autoignition constraint also occurs closer to TDC, despite the end-gas region having a reduced equivalence ratio. However, there are regions towards the middle of the cylinder that the flame had not yet consumed but has a relatively rich composition. This results in earlier autoignition phasing overall. Note that, as SOI for the second injection is held constant, spark timings before this second injection are ignored.

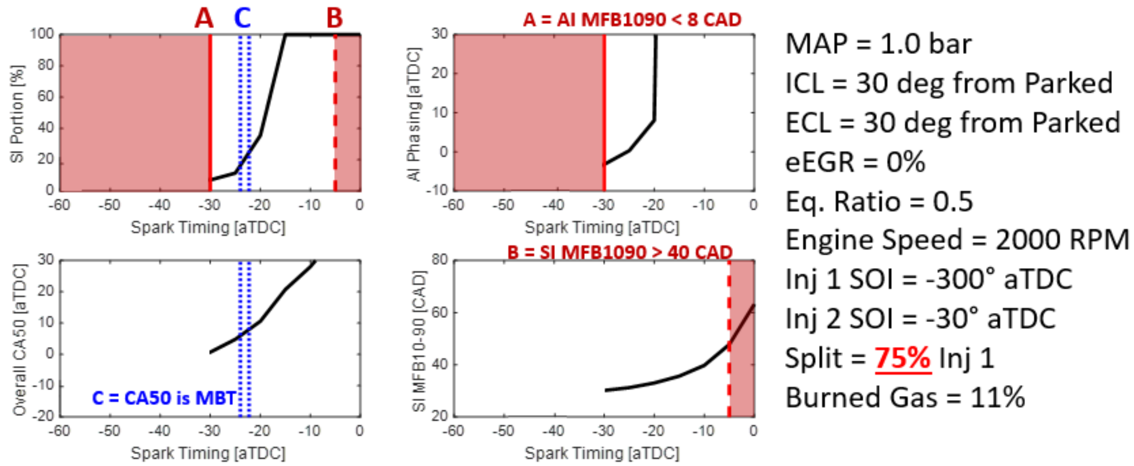

Figure V-10: Combustion response to increased charge stratification. Spark timing prior to -30° aTDC not shown as they are prior to the second injection.

The split fraction is swept from 0.75 to 1.0 to illustrate the calibration sensitivity of this parameter. The only factor that is changed is that the second injection timing is phased to be 10 CAD prior to spark. Figure V-11 depicts the results of this sweep. A split ratio of less than 0.95 is required to achieve stable SI combustion, and a split ratio of less than 0.9 has a significant margin to both constraints A and B, each about 10 CAD of spark timing.

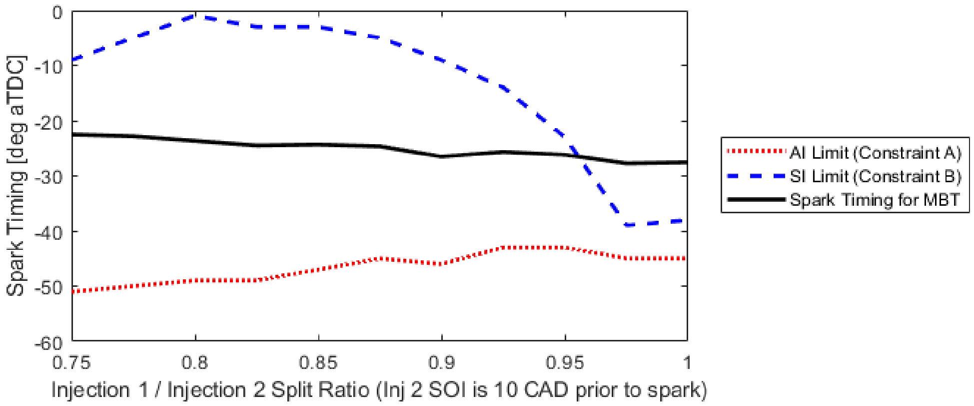

Figure V-11: Combustion constraints as a function of split ratio. Increasing charge stratification improves the margin to both AI and SI constraints.

A similar investigation is performed for the stoichiometric condition. The base case demonstrates a margin for MBT between to each of the AI and SI burn rate limits (Figure V-12). Increasing the external EGR from 10% to 20%, increases the total burned gas portion from 32% to 44% (Figure V-13). Over 40% total burned fraction is towards the upper limit of SI flame propagation. The high dilution does slow SI burn rates, especially for spark timing between -20° and -40° aTDC. SI portion increases from about 20% at MBT to about 40%, with a slight increase in margin to the autoignition burn rate limit. Though the model predicts SI combustion within limits, the proximity to this limit should be treated with caution.

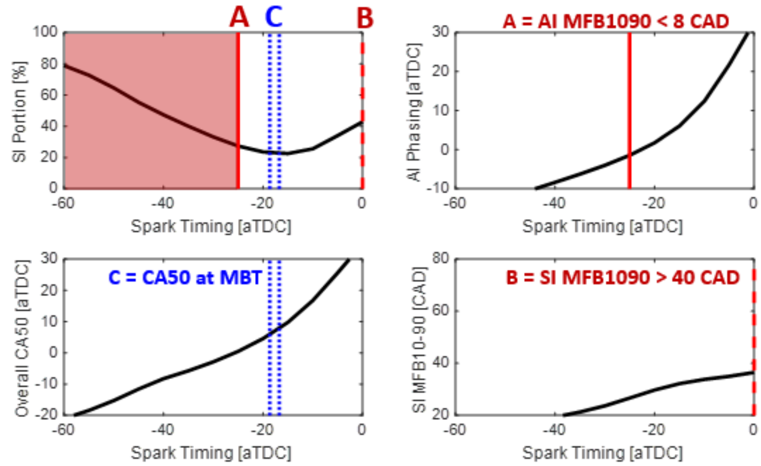

MAP = 1.0 bar
ICL = 10 deg from Parked
ECL = 10 deg from Parked
eEGR = 10%
Eq. Ratio = 1.0
Engine Speed = 2000 RPM
Inj 1 SOI = -300° aTDC
Inj 2 SOI = -30° aTDC
Split = 100% Inj 1
Burned Gas = 32%

Figure V-12: Key combustion parameters for a sweep of spark timing for stoichiometric conditions.

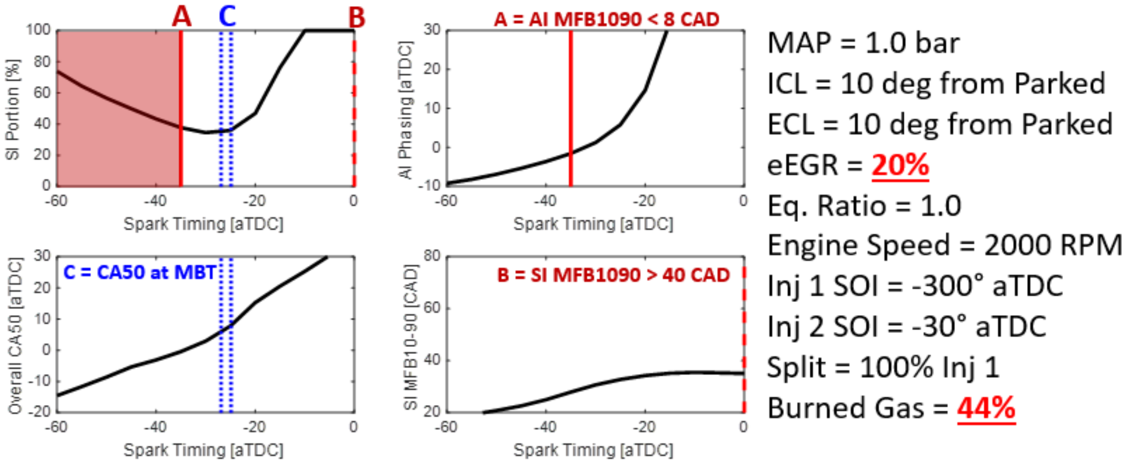

Figure V-13: Combustion response to increased EGR for stoichiometric conditions.

Summary

In this chapter, the complete simplified cylinder model is introduced. The model results are compared to the reference 1D engine simulation, which suggested that despite a reduction in computation expense by over 99%, the model predicted key combustion parameters with an R^2 of about 75-96%. From these results, several investigations are performed which suggest potential calibration and control strategies. In particular, the ability of fuel stratification to expand feasible operating conditions is demonstrated.

VI. CANDIDATE MODEL APPLICATIONS

Engine control and calibration often feature some form of optimization, be it off-line or online and real-time. Optimization aims to identify the suite of ideal actuator positions to achieve a specified target with minimal error. Many optimization algorithms begin at a specified starting point and reduce the error in the function output by progressing towards the negative derivative of error. This process, often performed locally, can only find the local minimum, rather than the global minimum. Furthermore, if the starting point exists in a space where constraints are not satisfied, the algorithm may not have a means to leave the region to find a region that meets the specified constraints.

A potential solution to this problem is to perform a full-factorial design of experiments (DOE). This strategy evaluates all possible actuator position combinations. Table VI-1 lists the range and interval for each of the nine actuators. Note that the total number of cases is just under 700 million. To evaluate even the fast-running cylinder model (~0.8 seconds per case) over this many cases would take 16 years. The 1D reference engine model requires about 3 minutes to perform a single case, which would take almost 40 centuries for the entire DOE.

Table VI-1: Actuator positions for a full-factorial design of experiments.

Control Actuator	**Minimum**	**Maximum**	**Interval**
Spark Timing [°aTDC]	-50	0	2 CAD
Intake Manifold Pressure [bar]	0.4	1.2	0.1 bar
Intake Cam Location [Deg. Cr. From Park]	0	50	5 CAD
Exhaust Cam Location [Deg. Cr. From Park]	0	50	5 CAD
Equivalence Ratio	0.5	1.0	0.5
External EGR [%]	0	30	5%
First Injection SOI [° aTDCf]	-360	-90	30 CAD
Second Injection SOI [° aTDCf]	-180	0	10 CAD
Injection Split Fraction	0.2	1.0	0.1

Full Factorial Number of Cases: ***6.78×10^8***

The final challenge for optimization is the finite actuator rate of change and transport delays. If a steady-state optimization were performed as a function of speed and load, for example, there is no guarantee that the actuators can move from the optimal position at one condition to the optimal position for the next condition within the transient time constraints. Furthermore, a high degree of actuator movement is undesirable, even if it is within actuator rate constraints.

Solution to the Optimization Problem

The solution to the first problem, several local minima, is resolved with a multi-search strategy. The objective of this strategy is to explore the model in several locations to identify potential regions of actuator inputs that are within their bounds, produce the desired response, and do so within the specified constraints. Given the complexity of the model and high degree of freedom, a full-factorial DOE is ideal, however, it is not feasible. Several solutions to this issue for optimization have been developed. Simulated annealing, for example, is an optimization algorithm that varies the probability of the algorithm moving to another region, even if it is worse [104]. This probability deceases as the optimization continues, resulting in the global optimum. MATLAB's global optimization toolbox includes a function called "MultiStart" which randomly selects several start points for the optimization.

Rather than use these methods, a reasonable subset of all possible actuator positions is carefully selected. One possibility is to use a Latin hypercube selection method, rather than a purely random selection. While Latin hypercube sampling may be valuable for exploring all regions of model input, post-processing is more challenging as the actuator positions will all vary. Instead, a carefully reduced subset is evaluated based on only the most well-established constraints. Parameters that are expected to have a minimal affect have a reduced fidelity, and pre-determined restrictions (such as no boosting or external EGR for lean operation) are leveraged to reduce the total case count. Table VI-2 lists the reduced full-factorial design of experiments.

Table VI-2: Actuator positions for a reduced full-factorial design of experiments.

Control Actuator	**Minimum**	**Maximum**	**Interval**
Spark Timing [°aTDC]	-50	0	5 CAD
Intake Manifold Pressure [bar]	0.8	1.2	0.05 bar
Intake Cam Location [Deg. Cr. From Park]	0	50	10 CAD
Exhaust Cam Location [Deg. Cr. From Park]	0	50	10 CAD
Equivalence Ratio	0.5	1.0	0.5
External EGR [%]	0	30	10%
First Injection SOI [° aTDCf]	-300	-300	–
Second Injection SOI [° aTDCf]	-60	-30	30 CAD
Injection Split Fraction	0.25	1.0	0.25
Engine Speed [RPM]	1000	3000	500 RPM

Full Factorial Number of Cases: *~250,000*

This reduced DOE enables a suitable broad exploration of the design space within reasonable computation constraints. Of the 250,000 results, only 17,000 (~7%) demonstrate SACI combustion within constraints at MBT. This small fraction of suitable points further emphasizes the optimization challenge. A random or pseudo-random multi-start global optimization strategy may not find enough of these suitable points within a reasonable time to be useful. The model is exercised over these 250,000 test points, requiring only 62 hours to run on an Intel Xeon E5-1620 v3. The reference 1D engine model would require 1 year and 165 days to model the same number of points (without parallelization).

Calibration Selection from Cylinder Model Results

From model results, suitable actuator positions are filtered to produce the first step in calibration determination. For a given engine speed and equivalence ratio, all results that are near MBT without violating constraints are selected. This resulted in a few hundred results per split fraction. A process to select the most feasible calibration is developed and illustrated in Figure VI-1. The results are sorted by IMEP, and of the low IMEP results, one is selected as a starting point for the low-load limit for calibration. From this starting point, an algorithm is developed to generate a suitable calibration for the specified engine speed and equivalence ratio. The algorithm selects the result that produced the minimum actuator change from a grouping of results for every 0.5 bar IMEP increment. The actuator change is computed as the sum of the squared normalized difference from the previously selected actuator positions. The normalization is achieved by dividing the absolute difference by the range of that actuator. For example, a 0.05 bar change in MAP would be divided by the 0.4 bar range to arrive at a change of 12.5%. A sample result for 2000 RPM, stoichiometric operation with a split fraction equal to 1.0 is presented in Table VI-3.

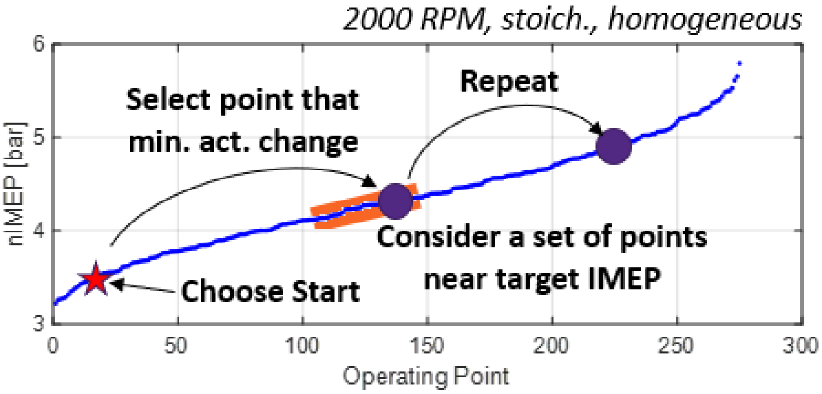

Figure VI-1: Illustration of the process for finding the optimal calibration from the down selected fast-running model results.

Table VI-3: Sample calibration for 2000 RPM and stoichiometric operation. Split fraction is selected to be 1.0 for all points.

nIMEP [bar]	**Spark Timing [°aTDC]**	**MAP [bar]**	**ICL (Cr. Deg)**	**ECL (Cr. Deg)**	**eEGR [%]**
3.5	-25	0.80	10	10	15
4.4	-25	0.80	30	15	10
4.8	-25	0.90	25	10	15
5.3	-20	0.85	30	20	10
5.8	-20	0.85	35	25	10
6.3	-15	0.85	15	65	15
6.8	-15	0.90	20	50	15
7.3	-15	0.85	30	60	10
7.8	-15	1.00	30	55	20
8.3	-15	0.95	40	65	15
8.8	-15	0.90	60	65	10
9.3	-15	1.00	60	45	10
9.8	-15	1.00	60	55	10

Several observations can be gleaned from this result. First, the IMEP range for stoichiometric SACI at 2000 RPM appears to be ~4–10 bar IMEP. If the model overestimates the ability of the flame to propagate in these conditions, then the realized load range will be reduced. Secondly, though there are several apparent trends, occasionally, there are unreasonable shifts in calibration. For example, from 7.3 bar to 8.3 bar, the MAP increases from 0.85 bar to 1.00 bar, then down to 0.95 bar. Certain actuators are likely to require a monotonicity constraint during a load sweep, or at least partially monotonic. As far as the calibration, generally, spark advance decreases as load increases as the higher energy charge enables faster flame propagation. SI portion is about 20–30% for all these points. Manifold pressure generally increases with IMEP to enable a higher fuel mass in-cylinder. Phasing for both intake and exhaust cams tended towards more positive overlap with IMEP. At low IMEPs, NVO is leveraged to both provide a high residual fraction to maintain a low load and to retain hot residual to increase charge energy.

Calibration Optimization in GT-Power

While the cylinder model is fully capable of being optimized within MATLAB, the final optimization of this calibration is performed in the 1D engine simulation software, GT-Power. The software has several optimization algorithms and optimization in the native 1D reference engine environment will be necessary to eliminate any discrepancies between the candidate cylinder model and the reference model.

Prior to running any optimization, the calibration is evaluated in the 1D reference engine model to identify the error in model prediction. If the error is large, then the optimization will likely be unproductive since the cylinder model is unable to accurately represent the reference model. Since the focus of this work is combustion control, SI portion and AI phasing will be compared. In this comparison, depicted in Figure VI-2, SI portion matches well, though AI phasing is often about 5 CAD earlier than the GT-Power model. Though burned gas fraction matches well, the cylinder model slightly overpredicts in-cylinder temperature (10 K or less). This, along with the high sensitivity of autoignition leads to the slight error for several of the points. Since the cylinder model matches the GT-Power model well, there is good reason to have high confidence that the starting point for the calibration optimization should be close to the constrained global minimum and optimization can proceed.

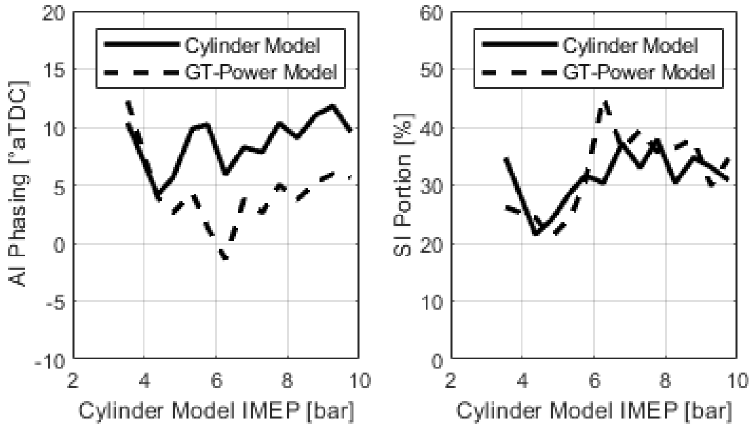

Figure VI-2: Autoignition phasing and SI portion comparison between the cylinder model and GT-Power.

GT-Power has several optimization algorithms to choose from. Some, such as a genetic algorithm (GA), are unsuitable for this application [105]. A genetic algorithm will initially vary the inputs widely to map out the design space. This is entirely unnecessary as the fast running cylinder model has already performed this task. Instead, the single-objective "Advanced Direct Optimizer" is selected using the Simplex search algorithm [106].

Only actuator limit constraints are applied, as GT-Power lacks the capability to accurately measure NO_x for SACI and does not model burn duration for autoignition. The optimized variables and constrained ranges are: intake cam location [0–70 crank degrees from park], exhaust cam location [0–70 crank degrees from park], intake manifold pressure [0.6–1.2 bar], and spark timing [-50–0 °aTDC].

The objective function considered errors in SI portion, AI phasing, and IMEP. SI portion is selected as part of the cost function for two reasons. First, the overall CA50 is not computed in GT-Power, so combining SI portion and AI phasing provide some measure of overall combustion phasing. Additionally, SI portion may be a target if ringing intensity is a concern, as the slow burn rate of SI can lower ringing. Fuel efficiency is not possible in version v2019 of GT-Power as autoignition is not fully modeled. The combustion efficiency is limited by the maximum combustion efficiency of the SI phase alone. Thus, even if autoignition can consume the entire charge, if the flame cannot propagate through the chamber, a combustion efficiency of much less than 100% will be reported for the overall combustion efficiency. This negatively impacts overall fuel efficiency. The errors in SI portion and AI phasing are based on a constant target for each. A constant SI portion of 30% and an AI phasing of 4° aTDC are selected for simplicity. These are selected based on the typical SI portion and AI phasing from the candidate cylinder model, as well as several sources in the literate that suggest a constant SI portion may be desirable [29,49]. The computed error in SI portion, IMEP, and AI phasing are scaled so that the error is equal to one at an error threshold within which, a reduction of error is not significant. For autoignition phasing, this error is 2 CAD, for SI portion, it is 10%, and for IMEP it is 0.5 bar. The scaled errors are squared and then summed. The final cost function *F* for optimization is depicted in (33), where E_{AI} is autoignition phasing error, E_{SI} is SI portion error, and E_{IMEP} is net IMEP error.

$$F = \left(\frac{E_{AI}}{2\ CAD}\right)^2 + \left(\frac{E_{SI}}{10\%}\right)^2 + \left(\frac{E_{IMEP}}{0.5\ bar}\right)^2 \tag{33}$$

The optimization progressed without error, and significantly reduced the cost function within about 50 iterations. Figure VI-3 depicts the median cost function value for the set of IMEPs as a function of iteration count.

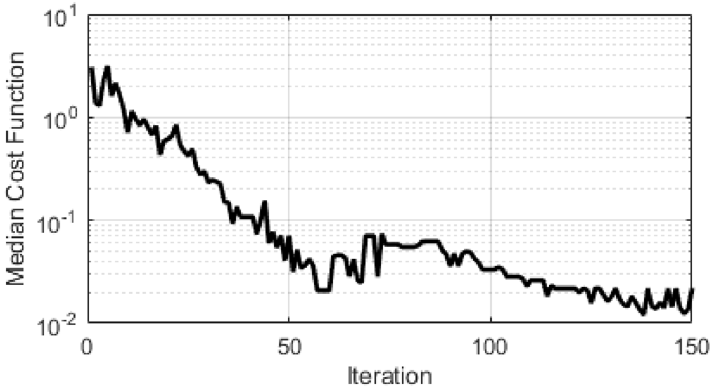

Figure VI-3: GT-Power optimization progress. The median cost function for the set of IMEP cases is plotted against the iteration count.

As each case is optimized individually, the result of the initial optimization does not have the monotonicity and "smoothness" of a production steady-state calibration. The results are evaluated and the final calibration for all actuators except for spark timing is determined by fitting smooth curves to the optimization result. Figure VI-4 depicts a sample of this for exhaust cam location (ECL) and intake manifold absolute pressure. There is a clear linear trend for ECL, though MAP varies much more. Finally, spark timing only is optimized again to produce the final optimized calibration.

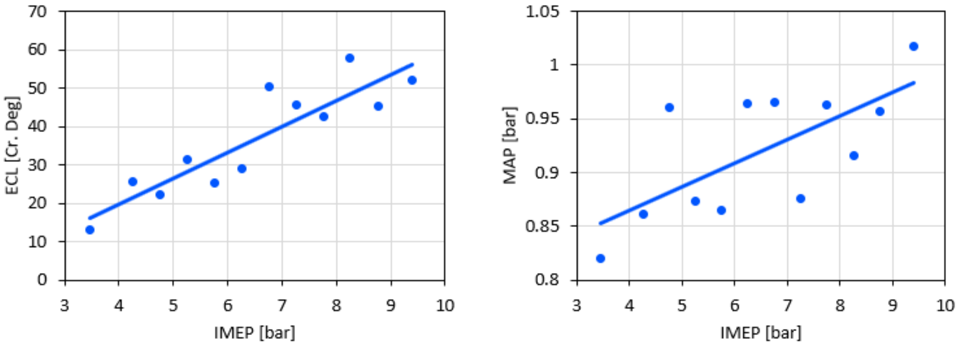

Figure VI-4: Optimization results (data point) and final calibration (solid line) for exhaust cam location (ECL) and manifold absolute pressure (MAP).

The resulting calibration performs well for steady-state testing. Some discrepancy for IMEP is observed, which resulted in a restricted operating range from about 4–9 bar, instead of 3.5–9.5 bar. Figure VI-5 depicts the control actuator locations for the load sweep under stoichiometric conditions at 2000 RPM. Figure VI-6 depicts the combustion response for the optimized result. Note that both the SI portion and autoignition phasing match the target value well (30% and 4° aTDC, respectively).

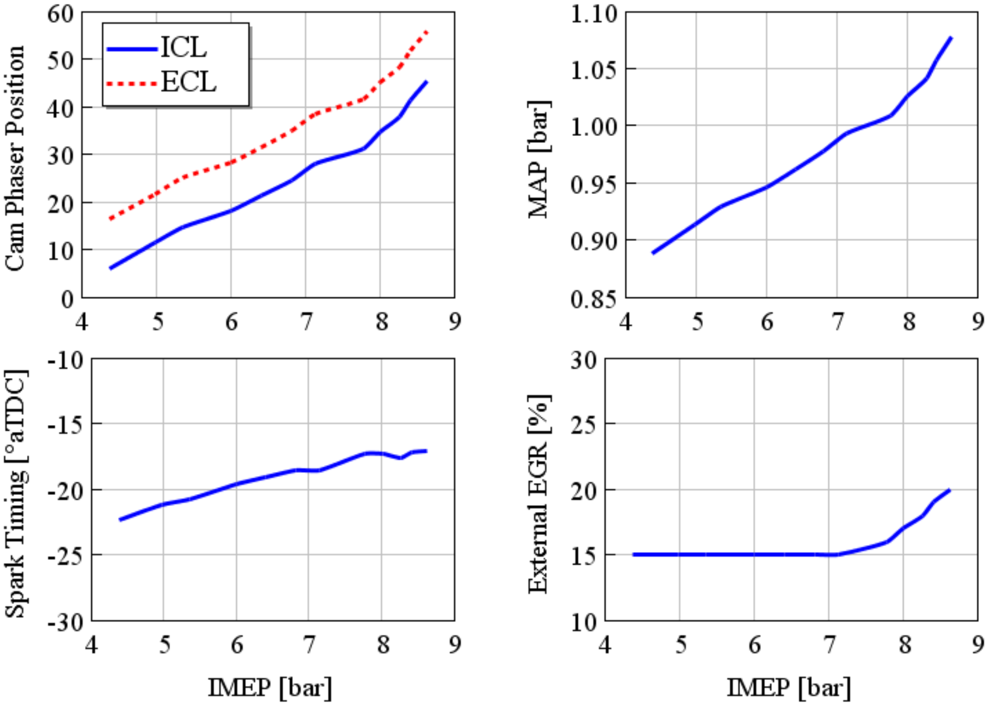

Figure VI-5: Key control actuator calibration for 2000 RPM, stoichiometric operation.

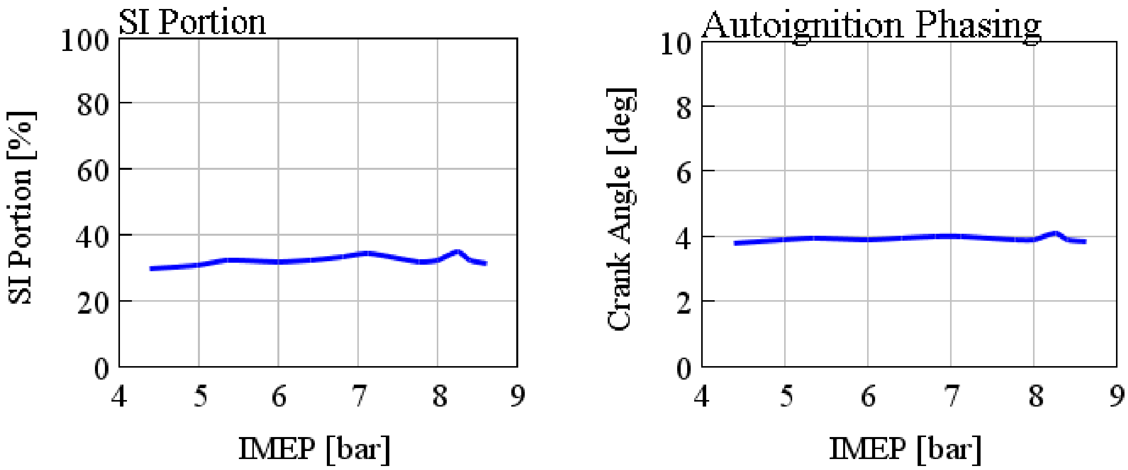

Figure VI-6: Optimized calibration results for SI portion and autoignition phasing. The target SI portion is 30%, and the target AI phasing is 4° aTDC.

Transient Simulation and Control

In addition to calibration optimization, one advantage of a fast and accurate model is the potential to be used for real-time control. The fast-running cylinder model is leveraged to adapt the steady-state calibration during transients. Initially, the plan included a Simulink model that linked to GT-Power. Figure VI-7 depicts the top-level of the Simulink model, and Figure VI-8 illustrates the connection to the GT-Power model using library block provided as part of the GT-Power software package. Though this method has significant potential, the control elements of a model such as this require an applications-focused controller formulation. Simulink lacks an optimizer such as *fmincon*, and MATLAB scripts have limited capability in the Simulink environment. To use the cylinder model, it would ideally be restructured in state-space form, which would significantly alter the function of the model. For example, SI portion is computed based on the zonal structure, which would have to be re-computed some other way. As the objective of this research is to develop and demonstrate the potential control applications, rather than an application-specific control model, Simulink is not used. Instead, the model is run with only the steady-state calibration in GT-Power. Then the results are saved and passed to the MATLAB model after completion of the simulation. From the error in AI phasing and SI portion, the MATLAB model decides an adjustment to the steady-state calibration to improve the result. These adjustments are then applied on top of the steady-state calibration and the simulation is re-run in GT-Power. This approach still demonstrates the control potential of the model, without requiring a restructuring of the model.

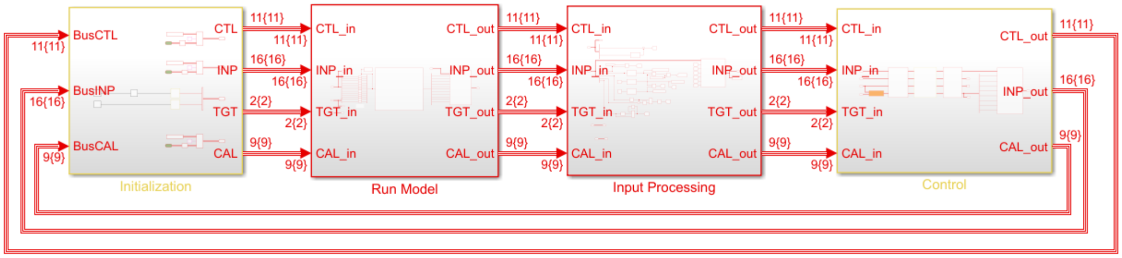

Figure VI-7: Simulink model top-level view.

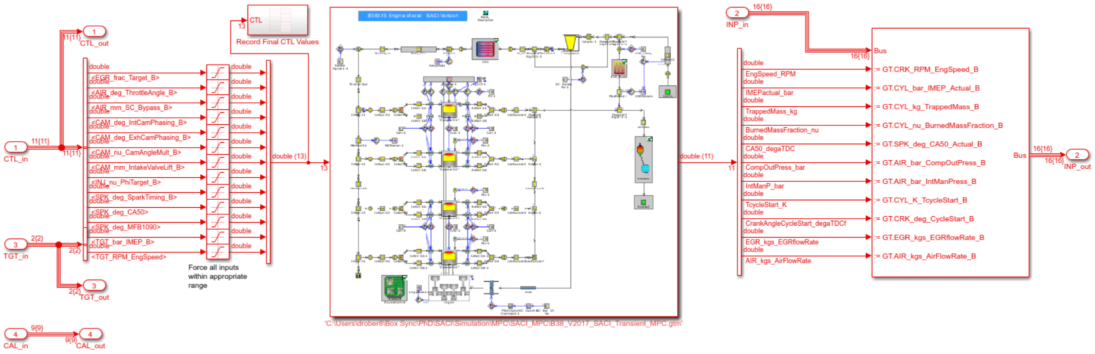

Figure VI-8: Simulink connection to GT-Power model within the Simulink "Run Model" subsystem.

For the transient response, a tip-in and tip-out at 2000 RPM is first evaluated. A tip-in allows a clear understanding of the transient response as it only varies load in a simple way, unlike a drive-cycle, where both speed and load change and the rate of change varies over the cycle. A tip-in or tip-out is also a higher rate of load change than a drive cycle, and therefore stresses the model to a greater degree than a drive cycle. For this case study, a 4.5 to 8.5 bar nIMEP tip-in is performed at 2000 RPM with stoichiometric fueling.

Executing the tip-in and tip-out reveals excellent performance for the steady-state calibration (Figure VI-9). The response of the engine load lags the target by only 0.1 seconds. The steady-state IMEP error is minimal, and deviations during the transitions are at most 0.25 bar IMEP. No misfires are observed. Combustion performance is near the target, with only a slight 2 CAD deviation in autoignition phasing (Figure VI-10). These results are passed back to the model. The tip-in portion, having a greater than 1 CAD deviation in AI phasing is the focus for the optimization. The model is optimized to advance autoignition phasing by two degrees adjusting only the spark timing. The output is then used in place of the steady-state spark timing calibration, and the model is re-run with this updated spark timing. Although the model improved the phasing error to about 1.5 CAD, it is not able to bring it to zero based solely on the model. No gain is applied on this error. Since the model is designed to have low computational expense, some error is anticipated. Furthermore, the model is developed using steady-state results, and therefore, discrepancies during transient maneuvers are not surprising. Overall, the strong performance of the steady-state map limits the opportunity to demonstrate the model capability.

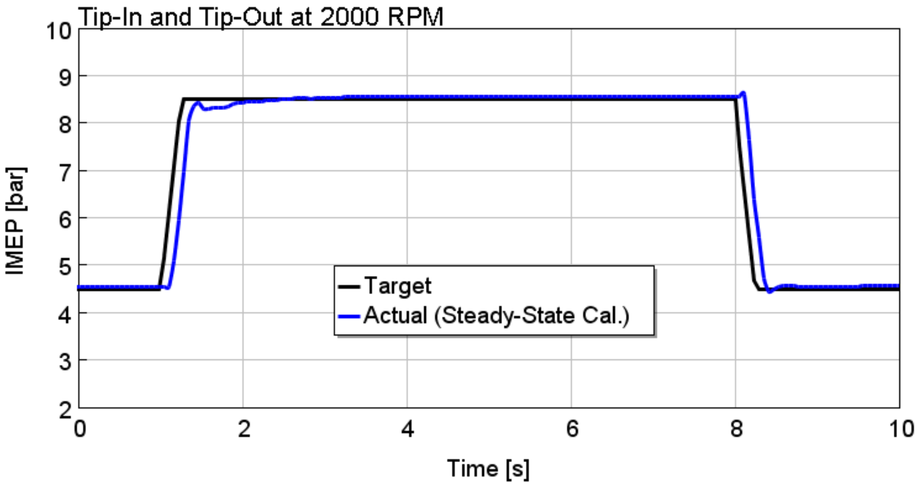

Figure VI-9: Tip-in and tip-out response in GT-Power for the steady-state calibration.

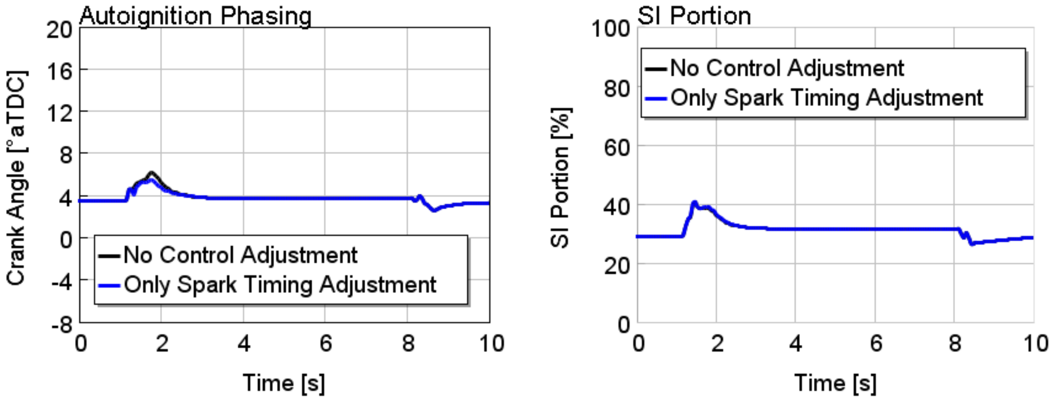

Figure VI-10: Combustion response to tip-in and tip-out for the steady-state calibration and the updated calibration.

Instead of relying on a transient to capture the cylinder model capability, a step-change disturbance is considered. In this case, a step change in intake temperature is performed under otherwise steady conditions. The temperature shift can represent a literal change in temperature (as if the EGR cooler or charge-air cooler malfunctions), or it can represent another change to the engine system the controller could not anticipate, such as a change in fuel composition. The model will be evaluated in two ways: 1) with knowledge that the manifold temperature has changed, and 2) without knowledge that the manifold temperature has changed. In other words, for 1), the model will recognize intake temperature has increased and using all available actuators, adjust the in-cylinder state to achieve the target response. In the case of 2), the model does not have knowledge of why AI phasing changed, and only adjusts spark timing to correct autoignition phasing.

First the 1D reference engine model is exercised with the disturbance to identify the error in AI phasing. Since AI phasing is exponentially sensitive to temperature, this is the response that will be focused on in this section. Figure VI-11 illustrates the ~25 K increase in intake manifold temperature and the corresponding ~2 CAD advance of autoignition. This is consistent with Mendrea et al., who identified a 4 CAD advance in CA50 for a 20 K increase in intake temperature [107]. Though the 2 CAD presented here is not as large, the Mendrea et al. study is limited. The study only examines two temperatures at one operating point. The autoignition phasing is also not reported, only overall CA50.

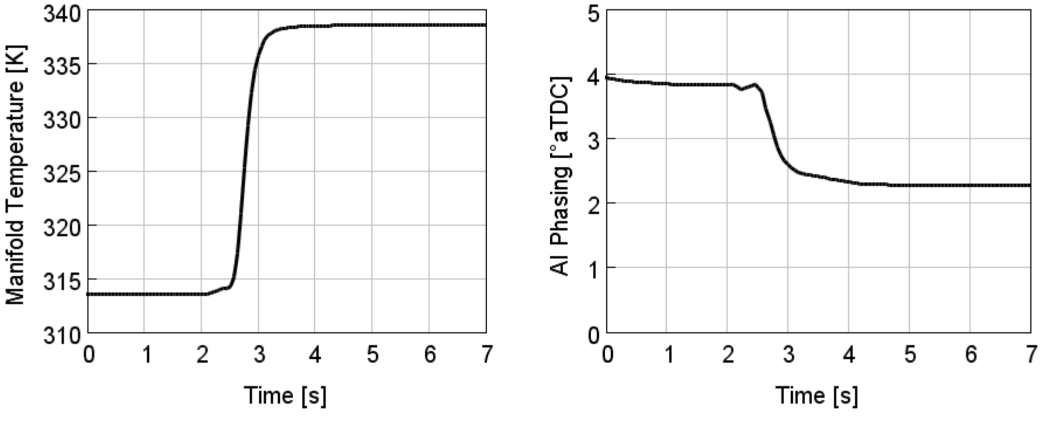

Figure VI-11: Intake manifold temperature disturbance and corresponding AI phasing response with no control adjustment.

The measured temperature increase is input into the MATLAB-based model, and for each time-step, the model is optimized. The *fmincon* function is used, with the target AI phasing and SI portion being those at t = 0 seconds. The optimizer has the flexibility to adapt intake cam phaser, exhaust cam phaser, intake manifold pressure, external EGR, and spark timing. The bounds of each actuator are computed from the previous time-step value and the anticipated maximum slew rate of the actuator. The cam phasers are limited to a slew rate of 50 crank degrees per second, EGR is limited to a change of 15% per second, intake manifold pressure is limited to a 1 bar per second rate, and spark timing is limited to a 20 CAD change per time-step (for optimizer stability).

The actuator response is depicted in Figure VI-12. The model optimization adapts the cams and external EGR to reduce the proportion of hot internal residual, and instead favor cooler external EGR to help bring the in-cylinder state to a lower-energy level. Spark timing retards as the in-cylinder state is still relatively high compared to the starting time. This is confirmed by examining the temperature at cycle start and total burned gas fraction (Figure VI-13). Despite the shift towards external cooled EGR, the in-cylinder temperature is still ~ 4 K hotter than at t = 0 seconds. Along with a slightly reduced burned gas fraction, the higher energy state and lower dilution require a ~2 CAD later spark timing to maintain autoignition phasing.

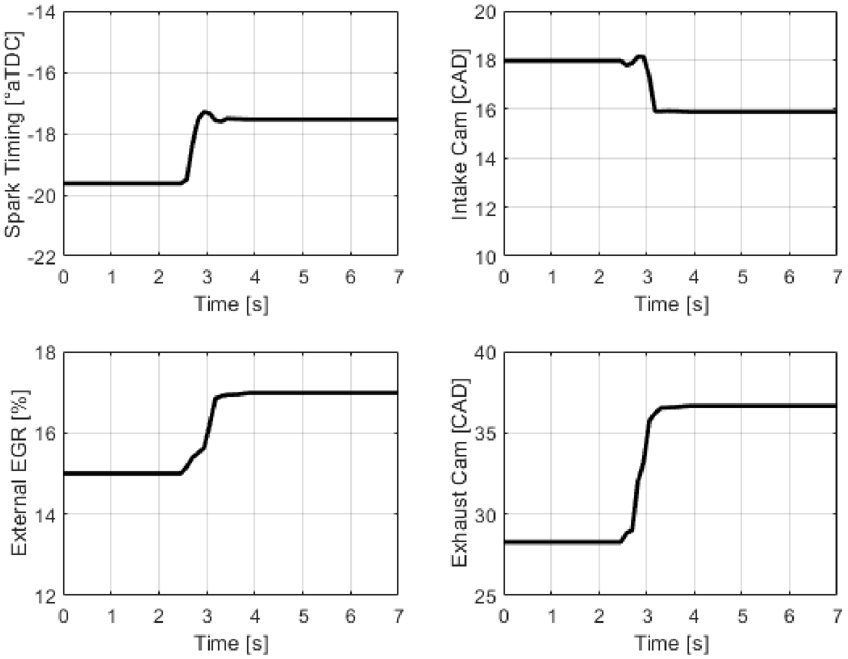

Figure VI-12: Actuator response after optimization to maintain AI phasing during an intake temperature disturbance of +25 K.

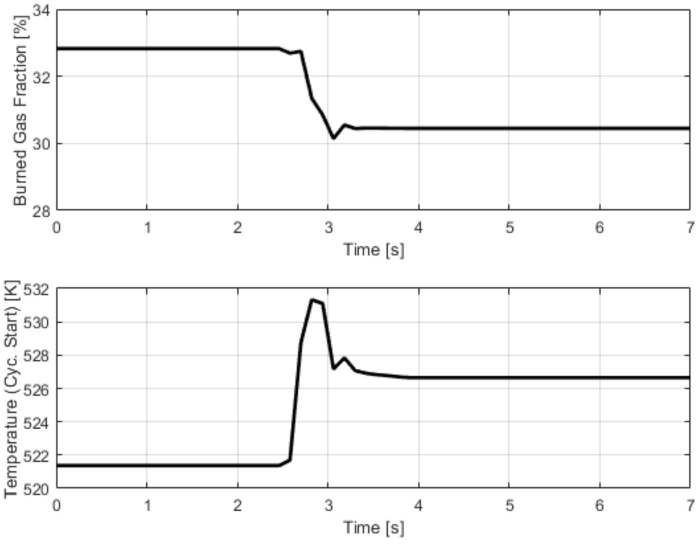

Figure VI-13: Burned gas fraction temperature at cycle start during the optimized temperature disturbance. The in-cylinder state is at a higher level with less dilution than at the start of the transient, necessitating spark retard.

In addition to this strategy, the optimization is also performed using with only the spark as the available actuator. No constraints are applied for this optimization. This simulates a condition where a disturbance occurs outside of the scope of the model or engine sensors. Both results are evaluated in GT-Power and compared to the case where no controller action is taken. Figure VI-14 depicts the response for both cases. Both can reduce the AI phasing error to about 1 CAD, though each achieve this result in different ways. Despite the higher in-cylinder temperature, the spark-only response required more advanced spark timing than the full model response. The reduced dilution for the full model response appears to be the differentiating factor. There is still an error, however, the error is ~1 CAD, which is well within expectation for the fast-running cylinder model. This is also consistent with work by Nakai et al., where their production-intent autoignition model error is up to 3 CAD [60].

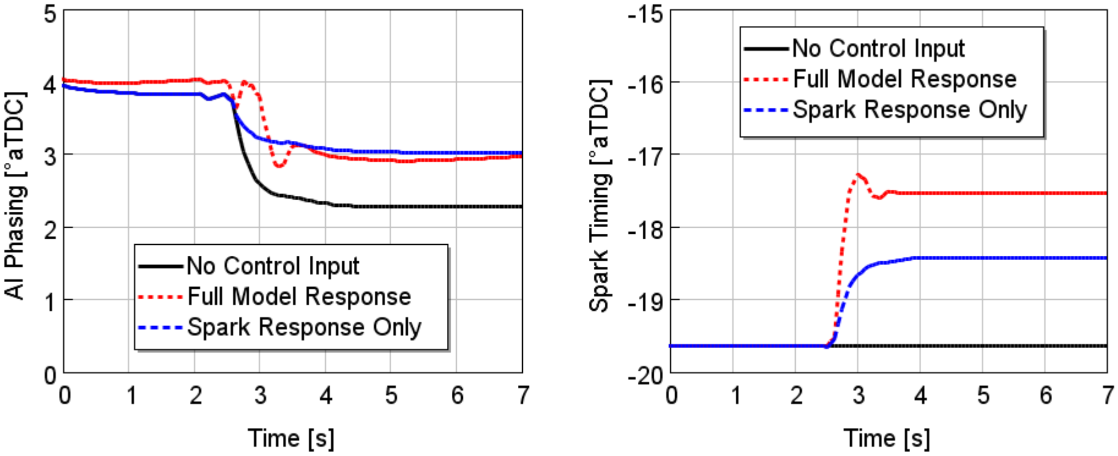

Figure VI-14: Model response for two conditions, one where the model can account for the disturbance, and one where it only has a measure of AI phasing error.

Mode-Switching

The relatively limited range of operation for a given SACI mode suggests the need for mode-switching. The reduced-order cylinder model again can provide use by identifying regions in other combustion modes that can readily be switched to within all actuator slew rate limits and combustion constraints.

To illustrate this, consider a transition from lean to stoichiometric. To perform an instantaneous transition, several actuators will not have sufficient time to move. To resolve this challenge, the candidate model can be leveraged to compute the combustion response for a sweep of the actuators that can rapidly change, namely, spark timing and injection strategy (Figure VI-15). The split ratio is maintained at 1.0 for this sweep for consistency with the results from GT-Power. Only the equivalence ratio and spark timing are adjusted. To maintain the same nIMEP with double the fuel energy, the spark timing is retarded to 16° aTDC. The model adapts accordingly for changing cylinder conditions. At the zeroth cycle, for example, though there will be a stoichiometric mixture of fuel and air, the residual fraction is from the previous cycle which is much leaner than stoichiometric. The candidate cylinder model therefore maintains the previous cycles residual fraction through to the next cycle. Once the first cycle finishes, the burned gas fraction increases and spark advances to 12° aTDC to account for the increase of the BGF.

This late spark timing yielded a combustion phasing of CA50 = 56° aTDC, which is borderline unacceptably late for production constraints, even for just one cycle. The SI burn duration is also near the flammability limit at about 39 CAD MFB10–90. There are two conclusions from this observation. First, a mode switch using just spark timing and equivalence ratio at this condition may not be possible. The candidate model can only describe what the aggregate submodels predict will occur based on their tuning. It is the responsibility of the calibrator to determine if these are production feasible. The objective of the candidate cylinder model is to provide maximum information to the calibrator during their investigation. The other conclusion is that the borderline nature of this particular mode switch can be mitigated by coupling a SACI engine with mild hybridization. In this case, the mild hybrid system can absorb torque, allowing the stoichiometric SACI engine to operate closer to MBT without affecting driveline torque. A detailed independent discussion of this topic can be found in Appendix B.

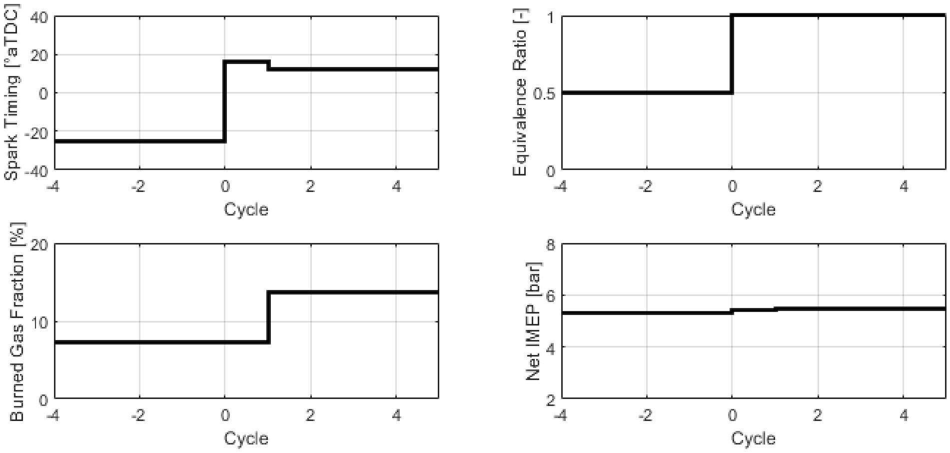

Figure VI-15: Mode switch example from lean to stoichiometric. Only fueling rate and spark timing is altered, while maintaining the same nIMEP.

Summary

The simplified cylinder model can represent the complex in-cylinder picture and make appropriate changes within constraints to achieve the target objective. That objective may be calibration optimization, transient control, disturbance response, or mode-switching. All are briefly demonstrated as case studies in this work. Though there are some non-zero error in several combustion metrics (especially AI phasing), these are within expectation and consistent with other production intent models.

VII. SUMMARY AND CONCLUSIONS

SACI is an advanced combustion strategy that offers emissions and fuel economy potential. SACI combines flame propagation with controlled autoignition, which requires high dilution to avoid excessive ringing or knock. The high dilution drives flame propagation towards flame quench, which can result in partial or complete misfires. Of the few control-oriented models for SACI combustion in the literature, all are two-zone and compute combustion metrics on a crank-angle basis. The two-zone model structure the modeling of fuel stratification, and the focus on the crank angle domain increases computational expense.

To resolve the modeling challenge, a fast-running cylinder model is developed and presented in this work. It comprises of five bulk gas states and a fuel stratification model consisting of ten (10) zones within the cylinder. The zones are quasi-dimensional, and their state varies with crank angle. In this model, the crank-angle domain is limited to equivalence ratio and temperature; combustion models are computed based on a single crank angle. Each of the bulk gas state models is an artificial neural network (ANN) tuned to experimentally-validated 1D engine reference simulation results. The fuel stratification model is physics-based and tuned to experimentally-validated 3D computational fluid dynamics (CFD) results.

The combustion submodels predict flame propagation burn rates, autoignition phasing, and NO_x concentration for each zone. During the development of the combustion submodels, both physics-based and data-driven techniques are considered. However, an examination of the balance between accuracy and computational expense indicates data-driven techniques are superior. All combustion submodels are artificial neural networks (ANNs). The networks are trained to an experimentally-validated 1D engine reference model.

The fast-running model matches the reference 1D engine model well, with an R^2 value of 70–96% for the most important combustion parameters. The model requires 0.8 seconds to perform a single case, a 99.6% reduction from the reference 1D engine model. The reduced model simulation time enables rapid exploration of the operating space. Over 250,000 cases are evaluated across the entire range of actuator positions. The exploration of the input space indicates valuable control strategies, such as the increased margin to flame quench by leveraging radial fuel stratification.

A transient-capable calibration is also formulated. This preliminary calibration is optimized using the 1D reference simulation to produce the final steady-state calibration. To evaluate the strength of this calibration, it is operated over a tip-in and tip-out. The response to the transients requires little adjustment, suggesting the steady-state calibration is robust. The model also demonstrates the capability to adapt in-cylinder state and spark timing to offset disturbances to combustion phasing consistent with fundamentals. For example, during a 25 K step increase in intake temperature, the model adjusts the balance of hot internal EGR and cooled external EGR to reduce overall in-cylinder temperature despite the increased intake temperature. The positive model performance during transients and input disturbances indicates that the candidate cylinder model maintains sufficient accuracy, despite its significantly reduced computational expense.

Research Contributions

This research provides a comprehensive control-oriented model of an advanced combustion strategy called spark-assisted compression ignition (SACI). The following contributions are achieved as part of this work:

1. **A demonstration of the impact of combustion fundamentals on SACI combustion.** Sensitivity to intake conditions, in-cylinder composition, spark timing and how they

translate to ignition energy are comprehensively explored. For example, under certain low-load conditions, throttling can effectively enable a lower load with little impact on ignition delay, potentially eliminating a switch to another combustion mode. Another example is the capability of the burn rate of flame propagation to accurately reflect flame structure for the purposes of defining the flame quench constraint.

2. **A comparison of model structures for combustion models and an identification of suitable techniques for data-driven modeling.** For both flame propagation and autoignition, a detailed study of physics-based and data-driven models is performed. Ultimately, the data-driven techniques are found to be most suitable for control-oriented models as their computation expense does not scale with model accuracy as strongly as physics-based models. Artificial neural networks are leveraged as the model structure for all combustion models. Overfitting techniques such as Bayesian regularization and early-stopping are implemented. A hybrid regression-classification network approach for SI burn duration and AI phasing models is demonstrated. The AI phasing ANN has encouraging extrapolation performance while being sufficiently detailed to capture the NTC region.

3. **A quasi-dimensional fuel stratification model for radially-stratified engines.** One control strategy for SACI is the use of late injection to increase equivalence ratio near the center of the combustion chamber. The relatively rich region improves conditions for flame propagation. No suitable control-oriented stratification model is found in the literature or in the 1D engine simulation package selected for this work. Consequently, a physics-based stratification model is developed. It is validated to CFD results and

demonstrates a 50% improved root mean square error compared to a model that assumes a uniform fuel distribution.

4. **A comprehensive cylinder model that maintains high accuracy despite substantially reduced computational expense.** The final cylinder model matches the reference 1D engine model to 70–96% (based on R^2 of key combustion metrics). The simplified model, however, requires less than 1 second to produce this result, as opposed to three minutes per case for the reference 1D engine model. Rapid calibration optimization and exploration is therefore enabled and demonstrated.

Future Work

This research focused primarily on model development, though calibration and controls are included. Based on this study, the following future work is recommended:

1. Develop a production-intent SACI engine test stand to further refine the cylinder model. Expand on the number of test points and operating regimes to aid in model development. One particular area to focus on is the impact of fuel stratification on combustion.
2. Consider augmenting GT-Power with improved models to aid in controller development for SACI combustion. As future releases of GT-Power may include some of this necessary functionality, a discussion with the makers of GT-Power is recommended as the first step.

3. Using the knowledge gleaned from this work, begin development on an applications-focused SACI controller. This controller can be developed in simulation in parallel with the experimental setup using the already developed Simulink control platform.

APPENDICES

A. AUTOIGNITION MODEL STRUCTURE

There are several approaches to modeling autoignition, each varying in computational expense and accuracy. Careful selection of an autoignition model is critical for SACI control to be effective. Three types of models are included in this work: chemical kinetics, ignition delay, and regression. A thorough comparison of several models is best achieved if noise and other stochastic processes are minimized and the maximum amount of data is available for an in-depth analysis. Therefore, a detailed simulation model is exercised to isolate the autoignition process from confounding effects and provide data that is difficult or measure experimentally. While a chemical kinetics mechanism potentially introduces errors compared to experimental data, the objective of this work is a relative comparison of different model types. The assumption underlying this work is that a detailed kinetics model is sufficiently complex to reproduce real engine phenomenon such that the performance of the production-feasible models is effectively the same as if it is based on experimental data. The regression and ignition delay models are evaluated as candidate models for production control.

Figure A-1 illustrates the modeling process for each of the three types of models. Though all three have the same input and output, there are significant differences among the three types. The kinetics model is part of an engine cycle simulation, where the cycle composition and state are computed at each time step. The ignition delay model is evaluated over predefined pressure and temperature profiles based on the inputs. Both types of models have an autoignition phasing criteria. Autoignition occurs in the autoignition model when the rate of change of temperature in the unburned gas is 50 K/CAD. This threshold is selected after careful examination of several cases to identify a representative start of autoignition. The ignition delay models use the induction time integral criterion [96]. The regression models directly map the inputs to the outputs.

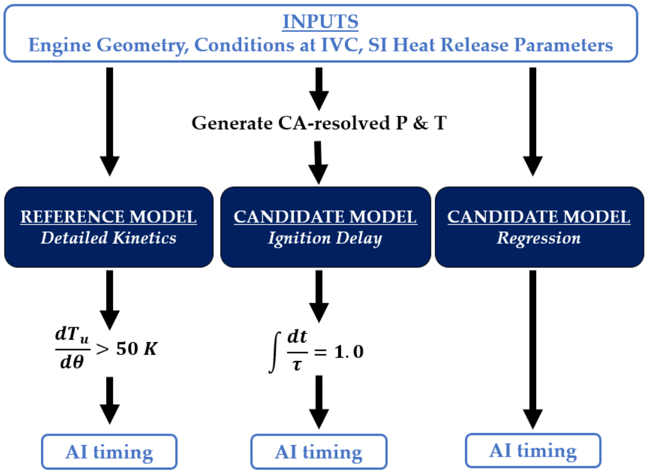

Figure A-1: Schematic describing the simulation and analysis process. Note that the ignition delay candidate models require additional pre-processing, and the detailed kinetics and ignition delay models require some evaluation criteria to determine autoignition timing. The regression model has the simplest application.

Reference Model

The reference model is a detailed chemical kinetics model coupled to a 1D engine model. The kinetics model simulates an engine cycle from intake valve closing (IVC) to the end of combustion and applies the pressure and temperature history to the kinetics mechanism. The kinetics model is first swept over a wide set of conditions. The results are analyzed and used to guide a 1D simulation effort. Two engine datasets contribute to the two parts of the model. An experimental homogeneous charge compression ignition (HCCI) engine dataset is used to calibrate autoignition in the kinetics model, and the 1D engine model is tuned to measured data from a baseline SI engine. From this baseline configuration, several engine parameters are adapted to produce the final SACI engine configuration. Table A-1 lists key engine parameters for these two engines.

Table A-1: Specifications of the engines used for simulation validation.

	HCCI Engine	**Baseline Engine**
Bore x Stroke [mm]	86 x 94.5	82 x 94.6
Compression Ratio	12.5:1	11.0:1
Valvetrain	Exhaust Rebreathe	Intake and Exhaust Cam Phasers
Relative AFR (λ)	1.4 – 2.0	1.0

The SI phase of SACI combustion is modeled with a Wiebe function. The burn duration is tuned based on the calibrated predictive combustion model in [108] and from data presented in [109,110]. A regression is performed on the results to generate a second-order burn duration model. The model is a function of relative air-fuel ratio (λ), total burned gas, intake manifold pressure, and combustion phasing. A sample of MFB10–90 is shown in Figure A-2, across a range of air-fuel ratio (AFR) and exhaust gas recirculation (EGR) levels at a fixed combustion phasing and manifold pressure. SACI is tolerant of slow burn durations, so an upper limit of 45 CAD MFB10–90 is selected as the SI phase flammability constraint.

Fuel stratification is an enabling strategy for SACI. Nakai et al. leveraged stratification to increase SI flame stability in fuel-lean operation and suppress ringing under high load [60]. Olesky et al. noted that charge stratification is a key factor in the cycle-to-cycle variation of SACI combustion [51]. Capturing charge stratification in a two-zone model is achieved by assuming the combustion chamber has two regions: the SI region and the AI region. The anticipated AFR for the SI region is input to the SI burn duration model to generate the appropriate SI Wiebe curve. This simulates the impact of a late direct injection strategy within the constraints of the model architecture. The kinetics model used the AI region AFR. This two-zone stratification model does not fully represent the in-cylinder fuel distribution, so it may not appropriately capture certain effects, such as the variation of SI flame speeds when the flame consumes most of the charge.

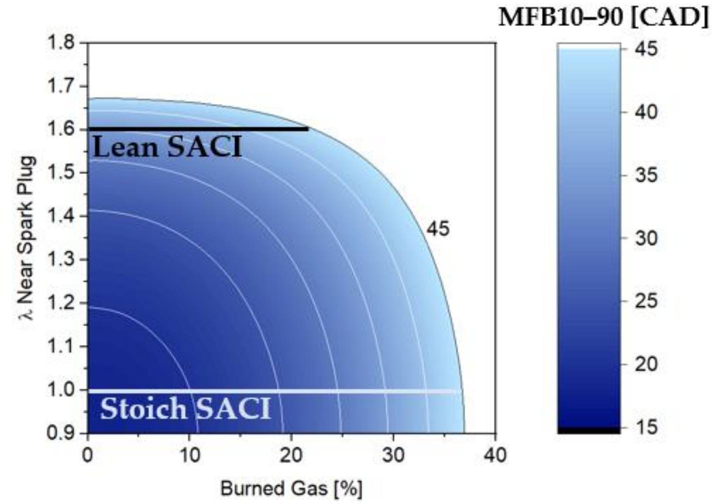

Figure A-2: SI phase combustion duration model. The fuel-lean SACI conditions for the SI portion are slightly richer than the overall AFR to account for fuel stratification.

The unburned zone is modeled using detailed chemical kinetics. The kinetics mechanism targets RD3-87 over a wide range of conditions [94]. The fuel selected for this study is a four-component E10 87 AKI gasoline surrogate. It is based on a ternary RD3-87 blend with the addition of ethanol [111]. Details of the fuel composition can be found in Table A-2. Autoignition occurs when the combined effect of the piston motion and SI Wiebe-modeled combustion produce sufficient temperature and pressure for the unburned zone to ignite as determined by the kinetics mechanism.

Table A-2: Fuel specifications for the chemical kinetics model. The reference model only considered TRF-E, though a later sensitivity study uses all three fuels.

	TRF-E	**PRF-E**	**PRF87**
Ethanol	10%	10%	–
Toluene	26%	–	–
Isooctane	47%	76%	87%
n-Heptane	17%	14%	13%
RON	89.2	87.3	87.0
MON	84.9	86.8	87.0
AKI	87.0	87.0	87.0

Though kinetics mechanisms capture the behavior of chemical reactions well, translating these results between the kinetics model and 1D simulation requires additional tuning. In addition to error in the kinetics model, the simplified cylinder model may not represent the hottest gas regions. To resolve these discrepancies, a temperature offset is applied to the temperature at intake valve closing (T_{IVC}).

To tune the autoignition phase, the chemical kinetics model is configured to match engine and fuel data from the HCCI engine in Table A-1. A direct comparison between measured engine and the chemical kinetics model cannot be performed. In-cylinder composition and bulk gas temperature at IVC are critical parameters for the kinetics model, however, these are challenging to measure on a firing engine. Instead, a 1D simulation is experimentally validated to the HCCI engine data set, Figure A-3.

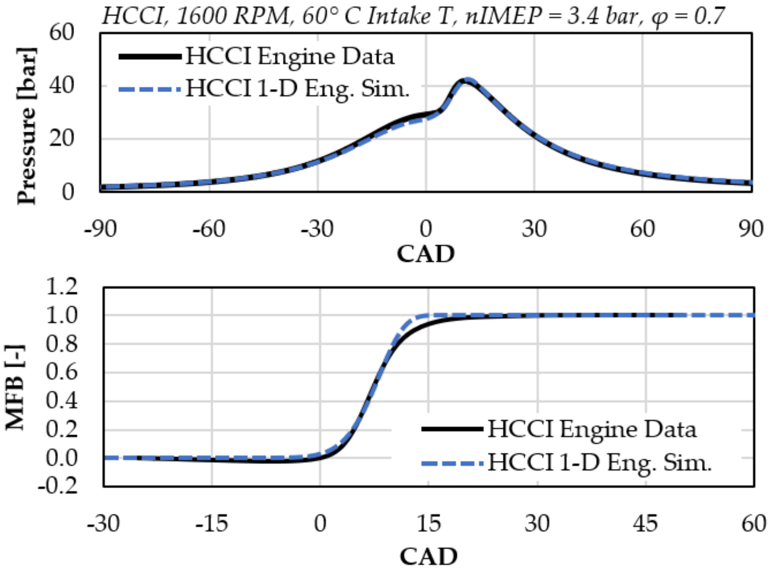

Figure A-3: Sample comparison of the validation of the 1D model to engine data for HCCI combustion. The validated 1D model is used for calibration of the single-zone kinetics model, as it includes temperature and composition throughout the cycle.

The temperature at IVC of the kinetics model is calibrated to the experimentally-validated 1D simulation results to match the CA01 phasing. A sample comparison of the calibration process is presented in Figure A-4. Across a range of speeds and intake temperatures, the kinetics model T_{IVC} must be 45 K above the 1D model T_{IVC} to match the AI phasing. This 45 K offset is applied when translating between the kinetics and 1D models. The engine data, 1D simulation, and chemical kinetics configuration of the HCCI engine is only used for the kinetics model validation.

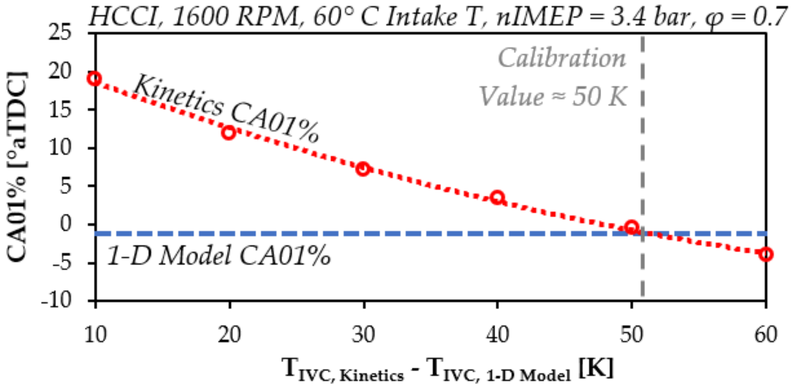

Figure A-4: Sample calibration process of the autoignition kinetics model at a single condition. The temperature at IVC is increased to match the CA01 of the single zone kinetics model to the 1D model. In this case, the T_{IVC} of the kinetics model must be ~50 K higher than the 1D simulation T_{IVC}.

A single-zone autoignition model is not sufficiently resolved to capture thermal stratification. Without this stratification, the model alone cannot accurately predict the burn durations of the AI phase. The duration of the AI event will strongly affect the rate of pressure rise, which is an important constraint for autoignition-based combustion strategies. Ringing intensity (RI) relates the rate of pressure rise to noise and is described in (2). For this analysis, a RI limit of 5 MW/m^2 is selected.

The single-zone model is augmented with a burn duration correlation. Three correlations are compared; two are tuned for HCCI combustion and one for both HCCI and SACI.

Babajimopoulos et al. [101] developed their correlation based on HCCI simulation results, while Zhou et al. [102] considered HCCI engine data. Both are a function of ϕ' and autoignition timing, among other variables.

Both HCCI correlations produce similar burn durations for autoignition near top-dead center (TDC). However, as AI phasing is retarded, the burn duration increases significantly for the Babajimopoulos et al. model. This likely represents a cycle-cycle variation (CCV) limit for HCCI. Unlike HCCI, SACI can sustain later AI timings because the flame continues to release heat after TDC. Experimental results by Manofsky et al. [35], Nakai et al. [60], and Triantopoulos et al. [103] all demonstrated the CA50 up to ~15° aTDC within CCV limits.

Ortiz-Soto developed an HCCI and SACI autoignition burn duration model [58]. To achieve the wider range of operation, several additional parameters are required, including the temperature at pressure at autoignition and the fraction of charge remaining at autoignition. The Ortiz-Soto model is selected for this study as it is the most-appropriate fit for SACI combustion.

Identifying end-gas knock is difficult to quantify, especially for a single-zone autoignition model. Rapid burn rate indicates a high rate of energy release, which is consistent with knock and will produce a higher RI. However, identifying a knock limit based solely on burn rate or RI is challenging. Alternatively, the following three bounds are imposed to appropriately limit the model results under stoichiometric conditions.

- The relative charge energy content (ϕ') must be below 0.75. Early SACI experimental work by Manofsky et al. used a ϕ' of 0.7 at high loads [35]. More recent work by Triantopoulos et al. varied ϕ' from 0.57 – 0.72 [103]. Patent information from Mazda suggest the low-dilution limit is ϕ' = 0.8, and test data show a modest 9% external EGR at stoichiometric high-load conditions [29,60]. Internal residual fraction is not mentioned in that study.

- Autoignition must occur after TDC. For a given ϕ' and autoignition burn duration, phasing AI after TDC reduces the rate of pressure rise. The increasing cylinder volume partially offsets the pressure rise from autoignition.
- SI portion must be above 25%. SI portion is a key metric for SACI combustion. It describes the relative portion of the fuel energy burned by the flame.

Flame propagation has a lower heat release rate, and therefore a lower peak pressure rise rate. Additionally, as SI portion increases, there is a lower quantity of energy available for autoignition. The lower bound of SI portion is determined by examining heat release rates from experimental datasets for high-load operation [60,103].

Chemical Kinetics Parameter Sweep

The objective of the kinetics study is to identify trends, limits, and potential production challenges by mapping out the space of operation. This model is exercised with the following parameters sweep:

- Effective compression ratio CR_{eff} (10:1 – 18:1)
- Total Residual (0% – 30%)
- T_{IVC} (350 – 500 K)
- Relative AFR ($\lambda = 1, 2$)
- SI Combustion Phasing (SOC = -30° – 0° aTDC)
- Pressure at IVC (1.0 – 1.4 bar)
- Engine Speed (1000 – 3500 RPM)

The sweep points are correlated to controls-specific actuator positions. Effective CR can be achieved by early or late intake valve closing (EIVC, LIVC). Air-fuel ratio is the local AFR of the end-gas area. SI combustion phasing is directly linked to spark timing. For these analyses, start of combustion is defined by CA01 of the SI Wiebe heat release profile. Total residual is a combination of internal and external EGR, and both are assumed to have the same chemical composition. The temperature at IVC can be regulated by both hot internal residual and intake manifold temperature. Four factors combine to control load: AFR, residual fraction, effective CR, and intake manifold pressure.

The results of the sweeps identify potential load limits, and possible strategies to resolve these limits. The analysis of the results is divided into subsections that each focus on combustion fundamentals. The conclusion of each subsection identifies the implication for production controls.

Combustion Phasing

The critical feature of SACI is the direct control of the start of the autoignition process. However, the coupling of the AI event to the SI heat release adds a significant degree of complexity. The simulation results help to clarify the control authority SI phasing has on autoignition. For this model, spark timing is not explicitly specified. As the SI portion is a Wiebe function, a combustion model for flame kernel development would need to be introduced. The added uncertainty is considered detrimental, and instead CA01 is used as an analogue for spark timing.

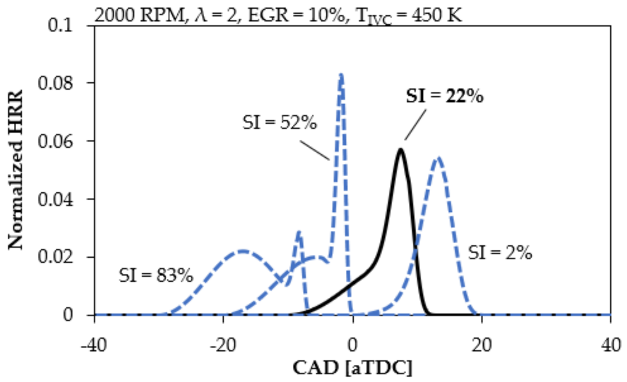

Figure A-5: Heat release rate (HRR) curves for a CA01 sweep at 16:1 effective compression ratio. The SI portion increases and CA50 advances as the start of combustion advances.

A sample set of heat release curves is presented in Figure A-5. The curves are generated in two steps. The SI component is a Wiebe function based on the specified start of combustion and burn duration from the SI MFB10–90 model. The AI part is phased based on the kinetics-predicted autoignition timing. A Wiebe curve is then generated based on the autoignition burn duration correlation. These two curves are combined to produce the curves in Figure A-5. The solid black line (SI portion = 22%) indicates MBT timing. Early combustion phasing increase SI portion, and the peak heat release rate of autoignition increases as θ_{AI} approaches TDC. While this may be counter to the response that SI knock has to spark timing, the range of autoignition timing is much earlier than that for SI knock. As autoignition phasing advances beyond TDC, lower temperature and pressure during the compression stroke result in the autoignition event occurring later relative to the SI phase. The latest combustion phasing, SI = 2%, shows a nearly HCCI HRR curve. If combustion phasing is retarded much beyond this point, however, autoignition will not occur.

Figure A-6 depicts the SI portion and autoignition phasing θ_{AI} as a function of the CA01 for three select CR_{eff}. Autoignition timing responds linearly with CA01, and with a roughly constant slope regardless of effective CR. The value found for the change in θ_{AI} per unit change in combustion phasing is about 0.5, consistent with results found in the literature [29,112].

The change in SI portion appears linear in the region of high sensitivity. For combustion phasing later than this region, the delayed heat release from SI does not provide sufficient energy to autoignite the charge before pressure and temperature decreases during expansion. Conversely, if combustion is phased early, the flame consumes the charge before autoignition occurs.

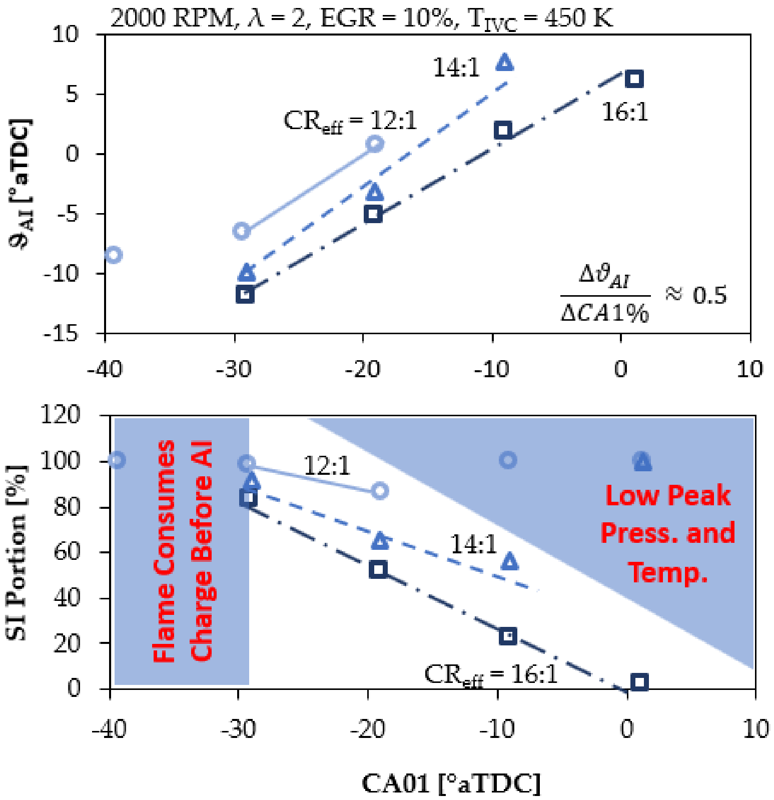

Figure A-6: Autoignition characteristics as a function of the SI heat release phasing. The range of feasible SACI conditions occupies a ~20 CAD range.

The controls implications are that there is a narrow range where SACI is feasible and each combustion phasing produces one particular SI portion. Though the results suggest that SI portion will equal 100% outside of this region, the prescribed Wiebe function does not consider misfire. The highly dilute charge makes the potential for complete SI combustion unlikely.

Combustion Response to Partial SI Burn

Radial fuel stratification of the charge may make it unlikely for the flame to consume the full charge if autoignition does not occur. An investigation is performed for the 14:1 CR_{eff} at the same conditions in Figure A-6. The maximum fraction of fuel burned by the SI phase is limited to simulate the effect of the flame quenching as it progressed into leaner regions of the chamber. Figure A-6 depicts the autoignition timing and SI Portion as the SI burn limit is varied from 0.25 to 1.0. As the SI burn fraction approaches zero, the SI portion reduces and autoignition is delayed (Figure A-7). A low SI burn fraction limit still produces an increased temperature and pressure relative to no flame. However, a limited SI Portion does not consume the charge prior to autoignition. Therefore, a partial SI burn can produce SACI combustion, and may enable a wider range of SI Portion for a particular condition.

Charge stratification may be capable of extending the operating range of SACI, though it adds controls complexity. Furthermore, a partial SI burn still enables an AI event and may not necessarily lead to an overall misfire. This is consistent with the literature demonstrating a greater tolerance for slow SI combustion [51].

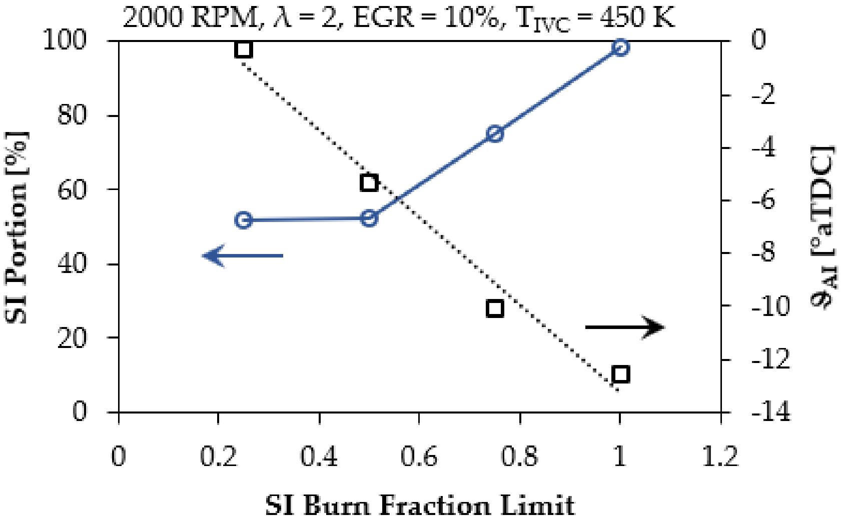

Figure A-7: SACI combustion metrics versus the maximum fuel fraction burned by the SI phase. This simulation replicates the impact of a partial SI burn. The SI portion is reduced and θ_{AI} *delays as the SI burn fraction limit decreases.*

Load Limits

Identifying the limits for SACI is critical for achieving a viable production control strategy. To consolidate the impacts of overlapping control inputs, certain results will be presented as T_{TDC} *(No Flame)* versus volumetric efficiency (VE). T_{TDC} *(No Flame)* is determined by the intake temperature, effective compression ratio, and ratio of specific heats. The VE term is calculated as follows, where BGF is the fraction of total residual (34).

$$VE = \left(\frac{P_{intake}}{P_{ambient}}\right)\left(\frac{CR_{effective}}{CR_{geometric}}\right)(1 - BGF) \tag{34}$$

The translation from a particular location in this space to control actuator positions is presented in Figure A-8. From the results in the subsequent sections, the subset of feasible control actuator movements and positions can be deduced.

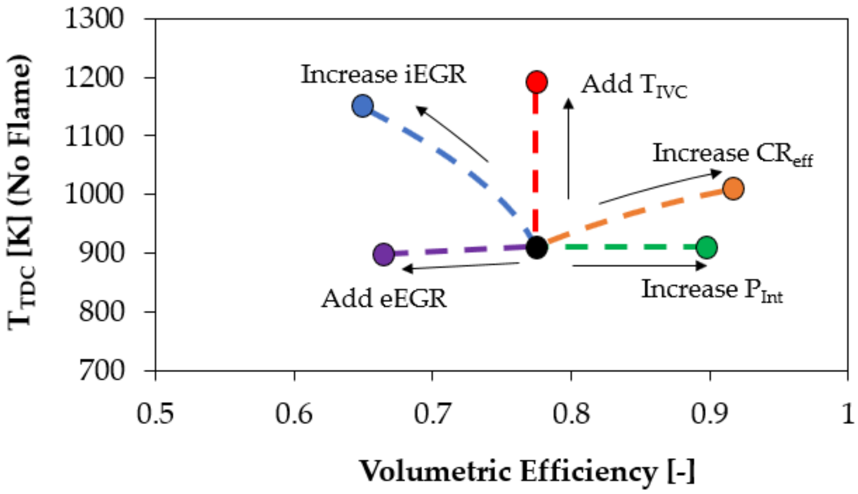

Figure A-8: Diagram translating actuator adjustments to temperature at TDC versus VE. Internal EGR and CR_{eff} strongly effect both T_{TDC} and VE, while the others predominantly impact one or the other.

The relationship between SI portion and T_{TDC} and VE is presented in Figure A-9 for fuel-lean operation. Since MBT phasing is maintained, the SI portion indicates the extent that the flame is involved in the overall combustion process. High SI portions reduce ringing, but also increase the peak burned gas temperature. Higher temperatures under lean conditions will produce higher NO_x emissions, though NO_x is modeled in this study. The region of high T_{TDC} and low VE indicates intake heating may be required, a potential limit for production. Towards high VE and high T_{TDC}, autoignition occurs without the flame (SI portion << 25%). This condition may be undesirable in SACI as the control authority from the flame is lost. The region of low T_{TDC} (SI portion >> 75%) indicates little-to-no autoignition. This region is nominally SI combustion. However, since the conditions are potentially unsuitable for complete SI combustion, this region may be undesirable. Lowering VE is the primary load-control strategy in this study. To lower VE, either EGR dilution must increase or compression ratio must decrease. Achieving enough ignition energy requires an increase in the temperature at TDC. A 10% reduction in VE using these methods requires about a 30 K increase in T_{TDC} to maintain the same SI portion.

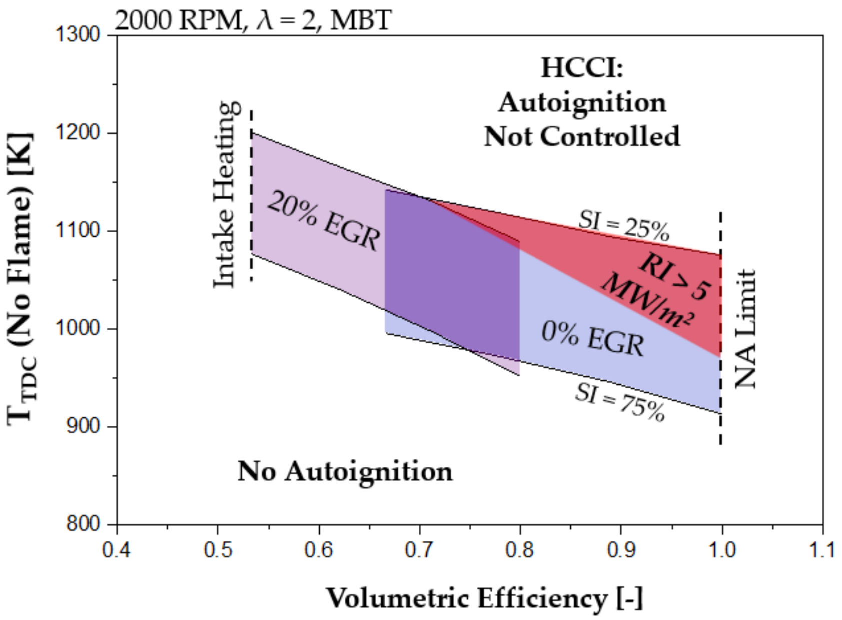

Figure A-9: Regions of feasible SACI combustion as a function of cylinder charge (VE) and state ignition energy (T_{TDC}). There is a relatively narrow range of operation. The low load is limited by ignition energy and the high load by the maximum air mass that can be trapped while naturally aspirated (NA).

Extending the high load limit of fuel-lean SACI can be achieved with boosting, however, two key constraints are present. The RI constraint demands an increased SI portion. The high SI portion, however, increases the mass of fuel burned by the flame. The higher temperatures during combustion likely increase the concentration of NO_x, the second constraint. NO_x is not modeled in this study.

The low-load limit for fuel-lean SACI is determined by ignition energy. An analysis of ignition delay indicates potential strategies to minimize ignition delay as ignition energy becomes constrained. Figure A-10 depicts the pressure-temperature trajectory overlaid onto an ignition delay contour plot for a point near the low-load limit. The negative temperature coefficient (NTC) region is clear, and the MON test trajectory is included for reference.

The three SACI traces indicate the pressure-trajectory up to TDC for three cases: no combustion, -10° aTDC CA01, and -20° aTDC CA01. The heat released from combustion phasing at -20° aTDC CA01 provides sufficient ignition energy to achieve autoignition for this case. These trajectories indicate that the SI phase has a similar effect as higher compression ratio.

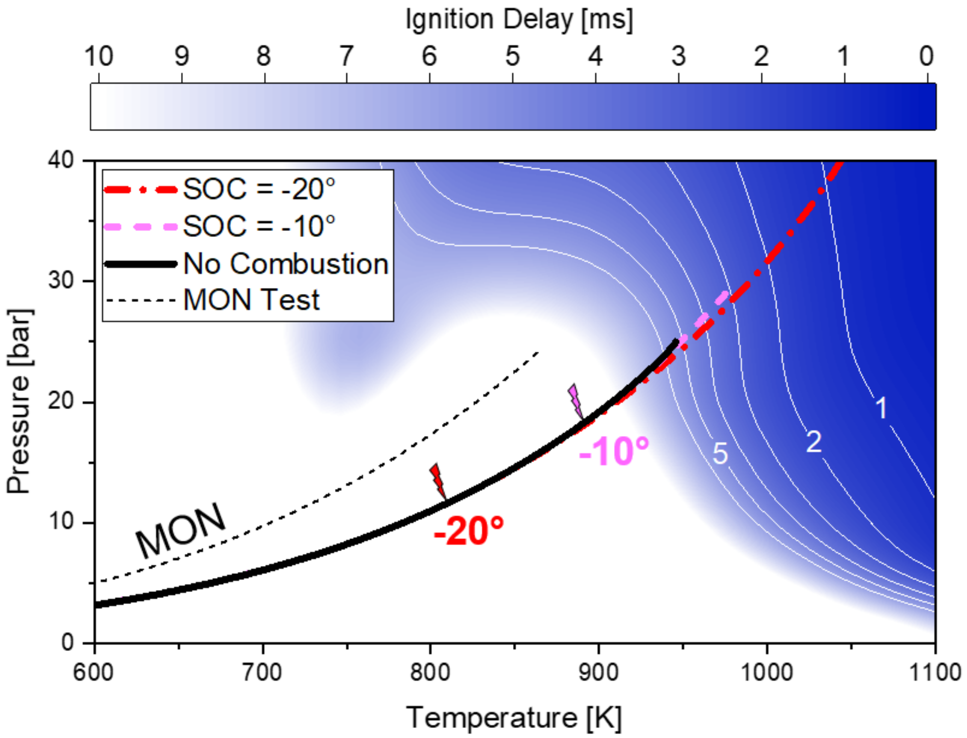

Figure A-10: Pressure-temperature trajectory for three SACI cases overlaid onto the ignition delay plot. At this low-load point, there is a greater sensitivity to temperature than pressure.

In Figure A-10, the steepest downward gradient from the no combustion case is towards higher temperature. Reaching the 2 ms contour line via pressure alone requires more than a two-fold increase in P_{IVC}, while only a 6% increase in T_{IVC} (e.g., 400 K to 425 K) yields the same ignition delay. High temperatures at low loads also keeps the trajectory away from the NTC region, where ignition delay is nonlinear and relatively insensitive.

The relevence for a controls strategy is two-fold. First, throttling the intake charge helps to maintain the ignition delay while reducing VE. Reducing the effective compression ratio to reduce effective displacement lowers both pressure and temperature. Reducing the intake pressure will shift the curve down, but throttling will only have a small effect on temperature. Since ignition delay is a much stronger function of temperature, the autoignition event can therefore be maintained at lower loads with throttling (Figure A-11). Pumping work will increase, so throttling may be undesirable unless the intake temperature demand is not feasible. Reducing intake pressure will also have a significant negative effect on the SI flame propagation. The pumping work, intake temperature demands, and SI flammability limits combine to determine the low-load limit.

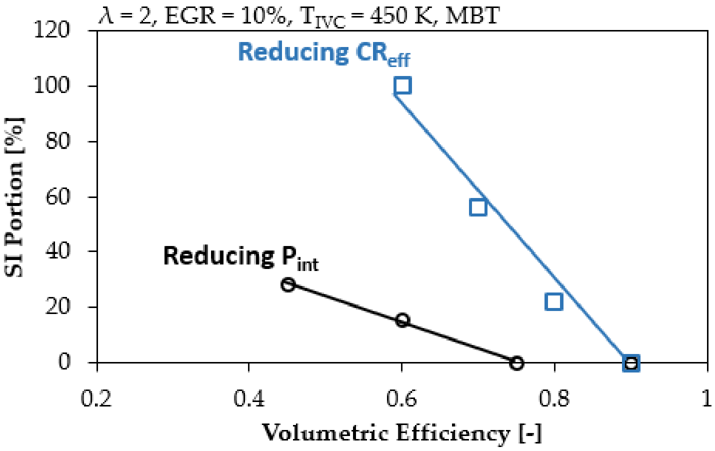

Figure A-11: Comparison between reducing in-cylinder mass via throttling or reducing CR_{eff} via LIVC. The higher sensitivity of autoignition to temperature rather than pressure yields greater controllability for throttling than CR_{eff}. The impact on pumping is studied in a later section.

The other controls factor is the relative sensitivity of ignition delay to pressure and temperature. A real-time model that can capture the NTC region of autoignition can guide the engine controller to adjust the actuators that produce the highest sensitivity. Additionally, market gasoline blends vary, so under certain operating conditions, a sensitivity to the precise fuel blend is anticipated.

The NO_x emissions of fuel-lean SACI at high load can be resolved by switching to stoichiometric operation. To study the effects of stoichiometric SACI, the model is also exercised at $\lambda = 1$. Figure A-12 depicts feasible SI portion as a function of T_{TDC} and VE. A greater SI portion is required at high loads to alleviate ringing. Unlike fuel-lean SACI, the VE only extends to 0.85 (with boosting), as a minimum of 25% EGR is specified to avoid knock. The T_{TDC} required to achieve a particular SI portion at a given VE is lower for stoichiometric SACI, owing to the higher fuel content in the charge. The ϕ' of the stoichiometric SACI is between 0.65 – 0.80, while the ϕ' for fuel-lean SACI never exceeds 0.50.

At high load, ringing intensity is the key limit. The data indicate that the peak VE within constraints is just below 0.9. Improving the high-load limit can be achieved by increasing the SI portion through lowering the end-gas temperature. To achieve 950 K at T_{TDC} at high loads with a relatively high 14:1 CR, T_{IVC} must be about 350 K. This T_{IVC} requires an intake temperature below 25 °C. Intake temperatures can be lowered by active cooling; however, a careful fuel injection strategy may achieve the same effect. This strategy is successfully implemented in [60], where charge cooling from late injection of fuel enabled knock mitigation. The overall λ is 0.87, so the aftertreatment will be unable to oxidize hydrocarbons and carbon monoxide.

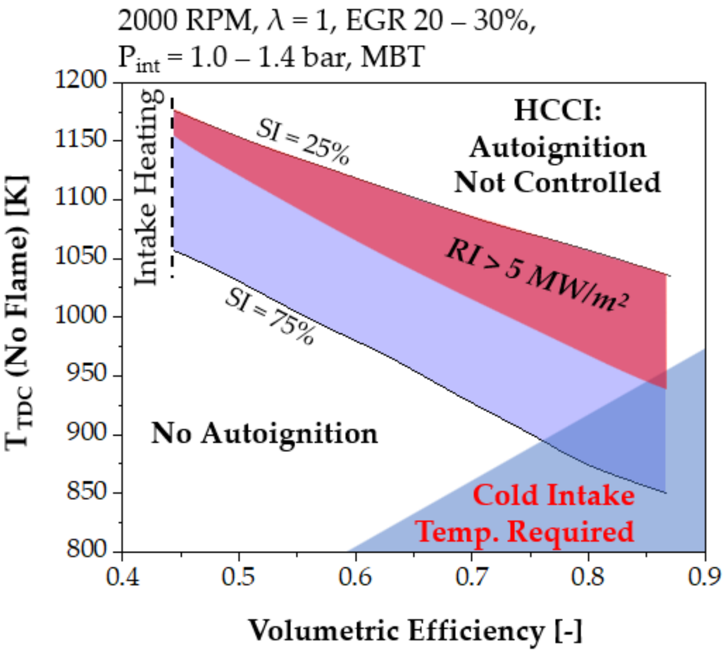

Figure A-12: Regions of feasible SACI combustion as a function of cylinder charge (VE) and state ignition energy (T_{TDC}). There is a relatively narrow range of operation, bound at low and high VE by intake temperature.

The impact of boosting is evaluated at a common VE for three conditions: 20% EGR at 1 bar intake pressure, 30% EGR also at 1 bar intake pressure, and 30% at 1.2 bar intake pressure. For these three cases, the VE is ~0.65, and the effective compression ratio is varied accordingly to offset the VE increase from boosting. Figure A-13 compares the SI portion of three strategies for increasing EGR at high loads. Increasing EGR by 10% while holding intake pressure constant requires a two-point higher CR_{eff} to maintain the same charge mass. The higher pressure and temperature from compression more than offset the effect on ignition delay from dilution. When boosted, the CR_{eff} must drop by two points to maintain VE. The reduced temperature and pressure at TDC lower the propensity to autoignite, and the SI portion increases. Overall, for a fixed CR_{eff}, increased EGR while simultaneously boosting to maintain VE (i.e., load) has a small impact on SI portion.

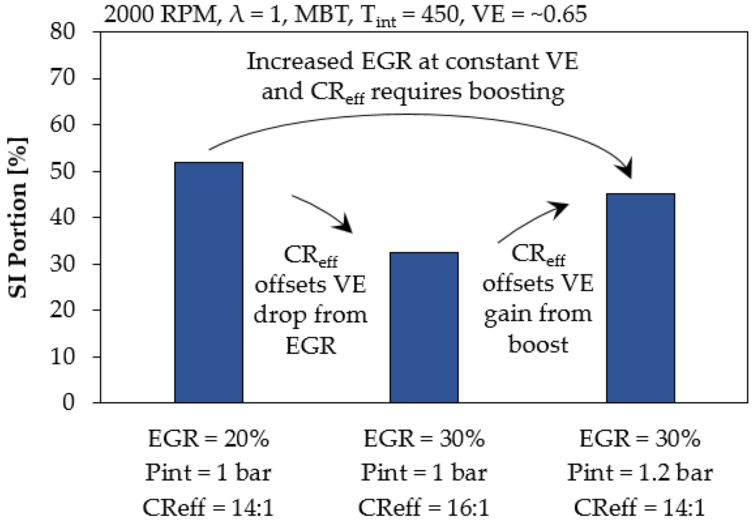

Figure A-13: Comparison between three points with the same VE and increasing EGR level. The effective compression ratio has the strongest impact and boosting while maintaining CR_{eff} has a small impact on SI portion.

While the low temperature requirement indicates potential for low-load performance, the stoichiometric constraint requires very high residual fractions. To achieve the same low loads as the lean-burn case, the required ϕ' is about 0.45, i.e., the charge is diluted with 55% residuals. Achieving SACI combustion at this load is possible, as indicated in [103], however, 45 °C intake temperatures and a high negative valve overlap (NVO) valve strategy are used to achieve the high T_{TDC}.

Engine Speed

Recognizing the sensitivity of autoignition to residence time, a sweep of engine speed is performed. A subset of the speed sweep is presented in Figure A-14 for two CR_{eff}. Both cases approach near-HCCI combustion at 1000 RPM. At low engine speeds, residence time increases which advances the timing of the autoignition event. The 14:1 CR_{eff} has a stronger relationship to engine speed than the higher CR. Though heat transfer increases at lower speeds, the data suggest that above 1000 RPM, time is the dominant factor.

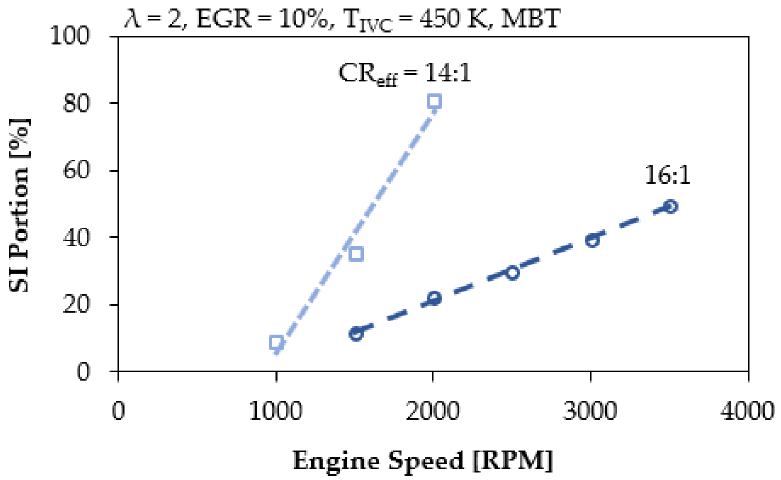

Figure A-14: Impact of engine speed on SI portion for two CR_{eff} at the same conditions. Near-HCCI combustion is reached near 1000 RPM. SI portion increases with engine speed as the time for autoignition decreases. The higher compression ratio is much less sensitive to engine speed.

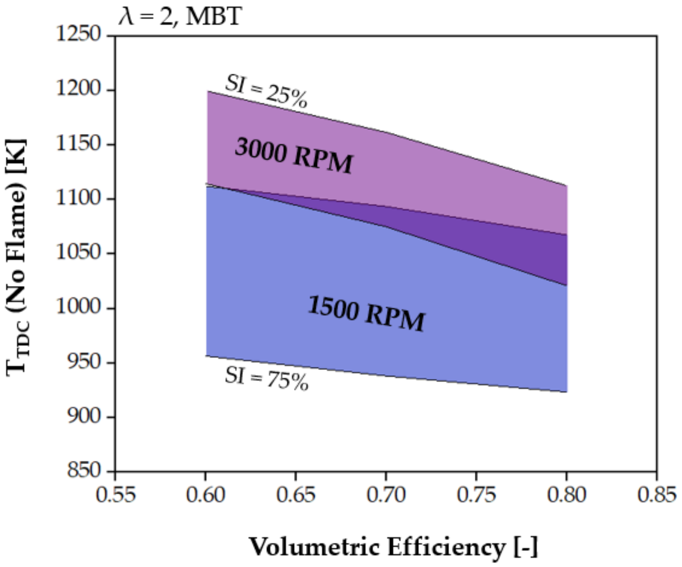

Figure A-15: SACI operating range for 1500 RPM and 3000 RPM. As engine speed increases, SACI operation narrows and is driven to higher T_{TDC}.

The range of feasible SACI combustion is evaluated for several speeds and conditions by examining the SI portion. Figure A-15 summarizes the general trend with a comparison of 1500 RPM to 3000 RPM. The SACI operating range narrows and shifts towards higher T_{TDC} as engine speed increases. Increased engine speed will also intensify the RI constraint challenge. RI is defined by a time-rate of change of pressure, and thus, at higher speeds, a certain pressure rise rate per crank angle yields a higher RI. These three factors combine to set the high-speed limit of SACI combustion. No clear low-speed limit is identified.

Induction Time Integral Models

A widely used physics-based autoignition model computes the integral of the inverse of ignition delay τ at each time step (35) [96]. The ignition delay can be modeled with a correlation or tabulated from measured or simulated values. Autoignition occurs when the integral reaches unity.

$$\int_{t_0}^{t} \frac{dt}{\tau} = 1.0 \tag{35}$$

The induction time integral is evaluated from intake valve closing (IVC) until a point late enough in the cycle to capture any potential autoignition events. Though each ignition delay models have a unique set of inputs, pressure and temperature are common to all models evaluated. The pressure and temperature are computed by considering the initial state, heat transfer, heat release from the flame, and a model for the ratio of specific heats. The Woschni heat transfer model is selected, a Wiebe function modeled SI heat release, and the function for gamma is linear with respect to temperature and composition. The Wiebe function parameters for the ignition delay model are identical to the candidate model.

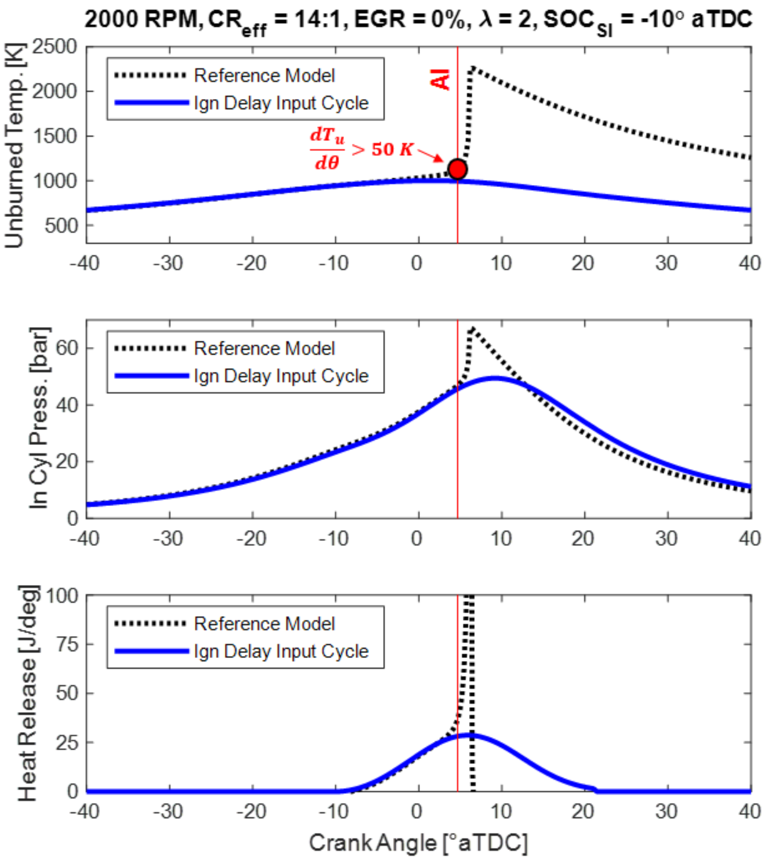

Figure A-16: Comparison between two-zone detailed reference model and the pressure and temperature computed as an input to candidate induction time models. Autoignition target is identified in each plot and is tuned to a rate of change of the unburned temperature greater than 50 K/deg.

A sample comparison between the generated pressure and temperature and the result from the reference model is presented in Figure A-16. The crank angle where the rate of change in unburned temperature exceeds 50 K/deg is noted. This point is computed for all test runs and serves as the reference autoignition phasing for the candidate models. There is good agreement up to just before autoignition occurs in the reference model. Figure A-17 depicts the unburned zone temperature and pressure at the onset of autoignition for all test points. These results include the impact of SI combustion and a roughly even distribution of burned gas fractions from 0 to 0.3.

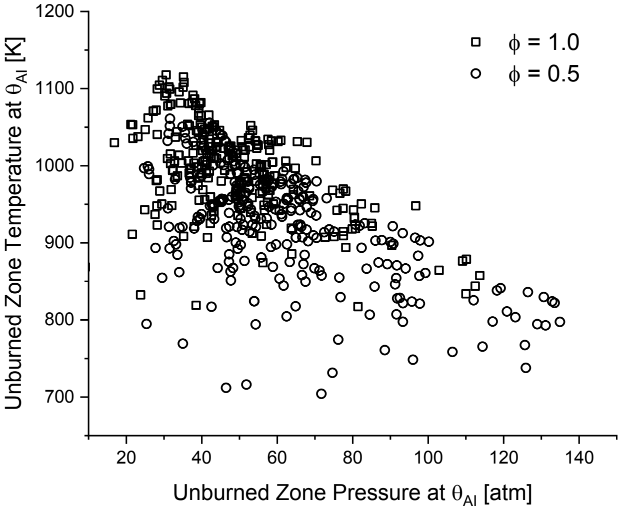

Figure A-17: Unburned zone temperature as a function of pressure at the onset of autoignition.

However, immediately prior to autoignition, the detailed chemical kinetics reference model predicts a slight heat release from cool flame reactions. This low-temperature heat release (LTHR) is not included in the specified in-cylinder temperature and pressure profile and will lead to error in the candidate models. Furthermore, the pressure and temperature must be generated sequentially at each time step as the current state depends on the previous state. This adds computational load. Any measure to reduce this computational expense may lead to an increase in model error. The autoignition phasing is identified in Figure A-16 and is consistent with the start of the autoignition process.

Ignition Delay Lookup Table

The first ignition delay model considers ignition delay results tabulated from a constant volume vessel simulation with the same mechanism and fuel as the reference model. For each of eight combinations of equivalence ratio and residual fraction, ~1000 datapoints are compiled across a range of 0.5–150 atm pressure and 550–1500 K temperature. The ignition delay is linearly interpolated between points to replicate a table used in a production engine controller.

A comparison of the ignition delay lookup model with the reference model is presented in Figure A-18. The best agreement occurs when the reference model predicts early autoignition phasing. However, a significant portion of the ignition delay lookup results under predict autoignition phasing.

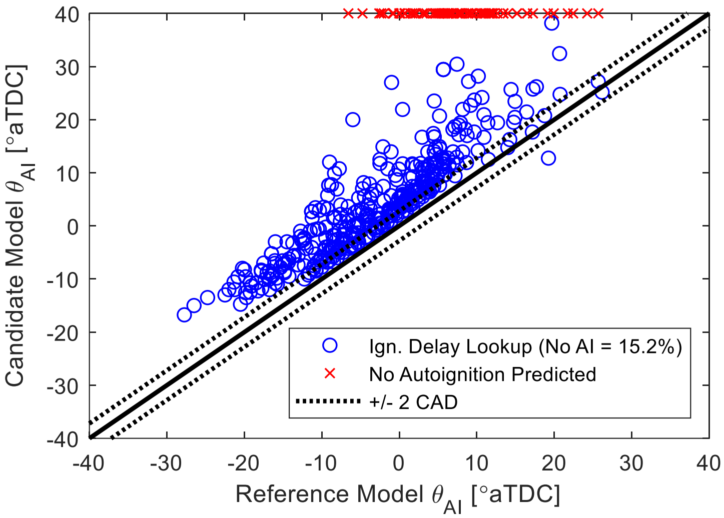

Figure A-18: Comparison between the ignition delay lookup model and the reference model. No corrections are applied to these results.

The error in the autoignition phasing is significant, and an in-depth analysis identified a fundamental gap in ignition-delay based models. The ignition delay at a particular temperature and pressure is computed using a constant volume combustion chamber model. The specified starting composition for all conditions is air, fuel, and EGR only. No partially oxidized products are included, as that is specific to the temperature and pressure history of the mixture. However, the reference model (as well as the engine), the ignition delay at a particular point is path dependent.

The composition can vary significantly throughout the cycle, and the early reactions increase temperature and pressure. This influence cannot be directly accounted for in the ignition delay models. Instead, this gap in the model is corrected by adjusting the ignition delay multiplier to minimize the root mean square error (RMSE).

Ignition Delay Correlations

Several ignition delay correlations are considered. The objective is to identify trends and potential challenges with this structure of autoignition model, rather than select the optimal model calibration. The previously described ignition delay lookup model represents the minimum error that an ignition delay correlation can achieve (unless a LTHR model is also included). Consequently, a representative sample of ignition delay correlations is selected and evaluated.

The most widely used correlation for autoignition is developed by Douaud and Eyzat [95] for SI knock, (36). It is a function of octane number (*ON*), pressure (*p*) in atm, and temperature (*T*) in Kelvin. For this model, the multiplier *M* is selected to be 1.2 to minimize RMSE. This widely used correlation is based on data from a cooperative fuels research (CFR) engine and rapid-compression machine (RCM) data for no EGR cases typical of SI knock. Typical end-gas temperatures and pressures are 1000–1200 K and 20–30 atm, respectively.

$$\tau = M \cdot 17.68 \left(\frac{ON}{100}\right)^{3.402} p^{-1.7} \exp\left(\frac{3800}{T}\right) \tag{36}$$

Recognizing the influence of composition, a correlation by He et al. [113] for isooctane is included, (37). In addition to pressure (atm) and temperature (K), equivalence ratio (ϕ) and the percent of fresh O_2 (χ_{O2}) in the charge. *R* is the universal gas constant (1.987 cal/K·mol). For this model, the multiplier *M* is selected to be 0.53 to minimize RMSE. This correlation is based on a wide range of test data, except for temperature. This model is validated and tuned to temperatures between 943 K and 1027 K, as these are typical conditions for HCCI autoignition. As will be shown later in this work, the narrow range of temperature data introduces significant error for temperature and pressures during compression.

$$\tau = M \cdot (1.3\ x\ 10^{-7}) p^{-1.7}\ \varphi^{-0.77} \chi_{O_2}^{-1.41} \exp\left(\frac{33700}{RT}\right) \tag{37}$$

A correlation for gasoline that is based on a kinetics mechanism [114] and includes the impact of low, intermediate, and high temperature heat release is also included, (38). The quantities in brackets are the concentrations of fuel, O_2, and total diluent (CO_2, H_2O, N_2, etc.) expressed in mol/m^3. Three ignition delays are combined as indicated in (39) [115]. The six coefficients (a_i to f_i) are fit to a kinetics mechanism and are unique for each ignition delay term. For this model, the multiplier *M* is selected to be 1.4 to minimize RMSE across all three ignition delay terms.

$$\tau_i = M \cdot a_i \left(\frac{ON}{100}\right)^{b_i} [\mathrm{Fuel}]^{c_i} [O_2]^{d_i} [\mathrm{Diluent}]^{e_i} \exp\left(\frac{f_i}{T}\right) \quad i = 1, 2, 3 \tag{38}$$

$$\frac{1}{\tau} = \frac{1}{\tau_1 + \tau_2} + \frac{1}{\tau_3} \tag{39}$$

In addition to the NTC region and composition, the correlation presented by Khaled et al. included the temperature and pressure rise from LTHR [116]. The modeling of the LTHR may aid in improving the error associated with ignition delay correlations in general. Equations (40) to (42) describe the computation for the overall ignition delay, τ, as a function of the first stage ignition delay, τ_1, and high temperature ignition delay τ_h. The exponential constants (n, m, and β) are specific to each ignition delay and fuel. The temperature and pressure changes from the cool flame are ΔT_{CF} and ΔP_{CF}. These are computed separately at each timestep. There is a notable absence of the influence of burned gas, as ϕ is the fuel-air equivalence ratio. This does not include the impact of EGR, though the charge-fuel equivalence ratio, $\phi' \approx \phi(1 - EGR)$ is used in place of ϕ .

$$\tau(T, P) = \tau_1 + \tau_h(T + \Delta T_{CF}, P + \Delta \mathrm{P_{CF}}) \left(1 - \frac{\tau_1(T, P)}{\tau_h(T, P)}\right) \tag{40}$$

$$\tau_1 = A_1 P^{n_1} T^{m_1} \phi^{\beta_1} \exp\left(\frac{B_1}{T}\right) \tag{41}$$

$$\tau_h = A_h P^{n_h} \phi^{\beta_h} \exp\left(\frac{B_h}{T}\right) \tag{42}$$

An examination of the ignition delay curves for a fixed pressure uncovers several interesting observations. Figure A-19 depicts the ignition delay curves for all three correlations and the ignition delay lookup table. Only the kinetics fit model and the Khaled et al. model capture the NTC region and the general trend well. The He et al. model matches at high temperatures, however, without the capability to capture the NTC region, the ignition delay is significantly overestimated below 850 K. To compensate for this, the multiplier is set to 0.53 to minimize error over the test points, which results in an underprediction of ignition delay above 950 K. The Douaud & Eyzat model is interesting in that it effectively averages ignition delay through the NTC region.

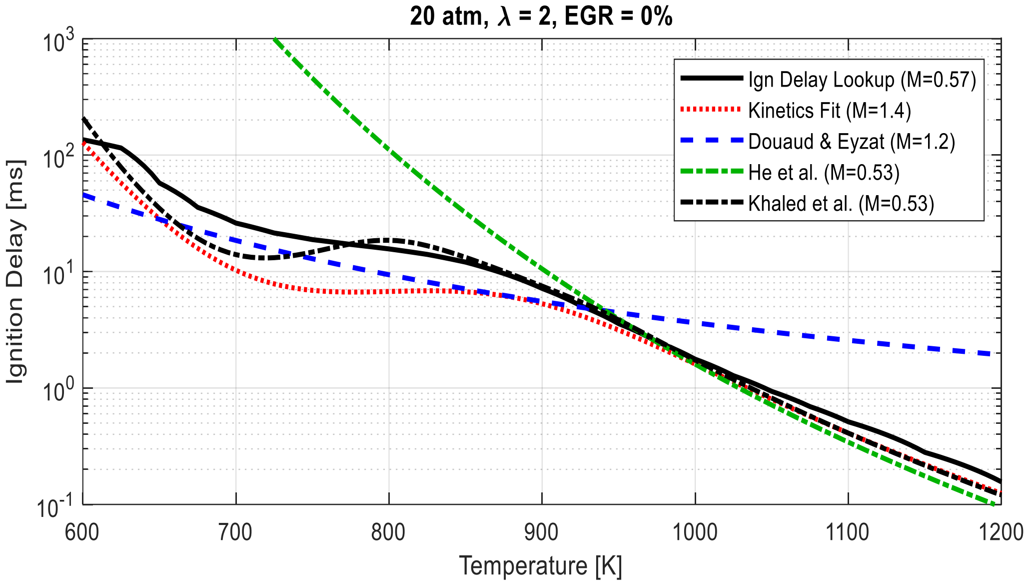

Figure A-19: Comparison of ignition delay among relevant models at a representative point. Each model has the final induction time multiplier M applied indicated in the figure legend.

Throughout the cycle, ignition delay among the candidate models varies both in magnitude and topography, Figure A-20. The induction time integral value begins to increase from -20° aTDC, where ignition delay begins to drop below 10 ms. As indicated in Figure A-20, the combined ignition delay error for all models is a minimum at just below 10 ms ignition delay. As in-cylinder conditions vary from this point, however, the character of each correlation becomes clear. The He et al. model has the simplest character as it does not account for the NTC region. The Douaud & Eyzat model also does not model the NTC, but it is relatively sensitive to pressure so as the heat release from SI heat release raises pressure after TDC, the ignition delay remains relatively low.

The varying character and magnitude will yield a wide array of results, and this is evident in the results compared to the reference model (Figure A-21). All models perform better as autoignition phasing (θ_{AI}) advances. However, there remains a relative insensitivity to combustion phasing relative to the reference model. Early AI phasing is underpredicted, and later AI phasing is overpredicted. Also indicated in Figure A-21, the percent of the total test runs which do not predict autoignition are listed in the legend. The He et al. model predicts no autoignition for 24% of all cases (autoignition occurred for all reference model cases). This can be linked to the significant under representation of ignition delay at low temperatures. The other two correlations have less than 1% of cases which did not predict AI.

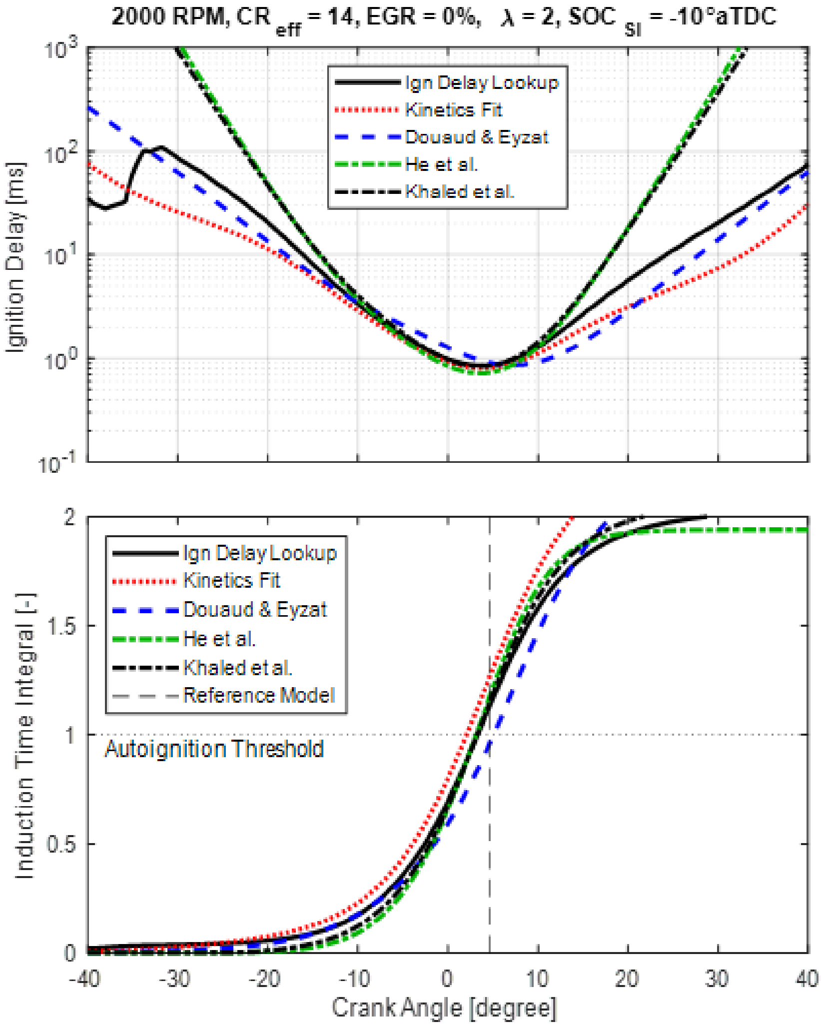

Figure A-20: Ignition delay (top) and induction time integral value (bottom) throughout the cycle. Each of the models has a slightly different ignition delay character which can impact the resulting induction time integral.

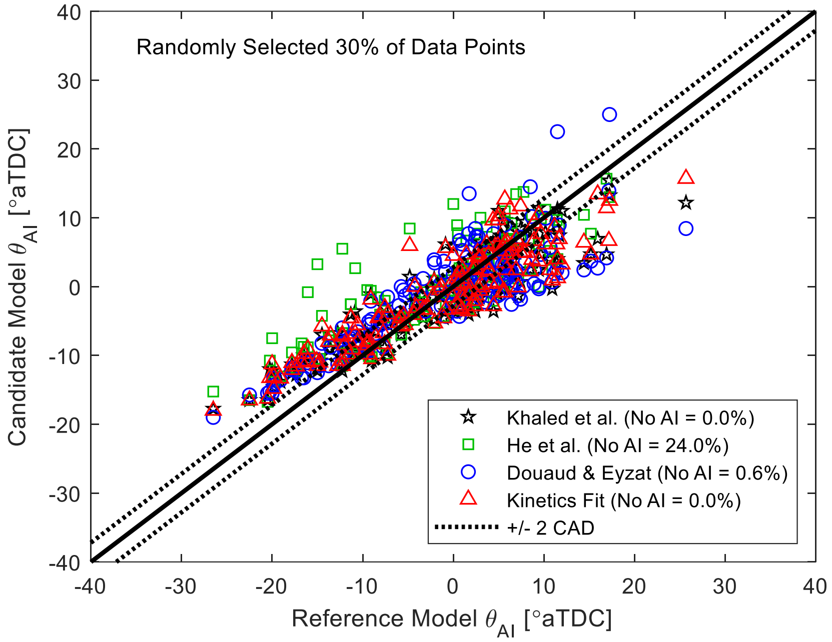

Figure A-21: Comparison of ignition delay correlation models. The ignition delay correlations demonstrated reduced sensitivity to AI phasing, and the He et al. model predicted 24% of cases would not autoignite (non-AI cases are not shown), despite all reference model cases producing autoignition.

The Khaled et al. model produces an increased temperature profile from low-temperature heat release, however, it is often significantly lower than the LTHR predicted by the reference model with full chemical kinetics (Figure A-22). This resulted in model performance that is consistent with the best-performing ignition delay correlations, but not significantly improved.

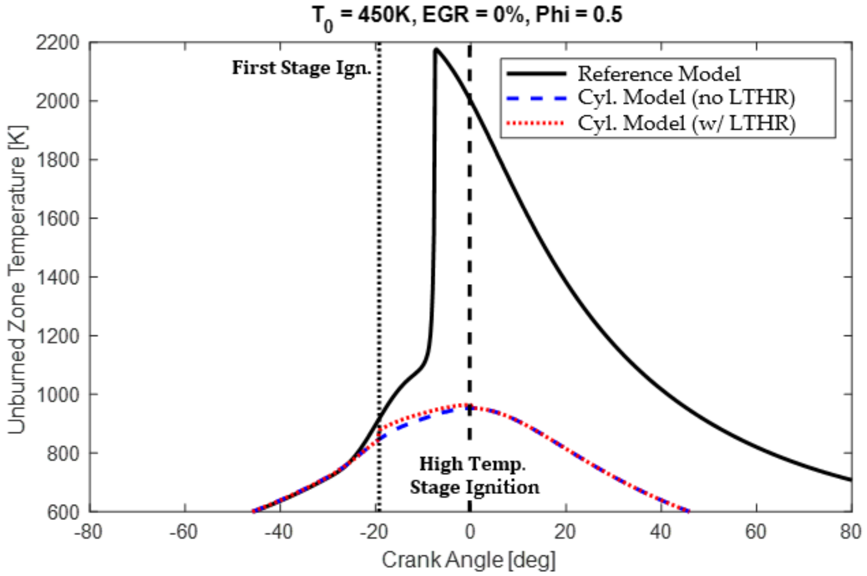

Figure A-22: Comparison of unburned gas temperature for the reference model (showing the autoignition event) and the cylinder model (with influence of SI heat release). The cylinder model also includes the modeled LTHR and the two ignition points of the Khaled et al. model for this operating point.

Regression Models

Several challenges associated with modeling the engine cycle after IVC are eliminated by selecting a regression model. Choi et al. noted that an empirically-based model does not produce a suitably low error over the range of conditions for HCCI, and subsequently elected to apply an ANN to ignition delay prediction [117]. In this work, three linear regression fits are considered in addition to an artificial neural network. All strategies have the same input dataset: 520 runs that covered a wide range of SACI operation. The output of these models is the AI phasing, while the inputs are control parameters or closely related to control parameters. More specifically, the inputs are engine speed, p_{IVC}, burned gas fraction, T_{IVC}, equivalence ratio, effective compression ratio, and the start of combustion (CA01%) for the SI phase.

Table A-3: Input parameters and ranges for linear regressions and ANN.

Input Parameter	**Range for Regression Fit**
Engine Speed	1000 – 3500 RPM
Equivalence Ratio	0.5 – 1.0
Burned Gas Fraction	0 – 40%
T_{IVC}	350 – 500 K
P_{IVC}	0.5 – 1.4 atm
Effective CR	10:1 – 18:1
SI SOC (CA01%)	-40 – 10 °aTDC

The linear regressions are performed using the MATLAB function *lsqnonlin,* where the objective function to minimize is the squared error of autoignition phasing. The input range is indicated in Table A-3. To test the predictive capability of the model and prevent overfitting, the regressions are fit to a randomly selected 70% of the observations. Though a *p*-value analysis of each coefficient tends to push the model towards a linear fit, all coefficients are included for the quadratic and cubic regressions to identify the potential error reduction and computational expense. All linear model coefficients are statistically significant with a *p*-value of 0.05 or lower.

The ANN is configured to train on the same 70% of the data used to fit the linear regression. The remaining 30% is split evenly between the test and validation datasets. A sweep of training data size indicates a relative intensity of the training dataset portion between 40–80% of the input data. The Levenberg-Marquart backpropagation algorithm is selected as computation speed and memory usage during training is inconsequential. Mean-squared error is selected as the optimization function to significantly penalize large errors in autoignition phasing. A higher error weight for autoignition phasing at MBT and later is evaluated to bias the model accuracy towards typical combustion phasing. However, this does not significantly improve the performance of the model, and therefore the error waiting is reconfigured to a uniform weighting. To prevent overfitting, the number of hidden layers neurons is swept to determine the appropriate model size. Ten (10) hidden neurons in one hidden layer are chosen as the test error stabilized at this point. A further increase in the number of hidden layers or the number of hidden neurons does not improve model accuracy and increases overfitting.

The ANN model demonstrates the best accuracy for any model (Figure A-23). The linear, quadratic, and cubic regression are similar to each other, the error is slightly higher than the ANN. This is consistent with several other sources which found that the performance difference between linear regressions and ANNs are relatively small [55,118,119]. All regression models have superior performance than any ignition delay model (compare to Figure A-21). All cases for all regression models predict autoignition, the sensitivity with autoignition phasing is strong, and late combustion phasing accuracy is significantly improved. The relatively high accuracy associated with the linear-fit regression model suggests that SACI occurs over a relatively narrow range of operation points that a linear model reasonably captures the response.

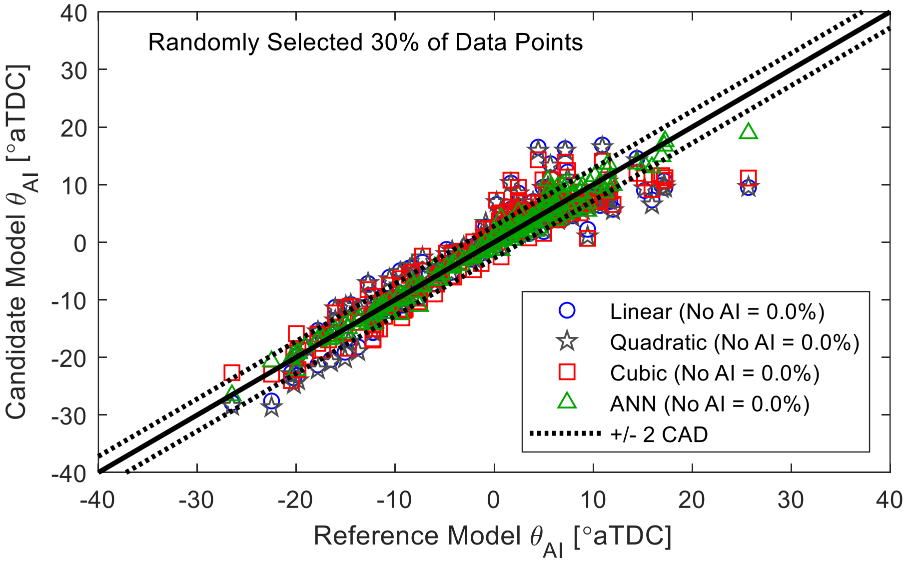

Figure A-23: Comparison of regression models to the reference case. All cases for all regression models predicted autoignition, the sensitivity with autoignition phasing is strong, and late combustion phasing accuracy is significantly improved compared to all ignition delay models.

Comparison of All Models

Examining all models together identifies some key trends. All models and types of models are better at predicting early autoignition than later ignition timing. Early autoignition timing occurs when compression from SI heat release and the piston are phased together and pressure and temperature both increase significantly. Later SI phasing are more troublesome for two reasons. First, the downward moving piston and SI flame propagation have roughly equal and opposite effects. As the in-cylinder temperature and pressure steady, if there is an error in the ignition delay at or around this condition, the predictively capability is diminished. The other potential challenge is the transition from SACI to SI at later combustion phasing. If the added heat from the flame, if it occurs late enough, the total pressure and temperature history is not sufficient for AI to occur. This condition is exemplified in Figure A-24. All models suffered in accurately predicting autoignition time at this sharp transition point. It is important to note, however, that this effect only becomes significant when the start of autoignition occurs after about 10° aTDC. The CA50 of the autoignition phase would be sufficiently late for this high-error region to be insignificant for MBT operation. Later combustion phasing to avoid knock, however, may enter this high-error region.

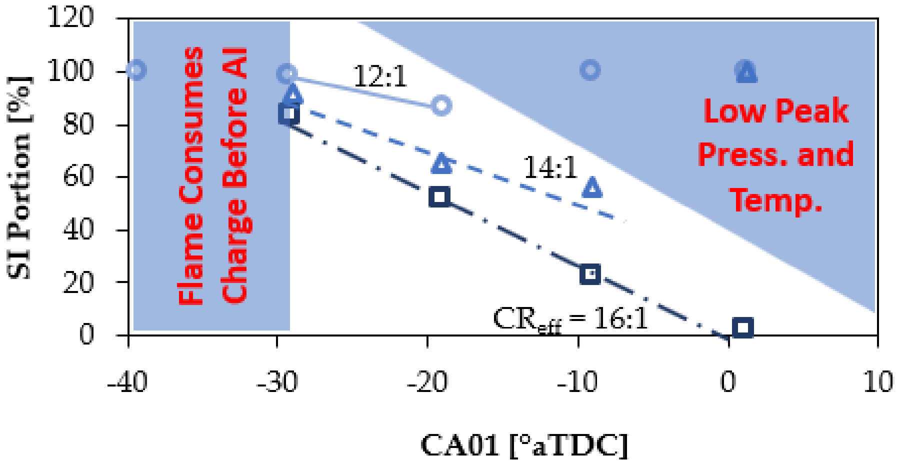

Figure A-24: The transition points from SACI combustion to non-SACI combustion (i.e., no autoignition). The shaded regions indicate no autoignition and towards later combustion phasing, the transition is relatively sharp.

Table A-4: Root mean square error (RMSE) and execution time for each candidate model. The accuracy of the regression models outperformed the physics-based models, and the computational expense is similar or better.

Model	**RMSE [CAD]**	**Mean Error [CAD]**	**Minimum Error [CAD]**	**Maximum Error [CAD]**	**No AI Predicted**	**Estimated Execution [s]**
ANN	1.3	-0.1	-6.7	5.6	0.0%	1.45 x 10^{-6}
Cubic Fit	3.4	0.1	-15.5	9.9	0.0%	3.64 x 10^{-6}
Quadratic Fit	3.8	0.0	-16.5	11.4	0.0%	6.95 x 10^{-7}
Linear Fit	3.8	0.0	-16.4	12.0	0.0%	1.69 x 10^{-8}
Lookup (ID)	5.0	0.1	-18.3	16.0	1.7%	4.13 x 10^{-5}
Kinetics Fit (ID)	4.9	0.0	-21.0	11.5	0.0%	3.76 x 10^{-6}
Douaud & Eyzat (ID)	5.5	-0.1	-25.5	21.0	0.6%	3.72 x 10^{-6}
He et al. (ID)	5.6	1.5	-19.5	18.8	24%	3.73 x 10^{-6}
Khaled et al. (ID)	4.9	-0.4	-23.8	22.3	0.0%	3.97 x 10^{-6}

Note: The pressure and temperature computation used as the input for ignition delay models had an estimated time of 3.02 x 10^{-6} s.

Table A-4 and Figure A-25 present the RMSE and execution time for the eight candidate models. The ANN is the most accurate and the only model with an RMSE below 2 CAD. Also included in Figure A-25 are typical standard deviations of CA05 (σ_{CA05}) for HCCI and conventional

SI for context. The RMSE of AI models and σ_{CA05} are not directly comparable as σ_{CA05} is representative of a particular operating point, while the RMSE of an autoignition model is a statistical assessment of the mean error over the 520 data points. Nonetheless, this comparison illustrates that the regression models' accuracy is similar to or better than the typical variation of the SI combustion process, and the ANN is roughly as accurate as the cycle-to-cycle variation of HCCI.

The linear regression has the lowest computational expense with an execution time of 10^{-8} seconds. No attempt is made to optimize performance of any model as this would result in a loss of accuracy, and the selection of the optimal balance between speed and accuracy for a particular model is outside the scope of this work. All the ignition delay correlations have similar execution times. Considering their simplicity, the relatively long execution time requires some elaboration. These models require a computation of the pressure and temperature throughout the cycle, and the non-linear dependent relationship of pressure, heat release, heat transfer, and temperature must be computed crank angle by crank angle. The computational expense of this step alone is 3×10^{-6} seconds, setting the lower bound of any ignition delay correlation. If this step is somehow eliminated, the resulting execution time estimate is $7–10 \times 10^{-7}$ seconds, about equal to the quadratic fit linear regression. The ignition delay lookup model, though relatively accurate, is also the most resource intensive as frequent table look-ups and interpolations are required. The linear regression is the fastest as it did not rely on resource intensive operations such as exponential functions or non-linear relationships.

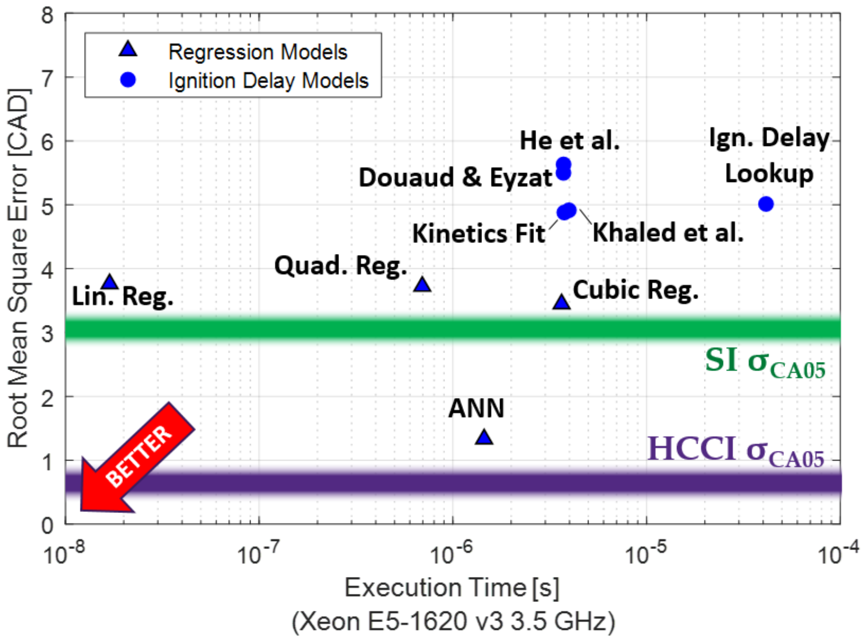

Figure A-25: Comparison of accuracy and execution time for the eight candidate models. standard deviation of CA05 (σ_{CA05}) for both HCCI and SI combustion are included for comparison.

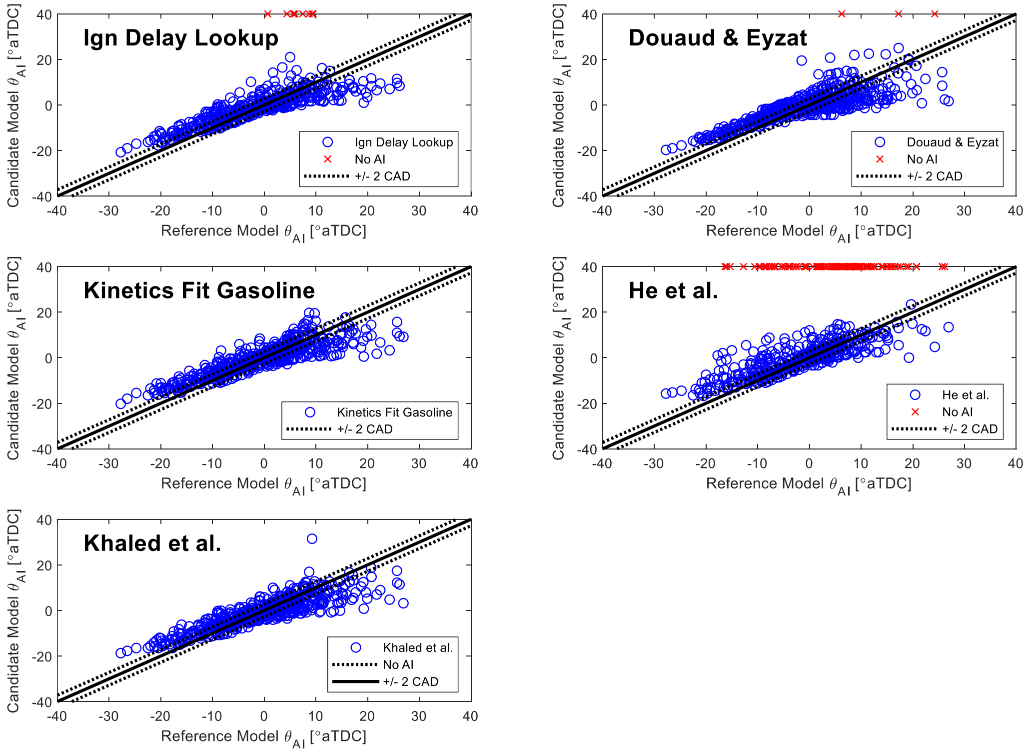

Figure A-26: Performance of each ignition delay model compared to the reference model.

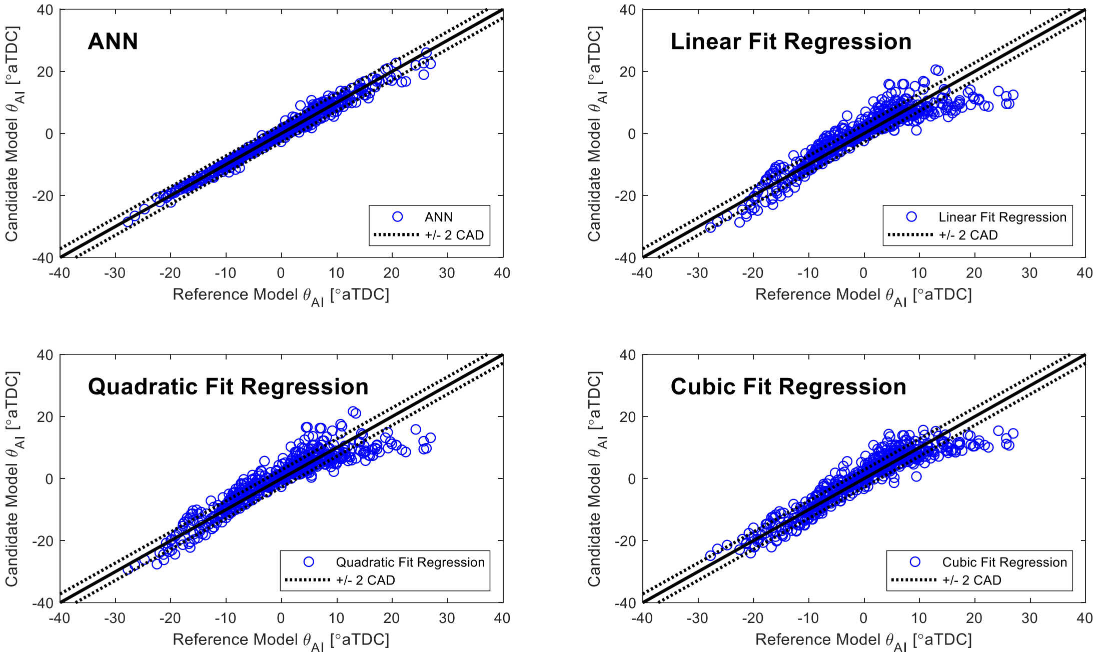

Figure A-27: Performance of each regression model compared to the reference model.

Reduced Chemical Kinetics Mechanisms

Three reduced chemical kinetics mechanisms are compared to aid in illustrating the modeling challenge. The detailed mechanism is the reference model and the sole difference in this comparison is the mechanism. If the reduced mechanism did not include components of the base four-component gasoline surrogate, then the fuel is also modified accordingly (see Figure A-28). Each of these mechanisms are, of course, physics based. However, as the model complexity decreases, the ability to capture the highly complex physics diminishes. Consequently, the root mean square error (RMSE) increases. The simplest mechanism, a 33-species PRF mechanism [120], approaches the same error as much simpler physics-based models and exceeds the error of all regression models. Other mechanisms included are a 165 species model [97] and an 80 species

PRF-E mechanism [121]. The execution time of these models is several orders of magnitude slower than the regression and simplified physics-based models.

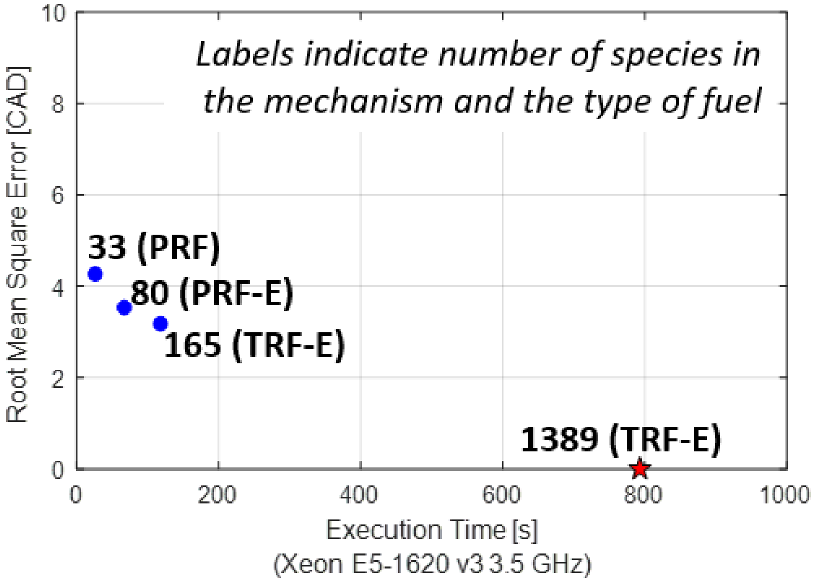

Figure A-28: Comparison of accuracy and execution time for the reduced kinetics models. Execution time is measured in real time using Chemkin solver on an Intel Xeon E5-1620 v3. The reference model (1389 species) has an error of zero by definition.

To recover accuracy, either complexity must be reintroduced, or non-physics-based corrections must be applied. If a significant quantity of model corrections is applied, the value of the physics-based model is lost. The progressively increasing error as execution time decreases illustrates the modeling challenge for physics-based models. Regression-based models resolve this challenge, however their performance in untested regions has higher risk than a physics-based model.

Sensitivity of the Regression Model Structure to Engine Phenomenon

While the ignition delay models are structured to match the underlying physics and chemistry, the regression models identify the best fit to the data. Through previously described regularization techniques should maintain generalizability beyond the test points, a critical assessment may cast doubt on the trends presented in this work.

To enhance the confidence in the findings of this work, an investigation of the fit and predictive capability of the regression models for engine data is performed. Though a SACI dataset may provide unique insight, the potentially confounding influence of cycle-by-cycle variability of flame propagation can potentially mask autoignition model performance. As this work focuses on autoignition, the experimental analysis will examine autoignition-dominant combustion. Therefore, an HCCI engine is selected as the next step in model evaluation. Furthermore, HCCI is a bounding condition for SACI, and the boundary where accurate autoignition phasing prediction is most critical. The objective of this experimental evaluation is to identify the relative importance of engine phenomenon not included in the analysis on the selection of model structure. It is not intended to be a validation of a particular model calibration.

The same process and parameters for the regression models is performed as previously described, though each model is refit to HCCI data. Despite an attempt to achieve a broad range of experimental points the hardware and combustion strategy constraints limits the range of points within misfire and noise limits. Of the seven degrees of freedom of the SACI model, two are eliminated for HCCI. The cams and geometric compression ratio are fixed, so the effective compression ratio is constant. There is also no SI flame, so the SOC of SI is irrelevant. While the influence of CR_{eff} and SOC are significant for SACI, the impact of engine phenomenon such as thermal and fuel stratification on model selection can still be evaluated. Of the remaining five degrees of freedom, HCCI combustion cannot operate over a wide range of combustion phasing and compositions. Thus, there is a limited range of T_{IVC}, ϕ, residual fraction, and engine speed that are experimentally feasible. Intake pressure varied only slightly around ambient pressure. Nonetheless, a total of 161 data points is selected for this evaluation. The HCCI engine parameters are listed in Table A-5. The internal residual fraction is determined from the state estimation method outlined by Ortiz-Soto et al., and subsequently used to determine the total trapped mass at intake valve closing [122]. The ideal gas law is used with the measured in-cylinder pressure, cylinder volume, and trapped mass to determine the temperature at IVC.

Table A-5: HCCI engine parameters for regression model evaluation.

	HCCI Engine
Bore x Stroke [mm]	86 x 94.5
Compression Ratio	12.5:1
Valvetrain	Exhaust Rebreathe
Engine Speed	1200 – 2000 RPM
Relative AFR (λ)	1.37 – 1.58
Intake Pressure	1.03 – 1.06 atm
Intake Temperature	65 – 95 °C (Intake Heating Required)
Temperature at IVC	475 – 525 K
Burned Gas Fraction	30 – 35%

The resulting comparison can be found in Figure A-29. As the HCCI datapoints are limited in range, the resulting RMSE has improved relative to the SACI dataset. This suggests that variations in charge stratification, thermal stratification, etc. may be relatively insignificant relative to autoignition phasing prediction. The trend among the models remains the same. The regression models increase in accuracy as model complexity increases. This comparison illustrates that for these two independent applications, the ANN demonstrates the lowest error, and all polynomial regressions have similar error that is only slightly worse than the ANN.

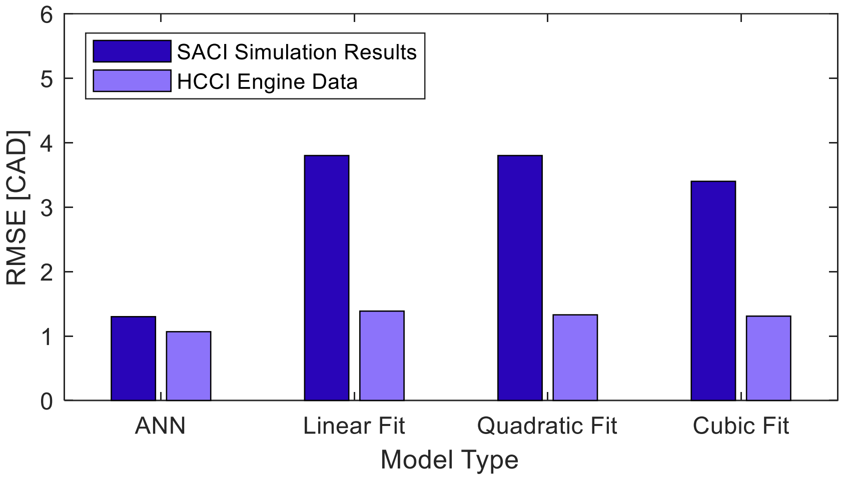

Figure A-29: Comparison among regression models for SACI simulation results and HCCI engine data. The trends are consistent with the model performance for SACI simulation results. The overall reduction in RMSE for the HCCI engine data cases provide confidence that engine phenomenon such as stratification may not confound the regression model approach.

B. VEHICLE SIMULATION AND MODE SWITCHING

Though there are potential efficiency benefits, SACI combustion magnifies the control complexity of conventional engines. The charge composition requirements for the SI and AI combustion phases are different and often competing. These competing constraints lead to a potentially narrow operating range and charge preparation challenges. Consequently, additional actuators are required, the degrees of freedom are expanded, and the engine may need to transition between different combustion modes. Hybrid LTC strategies has been shown to have a uniquely synergistic impact on improving efficiency beyond either hybridization or advanced combustion modes alone, though this has not been established for SACI specifically [123].

There are several hybrid electric vehicle (HEV) architectures. For this work, only a P0 hybrid and a P2 hybrid are considered. For a P0 hybrid, the electric machine is coupled to the engine through the accessory belt. A P2 hybrid is connected to the transmission input shaft. In the case of the P2 hybrid, a clutch between the engine and the transmission enables the vehicle propulsion by the electric motor only without any parasitic losses from spinning the engine. Electric-only drive is not possible in a P0 configuration as the torque output is limited by the belt drive. Since a SACI engine is likely to be more expensive than a conventional engine, low-cost hybrid architectures are selected. The P0 configuration is the lowest cost architecture, and a P2 hybrid configuration is the lowest cost architecture that enables engine de-clutching.

Recognizing the transient challenges with advanced combustion modes, the first part of this work evaluates a tip-in on a 1D engine model. This engine model is exercised to evaluate the impact of transport delays and finite actuator movement rates on transient torque output and mode switching. The findings from the 1D simulation add the necessary context for the next part of the work, a vehicle simulation. Two HEV configurations and a non-HEV configuration are simulated over four drive cycles. A control strategy to minimize the mode switching for the SACI engine is introduced and the results compared among the SI engine and the SACI engine without the mode-switch minimization strategy.

Vehicle Model

The vehicle model is configured to run over a prescribed drive cycle and switch between several hybrid modes as appropriate. The vehicle and engine parameters are listed in Table B-1. Vehicle parameters are held constant for simplicity, as automakers invest in light-weighting, aerodynamic improvements, and rolling resistance reduction to different degrees.

Table B-1: Vehicle Configurations.

	Conventional Vehicle	**P0 Hybrid Vehicle**	**P2 Hybrid Vehicle**
Configuration	Front-engine, front-wheel drive		
Total Vehicle Mass	1200 kg		
Vehicle Aerodynamics	3.5 m^2 Area / $C_d = 0.32$		
Rolling Resistance Coefficient	0.01		
Battery Size	–	0.55 kWh	1.1 kWh
Electric Machine Power	–	5 kW	10 kW

The control strategy for managing the hybrid vehicle is rule-based and summarized in Table B-2. A charge sustaining strategy is implemented in the battery management system (BMS). Therefore, a balance of electric assist and electric absorption is required for each HEV configuration. Regenerative braking is the desirable means of generating electricity, however, the BMS can direct the electric machine (EM) to absorb torque from the engine based on the current and desired state of charge (SOC). EM output occurs under two conditions. Electric-only drive is available for the P2 HEV configuration only, as electric-only operation is not possible for the P0 HEV. Both HEV configurations have EM-assist available, where the electric machine adds additional torque beyond the output of the engine. This mode is limited to when the SOC is above 50% to prevent the use of this mode from depleting the battery only to then require recharging.

Table B-2: HEV control strategy.

Condition	**Description**	**Engine Torque**	**Electric Motor**
If $T_{demand} < 0$	Braking event: Regen	Fuel Cut	T_{demand}
If $T_{demand} > 0$ *and* $T_{demand} < T_{max,EM}$	Electric only drive possible (P2 HEV case only)	Fuel Cut	T_{demand}
$T_{max,Eng} < T_{demand} < T_{max,Eng}$	Charge sustain, charging power determined by BMS	$T_{demand} - T_{charge}$	T_{charge}
$T_{demand} > T_{max,Eng} - T_{max,EM}$ *and* $SOC > 50\%$	High torque demand with excess electrical energy available	$T_{demand} - T_{max,EM}$	$T_{max,EM}$

The SACI engine comprises three different modes of operation. SI at low loads, high loads, and engine speeds above 2500 RPM. SACI combustion is split between two regions. At low to medium loads below 2500 RPM, SACI is operated lean ($\phi = 0.5$), at medium to high loads below 2500 RPM, stoichiometric SACI is used as NO_x production is likely above regulatory thresholds. Lean-NO_x aftertreatment is not considered, therefore the engine-out NO_x must be minimized when running lean. The conventional engine data is computed with an experimental dataset (Figure II-7). The SACI combustion model is determined through extensive kinetics simulations and a review of autoignition burn duration models [124]. The high compression ratio is required to obtain sufficient ignition energy, and is consistent with a production SACI engine [60]. Operating in SI mode at high loads with this high of a compression ratio is challenging. Extensive use of Millerization via late intake valve closing is required, consistent with similar high compression ratio gasoline engines [42]. A kinetics-fit knock model is leveraged to ascertain knock propensity. Across the entire operating range, the Multi-Mode SI-SACI engine shows about a 5% improvement, with the lean SACI region having the highest improvement at 9% improvement relative to the SI engine. The high compression ratio and low brake mean effective pressure (BMEP) keeps exhaust temperatures just below the threshold for component protection enrichment at high power. Despite the late combustion phasing, the SACI engine has lower BSFC at peak power compared to the conventional engine. The configurations for both models are illustrated in Figure II-3 and Figure II-8. The boost device and intake, exhaust, and EGR pathways for both models are explicitly modeled to capture the relevant transient dynamics.

Mode Switching During Tip-In

The challenge of a multi-mode SACI engine is the requirement to switch operating modes. Unlike the vehicle model, the engine model considers the detailed control of the engine actuators. The actuators have realistic movement constraints and must respond accordingly to transport delays. The combustion model for both is a Wiebe function, and both boost devices are explicitly modeled. The supercharger is clutched by setting the pulley ratio to 0.001 and opening a supercharge bypass valve.

The evaluation of an electrified SACI powertrain is performed via a tip-in from 20 Nm to 200 Nm at 2000 RPM over about 2 seconds. The speed of this transient is carefully selected to maximize the control challenge. This tip-in is slow enough to require a progression through all modes of operation, but fast enough for actuator movement constraints and transport delays to be significant. A faster tip-in can exclude all SACI operation, and the control burden is lessened if the tip-in is slowed. Figure B-1 illustrates the progression of target states throughout the tip-in. There are several step-changes in actuator output, e.g., equivalence ratio, external EGR (eEGR), and cam phaser position. These represent the target actuator position and finite actuator movement rates must be accounted for. Even for actuators that can respond near instantaneously, there can be a significant control challenge as well. Consider the shift in equivalence ratio from one cycle to the next. A change in equivalence ratio from 0.5 to 1.0 will roughly double the torque output, which is not acceptable. The model must be adjusted to account for each of these constraints.

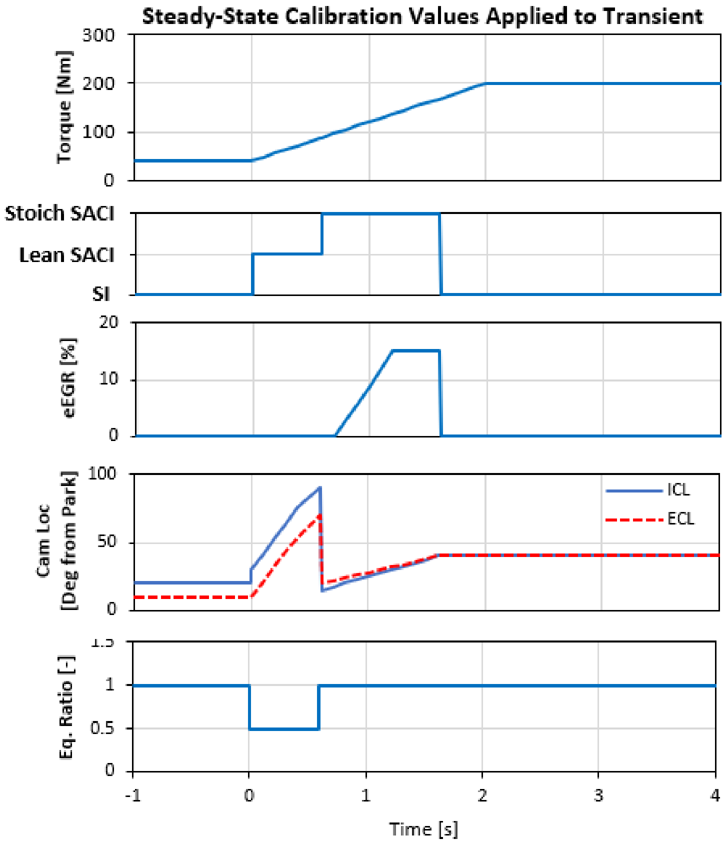

Figure B-1: SACI actuator set points during transient maneuver. These values represent the stead-state targets and do not account for finite actuator speed or transport delays. The engine controller and supervisory vehicle controller will have to adapt to these dramatic differences in in-cylinder state.

Feasible actuator speeds are achieved by either explicitly limiting the rate of change in the controller, or by filtering the target signal to eliminate rapid changes in actuator position. Figure B-2 illustrates the impact of the actuator constraints. For the EGR valve, an imposed limit of 200 deg/s slows the drop in EGR at the 1.4 second mark as the engine transitions to high-load SI operation. Also shown in Figure B-2 is the target and actual intake cam phaser position expressed as degrees from the parked position. The actual intake cam phaser location is achieved by filtering the target rate to produce a reasonable phase rate. The exhaust cam phaser (not shown) has a similar response. The peak phase rate of the filtered command is 95 crank degrees per second.

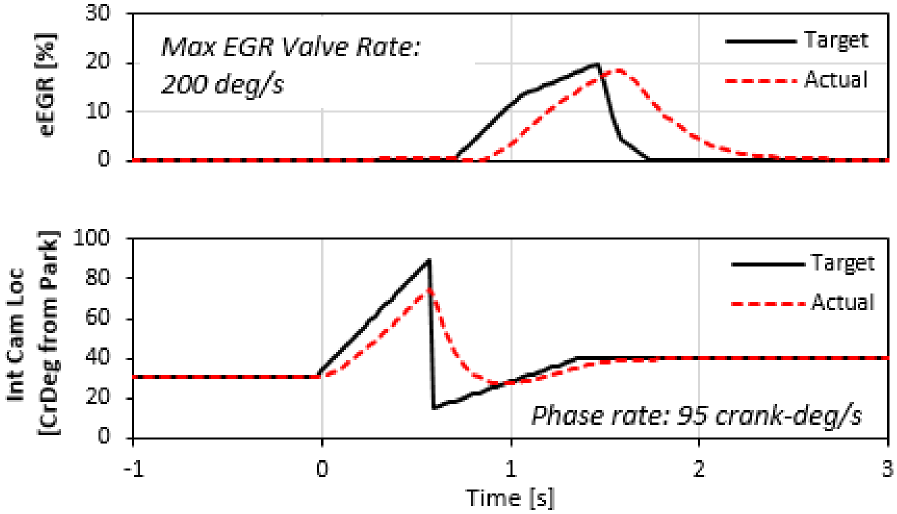

Figure B-2: Illustration of modification to steady-state control strategy to achieve feasible combustion.

Actuator movement constraints and transport delays combine to prevent the target combustion mode from being feasible. When transitioning from lean SACI to stoichiometric SACI, for example, the in-cylinder state must change drastically. Low EGR dilution is ideal for lean SACI as the air dilution is sufficient and flame propagation would suffer with increased EGR levels. The opposite is true of stoichiometric SACI, where relatively high amounts of EGR dilution is needed to slow autoignition reaction rates and reduce load. The dramatic change in in-cylinder composition requires several cycles to complete. During this time, the very lean (ϕ = 0.5) operation is no longer feasible as dilution levels increase. Increasing the equivalence ratio is required, however, at higher loads the NO_x produced by the flame may exceed regulatory limits. Thus, a step change to stoichiometric operation is required, however, for a short time, there is still insufficient EGR for stoichiometric SACI within noise constraints. Therefore, SI combustion is selected until conditions are feasible for SACI. As previously mentioned, the torque output when transitioning from lean to stoichiometric can be substantial. SI enables late combustion phasing to keep the change engine load appropriate. Late combustion phasing also permits controlled torque increase as the target load increases. When the high dilution levels required for SACI are achieved, stoichiometric SACI is viable and this mode is engaged. As load increases, the high dilution reduces volumetric efficiency which prevent the engine output from reaching the target torque. Consequently, the EGR valve is closed and high-load SI mode is selected. However, SACI operation must be held until the EGR levels drop sufficiently for late combustion phasing of the high-load SI to be feasible. Figure B-3 illustrates this process.

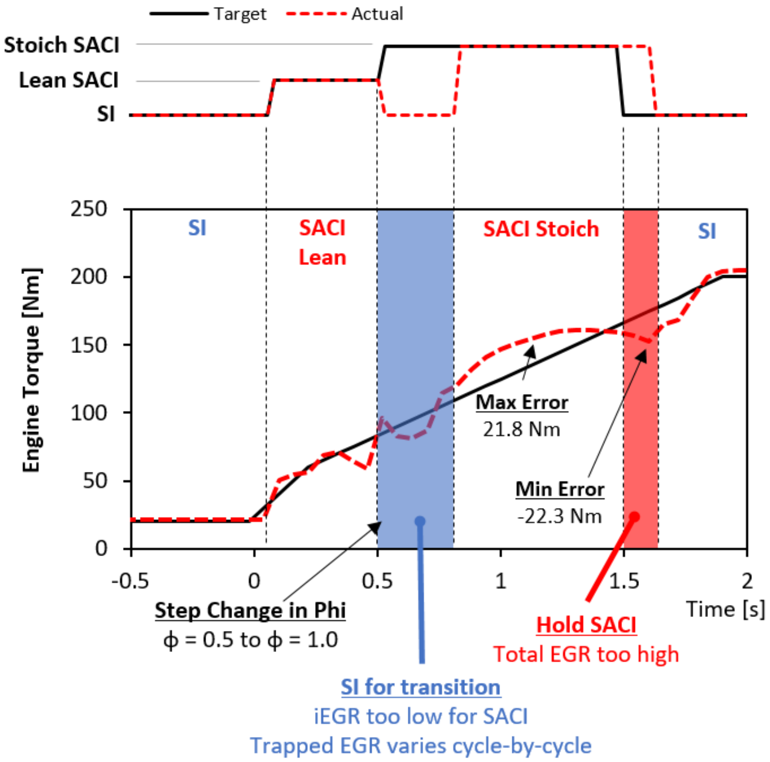

Figure B-3: Detailed examination of SACI tip in. Each combustion mode is encountered, including SI mode during the lean to stoichiometric SACI transition. The largest error from target is about 23 Nm, which is less than 5 kW at 2000 RPM. A 5 kW electric machine therefore has the capability to smooth the torque fluctuations.

Engine transitions between modes and variations in cylinder composition within a particular mode generate substantial torque fluctuations. These fluctuations are an excellent opportunity for a P0 or P2 hybrid powertrain to work synergistically with a SACI powertrain to smooth the torque fluctuations. As indicated in Figure B-3, the maximum torque fluctuations are within 23 Nm, which equates to 5 kW at 2000 RPM. A 5 kW electric machine therefore has the capability to absorb or augment engine torque and minimize the torque error.

The result of the tip-in for both engines can be seen in Figure B-4. Two SACI variations are compared to a conventional turbocharged SI engine. One SACI variation is the multi-mode transient previously described. A 5 kW electric machine (EM) to eliminate the torque variations during the transient as included in this result. The other SACI variation uses only SI combustion to illustrate the maximum transient performance. This variation demonstrated a significant improvement in transient performance compared to the conventional engine. The elimination of turbocharger lag by using a supercharger reduces the time to 90% torque (180 Nm) by almost a full second. The SACI with both combustion modes and a 5 kW electric machine had similar performance to the conventional SI engine, though the initial torque increase is relatively slow. A larger EM may further reduce the controls burden for mode-switching. The 10 kW EM used for the P2 HEV, for example, enables 50 Nm of torque authority. In this case, the need to switch to transitional modes may be eliminated entirely while still maintaining the same brake torque output. The EM can supplement engine torque for a short time to achieve a torque target. This strategy can eliminate the mode transition entirely if the torque demand remains just above the peak torque of that particular combustion mode. Otherwise, the transport delay and actuator movement constraints can be lessened.

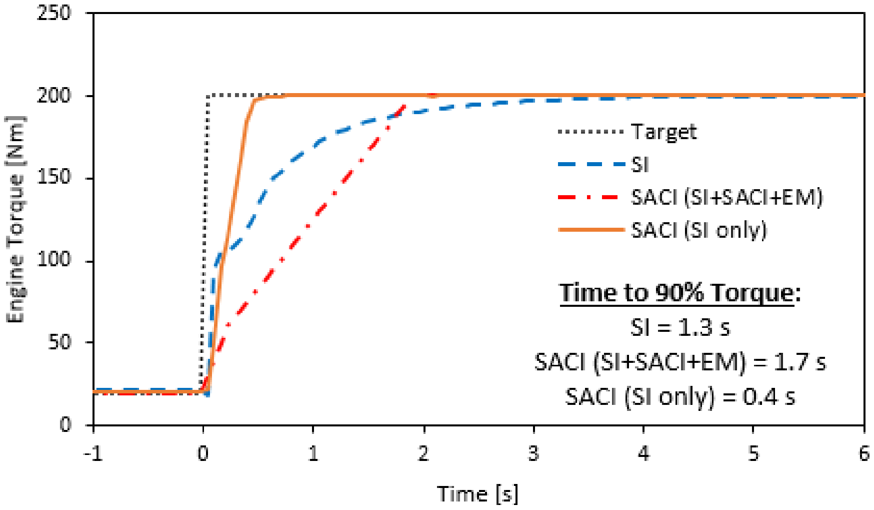

Figure B-4: Tip-in and tip-out for conventional SI and multi-mode SACI. Note the clear turbocharger lag which slows the rate of increase in torque. The larger displacement supercharged SACI engine can increase the trapped mass much quicker, but the complex controls slows the rate of change of engine load.

Vehicle Model Results

The vehicle model is exercised over four drive cycles: US06, FTP-75, HWFET, and the NEDC. The miles per gallon (MPG) relative to a non-HEV conventional engine for each configuration and each drive cycle is plotted in Figure B-5. For both engines, greater electrification improves fuel economy by eliminating low-efficiency operation and recovering braking energy. The SACI powertrain demonstrates a 4–5% improvement over the conventional SI engine in all cases. The improvement is not as strong as shown by HCCI with Lawler et al. [123], however, the type of reference engine is different. In their work, a naturally aspirated 2.5 L SI engine is the baseline. In this work, a modern downsized 1.5 L turbocharged engine serves as the benchmark. This degree of downsizing alone is expected to achieve 6–15% improvement depending on the drive cycle (excluding hybridization) [125]. Thus, despite the loss of drive cycle fuel economy due to upsizing and with both engines having the same HEV configuration and control strategy, the

SACI engine still offers a net fuel economy benefit. Furthermore, a SACI P0 hybrid engine has a similar fuel economy as a P2 hybrid with a conventional powertrain. A cost analysis is outside the scope of this work, but it is plausible that a P0 SACI hybrid is preferable to a P2 SI hybrid after considering the relative cost, packaging, and complexity. There is a significant improvement from a P0 hybrid as engine stopping during the FTP-75 and NEDC cycles saves fuel. The HWFET cycle has little opportunity for regenerative braking, thus there is limited recuperated energy to be used to offset fuel consumption. Further electrification continues to improve fuel economy; however, the gains are incremental.

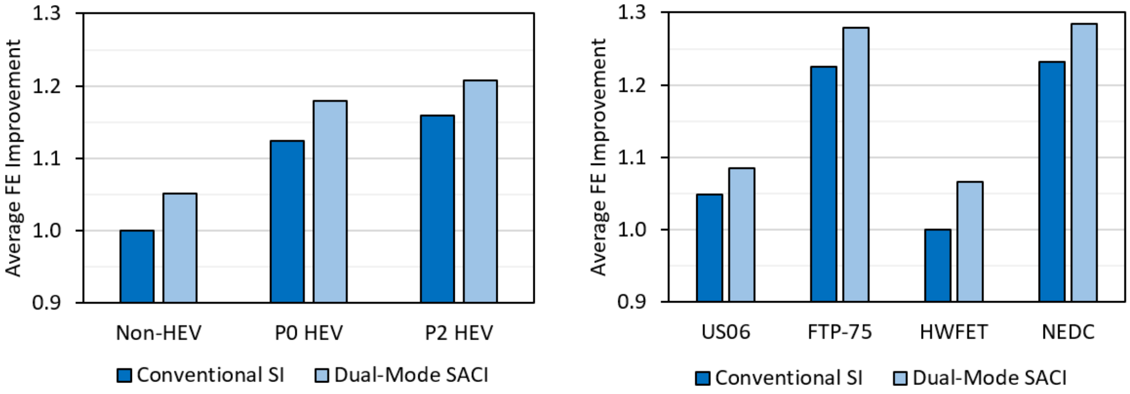

Figure B-5: (left) MPG improvement relative to conventional SI engine for all drive cycles and HEV configurations. (right) Relative MPG improvement for the P0 HEV for each drive cycle.

The SACI engine frequently switched combustion modes over a drive cycle. While there may also be a fuel economy impact of these transitions, the control implications are substantial. The previous section described the cycle-by-cycle charge preparation challenge that must be overcome to switch between SACI and SI and between lean and stoichiometric SACI. Electrification is helpful in easing the control burden of the mode transition, but it can also eliminate mode transitions by extending each mode to higher and lower torque boundaries. In the P0 HEV configuration, the electric machine can add or absorb up to 5 kW to the engine power, while the engine can remain in the current mode. For example, consider a portion of the US06 cycle, Figure B-6. The base strategy, which makes no attempt to maintain the current combustion mode, switches among four combustion modes ten times over the course of 35 seconds. Leveraging the modest 5 kW electric machine eliminates one combustion mode (high-load SI) and reduces the number of mode switches to six. Mode switches that are not eliminated are delayed by about 1 second, extending the time for the engine controller to manage the mode transition.

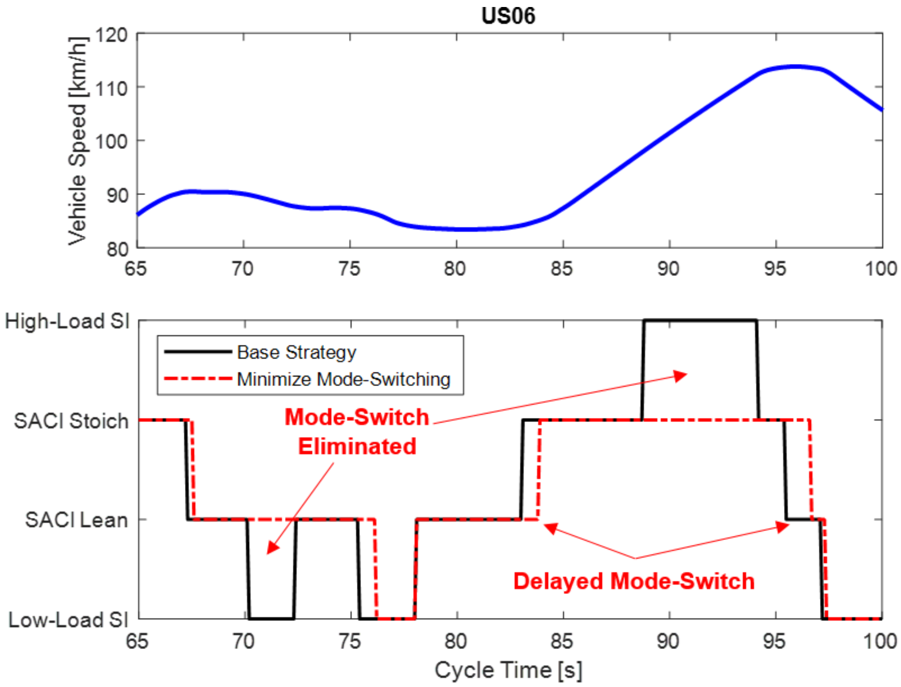

Figure B-6: Combustion mode strategy comparison. The strategy that leverages the electric machine to minimize mode switching delays or eliminates mode switches.

Mode switches that are eliminated require the engine controller to hold engine torque at the transition point, while the electric machine absorbs or augments driveline torque to achieve the desired traction power (Figure B-7). For this example, the 5 kW electric machine has about 25 Nm of torque capability at this speed (~2000 RPM). For the cases where the mode switch is delayed, the rapid engine torque change when the mode-switch does occur is not feasible. The production controller would instead leverage this time to begin the mode transition so that it is completed by the time the electric motor capacity is reached.

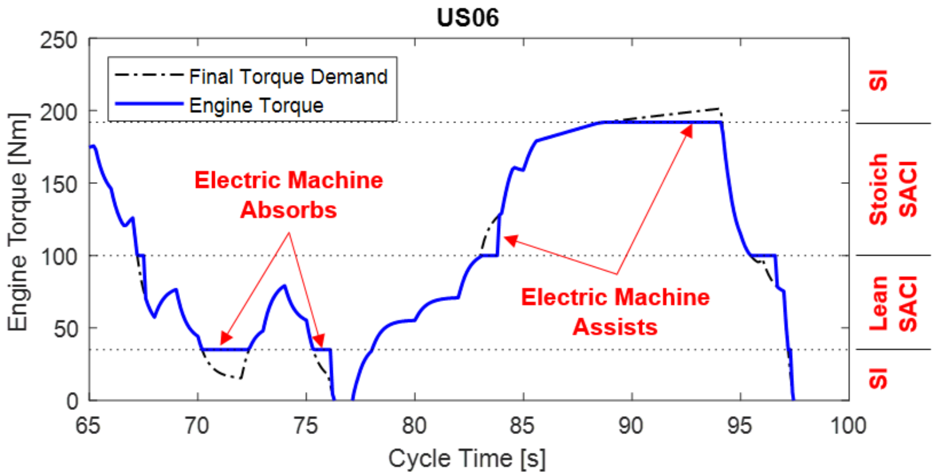

Figure B-7: Total torque demand and engine torque over a portion of the US06. The combustion strategies are indicated on the right side of the figure. The 5-kW electric machine absorbs or assists in regions where a mode-shift has been eliminated or delayed.

Evaluation the performance of this control strategy over the four drive cycles can be challenging, as there may be an imbalance in the absorption and assisting by the electric machine. For example, over the NEDC cycle the controller spends about 30% of the time absorbing engine torque, mostly while the engine is operating in the lean SACI mode. Conversely, less than 3% of the time is spent using the stored electrical energy to augment the engine torque either to maintain the current mode or for extra peak power. A charge sustaining strategy would either need to reduce the energy absorbed or find a suitable alternative use for this energy. The development of the control strategy to achieve charge sustaining and mode-switch-minimization is outside the scope of this work, however, a valuable comparison can still be made. Rather than comparing drive cycle fuel economy, three results will be examined. First, the percent reduction in mode switches offers a quantifiable metric for the simplification of the controls challenge. Second, the portion of time spent in either the lean or stoichiometric SACI mode provides an indication of potential fuel economy improvements. Finally, the average BSFC over the drive cycle quantifies this potential fuel economy improvement.

Table B-3 lists the reduction in mode switches and the time in either SACI mode for each drive cycle. The minimization of mode-switching (MMS) strategy reduces mode switches by 15–40% depending on the cycle, with the HWFET cycle benefiting the most. The other three cycles have a significant number of times where the vehicle must come to a complete stop. Mode-switching during a complete stop cannot be avoided. However, these conditions may enable alternatives to progressing through all the combustion modes. For example, a fuel-cut during the deceleration or SI only during the acceleration from a stop are relatively straightforward from a control perspective. The time in SACI mode is most improved for the low-power drive cycles (FTP-75 and NEDC), as the typical engine torque is below the minimum SACI torque. These cycles improve mostly from the extension of the lean SACI mode to lower loads.

Table B-3. Drive cycle analysis of the minimization of mode-switching (MMS) strategy.

		Time in SACI Mode		
Drive Cycle	**Reduction in Mode Switches with MMS**	Base Strategy	MMS Strategy	Change (MMS/Base)
US06	20.9%	56.9%	60.3%	106%
FTP-75	15.4%	25.4%	36.2%	143%
HWFET	39.7%	77.1%	84.5%	110%
NEDC	20.3%	27.2%	48.8%	179%

Based on the substantial increase in SACI operation for the FTP-75 and NEDC, the average engine BSFC over these drive cycles improves the most. The other two cycles do show an improvement; however, it is only slight. Figure B-8 and Table B-3 compares the base and MMS SACI strategies to each other and the conventional SI engine for reference. Both SACI control strategies improve upon the conventional SI engine, though the MMS strategy has the strongest improvement. Avoiding the low-load SI operation is the most significant source of improvement for the two low-power cycles (FTP-75 and NEDC).

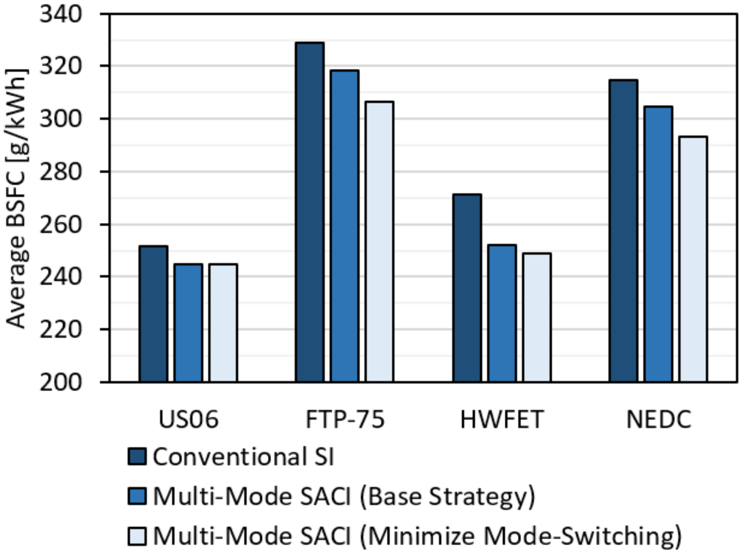

Figure B-8: Average BSFC over four drive cycles for three engine configurations. The SACI powertrain shows improvement for both control strategies, however, the minimization of mode-switching strategy has the strongest advantage.

Summary

A simulation is performed to demonstrate the fuel economy improvement potential of SACI compared to a modern downsized turbocharged engine for an electrified powertrain. The objective is to illustrate the potential synergy between SACI and electrification, specifically as it relates to the control challenge of mode-switching. A tip-in at 2000 RPM is simulated, which demonstrates the capability for a 5-kW electric machine to aid in eliminating torque disturbances during mode transitions. These torque disturbances arise from transport delays (e.g., external EGR), finite actuator movement rates, and cycle-by-cycle variation in in-cylinder composition, among others.

The two engines are evaluated over four drive cycles in non-HEV, P0 HEV, and P2 HEV configurations. For all architectures, the SACI powertrain demonstrates a 4–5% improvement in fuel economy, with greater electrification slightly reducing the SACI advantage. A minimization of mode-switching (MMS) strategy is introduced to reduce the control burden of mode switching. The load limits of both SACI modes are extended by using the electric machine to absorb or augment driveline torque as needed to maintain the current combustion mode. Over the four drive cycles, 15–40% of mode-switches are eliminated, mostly during continuous engine operation. The portion of time in SACI mode is significantly increased for low-power drive cycles (FTP-75 and NEDC) from the extending the lean SACI mode to lower driveline.

The following conclusion are drawn as it relates to the production control of an electrified SACI engine:

1. The efficiency benefit of a SACI engine is largely additive to powertrain electrification.
2. A 5 kW electric machine can eliminate torque disturbances as the engine transitions from one combustion mode to another. The impact of transport delays and finite actuator movement rates are effectively mitigated.
3. A 5 kW electric machine can eliminate or delay mode-switches during drive cycle operation.
4. More electrification further reduces the control complexity as a greater tolerance to torque error is acceptable. Thus, increased powertrain electrification is an enabling technology for SACI as it reduces the controls burden of mode switching.

REFERENCES

[1] Heywood, J. B., "Internal Combustion Engine Fundamentals," (New York, McGraw-Hill, 1988), ISBN: 0-07-028637-X.

[2] Glassman, I., "Combustion," (San Diego, Academic Press, 1996), ISBN: 0-12-285852-2.

[3] Turns, S., "An Introduction to Combustion," (Boston, McGraw-Hill, 2000), ISBN: 0-07-230096-5.

[4] Eng, J. A., "Characterization of Pressure Waves in HCCI Combustion," SAE Technical Paper 2002-01-2859, 2002, doi:10.4271/2002-01-2859.

[5] Idicheria, C. A. and Pickett, L. M., "Soot Formation in Diesel Combustion under High-EGR Conditions," 2005, doi:10.4271/2005-01-3834.

[6] Jacobs, T. J., Bohac, S. V., Assanis, D. N., and Szymkowicz, P. G., "Lean and Rich Premixed Compression Ignition Combustion in a Light-Duty Diesel Engine," 2005, doi:10.4271/2005-01-0166.

[7] Alger, T., Gingrich, J., Roberts, C., and Mangold, B., "Cooled exhaust-gas recirculation for fuel economy and emissions improvement in gasoline engines," *International Journal of Engine Research* 12(3):252-264, 2011, doi:10.1177/1468087411402442.

[8] Cairns, A., Blaxill, H., and Irlam, G., "Exhaust Gas Recirculation for Improved Part and Full Load Fuel Economy in a Turbocharged Gasoline Engine," SAE Technical Paper 2006-01-0047, 2006, doi:10.4271/2006-01-0047.

[9] Duchaussoy, Y., Lefebvre, A., and Bonetto, R., "Dilution Interest on Turbocharged SI Engine Combustion," SAE Technical Paper 2003-01-0629, 2003, doi:10.4271/2003-01-0629.

[10] Onishi, S., Jo, S. H., Shoda, K., Jo, P. D., et al., "Active Thermo-Atmosphere Combustion (ATAC) - A New Combustion Process for Internal Combustion Engines," SAE Technical Paper 790501, 1979, doi:10.4271/790501.

[11] Najt, P. and Foster, D. E., "Compression-Ignited Homogeneous Charge Combustion," SAE Technical Paper 830264, 1983, doi:10.4271/830264.

[12] Thring, R. H., "Homogeneous Charge Compression Ignition (HCCI) Engines: A Review," SAE Technical Paper 892068, 1989, doi:10.4271/892068.

[13] Noguchi, M., Tanaka, Y., Tanaka, T., and Takeuchi, Y., "A Study on Gasoline Engine Combustion by Observation of Intermediate Reactive Products during Combustion," SAE Technical Paper 790840, 1979, doi:10.4271/790840.

[14] Zhao, F., Asmus, T., Assanis, D., Dec, J., et al., "Homogeneous Charge Compression Ignition (HCCI) Engines," (Warrendale, SAE, 2003), ISBN: 978-0-7680-1123-4.

[15] Dec, J., Dernotte, J., and Ji, C., "Increasing the Load Range, Load-to-Boost Ratio, and Efficiency of Low-Temperature Gasoline Combustion (LTGC) Engines," *SAE Int. J. Engines* 10(3):1256-1274, 2017, doi:10.4271/2017-01-0731.

[16] Güralp, O., Hoffman, M., Assanis, D. N., Filipi, Z., et al., "Characterizing the Effect of Combustion Chamber Deposits on a Gasoline HCCI Engine," SAE Technical Paper 2006-01-3277, 2006, doi:10.4271/2006-01-3277.

[17] Hoffman, M., O'Donnell, R., and Filipi, Z., "Partial Transparency of Advanced Compression Ignition Combustion Chamber Deposits, Its Impact on Combustion Chamber Wall Temperatures and Application to Thermal Barrier Coating Design," *SAE International Journal of Engines* 11(2):179-194, 2018, doi:10.4271/03-11-02-0012.

[18] Hoffman, M. A. and Filipi, Z., "Influence of Directly Injected Gasoline and Porosity Fraction on the Thermal Properties of HCCI Combustion Chamber Deposits," SAE Technical Paper 2015-24-2449, 2015, doi:10.4271/2015-24-2449.

[19] Bunce, M. and Blaxill, H., "Methodology for Combustion Analysis of a Spark Ignition Engine Incorporating a Pre-Chamber Combustor," SAE Technical Paper 2014-01-2603, 2014, doi:10.4271/2014-01-2603.

[20] Dec, J. E., Yang, Y., Dernotte, J., and Ji, C., "Effects of Gasoline Reactivity and Ethanol Content on Boosted, Premixed and Partially Stratified Low-Temperature Gasoline Combustion (LTGC)," *SAE Int. J. Engines* 8(3):935-955, 2015, doi:10.4271/2015-01-0813.

[21] Lawler, B., Mamalis, S., Joshi, S., Lacey, J., et al., "Understanding the effect of operating conditions on thermal stratification and heat release in a homogeneous charge compression ignition engine," *Applied Thermal Engineering* 112:392-402, 2017, doi:10.1016/j.applthermaleng.2016.10.056.

[22] Sofianopoulos, A., Rahimi Boldaji, M., Lawler, B., and Mamalis, S., "Analysis of Thermal Stratification Effects in HCCI Engines Using Large Eddy Simulations and Detailed Chemical Kinetics," SAE Technical Paper 2018-01-0189, 2018, doi:10.4271/2018-01-0189.

[23] Dec, J. and Yang, Y., "Boosted HCCI for High Power without Engine Knock and with Ultra-Low NOx Emissions - using Conventional Gasoline," *SAE Int. J. Engines* 3(1):750-767, 2010, doi:10.4271/2010-01-1086.

[24] Christensen, M., Johansson, B., Amnéus, P., and Mauss, F., "Supercharged Homogeneous Charge Compression Ignition," SAE Technical Paper 980787, 1998, doi:10.4271/980787.

[25] Urushihara, T., Yamaguchi, K., Yoshizawa, K., and Itoh, T., "A Study of a Gasoline-fueled Compression Ignition Engine ~ Expansion of HCCI Operation Range Using SI Combustion as a Trigger of Compression Ignition," SAE Technical Paper 2005-01-0180, 2005, doi:10.4271/2005-01-0180.

[26] Zigler, B., "An experimental investigation of the ignition properties of low temperature combustion in an optical engine," PhD Thesis, The University of Michigan, Ann Arbor, 2008.

[27] Wang, Z., He, Z., Wang, J., Shuai, S., et al., "Combustion visualization and experimental study on spark induced compression ignition (SICI) in gasoline HCCI engines," *Energy Conversion and Management* 51(5):908-917, 2010.

[28] Kalian, N., Zhao, H., and Yang, C., "Effects of spark-assistance on controlled auto-ignition combustion at different injection timings in a multicylinder direct-injection gasoline engine," *International Journal of Engine Research* 10(3):133-148, 2009, doi:10.1243/14680874JER03209.

[29] Matsumoto K., Urushihara T., Inoue A., Kawai Y., et al., "Engine Control Device," Patent EP3421766A1, 2019.

[30] Olesky, L. M., Martz, J. B., Lavoie, G. A., Vavra, J., et al., "The effects of spark timing, unburned gas temperature, and negative valve overlap on the rates of stoichiometric spark assisted compression ignition combustion," *Applied Energy* 105:407-417, 2013, doi:10.1016/j.apenergy.2013.01.038.

[31] Lavoie, G. A., Martz, J., Wooldridge, M., and Assanis, D., "A multi-mode combustion diagram for spark assisted compression ignition," *Combustion and Flame* 157(6):1106-1110, 2010, doi:10.1016/j.combustflame.2010.02.009.

[32] Li, L., Xie, H., Chen, T., Yu, W., et al., "Experimental Study on Spark Assisted Compression Ignition (SACI) Combustion with Positive Valve Overlap in a HCCI Gasoline Engine," SAE Technical Paper 2012-01-1126, 2012, doi:10.4271/2012-01-1126.

[33] Weall, A. J. and Szybist, J. P., "The Effects of Fuel Characteristics on Stoichiometric Spark-Assisted HCCI," *Journal of Engineering for Gas Turbines and Power* 134(7):72805, 2012, doi:10.1115/1.4006007.

[34] Szybist, J. P. and Nafziger, E. J., "Load Expansion of Stoichiometric HCCI Using Spark Assist and Hydraulic Valve Actuation," *SAE Int. J. Engines* 3(2):244-258, 2010, doi:10.4271/2010-01-2172.

[35] Manofsky, L., Vavra, J., Assanis, D. N., and Babajimopoulos, A., "Bridging the Gap between HCCI and SI: Spark-Assisted Compression Ignition," SAE Technical Paper 2011-01-1179, 2011, doi:10.4271/2011-01-1179.

[36] Zhou, L., Dong, K., Hua, J., Wei, H., et al., "Effects of applying EGR with split injection strategy on combustion performance and knock resistance in a spark assisted compression ignition (SACI) engine," *Applied Thermal Engineering* 145:98-109, 2018, doi:10.1016/j.applthermaleng.2018.09.001.

[37] Wang, Z., Wang, J., Shuai, S., He, X., et al., "Research on Spark Induced Compression Ignition (SICI)," SAE Technical Paper 2009-01-0132, 2009, doi:10.4271/2009-01-0132.

[38] Chiodi, M., Kaechele, A., Bargende, M., Wichelhaus, D., et al., "Development of an Innovative Combustion Process," *SAE Int. J. Engines* 10(5):2486-2499, 2017, doi:10.4271/2017-24-0147.

[39] Koch, D., Berger, V., Bittel, A., Gschwandtner, M., et al., "Investigation of an Innovative Combustion Process for High-Performance Engines and Its Impact on Emissions," SAE Technical Paper 2019-01-0039, 2019, doi:10.4271/2019-01-0039.

[40] "Mazda Next-Generation Technology - Press Information," Contify Automotive News, 2017.

[41] Johnson, T. and Joshi, A., "Review of Vehicle Engine Efficiency and Emissions," *SAE Int. J. Engines* 11(6):1307-1330, 2018, doi:10.4271/2018-01-0329.

[42] Lee, S., Schenk, C., and McDonald, J., "Air Flow Optimization and Calibration in High-Compression-Ratio Naturally Aspirated SI Engines with Cooled-EGR," SAE Technical Paper 2016-01-0565, 2016, doi:10.4271/2016-01-0565.

[43] Stuhldreher, M., Kargul, J., Barba, D., McDonald, J., et al., "Benchmarking a 2016 Honda Civic 1.5-liter L15B7 Turbocharged Engine and Evaluating the Future Efficiency Potential of Turbocharged Engines," *SAE Int. J. Engines* 11(6):1273-1305, 2018, doi:10.4271/2018-01-0319.

[44] Zhang, Y., Xie, H., and Zhao, H., "Investigation of SI-HCCI Hybrid Combustion and Control Strategies for Combustion Mode Switching in a Four-Stroke Gasoline Engine," *Combustion Science and Technology* 181(5):782-799, 2009, doi:10.1080/00102200902868887.

[45] Yang, X. and Zhu, G., "SI and HCCI Combustion Mode Transition Control of an HCCI Capable SI Engine," *TCST* 21(5):1558-1569, 2013, doi:10.1109/TCST.2012.2201719.

[46] Angelos, J. P., Andreae, M. M., Green, W. H., Cheng, W. K., et al., "Effects of Variations in Market Gasoline Properties on HCCI Load Limits," SAE Technical Paper 2007-01-1859, 2007, doi:10.4271/2007-01-1859.

[47] Koopmans, L., Strömberg, E., and Denbratt, I., "The Influence of PRF and Commercial Fuels with High Octane Number on the Auto-ignition Timing of an Engine Operated in HCCI Combustion Mode with Negative Valve Overlap," SAE Technical Paper 2004-01-1967, 2004, doi:10.4271/2004-01-1967.

[48] Szybist, J. P. and Splitter, D. A., "Pressure and temperature effects on fuels with varying octane sensitivity at high load in SI engines," *Combustion and Flame* 177(C):49-66, 2017, doi:10.1016/j.combustflame.2016.12.002.

[49] Yun, H., Wermuth, N., and Najt, P., "High Load HCCI Operation Using Different Valving Strategies in a Naturally-Aspirated Gasoline HCCI Engine," *SAE Int. J. Engines* 4(1):1190-1201, 2011, doi:10.4271/2011-01-0899.

[50] Polovina, D., McKenna, D., Wheeler, J., Sterniak, J., et al., "Steady-State Combustion Development of a Downsized Multi-Cylinder Engine with Range Extended HCCI/SACI Capability," *SAE Int. J. Engines* 6(1):504-519, 2013, doi:10.4271/2013-01-1655.

[51] Olesky, L. K. M., Middleton, R. J., Lavoie, G. A., Wooldridge, M. S., et al., "On the sensitivity of low temperature combustion to spark assist near flame limit conditions," *Fuel* 158:11-22, 2015, doi:10.1016/j.fuel.2015.05.012.

[52] Vent, G., Enderle C., Merdes N., Kreitmann F., et al., "The new 2.0l turbo engine from the Mercedes- Benz 4-cylinder engine family," 2012.

[53] Atkinson, C., "Fuel Efficiency Optimization using Rapid Transient Engine Calibration," SAE Technical Paper 2014-01-2359, 2014, doi:10.4271/2014-01-2359.

[54] Brahma, I. and Chi, J. N., "Development of a model-based transient calibration process for diesel engine electronic control module tables – Part 1: data requirements, processing, and analysis," *International Journal of Engine Research* 13(1):77-96, 2012, doi:10.1177/1468087411424376.

[55] Brahma, I., "Development of Dynamic Constraint Models for a Model Based Transient Calibration Process," *SAE International Journal of Engines* 4(1):828-836, 2011, doi:10.4271/2011-01-0691.

[56] Suzuki, K., Nemoto, M., and Machida, K., "Model-Based Calibration Process for Producing Optimal Spark Advance in a Gasoline Engine Equipped with a Variable Valve Train," SAE Technical Paper 2006-01-3235, 2006, doi:10.4271/2006-01-3235.

[57] Yang, X. and Zhu, G., "A two-zone control oriented SI-HCCI hybrid combustion model for the HIL engine simulation," American Control Conference, June 2011.

[58] Ortiz-Soto E., "Combustion Modeling of Spark Assisted Compression Ignition for Experimental Analysis and Engine System Simulations," The University of Michigan, Ann Arbor, 2013.

[59] Grenda, J. M., "Numerical Modeling of Charge Stratification for the Combustion Control of HCCI Engines," SAE Technical Paper 2005-01-3722, 2005, doi:10.4271/2005-01-3722.

[60] Nakai, E., Goto, T., Ezumi, K., Tsumura, Y., et al., "Mazda SkyActiv-X 2.0L Gasoline Engine," *28th Aachen Colloquium Automobile and Engine Technology*, 2019.

[61] Levenberg, K., "A method for the solution of certain non-linear problems in least squares," *Quart. Appl. Math.* 2(2):164-168, 1944.

[62] Marquardt, D. W., "An algorithm for least-squares estimation of nonlinear parameters," *Journal of the society for Industrial and Applied Mathematics* 11(2):431-441, 1963.

[63] Abu-Mostafa, Y. S., Magdon-Ismail, M., and Lin, H., "Learning from Data," (New York, NY, AMLBook, 2012), ISBN: 978-1600490064.

[64] Foresee, D. and Hagan, M., "Gauss-Newton approximation to Bayesian learning," International Conference on Neural Networks, 1997.

[65] McKay, M. D., Beckman, R. J., and Conover, W. J., "A Comparison of Three Methods for Selecting Values of Input Variables in the Analysis of Output from a Computer Code," *Technometrics* 21(2):239-245, 1979.

[66] Nishida, K. and Hiroyasu, H., "Simplified Three-Dimensional Modeling of Mixture Formation and Combustion in a D.I. Diesel Engine," SAE Technical Paper 890269, 1989, doi:10.4271/890269.

[67] Sjöberg, M., Dec, J. E., and Cernansky, N. P., "Potential of Thermal Stratification and Combustion Retard for Reducing Pressure-Rise Rates in HCCI Engines, Based on Multi-Zone Modeling and Experiments," SAE Technical Paper 2005-01-0113, 2005, doi:10.4271/2005-01-0113.

[68] Babajimopoulos, A., Assanis, D. N., Flowers, D. L., Aceves, S. M., et al., "A fully coupled computational fluid dynamics and multi-zone model with detailed chemical kinetics for the simulation of premixed charge compression ignition engines," *International journal of engine research* 6(5):497-512, 2005, doi:10.1243/146808705X30503.

[69] Aceves, S. M., Flowers, D. L., Westbrook, C. K., Smith, J. R., et al., "A Multi-Zone Model for Prediction of HCCI Combustion and Emissions," SAE Technical Paper 2000-01-0327, 2000, doi:10.4271/2000-01-0327.

[70] Babajimopoulos, A., Assanis, D. N., and Fiveland, S. B., "An Approach for Modeling the Effects of Gas Exchange Processes on HCCI Combustion and Its Application in Evaluating Variable Valve Timing Control Strategies," SAE Technical Paper 2002-01-2829, 2002, doi:10.4271/2002-01-2829.

[71] Priyadarshini, P., Sofianopoulos, A., Mamalis, S., Lawler, B., et al., "Understanding partial fuel stratification for low temperature gasoline combustion using large eddy simulations," *International journal of engine research*:146808742092104, 2020, doi:10.1177/1468087420921042.

[72] Pomraning, E. and Rutland, C. J., "Dynamic One-Equation Nonviscosity Large-Eddy Simulation Model," *AIAA Journal* 40(4):689-701, 2002, doi:10.2514/2.1701.

[73] Richards K.J., Senecal P.K., and Pomraning E., CONVERGE 3.0, Convergent Science, Madison, WI, 2019.

[74] Desantes, J. M., Payri, R., Salvador, F. J., and Gil, A., "Development and validation of a theoretical model for diesel spray penetration," *Fuel* 85(7):910-917, 2006, doi:10.1016/j.fuel.2005.10.023.

[75] Tetrault, P., Plamondon, E., Breuze, M., Hespel, C., et al., "Fuel Spray Tip Penetration Model for Double Injection Strategy," SAE Technical Paper 2015-01-0934, 2015, doi:10.4271/2015-01-0934.

[76] Taglialatela Scafati, F., Pirozzi, F., Cannavacciuolo, S., Allocca, L., et al., "Real Time Control of GDI Fuel Injection during Ballistic Operation Mode," SAE Technical Paper 2015-24-2428, 2015, doi:10.4271/2015-24-2428.

[77] Skiba, S. and Melbert, J., "Dosing Performance of Piezo Injectors and Sensorless Closed-Loop Controlled Solenoid Injectors for Gasoline Direct Injection," *SAE International Journal of Engines* 5(2):330-335, 2012, doi:10.4271/2012-01-0394.

[78] Perini, F., Dempsey, A., Reitz, R. D., Sahoo, D., et al., "A Computational Investigation of the Effects of Swirl Ratio and Injection Pressure on Mixture Preparation and Wall Heat Transfer in a Light-Duty Diesel Engine," SAE Technical Paper 2013-01-1105, 2013, doi:10.4271/2013-01-1105.

[79] Zhang, Y., Pei, Y., Engineer, N., Cho, K., et al., "CFD-Guided Combustion Strategy Development for a Higher Reactivity Gasoline in a Light-Duty Gasoline Compression Ignition Engine," SAE Technical Paper 2017-01-0740, 2017, doi:10.4271/2017-01-0740.

[80] Sellnau, M., Foster, M., Hoyer, K., Moore, W., et al., "Development of a Gasoline Direct Injection Compression Ignition (GDCI) Engine," *SAE International Journal of Engines* 7(2):835-851, 2014, doi:10.4271/2014-01-1300.

[81] Buri, S., Kubach, H., and Spicher, U., "Effects of increased injection pressures of up to 1000 bar – opportunities in stratified operation in a direct-injection spark-ignition engine," *International Journal of Engine Research* 11(6):473-484, 2010, doi:10.1243/14680874JER608.

[82] Chen, M., Zhang, W., Zhang, X., and Ding, N., "In-cylinder CFD Simulation of a New 2.0L Turbo Charged GDI Engine," SAE Technical Paper 2011-01-0826, 2011, doi:10.4271/2011-01-0826.

[83] Dong, Z., Shuai, S., Wang, Z., and Zhao, H., "CFD Modeling of Mixture Preparation and Soot Formation in a Downsized Gasoline Direct Injection Engine," SAE Technical Paper 2016-01-0586, 2016, doi:10.4271/2016-01-0586.

[84] Giovannoni, N., Breda, S., Paltrinieri, S., D'Adamo, A., et al., "CFD Analysis of the Effects of Fuel Composition and Injection Strategy on Mixture Preparation and Fuel Deposit Formation in a GDI Engine," SAE Technical Paper 2015-24-2408, 2015, doi:10.4271/2015-24-2408.

[85] R. G. Abdel-Gayed, K. J. Al-Khishali, and D. Bradley, "Turbulent Burning Velocities and Flame Straining in Explosions," *Proceedings of the Royal Society of London. A. Mathematical and Physical Sciences* 391(1801):393-414, 1984, doi:10.1098/rspa.1984.0019.

[86] Dai, W., Russ, S. G., Trigui, N., and Tallio, K. V., "Regimes of Premixed Turbulent Combustion and Misfire Modeling in SI Engines," SAE Technical Paper 982611, 1998, doi:10.4271/982611.

[87] Lewis, A., Ortiz-Soto, E., Lavoie, G., and Assanis, D. N., "Scaling and dimensional methods to incorporate knock and flammability limits in models of high-efficiency gasoline and ethanol engines," *International Journal of Engine Research* 16(2):181-196, 2015, doi:10.1177/1468087414530387.

[88] Yang, S. and Reitz, R. D., "Improved combustion submodels for modelling gasoline engines with the level set G equation and detailed chemical kinetics," *Proceedings of the Institution of Mechanical Engineers, Part D: Journal of Automobile Engineering* 223(5):703-726, 2009, doi:10.1243/09544070JAUTO1062.

[89] Martz, J.B., "Simulation and model development for auto-ignition and reaction front propagation in low-temperature high-pressure lean-burn engines," University of Michigan, 2010.

[90] Yang, X., "Modeling and control of SI and SI-HCCI hybrid combustion engines," PhD Thesis, Michigan State University, 2011.

[91] Ortiz-Soto, E. A., Lavoie, G. A., Wooldridge, M. S., and Assanis, D. N., "Thermodynamic efficiency assessment of gasoline spark ignition and compression ignition operating strategies using a new multi-mode combustion model for engine system simulations," *International Journal of Engine Research* 20(3):304-326, 2019, doi:10.1177/1468087417752195.

[92] Downs, D. and Wheeler, R. W., "Recent Developments in "Knock" Research," *Proceedings of the Institution of Mechanical Engineers: Automobile Division* 5(1):89-99, 1951, doi:10.1243/PIME_AUTO_1951_000_015_02.

[93] Kim, N., Vuilleumier, D., Sjöberg, M., Yokoo, N., et al., "Using Chemical Kinetics to Understand Effects of Fuel Type and Compression Ratio on Knock-Mitigation Effectiveness of Various EGR Constituents," SAE Technical Paper 2019-01-1140, 2019, doi:10.4271/2019-01-1140.

[94] Mehl, M., Pitz, W. J., Westbrook, C. K., and Curran, H. J., "Kinetic modeling of gasoline surrogate components and mixtures under engine conditions," *Proceedings of the Combustion Institute* 33(1):193-200, 2011, doi:10.1016/j.proci.2010.05.027.

[95] Douaud, A. M. and Eyzat, P., "Four-Octane-Number Method for Predicting the Anti-Knock Behavior of Fuels and Engines," SAE Technical Paper 780080, 1978, doi:10.4271/780080.

[96] Livengood, J. C. and Wu, P. C., "Correlation of autoignition phenomena in internal combustion engines and rapid compression machines," *Symposium (International) on Combustion* 5(1):347-356, 1955, doi:10.1016/S0082-0784(55)80047-1.

[97] Wu, Y., Pal, P., Som, S., and Lu, T., "A Skeletal Chemical Kinetic Mechanism For Gasoline and Gasoline/Ethanol Blend Surrogates for Engine CFD Applications," International Conference on Chemical Kinetics, 2017.

[98] Wang, S., Prucka, R., Zhu, Q., Prucka, M., et al., "A Real-Time Model for Spark Ignition Engine Combustion Phasing Prediction," *SAE International Journal of Engines* 9(2):1180-1190, 2016, doi:10.4271/2016-01-0819.

[99] Liu, C., Jiang, D., and Obokata, T., "A Simplified Turbulence Model for In-cylinder Gas Flow in Quasi-dimensional Turbulence Combustion Model for Spark-ignition Engines," SAE Technical Paper 2000-01-2803, 2000, doi:10.4271/2000-01-2803.

[100] Gukelberger, R., Gingrich, J., Alger, T., and Almaraz, S., "LPL EGR and D-EGR® Engine Concept Comparison Part 2," *SAE International Journal of Engines* 8(2):547-556, 2015, doi:10.4271/2015-01-0781.

[101] Babajimopoulos, Prasad Challa, V. S. S, Lavoie and Assanis. "Model-Based Assessment of Two Variable CAM Timing Strategies for HCCI Engines: Recompression vs. Rebreathing," Internal Combustion Engine Division Spring Technical Conference, Jan 1, 2009, doi:10.1115/ICES2009-76103.

[102] Zhou, Y., Hariharan, D., Yang, R., Mamalis, S., et al., "A predictive 0-D HCCI combustion model for ethanol, natural gas, gasoline, and primary reference fuel blends," *Fuel* 237:658-675, 2019, doi:10.1016/j.fuel.2018.10.041.

[103] Triantopoulos, V., Martz, J., Sterniak, J., Lavoie, G., et al., "Operating Limits of Spark-Assisted Compression Ignition Combustion Under Boosted Ultra-EGR Dilute Conditions in a Negative Valve Overlap Engine," *Proceedings of the ASME 2019 Internal Combustion Engine Division*, 2018.

[104] Kirkpatrick, S., Gelatt, C. D., and Vecchi, M. P., "Optimization by Simulated Annealing," *Science (American Association for the Advancement of Science)* 220(4598):671-680, 1983, doi:10.1126/science.220.4598.671.

[105] Deb, K. and Jain, H., "An Evolutionary Many-Objective Optimization Algorithm Using Reference-Point-Based Nondominated Sorting Approach, Part I: Solving Problems With Box Constraints," *TEVC* 18(4):577-601, 2014, doi:10.1109/tevc.2013.2281535.

[106] "Nelder-Mead Simplex Algorithm," https://home.apache.org/~luc/commons-math-3.6-RC2-site/jacoco/org.apache.commons.math3.optimization.direct/NelderMeadSimplex.java.html, 10/03/2020.

[107] Mendrea, B., Chang, Y., Akkus, Y. Z. A., Sterniak, J., et al., "Investigations of the Effect of Ambient Condition on SACI Combustion Range," SAE Technical Paper 2015-01-0828, 2015, doi:10.4271/2015-01-0828.

[108] Robertson, D., Conway, G., Chadwell, C., McDonald, J., et al., "Predictive GT-Power Simulation for VNT Matching on a 1.6 L Turbocharged GDI Engine," SAE Technical Paper 2018-01-0161, 2018, doi:10.4271/2018-01-0161.

[109] Ayala, F. A. and Heywood, J. B., "Lean SI Engines: The role of combustion variability in defining lean limits," SAE Technical Paper 2007-24-0030, 2007, doi:10.4271/2007-24-0030.

[110] Conway, G., Robertson, D., Chadwell, C., McDonald, J., et al., "Evaluation of Emerging Technologies on a 1.6 L Turbocharged GDI Engine," SAE Technical Paper 2018-01-1423, 2018, doi:10.4271/2018-01-1423.

[111] Li, H., Yu, L., Lu, X., Ouyang, L., et al., "Autoignition of ternary blends for gasoline surrogate at wide temperature ranges and at elevated pressure: Shock tube measurements and detailed kinetic modeling," *Fuel* 181:916-925, 2016, doi:10.1016/j.fuel.2016.05.030.

[112] Robertson, D. and Prucka, R., "A Review of Spark -Assisted Compression Ignition (SACI) Research in the Context of Realizing Production Control Strategies," SAE Technical Paper 2019-24-0027, 2019, doi:10.4271/2019-24-0027.

[113] He, X., Donovan, M. T., Zigler, B. T., Palmer, T. R., et al., "An experimental and modeling study of iso-octane ignition delay times under homogeneous charge compression ignition conditions," *Combustion and Flame* 142(3):266-275, 2005, doi:10.1016/j.combustflame.2005.02.014.

[114] Sasaki, T., Bybee, M., and Gundlapally, S., "Knock Analysis and Prediction: Application to Motorcycle Engines," GT-Suite Conference, 2012.

[115] Yates, A. D. B., Swarts, A., and Viljoen, C. L., "Correlating Auto-Ignition Delays And Knock-Limited Spark-Advance Data For Different Types Of Fuel," SAE Technical Paper 2005-01-2083, 2005, doi:10.4271/2005-01-2083.

[116] Khaled, F., Badra, J., and Farooq, A., "Ignition delay time correlation of fuel blends based on Livengood-Wu description," *Fuel* 209:776-786, 2017, doi:10.1016/j.fuel.2017.07.095.

[117] Choi, Y. and Chen, J., "Fast prediction of start-of-combustion in HCCI with combined artificial neural networks and ignition delay model," *Proceedings of the Combustion Institute* 30(2):2711-2718, 2005, doi:10.1016/j.proci.2004.08.143.

[118] Pamminger, M., Hall, C., Wang, B., Wallner, T., et al., "Zero-Dimensional Heat Release Modeling Framework for Gasoline Compression-Ignition Engines with Multiple Injection Events," SAE Technical Paper 2019-24-0083, 2019, doi:10.4271/2019-24-0083.

[119] Egan, D., Koli, R., Zhu, Q., and Prucka, R., "Use of Machine Learning for Real-Time Non-Linear Model Predictive Engine Control," SAE Technical Paper 2019-01-1289, 2019, doi:10.4271/2019-01-1289.

[120] Tsurushima, T., "A new skeletal PRF kinetic model for HCCI combustion," *Proceedings of the Combustion Institute* 32(2):2835-2841, 2009, doi:10.1016/j.proci.2008.06.018.

[121] Wang, H., Jiao, Q., Yao, M., Yang, B., et al., "Development of an n-heptane/toluene/polyaromatic hydrocarbon mechanism and its application for combustion and soot prediction," *International Journal of Engine Research* 14(5):434-451, 2013, doi:10.1177/1468087412471056.

[122] Ortiz-Soto, E. A., Vavra, J., and Babajimopoulos, A., "Assessment of Residual Mass Estimation Methods for Cylinder Pressure Heat Release Analysis of HCCI Engines With Negative Valve Overlap," *Journal of Engineering for Gas Turbines and Power* 134(8):82802, 2012, doi:10.1115/1.4006701.

[123] Lawler, B., Ortiz-Soto, E., Gupta, R., Peng, H., et al., "Hybrid Electric Vehicle Powertrain and Control Strategy Optimization to Maximize the Synergy with a Gasoline HCCI Engine," *SAE International Journal of Engines* 4(1):1115-1126, 2011, doi:10.4271/2011-01-0888.

[124] Robertson, D. and Prucka, R., "Simulation-Based Evaluation of Spark-Assisted Compression Ignition Control for Production," SAE Technical Paper 2020-01-1145, 2020, doi:10.4271/2020-01-1145.

[125] Bassett, M., Hall, J., Cains, T., Underwood, M., et al., "Dynamic Downsizing Gasoline Demonstrator," *SAE International Journal of Engines* 10(3):884-891, 2017, doi:10.4271/2017-01-0646.